UNIVERSITÄT BAYREUTH

Dissertation

Optoelectronic properties of Bacteriochlorophyll chromophores: a first principles study

Von der Universität Bayreuth
zur Erlangung des Grades eines
Doktors der Naturwissenschaften (Dr. rer. nat.)
genehmigte Abhandlung

von
Zohreh Hashemi
aus dem Iran

Optoelectronic properties of Bacteriochlorophyll chromophores: a first principles study

Von der Universität Bayreuth
zur Erlangung des Grades eines
Doktors der Naturwissenschaften (Dr. rer. nat.)
genehmigte Abhandlung

von
Zohreh Hashemi
aus dem Iran

1. Gutachter: Dr. Linn Leppert
2. Gutachter: Dr. Björn Baumeier
3. Vorsitzender: Prof. Dr. Jürgen Köhler
4. Drittprüfer: Prof. Dr. Stephan Kümmel

Tag der Einreichung: 28.04.2023
Tag des Kolloquiums: 02.06.2023

Abstract

Indisputably, solar energy, which is by far the most sustainable energy resource, could be the ultimate solution to global energy demands in the future. The high efficiency and robustness of the natural photosynthetic apparatus of bacteria, algae, and plants in comparison to current artificial solar technologies render these systems the ideal inspiration for how to provide such energy. Bacteriochlorophyll and Chlorophyll aggregates, enclosed by transmembrane protein complexes, are the key building blocks of the photosynthetic systems. The energy of the absorbed sunlight is transported through light-harvesting systems and the primary charge separation process, triggered by this energy, initiates in the reaction center of the photosystem. An atomistic understanding of the primary photoinduced charge-transfer excitations controlled by these molecular aggregates, interpretation of their mechanisms, and the determination of their pathway in the reaction center can be inspiring for designing new photovoltaic and photocatalytic devices. Regardless of the great achievements of experimental approaches the assessment of first-principles quantum mechanical calculations is essential for achieving such information.

Linear response time-dependent density functional theory (TDDFT) is one of the main workhorses in most fields of physics and chemistry for calculating absorption spectra due to its reasonable computational cost and its potential for coupling with various types of methods for treating both solvent and solid-state effects. However, TDDFT encounters several challenges specifically in predicting charge-transfer excitations in these systems using (semi)local and even hybrid functionals, due to their non-local features. This problem is mostly overcome with range-separated hybrid functionals that significantly improve the prediction of charge-transfer excitations. An alternative method for studying excited state properties, with a tremendous agreement with gas phase experiments and higher accuracy theoretical methods, is through Green's

function-based many-body perturbation theory (MBPT) known as GW/BSE method. This method, which became more popular in recent years, has been successfully applied to different types of organic molecular systems and has shown a promising trend.

This thesis represents a comprehensive investigation of electronic and optical properties of molecular building blocks of photosynthetic systems by employing GW/BSE and state-of-the-art TDDFT approaches. In the first part of this thesis, we addressed the accuracy of TDDFT and the GW/BSE approach by carrying out a systematic study of the electronic and excited state structure of various types of Bacteriochlorophyll and Chlorophyll monomeric aggregates in combination with several exchange-correlation approximations. Consequently, we established reliable benchmark data for the performance of different density functionals in GW/BSE and TDDFT formalism in comparison with theoretical and experimental results. In the second part, I performed a set of calculations for BCL dimers, the smallest complexes in which charge-transfer excitations between molecules can be observed, to determine the effective factors on energy and character of these excitations. By means of this work, we identified the strengths and limitations of our methods and provided design rules for tailoring charge-transfer excitations in Bacteriochloropyll molecules. Finally, we studied realistic tetrameric and hexameric models of the reaction center of the purple bacterium *Rhodobacter sphaeroides*. The aim of this study was to determine the charge-transfer pathway and understand the importance of the protein environment on excitation energies. This study constitutes the first explicit TDDFT calculations on this reaction center including all six primary pigments and parts of the environment. A detailed picture of charge-transfer mechanism in this bacterial reaction center and the impact of direct inclusion of the protein environment on these excitations are provided. Our calculations confirmed the favorable charge-transfer pathway, supported by recent experimental studies, and furthermore, determined the lowest forward charge-transfer state of the system as the starting point of the charge separation process in these aggregates under the influence of nearby amino acids. Through this work, we paved the way for further first-principles investigations of the interplay between delocalized excited states of these pigments and other complex light-harvesting systems.

Kurzdarstellung

Unbestritten ist Solarenergie die nachhaltigste Energiequelle und könnte in Zukunft die ultimative Lösung für die Deckung des globalen Energiebedarfs darstellen. Die hohe Effizienz und Robustheit des natürlichen photosynthetischen Apparats von Bakterien, Algen und Pflanzen im Vergleich zu aktuellen künstlichen Solartechnologien machen diese Systeme zur idealen Inspiration für die Bereitstellung von Solarenergie. Das Rückgrat der Photosynthesesysteme bilden Bakteriochlorophyll- und Chlorophyll-Aggregate, welche von Transmembran-Protein-Komplexen umschlossen sind. Die Energie des absorbierten Sonnenlichts wird durch Lichtsammelsysteme transportiert, und der primäre Ladungstrennungsprozess, die Uebertragung dieser Energie ausgelöst wird, beginnt im Reaktionszentrum des Photosystems. Ein atomistisches Verständnis der primären photoinduzierten Ladungstransferanregungen, die von diesen molekularen Aggregaten kontrolliert werden, die Interpretation ihrer Mechanismen und die Bestimmung ihres Wegs im Reaktionszentrum können das Design neuer photovoltaischer und photokatalytischer Technologien statt Geräte inspirieren. Unabhängig von den großen Fortschritten der experimentellen Ansätze sind Bewertungen der quantenmechanischen Berechnungen erster Prinzipien unerlässlich, um solche Informationen zu erhalten.

Die zeitabhängige Dichtefunktionaltheorie (TDDFT) ist eine der wichtigsten Werkzeuge in vielen Bereichen der Physik und Chemie zur Berechnung von Absorptionsspektren aufgrund ihrer vertretbaren Berechnungskosten und ihres Potenzials zur Kopplung mit verschiedenen Arten von Methoden zur Behandlung von Loesungsmittel- und Festkörpereffekten. Allerdings hat die TDDFT bei der Vorhersage von Ladungstransferanregungen in diesen Systemen mit (semi-)lokalen und sogar hybriden Funktionen aufgrund ihrer nicht-lokalen Eigenschaften einige Herausforderungen zu Näherungen. Dieses Problem wird größtenteils durch reichweitenseparierte Hybridfunktionale überwunden, die die Vorhersage von Ladungstransferanregungen erheblich verbessern. Eine alterna-

tive Methode zur Untersuchung von angeregten Zuständen, die eine hohe Übereinstimmung mit Gasphasenexperimenten und theoretischen Methoden mit höherer Genauigkeit aufweist, ist die Vielteilchen-Störungstheorie (MBPT) auf der Basis der Greenschen Funktionen, bekannt als die GW/BSE-Methode. Diese Methode, die in den letzten Jahren immer beliebter geworden ist, wurde erfolgreich auf verschiedene Arten von organischen molekularen Systemen angewendet und hat eine vielversprechende Entwicklung gezeigt.

Diese Arbeit stellt eine umfassende Untersuchung der elektronischen und optischen Eigenschaften der molekularen Bausteine von Photosyntheticksystemen unter Verwendung von GW/BSE- und modernsten TDDFT-Ansätzen dar. Im ersten Teil dieser Arbeit haben wir uns mit der Effizienz von Methoden beschaeftigt, indem wir eine systematische Studie der elektronischen und angeregten Zustandsstruktur verschiedener Arten von Bacteriochlorophyll- und Chlorophyll-Molekuelen in Kombination mit mehreren Dichtefunktionalnaeherungen durchgeführt haben. Dadurch haben wir verlässliche Benchmark-Daten für die Leistung verschiedener Dichtefunktionale im GW/BSE- und TDDFT-Formalismus im Vergleich zu theoretischen und experimentellen Ergebnissen erhalten. In der zweiten Projektlinie haben wir eine Reihe von Berechnungen für Bacteriochlorophyll-Dimere durchgeführt, die kleinsten Komplexe, in denen Ladungstransferanregungen beobachtet werden können, um die effektiven Faktoren für Energie und Art dieser Anregungen zu bestimmen. Die dimerischen Systeme wurden aus verschiedenen Teilen des Photosynthesesystems von Purpurbakterien ausgewählt, um verschiedene Regime der intermolekularen Kopplung zu repraesentieren. Zuletzt wechselten wir zu tetrameren und hexameren BCL-Molekülsystemen, um den Ladungstransferweg und Umwelteinflüsse auf das Anregungsspektrum zu untersuchen, und schlossen explizit in den quantenchemischen Simulationen benachbarte Aminosäurereste ein. Diese Studie war die erste explizite TDDFT-Berechnung an einem Reaktionszentrummodell von *Rhodobacter sphaeroides*, das alle sechs primären Pigmente und Teile der Umgebung einschloss. Eine detaillierte Darstellung des Ladungstransfermechanismus im bakteriellen Reaktionszentrum und die Auswirkungen der direkten Einbindung der Proteinumgebung oder der vibronischen Kopplung auf diese Anregungen werden bereitgestellt. Unsere Berechnungen bestätigten den günstigen Ladungstransferweg, der durch aktuelle experimentelle Studien unterstützt wird, und bestimmten weiterhin den niedrigsten Vorwärts-Ladungstransferzustand des Systems als Ausgangspunkt des Ladungstrennungsprozesses in diesen Aggregaten unter dem Einfluss von nahegelegenen Aminosäuren. Durch diese Arbeit haben wir den Weg für weitere Untersuchungen der Wechselwirkungen zwischen den delokalisierten angeregten Zuständen dieser Pigmente und anderen komplexen Lichtsammelsystemen geebnet.

Contents

Chapter 1

Introduction

Due to the significant acceleration of energy consumption over the globe, one of the fundamental challenging areas ahead of humankind is to provide a long-term available and renewable source of clean energy [1]. Decades of investigation have shown that solar energy can be an unlimited provenance with boundless potential for these purposes [2]. To estimate the potential of this source, it is instructive to mention that the total absorbed energy by the earth is more than 116,000 TW (1 TW = 10^{12} W) while in 2010 the estimated average consumed energy by the modern world and planet life was only around 100 TW, that is a small fraction of absorbed sunlight [3]. Photosynthetic organisms through highly efficient processes, harvest solar energy and convert it into chemical energy. Photovoltaic devices are considered sustainable tools for this process, although the short-term analyses of the man-made energy-harvesting systems show, photochemical conversion can be two or three times more efficient than photovoltaic-driven electrolysis [4]. Meanwhile, in the natural photosynthetic apparatus of bacteria, algae, or plants the quantum efficiency of energy transfer and charge separation in some parts of the system are even higher than their man-made counterparts with values near to 95% [5, 6] and 70% [7], respectively. Despite their current lack of efficiency and robustness, artificial photosynthetic systems appear to be a promising puzzle piece in the quest to sustainably meet our energy demands of the future [8–10].

In natural photosynthetic systems, Bacteriochlorophyll (BCL) and Chlorophyll (Chl) molecules are the main pigments driving the primary excitation and charge-transfer processes in different types of photosynthesis bacteria. These aggregates, organized in highly coordinated multichromophoric complexes embedded in protein

matrices, guarantee an efficient transfer of excitation energy from the light-harvesting antennae (LH) to the reaction center (RC) where a charge-transfer excitation is triggered. Among different photosynthetic systems, the crystal structure of purple bacteria and their main features are well-characterized due to the high symmetry of these units [11–13]. In section 6.1 a complete overview of the mechanism of charge separation and charge-transfer in these systems along with the introduction of different units involved in this process is provided. The fundamental description of the electronic transitions in the RC attracted lots of attention in the past years due to its supreme role in the development of artificial analogs, solar technologies, or optoelectronic components [14]. Although spectroscopic techniques such as two-dimensional electronic spectroscopy (2DES) have allowed for a good understanding of the basic framework of these processes, the complexity of the photosynthetic systems resulted in some unanswered fundamental inquiries about their main features. Overcoming such problems and gaining a deeper atomic understanding of the molecular interaction between these aggregates requires tackling these systems from theoretical points of view. My thesis focuses on the electronic and excited-state structure of BCL(Chl) complexes found in the reaction center and light-harvesting apparatus of the purple bacteria.

Quantum mechanical (QM) methods, designed for the computation of excited-states properties play a pivotal role in the interpretation of experimental results for diverse types of systems without being overwhelmed by the complexity of the underlying processes. Furthermore, the combination of these methods with molecular dynamics and classical molecular mechanics constructed the ideal tools for the simulation of excitation processes in large pigment-protein complexes [15–18]. In principle, on atomic levels, the excited-state properties of these aggregates can be described by the concept of Frenkel exciton model for strongly bound excitons [19]. In this method, the Hamiltonian of multichromophoric systems is expressed in terms of the excitations of the single molecules and the electronic coupling between every two chromophores in the system [16]. In this regard, numerous types of QM methods, such as semiempirical and wavefunction-based methods have been used for the calculation of excitation energy and electron coupling of different types of chromophores [20–23]. However, maintaining a balance between accuracy and computational efficiency can be challenging when simulating such materials from first principles. For instance, while multireference wavefunction-based methods are known to be highly accurate for simulating photochemical processes, their application is currently limited to toy models of chromophores with small basis functions due to the high computational cost that scales as $O(N^{5-7})$ (N = electron number) [24]. As a result, considering higher order excitations and the larger number of molecules in the system is currently not an option in these methods [24].

Among the single-reference methods, linear-response time-dependent density func-

tional theory (TDDFT) [25] has become a widely used approach for simulating neutral and optical excitations. Its adiabatic approximation and favorable cost-accuracy ratio make it a versatile tool that has been applied to systems ranging from a single chromophore [26] to large photosynthesis pigment-protein complexes [27–29]. Even though the underlying conceptual framework of TDDFT is exact, in practice its traditional form is unreliable in the description of long-range charge-transfer excitations [30–32], doubly excited [33], and Rydberg [34] states as a result of inherently nonlocal nature of exchange-correlation functional in linear-response TDDFT. This challenge is mostly surpassed today by defining optimally-tuned range-separated exchange-correlation hybrid functionals that split the Coulomb interaction into a long-range and a short-range contribution. The innovation of this method is based on the so-called range-separation parameter ω, which controls the length scale of the transition from short-range to long-range. This parameter should be tuned non-empirically for each particular system for higher efficiency. The combination of TDDFT method with tuned range-separated hybrid functionals has shown great success in capturing the charge-transfer excitations of molecular systems [30, 35–37] and even with accuracy comparable to higher order wavefunction methods and experimental results [38–40]. Nevertheless, finding a universal and transferable separation parameter seems like an unfeasible task. Therefore searching for an alternative method is still a spending field of research.

The so-called many-body Green's function GW formalism within Bethe-Salpeter Equation (BSE) was developed alongside TDDFT to simulate optical excitations. However, it was not until recent years that GW/BSE gained attention for its ability to precisely predict the lowest electronically excited-states in organic and metallic molecular complexes [41–44]. Another interesting aspect of GW/BSE method is attributed to its remarkable success in the description of charge-transfer excitations [45–48], a feature shared only with the wavefunction-based approaches and TDDFT with optimally-tuned range-separated hybrid functionals [49]. The disadvantage of the primary formalism of GW/BSE method over TDDFT is its computational scaling of $O(N^5)$. Nowadays variant implementations and flavors of this method, that share the same formal scaling with TDDFT ($O(N^{3-4})$), made the simulation of finite size and extended molecular systems possible [24, 50].

In this thesis, I conducted a comprehensive first-principles investigation of neutral and charge-transfer excitations in various molecular complexes found in the photosynthesis apparatus. These complexes encompass a wide range of sizes, from individual BCL (ChL) molecules to hexameric structures, and were extracted from different regions of photosynthetic systems such as LHII and the RC of purple bacteria. To predict the structural, electronic, and photophysical properties of these aggregates, I employed linear-response TDDFT and GW/BSE with different types of exchange-

correlation functionals. The main intention of this thesis is not only to provide an atomistic understanding of charge-transfer excitations and their preferred pathway in the RC, but also to evaluate the performance of selected methods in comparison with wavefunction-based and experimental results.

Chapter 2 and 3 provide an introduction to the TDDFT approach, starting with its underlying ground-state method, DFT. These chapters cover important perspectives for distinguishing between different types of exchange-correlation approximations, characterizing neutral and charge-transfer excitations, and discussing the limitations of standard TDDFT in recognizing these types of excitations. In Chapter 4, the framework of GW method and the basic concepts behind the BSE scheme is reviewed. The advantages, limitations, and novelty of this method, compared to TDDFT and wavefunction-based methods, are also discussed comprehensively. In Chapter 5 different technical approaches related to the computational set-ups, which are crucial for maintaining the required accuracy of the calculations, are debated. Chapter 6 summarizes the resulting data and the main conclusions achieved in the course of this thesis, followed by four publications presented in Chapter 6 including further details.

Publication I and Publication II accessed the accuracy of G_0W_0/BSE, and $evGW$/BSE methods for describing excitation spectrum of BCL and Chl monomers and small molecular system of "Methylene blue" by employing different exchange-correlation functionals. Publication III is concerned with the charge-transfer excitations in different types of BCL dimeric systems - the smallest structural units in which excitations with intermolecular charge-transfer character can be observed. Building on the insights gained from previous publications, in Publication IV we investigated the electronic and excited-state properties of two tetrameric and one hexameric model system of BCL pigments found in the reaction center of purple bacteria.

Chapter 2

Density Functional Theory

The Density Functional Theory (DFT) is widely used for electronic structure calculations of various materials due to its simplicity and accuracy for systems with hundreds of particles. It is considered the dominant modeling method in condensed matter physics, quantum chemistry, and materials science [51, 52]. Although my thesis is mostly concerned with excited-states properties of molecular systems based on TDDFT or GW/BSE methods, it is essential to provide a general overview of the DFT approach as it forms the basis of these calculations. To keep the balance between brevity and coherence, I do not provide all the details in this thesis. A comprehensive description of this method can be found in the literature, such as Refs. [53–57].

The essence of this method is based on certain assumptions for solving the Schrödinger equation of a many-particle system with the wavefunction $\Psi(\mathbf{r}_1\sigma_1, \mathbf{r}_2\sigma_2, ..., \mathbf{r}_N\sigma_N)$ [58]. In the context of Hohenberg-Kohn and Kohn-Sham theorems in DFT, all physical observables of the N-electron system can be calculated by using an auxiliary non-interacting stationary system, whose ground-state density, $n(\mathbf{r})$, represents the ground-state density of the interacting system under consideration. Based on this assumption, the total energy of the system can be expressed as a function of this density, using a universal functional. Where the minimization of the total energy with respect to the density leads to the ground-state energy, E_0.

DFT simplifies the calculation of many-body systems by representing all quantities in terms of the ground-state density, $n(\mathbf{r})$, which depends only on the 3-dimensional coordinate space $\mathbf{r}$, rather than the original $3N$-dimensional many-body wavefunction. Such simplicity is practically in favor of encountering the many-body systems where

the computational costs of solving the original $3N$-dimensional wavefunction equation easily escalate exponentially to the expensive "exponential wall" [59]. Moreover, the spin-dependent formulation of DFT can account for spin-orbit coupling effects by replacing total density with the spin density, $n_{\sigma=\uparrow,\downarrow}(\mathbf{r})$, a feature which can be used in the case of open-shell systems or systems in a magnetic field. However, for convenience, the spin variable has been dropped in the formulations of all methods presented in this thesis as all calculations were performed under the spin-restricted condition. It should be noted, some conventional fundamental constants appear in the formalism of quantum chemical methods. To simplify the equations presented in this thesis, I use the atomic unit system where fundamental constants such as the reduced Planck's constant ($\hbar$), particle masses (m), and electron charge (e) are considered equal to one.

2.1. Schrödinger equation

All physical systems are a complex collection of electrons and nuclei that are attached to each other by repulsive and attractive Coulomb interactions. The time-dependent Schrödinger equation, which describes the alteration of a physical system wavefunction over time, is one of the fundamental equations in physics and the heart of quantum mechanics. The simple form of this equation in the nonrelativistic time-independent framework can be written as:

$$H \mid \Psi\rangle = E \mid \Psi\rangle \tag{2.1}$$

This equation relates the Hamiltonian operator H to the eigenvalue E, through associated eigenstates Ψ that are the solution of the above equation [52]. The effective Hamiltonian can be described as the sum of the kinetic and potential energy of the particles in which:

$$[\frac{-1}{2}\nabla^2 + U]\Psi = E\Psi \tag{2.2}$$

By writing the time-independent Schrödinger equation for a system of interacting particles, including repulsive and attractive Coulomb interaction of electrons and nuclei we obtain:

$$\begin{aligned}[-\frac{1}{2}\sum_i \nabla_i^2 - \sum_I \frac{1}{2M_I}\nabla_I^2 + \frac{1}{2}\sum_{i\neq j}\frac{1}{|\mathbf{r}_i - \mathbf{r}_j|} \\ + \frac{1}{2}\sum_{I\neq J}\frac{Z_I Z_J}{|\mathbf{R}_I - \mathbf{R}_J|} - \sum_{i,I}\frac{Z_I}{|\mathbf{r}_i - \mathbf{R}_I|}]\ \Psi = E\ \Psi\end{aligned} \tag{2.3}$$

where $\mathbf{r}_i$ ($\mathbf{R}_I$) are the position of electrons (nuclei) and M_I and Z_I are the atomic mass and number of the nuclei, respectively. The notation i/j and I/J run over the number

of electrons and nuclei (N and M). The many-body wavefunction $\Psi(\mathbf{r}_1, ...\mathbf{r}_N; \mathbf{R}_1, ..., \mathbf{R}_M)$ does not specifically carry any physical meaning and in principle can not be observed directly. Yet $|\Psi(\mathbf{r}_1, ...\mathbf{r}_N; \mathbf{R}_1, ..., \mathbf{R}_M)|^2$ can determine the probability of simultaneously finding particles $1, .., N/M$ at the equivalent coordinates $\mathbf{r}_1, ..., \mathbf{r}_N$ or $\mathbf{R}_1, ..., \mathbf{R}_M$ [52]. Solving the non-relativistic time-independent Schrödinger equation for a system that includes hundreds of particles is practically impossible due to the high number of components in the equation. One approach is to evaluate this equation for a stationary system under the Born-Oppenheimer (BO) approximation [60]. The BO approximation assumes that the nuclei, which are much heavier than electrons and move slower, can be considered fixed in position. As a result, the motion of nuclei can be separated from that of the electrons, and the wavefunction can be expressed solely in terms of electron positions:

$$\{-\frac{1}{2}\sum_i \nabla_i^2 + \frac{1}{2}\sum_{i\neq j}\frac{1}{|\mathbf{r}_i - \mathbf{r}_j|} - \sum_{i,I}\frac{Z_I}{|\mathbf{r}_i - \mathbf{R}_I|}\}\Psi = E\Psi \tag{2.4}$$

where the kinetic energies of the nuclei are excluded and the nuclei Coulomb repulsion is a constant value, $E = E_{tot} - \frac{1}{2}\sum_{I\neq J}\frac{Z_I Z_J}{|\mathbf{R}_I - \mathbf{R}_J|}$. The first and second terms are the introduced kinetic energy T and electron-electron repulsion potential U for a many-body system. The last term represents the electrostatic potential of the nuclei, which are assumed to be fixed in space and treated as an external potential V_{ext}. As a result, the many-body Hamiltonian can be expressed as a sum of these terms:

$$H = T + U + V_{ext} \tag{2.5}$$

Although the BO approximation simplified the time-independent Schrödinger equation by separating the nuclear-nuclear potential term, the electronic repulsion potential, U, causes entanglement between each pair of electron coordinates $\mathbf{r}_i$ and $\mathbf{r}_j$. This entanglement makes Eq. 2.4 a complicated partial differential equation, as the wavefunction depends on the $3N$ coordinates of all particles in the N-electron system. Since the late 1920s [52], many theories have been proposed to solve this complex problem. One of these theories is DFT, which is based on the Hohenberg and Kohn theorem.

2.2. Hohenberg-Kohn theorem

The concept of using the electron density distribution as a central factor for calculating electronic energy was first proposed by Thomas-Fermi's (TF) theory, shortly after the introduction of the Schrödinger equation [61]. Even though this approach established a link between the external potential, $V_{ext}(\boldsymbol{r})$, and the ground-state density $n(\boldsymbol{r})$, it

failed to describe the most general properties of the system, such as chemical binding. Eventually, the basic concept of Density functional theory, as we know it today was introduced by Hohenberg and Kohn in 1964 [62]. They proved that for a system of interacting electrons, the ground-state density $n(\boldsymbol{r})$ is sufficient to fully characterize any feature of the system, including ground-state energy and external potential V_{ext}, while these quantities are a unique functional of this density:

$$V_{ext}[n(\mathbf{r})] = \int n(\mathbf{r}) v_{ext} d^3r \tag{2.6}$$

$$E = E[n(\mathbf{r})]. \tag{2.7}$$

In this manner, instead of solving the Schrödinger equation in a complicated $3N$ dimension with a dependency on the N-particles wavefunction $\Psi(\boldsymbol{r}_1,\ldots,\boldsymbol{r}_N)$, one can define the ground-state energy as a functional of the density, a quantity that depends only on three specific coordinates $n(\boldsymbol{r})$. The ground-state density and ground-state energy of the system can be obtained by minimizing the total-energy functional [57]:

$$E = \min_{\Psi \to n} \langle \Psi | H | \Psi \rangle = \min_{\Psi \to n} \{F[n(\mathbf{r})] + V_{ext}[n]\} \tag{2.8}$$

where notation $\Psi \to n$ implies the minimization runs overall positive many-body wavefunctions. By convention, Hohenberg and Kohn called the first term in the equation, the universal functional $F[n]$ which is defined as:

$$F[n(\mathbf{r})] = \min_{\Psi \to n} [\langle \Psi[n] | T[n] + U[n] | \Psi[n] \rangle]. \tag{2.9}$$

This is simply the derivation of the kinetic and Coulomb interaction potential associated with ground-state density $n(\boldsymbol{r})$. This formalism establishes the existence and dependence of this universal functional to the ground-state density, but it does not specify the explicit form of the universal functional, $F[n]$. As Hohenberg and Kohn emphasized in their article, the twist is to accurately calculate this universal function, a challenge that continues even today. In addition, the many-body form of the Hohenberg-Kohn equation, Eq. 2.8, is computationally intractable for most systems. Kohn and Sham proposed a practical solution by introducing a set of non-interacting reference electrons, which is known today as the standard formulation of DFT.

2.3. Kohn-Sham equations

Kohn and Sham (KS) in 1965 [63] took one step further and assumed there is an auxiliary non-interacting system that has the exact same density $n(\boldsymbol{r})$ of the original

interacting system and built the ground-state density of this N-electron system based on the non-interacting orbitals $\phi_i(\boldsymbol{r})$ as:

$$n(\mathbf{r}) = \sum_{i=1}^{N} f_i |\phi_i(\mathbf{r})|^2. \tag{2.10}$$

Here f_i is the occupation number of orbital i and the sum over this variable will be equal to the total number of electrons in the system, $N = \sum_{i=1}^{N} f_i$.

Back to the definition of $F[n(\mathbf{r})]$ functional (Eq. 2.9), we need to rewrite kinetic and Coulomb energy terms based on the density of our non-interacting system. First, one can separate the non-interacting part of kinetic energy from the interacting ones:

$$T[n] = T_s[n] + T_c[n] \tag{2.11}$$

where $T_s[n] = -\frac{1}{2}\sum_{i=1}^{N} \int \phi_i^*(\mathbf{r}) \nabla_i^2 \phi_i(\mathbf{r}) d^3r$ is the sum of the kinetic energy of each particle in the non-interacting system with density $n(\boldsymbol{r})$ and $T_c[n]$ contains the reminder kinetic energies in the system or the correlation part. Furthermore, the Coulomb interaction can be approximated in terms of classical electrostatic Hartree energy as:

$$E_H[n] = \frac{1}{2} \int \int \frac{n(\mathbf{r}) n(\mathbf{r}')}{|\mathbf{r} - \mathbf{r}'|} d^3r d^3r' \tag{2.12}$$

Derived from Eq. 2.11, Kohn and Sham introduced the so-called *exchange-correlation energy* (xc), $E_{xc}[n]$, which stands as the unknown exchange and correlation energy of an interacting system with density $n(\boldsymbol{r})$. This quantity considers all quantum mechanical electron-electron interaction effects and is simply the summation of the error made by the non-interacting part of kinetic energy, $T_c[n]$, and the error of treating the electron-electron interaction classically:

$$E_{xc}[n] = (T[n] - T_s[n]) + U[n] - E_H[n] = T_c[n] + U[n] - E_H[n] \tag{2.13}$$

Finally, the electronic energy functional can be defined as the sum of all the above terms:

$$E[n(\mathbf{r})] = T_s[n] + E_H[n] + V_{ext}[n] + E_{xc}[n] \tag{2.14}$$

Following the same logic as Hohenberg and Kohn theorem we can access the ground-state density by minimizing this functional with respect to $n(\boldsymbol{r})$, under minimization condition $\frac{\delta E[n]}{\delta n(\mathbf{r})} = 0$:

$$\frac{\delta T_s[n]}{\delta n(\mathbf{r})} + \frac{\delta E_H[n]}{\delta n(\mathbf{r})} + \frac{\delta V_{ext}[n]}{\delta n(\mathbf{r})} + \frac{\delta E_{ex}[n]}{\delta n(\mathbf{r})} = 0 \tag{2.15}$$

where functional derivatives of $E_H[n]$ and $V_{ext}[n]$ are simply the Hartree potential, $v_H(\mathbf{r}) = \int \frac{n(\mathbf{r}')}{|\mathbf{r}-\mathbf{r}'|} d^3r'$ and the external potential, $v_{ext}(\boldsymbol{r})$, respectively. Also one can define the exchange-correlation potential $v_{xc}(\boldsymbol{r})$ as:

$$v_{xc}(\mathbf{r}) = \frac{\delta E_{ex}[n]}{\delta n(\mathbf{r})}. \tag{2.16}$$

Not all the elements in this equation can be minimized directly, as $T_s[n]$ has only an orbital functional dependency to the density, yet knowing $\frac{\delta n(\mathbf{r})}{\delta \phi_i^*(\mathbf{r})} = \phi_i(\mathbf{r})$ from the definition of density based on the non-interacting orbitals, the $T_s[n]$ also can be rewritten as:

$$T_s[n] = -\frac{1}{2}\sum_{i=1}^{N} \int \phi_i^*(\mathbf{r}) \nabla_i^2 \phi_i(\mathbf{r})\ d^3r \tag{2.17}$$

The sum of these three terms is called Kohn-Sham (KS) potential, while arbitrary to the universal functional, the exact form of $v_{xc}(\boldsymbol{r})$ is unknown:

$$v^{KS}(\mathbf{r}) = v_H(\mathbf{r}) + v_{ext}(\mathbf{r}) + v_{xc}(\mathbf{r}) \tag{2.18}$$

By inserting this potential as $\underset{\phi \to n}{min}\ \langle \phi | H | \phi \rangle$ into Eq. 2.8 we reach a Schrödinger-like equation of a non-interacting single-particle system or the so-called Kohn-Sham equation:

$$[-\frac{1}{2}\nabla_i^2 + v^{KS}(\mathbf{r})]\phi_i^{KS} = \varepsilon_i \phi_i^{KS} \tag{2.19}$$

The KS formalism is notable for its approach to separating the well-known part of the universal functional, $F[n]$, from the unknown exchange and correlation potential, $v_{xc}(\boldsymbol{r})$. Solving the resulting KS equation requires a series of self-consistence cycles. Initially, an arbitrary value is assigned to $n(\mathbf{r})$, and equations 2.10 to 2.19 are solved iteratively until the density values converge to a predefined accuracy, usually on the order of 10^{-7} or 10^{-8} e/Å^3.

2.4. Exchange-correlation functionals

Despite the nobility of Kohn-Sham's theorem in the reduction of the many-particle problem to a one-particle one, in practice, the equation is insolvable analytically due to the unknown exact form of exchange and correlation potential, $v_{xc}(\boldsymbol{r})$. Over the past few decades, various explicit or implicit density functional approximations have been developed to estimate the value of $E_{xc}[n]$, which remains a rapidly evolving field of research. Moreover, many studies show that often the accuracy of chosen functional has a direct dependence on the system of study. This accuracy is usually measured in

contrast with more accurate theoretical or experimental data.

One of the oldest approximations for estimating exchange-correlation energy is the Local Density Approximation (LDA) which is discussed in detail in Hohenberg and Kohn's article [62]. The authors proposed that one could use the nearly exact local value of density of a homogeneous electron gas to describe the $E_{xc}[n]$ of a non-homogeneous gas. They assumed, if the ground-state density of the system only varies slowly in space, then the xc energy will be a *local* function of this density:

$$E_{xc}[n] = \int n(\mathbf{r})\varepsilon_{xc}(n(\mathbf{r}))d^3r \tag{2.20}$$

where ε_{xc} is the exchange and correlation energy per electron of a uniform electron gas. The exchange part of the energy of this homogeneous gas has an exactly known formulation:

$$E_x^{LDA}[n] = -\frac{3}{4}\left(\frac{3}{\pi}\right)^{\frac{1}{3}} \int n^{\frac{4}{3}} d^3r \tag{2.21}$$

Contrary to the exchange part, the correlation energy has no analytical form and it has been calculated through highly accurate numerical Quantum Monte Carlo (QMC) simulations [64, 65]. By considering different scaling laws and constraints, one can develop various types of analytical forms to fit the parameters of QMC results. For this reason, many representations of this energy were proposed in the past decades [66–69]. All of these variants are conventionally referred to as LDA, as in practice they yield similar outcomes. The LDA functional is considered the standard approximation for investigating solid systems [70]. However, it has been demonstrated that this functional performs poorly in different areas of chemistry, especially in the case of atomic systems [59], due to its overestimation of the molecular bonding of structures [71]. This method overestimates the bond energies by up to 1eV/bond [72], leading to unrealistic close-packed structures. The following section will outline the failure of this functional in describing ground-state and excited-state properties, specifically charge-transfer excitations.

In 1968, Ma and Brueckner introduced different forms of xc functionals with explicit dependence on density, called Generalized Gradient Approximation (GGA) [73], which become a breakthrough to overcome LDA problems. In this functional the $E_{xc}[n]$ not only depends on electron density at point r but also depends on the local changes of this density, gradient $\nabla n(\boldsymbol{r})$, as well. The general form of these semi-local functionals has the following form:

$$E_{xc}^{GGA}[n] = \int \varepsilon_{xc}(n(\mathbf{r}), \nabla n(\mathbf{r}))d^3r \tag{2.22}$$

The information of analytical function $\varepsilon_{xc}(n(\boldsymbol{r})\nabla n(\boldsymbol{r}))$, can be determined in various ways such as the most common methods proposed by Perdew-Wang 1991 (PW91) [74], Perdew-Burke-Ernzerhof (PBE) [75], and Becke [76], Lee, Yang, and Parr [77] (BLYP). The PBE functional attempts to empirically optimize parameters where a model of the xc hole was constructed to satisfy known exact hole constraints, while in BLYP the exchange part (introduced by Becke [76]) can be calculated by fitting few parameters to exchange energies of atoms and the correlation part (proposed by Lee, Yang, and Parr [77]) can be taken from Colle-Salvetti [78] approach only by mapping the Kohn-Sham one-particle density matrix into a functional of the density. GGA functionals significantly improve the value of $E_x[n]$ or $E_c[n]$ [79, 80] and reduce LDA's overestimation of the binding energy, to 30% (0.3 eV/bond). Nonetheless, both functionals, commonly referred to as "standard" functionals, still suffer from two significant issues: the absence of a derivative discontinuity and the presence of the so-called Self-Interaction Error (SIE), which are recognized as two of the fundamental problems in DFT [70]. In Section 2.5, the origins of these problems and their impacts on certain quantities calculated using standard functionals are discussed in detail.

In 1993 Becke [81] defined the so-called Hybrid functionals to partially exceed the limitations of (semi-)local functionals. Nowadays, this type of functionals is known as one of the most popular and accurate DFT functionals in quantum chemistry. In this scheme, based on the adiabatic connection approach [82, 83], a fraction of exact (Fock) exchange energy known as:

$$E_x^{exact} = -\frac{1}{2}\sum_{ij}\int\int \frac{\phi_i^*(\mathbf{r})\phi_j^*(\mathbf{r}')\phi_j(\mathbf{r})\phi_i(\mathbf{r}')}{|\mathbf{r}-\mathbf{r}'|}\, d^3r d^3r' \tag{2.23}$$

can be mixed with DFT exchange-correlation energy which leads to the following formalism:

$$E_{xc}^{Hyb} = E_c^{DFT}[n] + (1-\alpha)E_x^{DFT}[n] + \alpha E_x^{exact}, \quad 0 \leq \alpha \leq 1 \tag{2.24}$$

where the mixing coefficient α, as originally Becke suggested, can be fitted empirically to atomization energies, ionization potentials, and proton affinities for a number of small molecules [70] or estimated theoretically [84–86]. Further studies showed that in practice the three-parameter form of this equation is more comprehensive while, the DFT exchange and correlation energy is a mixture of both LDA and GGA functionals:

$$E_{xc}^{Hyb} = E_{xc}^{LDA}[n] + \alpha_1(E_x^{exact} - E_x^{LDA}[n]) + \alpha_2(E_x^{GGA}[n] - E_x^{LDA}[n]) + \alpha_3(E_c^{GGA}[n] - E_c^{LDA}[n]) \tag{2.25}$$

Today, by far the most notable hybrid functional for isolated molecules is B3LYP [70, 87], where it uses 81% of Lee, Yang, and Parr (LYP) GGA correlation functional and only 19% of LDA correlation, while exchange part includes 20% exact exchange energy,

72% Becke GGA exchange and 8 % LDA exchange [88]. Also one can use BHLYP (or B-half-and-half-LYP) hybrid functional which has the simple formalism as below:

$$E_{xc}^{BHLYP} = E_c^{LYP} + 0.5E_x^{exact} + 0.5E_x^{Becke} \tag{2.26}$$

Both these functionals are used in Publication I with much better performance than LDA functional in comparison with experimental results.

Another compelling subgroup of hybrid functionals that do not utilize fixed fractions of exact and DFT exchange is the Range Separated Hybrid (RSH) functionals. These functionals mix the two contributions by partitioning the Coulomb operator into long- and short-range interactions using a soft function, called range separation parameter ω, and the standard error function $erf(.)$ [89, 90]. The long-range component is treated through the exact exchange, while the short-range component is handled using semi-local exchange [91]. The general form of the electron-electron interaction can be expressed as:

$$\frac{1}{|\mathbf{r}-\mathbf{r}'|} = \underbrace{\frac{1-[\alpha+\beta\ erf(\omega|\mathbf{r}-\mathbf{r}'|)]}{|\mathbf{r}-\mathbf{r}'|}}_{short-range} + \underbrace{\frac{\alpha+\beta\ erf(\omega|\mathbf{r}-\mathbf{r}'|)}{|\mathbf{r}-\mathbf{r}'|}}_{long-range} \tag{2.27}$$

where α and β can have any value between 0 and 1 as far as α+β=1 condition can be applied. Using these parameters the xc reads:

$$E_{xc}^{Hyb} = \alpha E_{x,SR}^{exact} + \beta E_{x,LR}^{exact} + (1-\alpha)E_{x,SR}^{DFT} - \beta E_{x,LR}^{DFT} + E_c^{DFT} \tag{2.28}$$

By considering various values for these parameters, we can construct different RSH functionals, e.g. the branches considering α=0 and β=1 denoted by LC (Long-range Corrected) while the next part in the label distinguishes the name of semi-local functional. The ω parameter can be determined either empirically [92, 93] or using more accurate non-empirical approaches known as optimally-tuned RSH (OT-RSH) functionals, which are sensitive to the physical properties of the systems [35, 94, 95]. In this thesis, I employed LC-PBE or so-called ωPBE based on GGA PBE [75] functional. To determine the ω parameter, a non-empirical tuning procedure was conducted. During this process, one aims to optimize the ω parameter in such a way that the negative ionization potential of the neutral and anionic system becomes as close as possible to the highest occupied molecular orbital (HOMO) eigenvalue as described in Ref.[96]. In recent years, research has shown that optimally-tuned Range Separated Hybrid (OT-RSH) functionals can significantly improve the description of ground-state properties, including the band gap, over all other types of xc functionals, even global hybrid ones. This improvement has been observed across a wide range of systems including molec-

ular aggregates [94, 97–100].

2.5. Challenges for standard functionals

In the previous section, we discussed various approaches that have been proposed to approximate the exact xc potential, and these methods have shown great success in a wide range of applications. However, despite their success, currently used functionals (specifically, semilocal and local functionals) suffer from systematic problems that have been at the heart of many failures within the DFT formalism and at higher levels, within excited-state approaches built on its ground [101]. Some of these problems can be attributed to unconventional properties of the exact functional, and some others relate to the approximate nature of xc functionals. In one way or another, these deficiencies directly affect the functional's ability in describing charge-transfer excitations that are cases of interest in this thesis. Here, I will briefly discuss some of these deficiencies to provide the necessary background for the methods introduced in the next chapters as well as for my publications. Further details on these subjects can be found in Ref. [70, 101–104].

The most important formal property of the exact xc functional is associated with its behavior with respect to fractional numbers of electrons in open systems. In 1982, Perdew et al. [68] extended the Hohenberg-Kohn theorem and demonstrated that for a system consisting of $N = N_0 + \lambda$ electrons, where N_0 is an integer and $0 \leq \lambda \leq 1$, the exact ground-state energy of the system is linked to the straight-line connection between the ground-state energies at points N_0 and $N_0 + 1$ as also shown in Figure. 2.1:

$$E(N) = (1 - \lambda)E(N_0) + \lambda E(N_0 + 1). \tag{2.29}$$

Therefore the $E(N)$ of a system with non-integer electrons number, varies linearly with the fractional occupation number. Based on this definition the curve of energy is a continuous value, however, its derivatives jump discontinuously at integer occupations [68]. The derivatives are defined as the chemical potential of the open system as $\mu = \partial E/\partial N$, or via the Euler-Lagrange equation of DFT for density $n(\mathbf{r})$ as $\mu(N) = \delta E[n]/\delta n(\mathbf{r})$ [68]. Therefore, the chemical potential has the below general form:

$$\mu(N) = \begin{cases} -IP(N_0) = \lim\limits_{\lambda\to 0} \left.\frac{\partial E}{\partial N}\right|_{N_0-\lambda} = \lim\limits_{\lambda\to 0} \left.\frac{\delta E[n]}{\delta n(\mathbf{r})}\right|_{N_0-\lambda}, & N_0 - 1 < N \leq N_0 \\ -AE(N_0) = \lim\limits_{\lambda\to 0} \left.\frac{\partial E}{\partial N}\right|_{N_0+\lambda} = \lim\limits_{\lambda\to 0} \left.\frac{\delta E[n]}{\delta n(\mathbf{r})}\right|_{N_0+\lambda}, & N_0 < N \leq N_0 + 1. \end{cases} \tag{2.30}$$

The ionization potential (IP) and electron affinity (EA) of the N_0-electron system can be defined as $-IP_i = E_0(N_0) - E_i(N_0 - 1)$ and $-EA_a = E_a(N_0 + 1) - E_0(N_0)$,

respectively. As will be discussed in more detail in section 4.1, the fundamental gap is defined as the energy difference required to add an electron to HOMO state of the neutral system and the energy needed to remove an electron from the LUMO state of the neutral system, *i.e.*, $E_{fund} = IP(N_0) - EA(N_0)$. By utilizing the general form of the total energy in the DFT formalism (Eq. 2.14) and the above relation for the chemical potential, E_{fund} can be written as the sum of two contributions:

$$\begin{aligned} E_{fund} &= \lim_{\lambda\to 0}\left\{ \left.\frac{\delta E[n]}{\delta n(\mathbf{r})}\right|_{N_0+\lambda} - \left.\frac{\delta E[n]}{\delta n(\mathbf{r})}\right|_{N_0-\lambda} \right\} \\ &= \underbrace{\varepsilon_{N_0+1}(N_0) - \varepsilon_{N_0}(N_0)}_{E_{KS}} + \lim_{\lambda\to 0}\Big\{ \underbrace{v_{xc}(\mathbf{r})\Big|_{N_0+\lambda} - v_{xc}(\mathbf{r})\Big|_{N_0-\lambda}}_{\Delta_{xc}} \Big\} \end{aligned} \tag{2.31}$$

The first term is known as the KS gap, which is defined as the difference between the lowest unoccupied and the highest occupied KS eigenvalues at an integer electron number. This conclusion follows from Janak's theorem [105], which proves that the derivative of the total energy with respect to the (fractional) occupation number f_i of the i-th KS orbital (see Eq. 2.10) is equal to the i-th KS eigenvalue, $\partial E/\partial f_i = \varepsilon_i^{KS}$. However, Almbladh and von Barth [106] later demonstrated that ε_i^{KS} can strictly be assigned to the HOMO eigenvalue in KS formalism for the exact functional, where its energy is equal to minus the ionization potential, $\varepsilon_{HOMO} = -IP$. The second term in Eq. 2.31 is known as the *derivative discontinuity* of xc energy, which describes how the exchange-correlation potential of the system jumps discontinuously by this constant while the density remains unchanged [104, 107].

The existence of this quantity is the main source of a long-standing issue in DFT method known as the *band gap problem*. Using Eq. 2.30 the fundamental gap E_{fund}, which is an excited-state property, should be formulated based on two ground-state calculations on the N and $N+1$-electron system as:

$$E_{fund} = IP(N) - EA(N) = \varepsilon_{HOMO}(N+1) - \varepsilon_{HOMO}(N). \tag{2.32}$$

However, assuming knowledge of the exact functional, the KS gap, defined as $E_{KS} = \varepsilon_{HOMO}(N) - \varepsilon_{LUMO}(N)$, can be evaluated based on a single ground-state calculation where the exact same potential describes both occupied and virtual orbitals. Despite the fact that the HOMO state is equivalent to the ionization energy, the LUMO state cannot be related to the EA [32], resulting in a difference between the KS gap and the E_{fund} gap expressed in the form of the derivative discontinuity, $\Delta_{xc} = \varepsilon_{HOMO}(N+1) - \varepsilon_{LUMO}(N)$. Since Δ_{xc} can only be evaluated from two separate ground-state calculations of the N and $N+1$-electron system, the KS gap never agrees with the E_{fund}

gap. This gap underestimation in the KS formalism is not a failure of approximate functionals but is inherent to KS theory. Therefore, finding an ultimate functional in the KS framework that can accurately predict the fundamental gap from a single ground-state calculation is intrinsically unattainable [70]. To overcome this problem, a frequently adopted approach is the generalized Kohn-Sham (GKS) formalism, which will be explained in Section 2.6.

The second problem related to the derivative discontinuity arises from the approximate nature of xc functionals. For exact functionals, one can assume that the energy at $N_0 - 1$ or $N_0 + 1$ can be obtained through the derivatives at N_0 [108]. However, this assumption may not hold for approximate density functionals. In the case of local and semilocal functionals, where the energy is an explicit functional of the density at each point in space and hence continuous in its gradient, Δ_{xc} is zero. This absence of the derivative discontinuity leads to incorrect behavior of the total ground-state energy between integer electron numbers, resulting in curves that are convex instead of linear [108, 109]. Figure 2.1 schematically illustrates the difference between the exact functional and local/semilocal functionals for fractional numbers of electrons. The

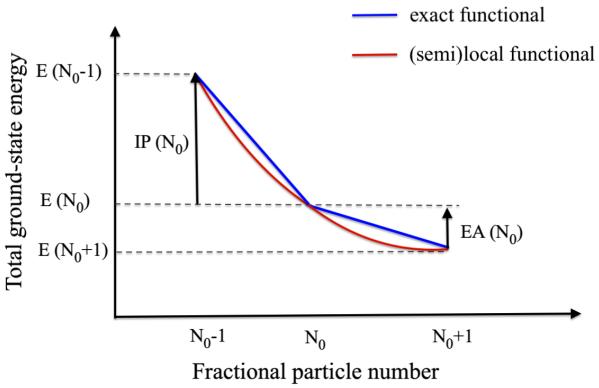

Figure 2.1: Sketch of the ground-state energy as a function of the number of electrons in the system. The exact exchange curve with its straight line segments and convex behavior of approximate xc functionals are illustrated with blue and red lines, respectively. Figure adapted from Ref. [102, 104].

unphysical variation of energy as a function of fractional particle numbers in these functionals leads to deficiencies of the first-order derivatives for calculating IP and EA and results in a large deviation from the exact values [108].

A final perspective is given by the self-interaction error (SIE) that was recognized already in Thomas-Fermi's theory [61]. The self-interaction error, which arises from the unrealistic interaction of an electron with itself, is well-understood in one-electron systems such as the hydrogen atom. By construction, Hartree energy, as expressed in Eq. 2.12, incorporates the unrealistic classical electron-electron repulsion. Since in

principle, DFT handles electron-electron interaction exactly, the self-interaction error in the Hartree term must be fully compensated by the exchange-correlation term, resulting in $E_{xc}[n_{1e}] + E_H[n_{1e}] = 0$ [70, 104]. This statement only holds for the exact functional, as it is not possible for approximate (semi)local functionals to fully satisfy this condition, leading to an overestimation of the electron-electron repulsion energy.

Perdew and Zunger [110] suggested by identifying KS orbitals with electrons, where $n_i(\mathbf{r}) = f_i|\phi(\mathbf{r})|^2$ are the orbital densities, the same freedom of one-electron self-interaction can be extended to a many-electron system for any approximate functional that known as self-interaction correction (SIC) term:

$$E_{xc}^{SIC}[n_i] = E_{xc}^{appr}[n_i] - \sum_{i=1}^{N} E_{xc}^{appr}[n_i, 0] + E_H[n_i] = 0. \tag{2.33}$$

Via this modification, the functionals are no longer density-dependent but orbital-dependent. Therefore, different choices of orbitals, rather than KS ones, lead to different versions of the self-interaction correction. While SIC methods for correcting (semi)local functional eigenvalues can improve the predicted band gap [103, 111], their application is computationally expensive due to the consideration of Coulomb integrals involving the orbitals. It is important to note that the equation mentioned earlier extends the one-electron self-interaction error, also known as the one-error [111], to a many-electron system. However, it is not sufficient to completely eliminate or recover the SIE of an N-electron system. Quantifying the many-electron self-interaction error for an extended many-particle system is not that simple, but a common way is the use of the straight-line energy condition as has been defined in Eq. 2.29, where for exact functional the energy varies linearly with fractional electron number.

In the case of (semi)local functionals, the missing derivative discontinuity problem resurfaces, as the incorrect convex behavior of these functionals leads to delocalization of the charge distribution for fractional numbers. This phenomenon is variously referred to as the "many-electron SIE" or "missing derivative discontinuity" error, or simply as the *delocalization error* in the literature [112]. These different terms reflect different aspects of the same principle issue at the core [102]. The artificial spread of electron density has vital consequences which highlight the limitations of local functional in the prediction of transition state energies and hence reaction barriers in weakly overlapping fragments of a system, crucial for the description of long-range charge-transfer states [32, 70, 112, 113], charge localization and distribution between subsystems [109, 114].

To overcome these limitations, (range-separated) hybrid functionals offer a viable alternative by incorporating non-local features that can partially mitigate delocalization errors. Hartree-Fock theory, which only considers the exact exchange part of the

energy and ignores the correlation term entirely, can lead to an overestimation of the energy $E(N)$ even for integer particle values. This results in deviations from linearity in a concave manner, known as the "localization" error [103]. Hybrid functionals partially correct for this error by including a fraction of the exact exchange, allowing for error cancellation of convex and concave components and accounting for long-range electron-electron correlation effects [112, 113]. Yet, to avoid the localization error and satisfy Eq. 2.29, the long-range exact exchange should be compatible with the KS correlation term. One solution is the use of OT-RSH functionals that enforce the ionization potential to be equal to the HOMO eigenvalue through a tuning parameter ω. Such functionals are particularly suitable for addressing delocalization errors in complex systems.

2.6. The Generalized Kohn-Sham Scheme

Although the primary practical application of DFT was based on the KS formalism, most of the *ab-initio* packages used today, including the one used in this work, operate based on the generalized KS (GKS) formalism [115]. This is especially true in the case of hybrid functionals. The reason for this shift is that while some quantities, such as the total energy, are usually well described by KS eigenvalues, the HOMO-LUMO gap is drastically underestimated by this method due to the discontinuity contribution of the exchange-correlation potential, denoted by xc.

In GKS formalism, instead of mapping the interacting N-electrons system to non-interacting ones, one may map this original system into an auxiliary partially interacting system. This approach lifts the complexity associated with approximating all exchange and correlation effects in the KS formalism by partially considering them in the auxiliary system [70]. This alternative mapping is achieved by defining an orbital-dependent potential $K[\phi]$ that satisfies the condition $F[n(\mathbf{r})] = \underset{\phi_i \to n}{min} K[\phi_i]$, which is equivalent to Eq. 2.9. In this manner, all density derivatives in Eq. 2.15 are replaced with derivatives with respect to the orbitals ϕ_i, and the generalized Kohn-Sham equation can be written as:

$$(O[\phi_i] + v_{ext}(\mathbf{r}) + v_R(\mathbf{r}))\phi_i = \varepsilon_i \phi_i \tag{2.34}$$

where $O[\phi_i]$ is the orbital-specific operator and $v_R([n], \mathbf{r})$ is the "remainder" local potential [70]. Despite the fact, similar to the original KS approach, in principle the GKS theory is exact, in practice, it is approximated due to the unknown form of $v_R([n], \mathbf{r})$.

Contrary to KS formalism, the GKS potential has no longer a universal form while

resulting nonlocal $O[\phi_i]$ operator, which is usually of Fock-like form, replaces the KS multiplicative xc potential for all orbitals. The non-multiplicative nature of the potential operator, also called non-locality [102]), helps to emulate the self-energy operator's function in many-body perturbation theory (MBPT) by accurately accounting for exchange and correlation effects and enabling the computation of excitation energies [116]. Chapter 4 provides a detailed explanation of the features of this operator. Furthermore, the explicit functional of ϕ instead of density in the xc potential leads to the elimination or significant diminution of the KS derivative discontinuity in the GKS gap E_{GKS}, making it closer to the fundamental gap with $E_{fund} \cong E_{GKS}$ [96, 117]. While the difference between KS and GKS orbitals has a minor impact on most system quantities, such as total energy or electron density, the HOMO-LUMO energy gap differs significantly due to the definition of the LUMO energy in the GKS formalism. In both schemes, the highest occupied state equals the negative ionization energy ($\varepsilon^{HOMO}_{KS/GKS} = -IP(N)$). However, the LUMO energy is defined as an excited electron in the KS theory but interpreted as the negative of electron affinity EA in GKS scheme [118, 119]. This definition leads to a more meaningful and realistic prediction of the HOMO-LUMO gap in comparison with the fundamental gap, particularly in cases where the KS approach with semi-local functionals fails drastically [107, 120]. Figure 2.2 illustrates the energy deviation between E_{fund}, E_{KS}, and E_{GKS} and highlights the interpretation of exact HOMO and LUMO eigenvalues in KS and GKS formalism.

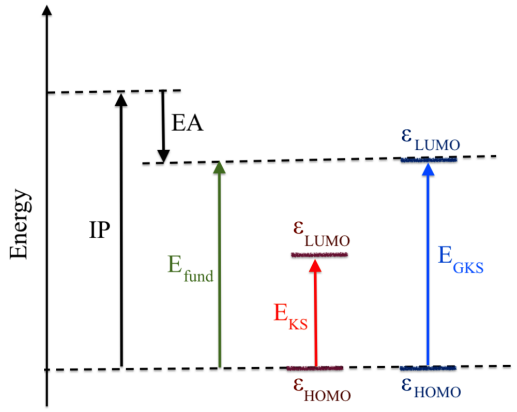

Figure 2.2: Definition of fundamental gap E_{fund} and DFT gap in KS formalism and their relation with ionization potential (IP) and electron affinity (EA). The figure has been modified from the original version in Ref. [121].

This fact should be stressed out almost all practical Hybrid functionals, which can be viewed as a special case of the GKS formalism [70], placed inside the realm of this theory as they use the orbital-specific non-multiplicative exchange potential defined in Eq. 2.23. The combination of local and nonlocal exchange energy assisted by the orbital dependency of OT-RSH functionals can yield a correct asymptotic behavior

of the potential. Furthermore, the percentage of delocalized parts controlled by the introduced ω parameter can simulate the electrostatic screening effects [30] which can be crucial for a correct description of particle interactions. An effect that also is considered inside the GW/BSE theorem and viewed as the strong suit of this method. In addition, the ω parameter controls the proportion of delocalized components, which can replicate the electrostatic screening effects [30]. This is an essential factor for accurately describing particle interactions, which is also taken into account in the GW/BSE theory and is regarded as a significant advantage of this approach. To sum up, the weighted combination of exact and semi-local exchange within the OT-RSH functionals, which is utilized in orbital-dependent GKS theory, is currently regarded as a promising solution to the band gap problem. This fact is also declared in Publication I for a single BCL molecule and is illustrated here in Figure 2.3. The density of state (DOS) structure and more especially HOMO-LUMO gap in GKS formalism with ωPBE functional is almost identical to more accurate GW calculations while LDA functional show more than 2 eV deviation from these results.

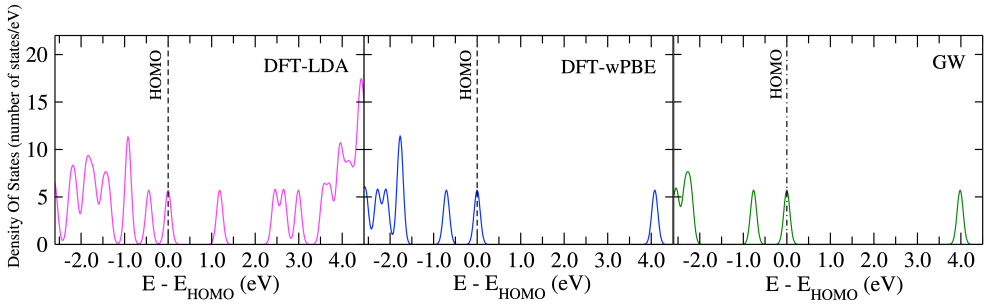

Figure 2.3: Generalized KS density of states calculated using DFT with LDA (pink), ωPBE (blue), and GW method (green). The HOMO energies are aligned to zero.

2.7. Calculation of forces and vibrational spectra

Quantum-mechanical methods, such as DFT, focus on the electron motion in a system, while the atomic nuclei remain fixed in geometry. Vibrational analyses, which consider the quantum and thermal motions of nuclear particles, are powerful tools for further identification of the electronic structure in the system. Vibrational modes more often have a pronounced effect on the neutral and charge-transfer excitations of molecular systems and can be important in the characterization of each excitation [17, 122]. Recent studies on photosynthetic systems have demonstrated the considerable impact of electronic-vibrational coupling on defining the character of internal charge-transfer and electron-density asymmetry of the special pair [123, 124], the robustness of the

charge separation process in the RC [125], and achieving a more analogous picture of the ground-state and excited-state between theoretical and experimental results [126].

The dynamical properties and effect of thermally-activated molecular vibrations can be calculated via different approaches, such as the force constant method. In this method, an infinitesimal displacement (δ) is applied to the equilibrium geometry to construct the Hessian matrix based on the second derivatives of the energy with respect to atomic coordinates [127]. In my work, the Hessian matrix is constructed at the DFT level of theory. However, due to the large number of matrix elements, these calculations are much more demanding than a simple DFT ground-state simulation. The vibrational potential energy, $V(\mathbf{R})$, can be written using a Taylor series expansion:

$$V(\mathbf{R}) = V_0 + \sum_i (\frac{\partial V}{\partial \mathbf{R}_i})\ \mathbf{R}_i + \frac{1}{2}\sum_{ij} (\frac{\partial^2 V}{\partial \mathbf{R}_i \partial \mathbf{R}_j})\ \mathbf{R}_i \mathbf{R}_j + ... \tag{2.35}$$

where $(\frac{\partial V}{\partial \mathbf{R}_i})$ for equilibrium geometry and $\mathbf{R}_n$ is the nuclear Cartesian displacement coordinates. The V_0 is the zero point energy that does not depend on the displacement coordinates and can be set to zero. Frequently $V(\mathbf{R})$ potential is approximated as the harmonic potential at the vicinity of an equilibrium point, in terms of mass-weighted Cartesian displacement coordinates, $q_i = \mathbf{R}_i\sqrt{M_i}$ with M_i being the nuclear masses, as:

$$V(\mathbf{R}) = \frac{1}{2}\sum_{ij} K_{ij}\ q_i q_j \tag{2.36}$$

where the mass-weighted molecular Hessian, or the harmonic force constant, $K_{ij} = (\frac{\partial^2 V}{\partial q_i \partial q_j})$, contains $3N-5$ $(3N-6)$ positive values that correspond to the linear (non-linear) translational and rotational motions of the molecule. However, the harmonic approximation tends to overestimate the frequencies as it neglects anharmonicity effects when compared to the experimental data. While molecular dynamics simulations can capture anharmonicity effects by investigating the alteration of the system along the dynamical path over a period of time, these calculations are generally more computationally expensive. Furthermore, the discrepancy between experiment and harmonic vibration results tends to be uniform, resulting in outcomes that are only proportional in terms of a scaling factor [128].

The harmonic vibrational frequencies can be determined by solving the equation $\omega = \sqrt{K_{ij}}$, where K_{ij} represents the mass-weighted Hessian matrix. Real (positive) frequencies are obtained when the structure is located at the minimum of the potential energy surface, while imaginary (negative) modes appear among the vibrational frequencies when the structure is located in a transition state. Hence, an accurate geometry optimization with a higher number of grid points and a more restricted threshold for finding a dynamically stable state is typically necessary as a prerequisite

step for vibration simulations. The ability to calculate vibrational frequencies can also be useful in considering thermal contributions in various ways. In classical distribution, it is assumed that at the maximum displacement of the oscillator, the kinetic energy has zero contribution to the potential energy, and therefore the thermal energy of the system is equal to the potential energy of the mode ω:

$$K_B T = \frac{1}{2} \sum_{ij} K_{ij}\ q_i q_j \tag{2.37}$$

where K_B is the Boltzmann constant and T is the desired temperature. Knowing the harmonic vibrational frequency ω_i associated with a particular displacement q_i allows us to simulate the system at a predefined temperature by distorting the equilibrium geometry along that mode with an amplitude corresponding to the temperature. This produces a thermally-activated structure whose excited-state properties can be calculated using methods like TDDFT or GW/BSE. Vibrational motions and thermal effects typically result in a redshift of the absorption spectra compared to static vertical excitations. The focus of my work is on studying the alterations in system properties due to vibrational effects, relative to the equilibrium geometry. To this end, we represent these effects using the concept of energy difference. The energy difference between the excitation energy of a dynamic structure and a static one is computed as $\Delta E_n = E_n^{static} - E_n^{dynamic}$, where n is the excitation number. The ΔE_n energies are frequently more distinct for low-frequency modes with larger nuclear fluctuations and higher-order frequencies will be neglected in the excited-state calculations.

Chapter 3

Time-dependent density functional theory

One of the primary intentions of computational simulations is to precisely predict the excited-state features. According to the Hohenberg-Kohn theorem, all properties of a system, including those of its excited-states, can be uniquely determined based on its ground-state density. However, in practice, the certain link between the ground-state electron density and reformation of electronic configuration is unknown, making the DFT method inadequate for interpretation of excited-state. Further developments are therefore needed to accurately predict optical absorption. One way to achieve this goal is to observe the evolution of a physical system's wavefunction over time by solving the time-dependent many-body wavefunction part of the Schrödinger equation. Yet, as previously stated, obtaining the exact analytical solution of the time-dependent or time-independent Schrödinger equation for a many-body system without approximation is an unsolvable mathematical problem. One rigorous approach for calculating excited-state properties of various molecular systems with great success in recent decades is through the time-dependent formulation of DFT theory.

3.1. Time-Dependent DFT

In 1984, Runge and Gross [25] proved that each external potential $v_{ext}(\mathbf{r}, t)$ with an initial many-body state $\Psi_0(t = 0)$ leads to a unique electron density $n(\mathbf{r}, t)$. This method, which is also known as the time-dependent extension of stationary Hohenberg-

Kohn theorem [62], suggests this one-to-one map can determine the external potential and all the observable properties of the system by only having the density of the system at time t while the initial state is fixed [129]. Almost a decade later, Van Leeuwen's theorem [130] proved that the time-dependent density $n(\mathbf{r},t)$ of the interacting system can be replaced with the density of non-interacting particles that change under the influence of a time-dependent electric field. Describing this local effective potential as $v_{KS}(\mathbf{r},t)$ leads to the primary formulation of Time-Dependent Density-Functional Theory (TDDFT), which is an extension of the DFT method to excited states [131]. In this interpretation, the time-dependent Schrödinger equation is rewritten as:

$$i\frac{\partial\phi_i(\mathbf{r},t)}{\partial t} = [-\frac{1}{2}\nabla^2 + v_H(\mathbf{r},t) + v_{ext}(\mathbf{r},t) + v_{xc}(\mathbf{r},t))]\phi_i(\mathbf{r},t) \tag{3.1}$$

with $n(\mathbf{r},t) = \sum_{i=1}^{N} |\phi_i(\mathbf{r},t)|^2$.

In the framework of DFT, the exchange-correlation potential $v_{xc}(\boldsymbol{r},t)$ accounts for all the non-trivial many-body effects in the system [129]. In static DFT, v_{xc} potential is simply a derivation of xc energy as introduced in Eq. 2.16, while in TDDFT such a definition leads to a contravention with causality in the system under the exchange of $(\mathbf{r},t)$ and $(\mathbf{r}',t')$ [130, 132] which is beyond the scope of this thesis. The time-dependent exchange-correlation potential, $v_{xc}(\boldsymbol{r},t)$, is a non-local potential that depends on the previous densities at time t' [70, 133]. It is defined as the functional derivative of the exchange-correlation action $A_{xc}[n]$ with respect to the density at some boundaries: $v_{xc}(\boldsymbol{r},t) = \frac{\delta A_{xc}[n]}{\delta n(\boldsymbol{r},t)}$ [134]. However, to construct $v_{xc}(\boldsymbol{r},t)$, one needs to know the time-dependent exchange-correlation energy $E_{xc}(\mathbf{r},t)$. Despite decades of research, the exact form of $E_{xc}(\mathbf{r},t)$ remains unknown, and approximations to this potential are still in their early stages of development [129, 133, 135]. One common alternative approach is the so-called *adiabatic approximation* that uses the static xc potential of DFT:

$$v_{xc}^{adiabatic}(\mathbf{r},t) \;=\; v_{xc}(\mathbf{r})|_{n=n(\mathbf{r},t)} \;=\; [\frac{\delta E_{xc}[n](\mathbf{r})}{\delta n(\mathbf{r})}]_{n(t)} \tag{3.2}$$

One of the most practical variations of TDDFT method is carried out through linear-response theory. As only this particular approach has been used in the calculation of neutral and charge-transfer excitations in my work, here only its layout will be discussed comprehensively. At the heart of this approximation, a small, time-dependent external field is applied to the system's ground-state, and the perturbation theory is used to analyze the resulting linear changes in density:

$$n(\mathbf{r},t) \;=\; n_0(\mathbf{r}) + n_1(\mathbf{r},t) + ... \tag{3.3}$$

where due to the weak perturbative field we can neglect the higher order expansion of the density and only consider the ground-state $n_0(\mathbf{r})$ density and the next term $n_1(\mathbf{r},t)$ [53]. In the context of Van Leeuwen [130] and KS theorems and using time Fourier transform, we can define $n_1(\mathbf{r},t)$ in frequency space as:

$$n_1(\mathbf{r},t) \;=\; n(\mathbf{r},t) - n_0(\mathbf{r}) \;= \delta n(\mathbf{r},t) = \int \chi[n_0](\mathbf{r},\mathbf{r}',\omega)\; \delta v_{KS}(\mathbf{r}',\omega)\; d^3r' \tag{3.4}$$

where χ is the linear response function of a non-interacting system in the ground-state under external potential δv_{KS}. When using KS orbitals, the representation of χ can be expressed as:

$$\chi_{KS}(\mathbf{r},\mathbf{r}',\omega) = \sum_{i,j}^{\infty}(f_j - f_i)\; \frac{\phi_i^*(\mathbf{r})\phi_j^*(\mathbf{r}')\phi_i(\mathbf{r}')\phi_j(\mathbf{r})}{\omega - (\varepsilon_j^{KS} - \varepsilon_i^{KS}) + i\eta} \tag{3.5}$$

where $\varepsilon_{i/j}$ and $f_{i/j}$ are the eigenstates and occupation factors of states i and j, respectively, and η is a positive infinitesimal. One can see the KS response function is purely a function of KS wavefunctions while χ_{KS} poles are located at $\omega = \varepsilon_i - \varepsilon_j$. Now going back to the definition of KS potential (Eq. 2.18) one can write δv_{KS}:

$$\delta v_{KS}(\mathbf{r},\omega) \;=\; \delta v_{ext}(\mathbf{r},\omega) + \int \frac{\delta n(\mathbf{r}',\omega)}{|\mathbf{r}-\mathbf{r}'|}\; d^3r' + \int\; f_{xc}(\mathbf{r},\mathbf{r}',\omega)\; \delta n(\mathbf{r}',\omega)\; d^3r' \tag{3.6}$$

where the *xc* kernel, f_{xc}, in the time-domain is defined as:

$$f_{xc}(\mathbf{r},t) \;=\; \frac{\delta v_{xc}[n_0](\mathbf{r},t)}{\delta n(\mathbf{r}',t')} \tag{3.7}$$

while v_{xc} is a function of ground-state density n_0. Now by plugging Eq. 3.4 to definition of δv_{KS} we reach to:

$$\begin{aligned}\chi(\mathbf{r},\mathbf{r}',\omega) \;&= \chi_{KS}(\mathbf{r},\mathbf{r}',\omega) + \int\int \chi_{KS}(\mathbf{r},\mathbf{r}_1,\omega) \\ &\times\; [f_{xc}(\mathbf{r}_1,\mathbf{r}_2,\omega) + \frac{1}{|\mathbf{r}_1-\mathbf{r}_2|}]\; \chi(\mathbf{r}_2,\mathbf{r}',\omega)\; d^3r_1\; d^3r_2\end{aligned} \tag{3.8}$$

with χ being the response function of the interacting system with a dependency on the non-interacting KS response function χ_{KS}. Occasionally, it is common to pack the Hartree and exchange-correlation potentials as follows: $f_{Hxc}(\mathbf{r},\mathbf{r}',\omega) = \frac{1}{|\mathbf{r}-\mathbf{r}'|} + f_{xc}(\mathbf{r},\mathbf{r}',\omega)$. Recasting this optical response function in Lehmann representation with a similar formulation as Eq. 3.5 shows, the poles of χ are located at excitation energies of the system, Ω, while they correspond to the transition frequencies ω. Therefore, the self-consistent solution of this equation, with an exact f_{xc}, provides optical information

about the system. In practice solving this equation is numerically cumbersome. In this regard, using a new derivation of Eq. 3.8, one can reach a non-Hermitian eigenvalue problem, known as Casida formalism [136], that could determine the poles of the response function, Ω, in the block form of:

$$\begin{pmatrix} A & B \\ -B^* & -A^* \end{pmatrix} \begin{pmatrix} X^s \\ Y^s \end{pmatrix} = \Omega_s \begin{pmatrix} -1 & 0 \\ 0 & 1 \end{pmatrix} \begin{pmatrix} X^s \\ Y^s \end{pmatrix} \tag{3.9}$$

where matrix elements are defined in occupied (i, j) and virtual (a, b) Hilbert space: $S = S_i \times S_a \oplus S_b \times S_j$, while the matrix size depends on this product space [137]. Eigenvalues of the above equation indicate the neutral and charge-transfer excitation energies of the many-body system, $\Omega = \omega$, while eigenvector X and Y, represent the amplitude or the oscillator strength of excitation $i \to a$ and deexcitation $a \to i$. In this distinct non-symmetric block form, matrix elements A and $-A^*$, that represent resonant $(i \to a)$ and antiresonant $(a \to i)$ transitions, and their coupling B and $-B^*$ define as:

$$A_{ia}^{jb} = \delta_{ij}\delta_{ab}(\varepsilon_a - \varepsilon_i) + (ia|jb) + (ia|f_{ab}|jb) = \delta_{ij}\delta_{ab}(\varepsilon_a - \varepsilon_i) + K_{ia,jb}(\omega), \tag{3.10}$$

$$B_{ia}^{jb} = (ia|jb) + (ia|f_{ab}|jb) = K_{ia,jb}(\omega). \tag{3.11}$$

Here, the two-electron integrals are given in Mulliken notation:

$$K_{ia,jb}(\omega) = (ia|f_{Hxc}|jb) = \int\int \phi_i^*(\mathbf{r})\phi_a(\mathbf{r})\ f_{Hxc}(\mathbf{r}, \mathbf{r}', \omega)\ \phi_j^*(\mathbf{r}')\phi_b(\mathbf{r}')\ d^3r\ d^3r' \tag{3.12}$$

where in KS formalism, $\varepsilon_{i,j/a,b}$ and wavefunctions $\phi_{i,j/a,b}$ are determined by a previous self-consistence DFT calculation. By diagonalization of Eq. 3.9, for reducing the size of the initial matrix, and with considering real-valued KS wavefunctions and f_{xc}, one can reach a simplified quadratic eigenvalue representation of Casida formalism:

$$C\mathbf{Z} = \Omega_n^2\mathbf{Z}, \tag{3.13}$$

where the symmetric matrix C and transition density matrices $\mathbf{Z}$ define as:

$$C = (A - B)^{1/2}(A + B)(A - B)^{1/2}, \tag{3.14}$$

$$\mathbf{Z} = (A - B)^{1/2}(X - Y) \tag{3.15}$$

while matrix $A - B$ is a positive definite. Following this formalism, some properties

such as transition density can be computed through the equation:

$$\gamma(\mathbf{r},\mathbf{r}') = \sum_{i}^{occ}\sum_{a}^{virt} [X_{ia}(n) + Y_{ia}(n)]\phi_i^*(\mathbf{r})\phi_a(\mathbf{r}') = \sum_{i}^{occ}\sum_{a}^{virt} \mathbf{Z}_{ia}(\varepsilon_a - \varepsilon_i)^{-1/2}\phi_i^*(\mathbf{r})\phi_a(\mathbf{r}') \tag{3.16}$$

that represents the change of the density matrix corresponding to the excitation n.

This representation of Casida formalism is the common form of the TDDFT method implemented in different program packages, including those used in this thesis. By replacing the definition of matrix element A and B we can rewrite the C matrix as:

$$C_{ij,ab} = (\varepsilon_i - \varepsilon_j)^2\delta_{ij}\delta_{ab}\delta_\sigma + 2\sqrt{\varepsilon_i - \varepsilon_j}\sqrt{\varepsilon_a - \varepsilon_b}\; K_{ij,ab}(\omega). \tag{3.17}$$

In the past decades, various estimations have been suggested for the prediction of the matrix B or more specifically $K_{ia,jb}(\omega)$. In Tamm-Dancoff approximation one neglects any coupling between two types of excitations by setting matrix B to zero [138]. Simplifying the configuration to $\mathbf{AX} = \omega\mathbf{X}$ eliminates the Y eigenvector while keeping the definitions of $\mathbf{A}$ and $\mathbf{X}$ the same as before. Although this approximation simplifies the represented eigenvalue, still finding the practical estimation for computing f_{xc} in matrix element, A is a troubling task. One approach is to neglect the dynamical effects by setting $f_{xc} = 0$ and only including the Hartree correlation part in the f_{Hxc} function, which is known as the Random Phase Approximation (RPA) [139]. Another widely used method for estimating f_{xc} is the adiabatic approximation [137], which is explained in Eq. 3.2. In the frequency-independent representation of $f_{xc}(\omega \to 0)$, the exact *xc* potential can be reached by having a slow variation in time, resulting in a potential that depends only on the density at time t. The f_{xc} function can be written in this formalism as:

$$f_{xc}(\mathbf{r},\mathbf{r}') \;=\; \frac{\delta^2 E_{xc}[n]}{\delta n(\mathbf{r})\;\delta n(\mathbf{r}')} \tag{3.18}$$

where E_{xc} is the static DFT *xc* energy functional that can have different types as it is discussed in the previous chapter.

The linear-response TDDFT method, under the adiabatic approximation, has been widely used for predicting the excitation spectrum of organic or biochromophore molecular systems with sufficient accuracy [26, 140–142]. The TDDFT approach in the concept of Casida formalism offers several advantages, such as access to diverse optical properties like oscillator strength, the difference between the ground-state and excited-state density, atomic point charges, and dipole moments. However, the calculated excitation spectrum strongly depends on the KS orbitals and *xc* energy functional, which can lead to underestimation of the results due to the DFT part. Furthermore, the "standard" approximations used in TDDFT have a significant drawback: the the-

ory drastically fails in predicting long-range charge-transfer excitations [31, 32, 113, 143, 144], Rydberg states [34, 145], and double excitations [33]. Charge-transfer excitation plays a crucial role in various energy-conversion processes in photosynthetic systems and is therefore of great interest in this thesis. In the next section, we will discuss the nature of this excitation, its features, and the inefficiency of (semi)local functionals for its prediction.

3.2. Charge-transfer excitation in standard TDDFT

Let us begin by considering a simple model of excited-state intermolecular interactions, which involves two separated molecules, A and B, with a distance of R. In a dimer system that is excited, $[AB]^*$, if both the electron and the hole are localized within the same individual unit, the excitation is called a local excitation, which is often short-lived. On the other hand, if a significant fraction of the electrons transfers from an occupied state of molecule A (donor) to an unoccupied state of molecule B (acceptor), the excitation is identified as a charge-transfer excitation, which is often long-lived [32, 146]. The orbital occupation diagrams for these two types of excitations are schematically illustrated in Figure 3.1. In the charge-transfer excitation, the positive and negative charges located on A and B molecules electrostatically attract each other, while the charge-transfer state has a $1/R$ dependence. To understand the failure of (semi)local functionals in predicting the correct $1/R$ behavior of charge-transfer excitation, we first assume that the orbitals of molecules A and B have zero or negligible overlap. Going back to Eqs. 3.10 and 3.11, the $(ia|jb)$ term exponentially vanishes due to the exponential orbital decay from both equations. The last term within the exchange-correlation kernel f_{xc} depends on the choice of the xc functional. Unless the f_{xc} kernel has a singularity in the derivative of the potential with respect to the density, and can counteract the exponentially decaying orbital overlap based on its non-local

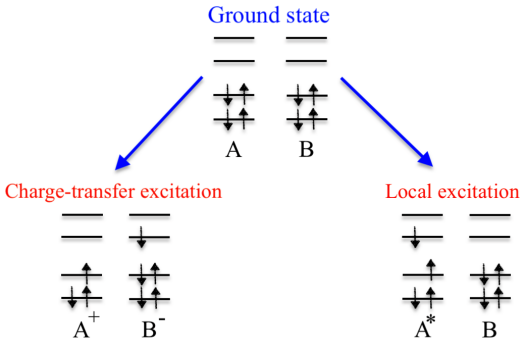

Figure 3.1: Illustration of classes of excitations.

feature, the matrix elements A and B, and consequently the excitation energy, reduce to the Kohn–Sham eigenvalue difference $\varepsilon_a - \varepsilon_i$ [30]. Despite the compensatory nature of the exact kernel, (semi)local functionals are unable to restore the correct $1/R$ long-range behavior. This is because, in the case of pure (semi)local functionals, TDDFT is applied within the adiabatic approximation, where the f_{xc} kernel has no time-dependency ($\omega = 0$). Moreover, since (semi)local functionals have a local character, f_{xc} only appears in regions of space where $\mathbf{r} \approx \mathbf{r}'$, and cannot grow rapidly in regions where the orbital overlap vanishes. These factors make LDA or GGA inadequate to compensate for vanishing overlap and diminish the charge-transfer excitation energy to KS eigenvalue difference. As demonstrated in section 2.5, KS gap encounters significant problems in the characterization of partial charge-transfer excitation between weakly overlapping subunits due to the lack of derivative discontinuities and the presence of SIE. This inefficiency of linear-response TDDFT with standard functionals is also reported repeatedly in the study of photosynthetic systems [32, 49, 147, 148].

In summary, this method fails to give a correct prediction of charge-transfer excitations. A failure attributed to the mentioned non-local features of TDDFT method, *e.g.*, frequency independence of f_{xc}, discontinuity, and more importantly incorrect asymptotic behavior of the Coulombic attraction, where f_{xc} decays too quickly (exponentially) instead of the correct $-1/r$ asymptotic, as has been vastly discussed in the literature [34, 113, 133, 149, 150].

In recent years, the combination of GKS formalism and RSH or more specifically OT-RSH functionals containing tuned long-range exact exchange has emerged as a promising approach to overcome the shortcomings of standard TDDFT in predicting charge-transfer excitations. This method utilizes the concept of orbital-specific potentials and tuned exact (Fock) exchange to accurately capture the asymptotic behavior of the Coulombic attraction while minimizing the derivative discontinuity by tuning ω. As a result, TDDFT has become an intrinsically suitable method for describing this type of excitation in molecular systems [35–40, 149]. Additionally the performance of TDDFT method with different functionals is investigated in Publication I and Publication III for single and dimer Bacteriochlorophyll model systems in comparison with GW/BSE approach. In the first publication, we established LDA functional fails remarkably in the prediction of local excitation energy of these monomers while TDDFT with ωPBE functional lead to much more reasonable description of excitation spectrum, in excellent agreement with GW/BSE approach, multireference wavefunction-based methods, and experimental data. The same trend is observed in the dimeric system, where the LDA functional gives a generally incorrect prediction of the entire excitation spectrum with unrealistic low oscillator strength excitations appearing at very low energies. On the other hand, ωPBE functional provides the appropriate approximation for fulfilling

this task with an almost equivalent performance as *GW*/BSE. Figure 3.2 depicts a comparison of the excitation spectra of the BCL dimer calculated by the LDA and ωPBE functionals.

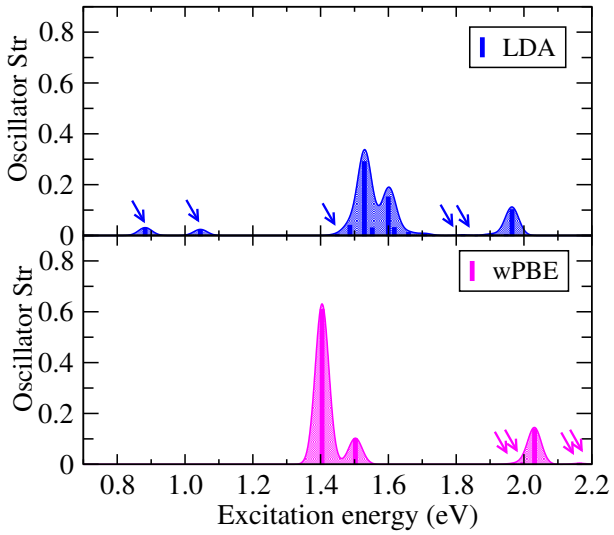

Figure 3.2: Excitation spectrum of BCL dimer using TDDFT within LDA (top) and ωPBE (bottom) functionals. Arrows mark low oscillator strength excitations. The shaded areas are calculated by folding the excitation energies with Gaussian functions with a width of 0.08 eV as a guide to the eye.

Chapter 4

GW/BSE formalism

The development of DFT in 1965 marked the beginning of a new era in computational chemistry, and since then, various alternative approaches have been proposed and continuously improved. However, some of these methods are primarily focused on ground-state properties and are not suitable for studying electronic excitations, which is the main focus of this thesis. Other methods, such as algebraic diagrammatic construction (ADC) or coupled-cluster (CC) [151, 152] , have been developed explicitly for simulating excited states and provide higher accuracy than TDDFT. However, these methods are computationally expensive and impractical for studying large systems. Today the real challenge for computational communities is to create a balance between the accuracy of the simulations and the computational costs.

The so-called many-body Green's function *GW* formalism within Bethe-Salpeter Equation (BSE) strikes a balance between accuracy and computational efficiency and has become a gold standard for measuring ground-state properties. It is also capable of accurately predicting excited-state of solids and, more recently, atomic or molecular systems [24, 44]. The fundamental parameter in the *GW* is the one-body Green's function *G*. In 1965, the concept of Green's function *GW* formalism was introduced by Hedin [153] in a set of equations known as Hedin's equations for predicting the electronic structure of an interacting homogeneous electron gas. However, it took more than a decade for its success to be demonstrated at the *ab initio* level of theory. The traditional form of this method is more computationally demanding compared with TDDFT with formal scaling $O(N^5)$. Nevertheless, the capability of this method in the prediction of direct charge-transfer excitations, its independence from any external assumptions as

a parameter-free formalism, and the fact the computational cost can be tuned down to O(N^4) or even O(N^3) using different suggested derivations of *GW* approximation are only a few aspects that yield to raising popularity of this approximation. In the following subsections, we will explore the MBPT method based on the *GW* formalism and compare its drawbacks, limitations, and advantages to those of TDDFT, using the following literature [24, 135, 154–157].

4.1. Green's function

Experimentally IP and EA potentials calculate through direct and inverse photoemission spectroscopy methods, respectively, where one electron separates or adds to the N-electron system [121, 156]. The charged excitation energy of an N-electron system with ground-state energy $E_0(N)$, can be defined as the difference between these energies as is mentioned before in section 2.5. More precisely, for an excited-state n, IP for occupied state energy levels and EA for unoccupied energy levels can be determined as:

$$-IP_i = \varepsilon_i = E_0(N) - E_i(N-1), \tag{4.1}$$

$$-EA_a = \varepsilon_a = E_a(N+1) - E_0(N) \tag{4.2}$$

while ionization potential is below the Fermi level, $\varepsilon_i < E_F$, with i representing all states of (N-1)-electrons system and EA is at or above the Fermi level, $\varepsilon_a \geq \mathrm{E}_F$, with indict a being all states of ($N+1$)-particles system. The fundamental band gap energy can be defined as the subtraction of EA and IP:

$$E_{gap} = (E_a(N+1) - E_0(N)) - (E_0(N) - E_i(N-1)). \tag{4.3}$$

For calculating such energy one needs to calculate the total energy $E(N)$ using Schrödinger equation of the N-electron system: $E(N) = \langle N|H|N\rangle$ where the ground-states $|N\rangle$ are many-body eigenstates of the system. The transition of an N-electrons system to an ($N\pm1$)-electrons system, as defined in Eq. 4.2 and 4.1, can be written based on their eigenstates that are representations of field operators $\widehat{\psi}(\mathbf{r})$ in real space:

$$\begin{aligned} \psi_i(\mathbf{r}) &= \langle N-1|\widehat{\psi}(\mathbf{r})|N\rangle \qquad for \quad \varepsilon_i < E_F \\ \psi_a(\mathbf{r}) &= \langle N|\widehat{\psi}(\mathbf{r})|N+1\rangle \qquad for \quad \varepsilon_a \geq E_F \end{aligned} \tag{4.4}$$

By switching to the Heisenberg representation of field operator $\widehat{\psi}(\mathbf{r})$ to include time dependence we will have [155]:

$$\widehat{\psi}(\mathbf{r},t) = e^{iHt}\widehat{\psi}(\mathbf{r})e^{-iHt} \tag{4.5}$$

Now we can extract information of our interest by introducing the definition of time-ordered single-particle Green's function G that is the central operator in MBPT. Green's function is the probability amplitude for a particle or hole that is created at the time $t^{'}$ to be detected at time t. This parameter can be calculated based on the overlap of the initial state with the final state:

$$G(\mathbf{r},t,\mathbf{r}',t') = -i\langle N|T(\widehat{\psi}(\mathbf{r},t)\widehat{\psi}^{\dagger}(\mathbf{r}',t'))|N\rangle \tag{4.6}$$

where T, or the so-called Dyson time-ordering operator, arranges a series of field operators in order that earlier time apply first on the ground-states $|N\rangle$ and imposes a change of sign for each exchange of $\widehat{\psi}(\mathbf{r},t)$ and $\widehat{\psi}^{\dagger}(\mathbf{r}',t')$.

$$\begin{aligned} T[\widehat{\psi}(\mathbf{r},t)\widehat{\psi}^{\dagger}(\mathbf{r}',t')] &= \widehat{\psi}(\mathbf{r},t)\widehat{\psi}^{\dagger}(\mathbf{r}',t') \qquad for \quad t > t', \\ T[\widehat{\psi}(\mathbf{r},t)\widehat{\psi}^{\dagger}(\mathbf{r}',t')] &= \pm\widehat{\psi}^{\dagger}(\mathbf{r}',t')\widehat{\psi}(\mathbf{r},t) \qquad for \quad t < t'. \end{aligned} \tag{4.7}$$

The definition of Green's function allows describing the process of addition or subtraction of an electron from the system and illustrates the propagation of an electron ($t > t^{'}$, G^{-}) or a hole ($t < t^{'}$, G^{+}). We can rewrite the definition of Green's function as:

$$G(\mathbf{r},t,\mathbf{r}',t') = -i\theta(t-t')\langle N|\widehat{\psi}(\mathbf{r},t)\widehat{\psi}^{\dagger}(\mathbf{r}',t')|N\rangle \tag{4.8}$$

where $\theta(t-t')$ is the Heaviside step function with the definition $\theta(t-t') = \begin{cases} 1, & \text{if } t > t', \\ 0, & \text{if } t < t'. \end{cases}$

To obtain the energies from the time representation of Green's function we can simply apply the Fourier transform of the Heaviside step function by employing Eq. 4.5 as:

$$\theta(\omega) = \frac{1}{2\pi}\int_{-\infty}^{\infty} d\tau\theta(\tau)e^{i\omega\tau-\eta|\tau|} = \frac{i}{2\pi(\omega+i\eta)} \tag{4.9}$$

that leads to the Lehman representation of Green's function [155]:

$$G(\mathbf{r},\mathbf{r}';\omega) = \sum_i \frac{\psi_i(\mathbf{r})\psi_i^{\dagger}(\mathbf{r}')}{\omega-\varepsilon_i-i\eta} + \sum_a \frac{\psi_a(\mathbf{r})\psi_a^{\dagger}(\mathbf{r}')}{\omega-\varepsilon_a+i\eta} \tag{4.10}$$

where η is a positive infinitesimal. The $\psi_{i/a}(\mathbf{r})$, also called "Lehman amplitudes", are simply occupied and unoccupied one-particle wavefunctions, defined in Eq. 4.4 that indicate overlap between the N-electrons system with ith/ath states of $(N\pm1)$-particles system. Here the poles of Green's function located at $\omega = \varepsilon_{i/a}$ are the real charged excitation energies of the system. In contrast to DFT, $\varepsilon_i, \varepsilon_a$ have the same values as they can be measured in direct and indirect photo-electron emission experiments [24]. Experimentally, instead of directly dealing with $G(\mathbf{r},\mathbf{r}',\omega)$, one uses the diagonal

spectral function $A(\mathbf{r},\mathbf{r}',\omega)$ definition. The spectral function, which is the density of the excited-states, interprets the probability of finding a system in energy ω while one electron is either added or removed from the system. This function can be defined via $A(\mathbf{r},\mathbf{r}',\omega) = \frac{1}{\pi} ImG(\mathbf{r},\mathbf{r}',\omega)\ sgn(E_F - \omega)$, as:

$$A(\omega) = \sum_i \psi_i(\mathbf{r})\psi_i^\dagger(\mathbf{r}')\ \delta(\omega - \varepsilon_i) + \sum_a \psi_a(\mathbf{r})\psi_a^\dagger(\mathbf{r}')\ \delta(\omega - \varepsilon_a) \tag{4.11}$$

4.2. Dyson's equations

The extension of introduced one-body Green's function to a true many-body system of interacting electrons in an external potential makes this function a powerful tool for calculating both ground and excited-state properties. The many-body perturbation expansion of G can be classified by arbitrary Feynman diagrams, which is a graphical representation of perturbation series [158]. Dyson's equation [159] summarizes the Feynman expansions in a particularly compact form by collecting all one-particle irreducible diagrams. Through Dyson's equation in the definition of the exact many-body Green's function, the non-interacting Green's function, G_0, links to the interacting ones by operator Σ or so-called self-energy as:

$$G(1,2) = G_0(1,2) + \int G_0(1,3)\Sigma(3,4)G(4,2)d(3,4)\ or\ G = G_0 + G_0\Sigma G \tag{4.12}$$

Σ represents the complicated correlation of a many-particle system and contains all electron-electron interactions. In this representation, notations ($\mathbf{r}$t, $\mathbf{r}'t'$, ...) are replaced with notations (1,2, ..) for simplicity. For describing our many-body system we recall the basic definition of time-dependent interacting Hamiltonian, based on filed operator $\psi(\mathbf{r},t)$ in BO approximation, defined in Section 2.1 as:

$$\int \psi^\dagger(\mathbf{r},t)H_0\psi(\mathbf{r},t)\ d^3r + \frac{1}{2}\underbrace{\int\int \psi^\dagger(\mathbf{r},t)\psi^\dagger(\mathbf{r}',t)v(\mathbf{r},\mathbf{r}')\psi(\mathbf{r},t)\psi(\mathbf{r}',t)\ d^3r d^3r'}_{V_H} = E\psi(\mathbf{r},t) \tag{4.13}$$

where $v(\mathbf{r},\mathbf{r}')$ is the Coulomb interaction (Hartree potential) and H_0 is the independent-electron Hamiltonian including kinetic energy ($-\frac{\hbar}{2m}\nabla_i^2$) and the electron–nuclei potential (V_{ext}). In the Heisenberg picture, applying definition of H in the commutator part of equation of motion, $i\frac{\partial\psi(\mathbf{r},t)}{\partial t} = [\psi(\mathbf{r},t), H]$, yields to:

$$i\frac{\partial\psi(\mathbf{r},t)}{\partial t} = [H_0(\mathbf{r}) + \int \psi^\dagger(\mathbf{r}',t)v(\mathbf{r},\mathbf{r}')\psi(\mathbf{r}',t)\ d^3r']\ \psi(\mathbf{r},t) \tag{4.14}$$

The equation of motion can be deduced for Green's function as:

$$[i\frac{\partial}{\partial t_1} - H_0(\mathbf{r}) - V_H]\ G(1,2) - \int \Sigma(1,3)\ G(3,2)\ d3 = \delta(1,2) \tag{4.15}$$

with δ being Dirac's delta function. Finally, by plugging the definition of Green's function from Eq. 4.10 in the equation of motion we reach a single-particle eigenvalue equation referred to as the quasiparticle (QP) equation similar to KS eigenvalue problem (Eq. 2.19):

$$[H_0(\mathbf{r}) + V_H(\mathbf{r})]\ \psi(\mathbf{r}) + \int \Sigma(\mathbf{r},\mathbf{r}'',\omega)\ \psi(\mathbf{r}'')\ d^3r'' = E\ \psi(\mathbf{r}) \tag{4.16}$$

By using the exact value of the self-energy, Σ, we can construct a many-body equation that generalizes the one-body eigenvalue equation, allowing us to calculate the entire spectrum of $\varepsilon_{i/a}$. The primary challenge is to express the self-energy as a function of Green's function, G. The quantum chemistry community has suggested various methods for representing this operator, resulting in different types of theories. For instance, in the ADC(n) methods [160], the self-energy is defined based on bare $v(\mathbf{r},\mathbf{r}')$. However, one of the most widely used and popular derivations of the self-energy was proposed by Hedin [153] in a self-contained set of five equations, known as Hedin's equations. These equations provide a powerful framework for calculating the self-energy and understanding the interactions between electrons in many-body systems.

4.3. Hedin's equations

Hedin introduced a new expansion of self-energy in terms of the screened Coulomb interaction, $W(1,2)$ where (1,2, ..) represent notations ($\mathbf{r}$t, $\mathbf{r}'t'$, ...). He only considered partial summation to infinite order of $v(1,2)$ instead of developing Σ in a power series of bare Coulomb interaction [153]. These two parameters can describe all the interactions in the system while screened Coulomb interaction represents the electron-hole attraction and self-energy is the electron-electron repulsion. By applying Schwinger functional-derivative method [161] Hedin reached a set of integrodifferential equations called Hedin's equations:

$$G(1,2) = G_0(1,2) + \int G_0(1,3)\Sigma(3,4)G(4,2)d(3,4) \tag{4.17}$$

$$P(1,2) = -i \int G(2,3)G(4,2)\Gamma(4,2,3)d(3,4) \tag{4.18}$$

$$W(1,2) = v(1,2) + \int v(1,3)P(3,4)W(4,2)d(3,4) \tag{4.19}$$

$$\Sigma(1,2) = i\int G(1,4)W(1^+,3)\Gamma(4,2,3)d(3,4) \tag{4.20}$$

$$\Gamma(1,2,3) = \delta(1,2)\delta(1,3) + \int \frac{\delta\Sigma(1,2)}{\delta G(4,5)}G(4,6)G(7,5)\Gamma(6,7,3)d(4,5,6,7). \tag{4.21}$$

The superscript $^+$ indicates the addition of a positive infinitesimal to the time ($t_1^+ = t_1 + \eta$) to ensure the correct time order of sequences. The third term in the many-body equation, represented by W(1,2), is the effective potential of electron 1 due to electron 2. When two electrons are in close proximity to each other, the second electron repels all other nearby electrons, leading to the formation of a positive cloud around each electron. This positive cloud weakens the interaction between the two electrons compared to the bare Coulomb interaction. Therefore, considering this effect in the term of screened Coulomb interaction, with a higher convergence rate in the perturbation expansion, is more reasonable than $v(1,2)$.

By introducing an external perturbation field, U, that is set to zero afterward, Hedin considered the variation of Green's function due to U based on the linear response approach. This consideration leads to the interpretation of irreducible and reducible polarizability as $P(1,2) = -i\frac{\delta G(1,1^+)}{\delta V(2)} = \frac{\delta n(1)}{\delta V(2)}$ and $\chi(1,2) = -i\frac{\delta G(1,1^+)}{\delta U(2)} = \frac{\delta n(1)}{\delta U(2)}$, respectively, and representation of 3-point vertex as $\Gamma(1,2,3) = -i\frac{\delta G(1,2)}{\delta V(3)}$. If we consider $V(\mathbf{r})$ is the summation over introduced external perturbation filed and Hartree potential as, $V(1) = U(\mathbf{r}) + V_H(\mathbf{r})$, P, χ, and Γ simply describe the variation of Green's function upon an external field.

4.4. From Hedin's equations to GW approximation

Going through a full self-consistent cycle from Eq.4.17 to Eq.4.21 governs an exact solution to the interacting Green's function of a many-body system. However, the inclusion of higher-order terms of the vertex function, Γ, which depends on three space-time points (1,2,3), makes the calculations intractable and difficult to solve. To simplify the theory, Hedin proposed an alternative solution, where only the first term of the vertex function is considered, and higher vertex corrections are neglected. This approximation, often referred to as the Random Phase Approximation (RPA), is given by $\Gamma(1,2,3) = \delta(1,2)\delta(1,3)$ [162, 163]. By applying this approximation to Hedin's differential equations, the self-energy takes on a more straightforward form, $\Sigma = iGW$,

and the resulting self-consistent equations are known as the GW approximation:

$$G(1,2) = G_0(1,2) + \int G_0(1,3)\Sigma(3,4)G(4,2)d(3,4) \tag{4.22}$$

$$\chi_0(1,2) = -iG(1,2^+)G(2,1) \tag{4.23}$$

$$W(1,2) = v(1,2) + \int v(1,3)\chi_0(3,4)W(4,2)d(3,4) \tag{4.24}$$

$$\Sigma(1,2) = iG(1,2)W(1^+,2) \tag{4.25}$$

$$\Gamma(1,2,3) = \delta(1,2)\delta(1,3) \tag{4.26}$$

where χ_0 is the independent electron susceptibility or response function that has been defined by employing RPA. This function is the main parameter in the definition of the dielectric function $\varepsilon^{-1}(1,2)$:

$$\varepsilon^{-1}(1,2) = \delta(1,2) \int v(1,3)\chi(3,2)\ d3 \tag{4.27}$$

that relates the screened Coulomb interactions to the bare one:
$W(1,2) = \int \varepsilon^{-1}(1,3)v(3,2)\ d3$. The GW approximation is typically solved iteratively, starting with an initial guess for the Green's function, G_0, and then calculating all parameters in the order presented in Eq. 4.22 to Eq. 4.26. The iterative process continues until the interacting Green's function in Eq. 4.22 converges to a predefined criterion value. Depending on the number of particles, going through full self-consistent GW approximation, or so-called *scGW*, with $O(N^5)$ calculation scale, can be computationally demanding and even not affordable. To reduce the computational cost of *scGW* calculations, alternative methods have been developed that apply different levels of self-consistency that yield various flavors of *scGW* approximation. Here only a few of these flavors based on their relevance to this thesis will be introduced.

4.5. G_0W_0 formalism

One of the simplest but meanwhile popular flavors of GW method is one-shot perturbative GW or G_0W_0. In this approach one terminates the self-consistency after the first iteration of Dyson's equations and G_0 parameter calculate directly. In this approach is more common to use KS or HF eigenvalues and orbitals and construct the interacting Green's function and χ_0 based on them. In KS-DFT framework the G_0 and χ_0 written as:

$$G_0^{KS}(\mathbf{r},\mathbf{r}',\omega) = \sum_i \frac{\phi_i(\mathbf{r})\phi_i^*(\mathbf{r}')}{\omega - \varepsilon_i^{KS} - i\eta} + \sum_a \frac{\phi_a(\mathbf{r})\phi_a^*(\mathbf{r}')}{\omega - \varepsilon_a^{KS} + i\eta} \tag{4.28}$$

$$\begin{aligned}\chi_0^{KS}(\mathbf{r},\mathbf{r}',\omega) &= -\frac{i}{2\pi}\int G_0(\mathbf{r},\mathbf{r}',\omega+\omega')G_0(\mathbf{r}',\mathbf{r},\omega')\ d\omega' \\ &= \sum_i^{occ}\sum_a^{virt}(f_a - f_i)\ \frac{\phi_i^*(\mathbf{r}')\phi_a(\mathbf{r})\phi_i(\mathbf{r})\phi_a^*(\mathbf{r}')}{\omega - (\varepsilon_a^{KS} - \varepsilon_i^{KS}) \pm i\eta}\end{aligned} \tag{4.29}$$

where f_i and f_a are the occupation factors of states i and a. Subsequently, the screened Coulomb interaction W_0, dynamical dielectric function ε, and the self-energy in RPA read as:

$$W_0(\mathbf{r},\mathbf{r}',\omega) = \int \varepsilon^{-1}(\mathbf{r},\mathbf{r}'',\omega)v(\mathbf{r}'',\mathbf{r}')\ d^3r'' \tag{4.30}$$

$$\varepsilon(\mathbf{r},\mathbf{r}',\omega) = \delta(\mathbf{r},\mathbf{r}')\ -\ \int \chi_0(\mathbf{r}'',\mathbf{r}',\omega)v(\mathbf{r},\mathbf{r}'')\ d^3r'' \tag{4.31}$$

$$\Sigma(\mathbf{r},\mathbf{r}',\omega) = \frac{i}{2\pi}\int e^{i\eta\omega'}G_0(\mathbf{r},\mathbf{r}',\omega+\omega')W_0(\mathbf{r},\mathbf{r}',\omega')\ d^3r\omega' \tag{4.32}$$

Back to QP eigenvalue Eq. 4.16 and replacing quasiparticle wavefunctions $\psi(\mathbf{r})$ with KS wavefunction $\phi(\mathbf{r})^{KS}$ one can reach the QP-energies by solving diagonal QP equation:

$$\varepsilon_s^{QP} = \varepsilon_s^{KS} + \langle\phi_s|\Sigma^{GW}(\varepsilon_s^{QP}) - v_{xc}^{KS}|\phi_s\rangle \tag{4.33}$$

where s runs over all occupied and unoccupied states. $\Sigma^{GW}(\varepsilon_s^{QP}) - v_{xc}^{KS}$ term represents the perturbative correction of DFT exchange-correlation potential. As the KS eigenvalues ε_s^{KS} should calculate based on a specific exchange-correlation functional, for example, PBE, it's more common to label applied G_0W_0 method as G_0W_0@PBE to also refer to the type of *xc* functional. The correction in G_0W_0 method can significantly improve the underestimation of DFT-based band gap and reduce the deviation from experimental results as also discussed in this thesis and many other studies [164–167]. Despite such an enhancement, the G_0W_0 results inherently depend on DFT functionals since the KS wavefunctions and eigenvalues are not updated in any self-consistent cycle. Even by optimizing the initial DFT results using hybrid functionals with a tuned amount of exact exchange, this dependency cannot be entirely eliminated [168]. Therefore partial self-consistent techniques with keeping self-consistency in different parts of *GW* equations (4.22 to 4.26) are proposed for removing such dependency.

4.6. Partially self-consistent GW

The GW_0 approach is an intermediate method that simplifies the *scGW* formalism by iterating only the eigenvalue self-consistency on the Green's function G, while keeping the χ_0 and screened interaction, W, fixed in each iteration. The χ_0 and W terms are the most challenging parts of the *scGW* formalism [169]. In this approach χ_0 and W_0

build directly from Eq.4.28 and Eq.4.29 and self-energy represent as:

$$\Sigma(1,2) = iG(1,2)W_0(1^+,2). \tag{4.34}$$

One useful flavor of the *scGW* method that can mitigate the starting point dependency is the partial self-consistent eigenvalue method, or the evG_nW_n approach (n=number of iterations) [170]. In this method, only the eigenvalues go through a self-consistent cycle, and these corrected eigenvalues are used to construct the new Green's function and screened interaction. In the first step, the non-interacting Green's function G_0 is constructed based on the KS wavefunction, and the QP energies are calculated using Eq. 4.33. In the second step, the eigenvalues ε_i^{QP} are injected into Eq. 4.28, while the wavefunctions remain unchanged. In each iteration, the eigenvalues from the prior GW cycle are used until the convergence criterion is fulfilled. Although the evG_nW_n approach can remove a major part of the starting point dependence and moderately improve the HOMO-LUMO gap and excitation spectrum compared to the G_0W_0 approach [43, 166, 171], it cannot eliminate it entirely [172, 173], as only the real part of ε_i^{QP} is iterated, and the KS wavefunctions are not updated self-consistently.

The next recently proposed scheme called quasiparticle self-consistent GW approximation (QSGW) [174], aims to construct the self-consistency in a manner to minimize the perturbation in MBPT. This method is best formulated in G_0W_0 framework and uses its one-body Hamiltonian $H_0 = -\frac{\hbar}{2m}\nabla_i^2 + V_{ext}$ as a starting point that updates in each iteration. By defining an effective one-electron Hamiltonian H_{eff}, determining the time-evolution of the one-body amplitude for the many-body system [174], we will have:

$$H_{eff}(\omega) = -\frac{\hbar}{2m}\nabla_i^2 + V_{ext} + V_H + \Sigma(\omega). \tag{4.35}$$

In which one can optimize H_0 with respect to $\Delta V(\omega) = H(\omega) - H_0$ value.

It is worth noting that despite the evaluation of partial self-consistent GW methods in the last decades, many benchmark studies have illustrated that the improvements in band gap or excitation energies brought by the introduced QSGW or even fully *scGW* methods are somehow unrewarding concerning the computational coast for extended atomic or molecular systems [175–178]. This outcome suggests that simple G_0W_0 and evG_nW_n methods combined with optimal generalized Kohn–Sham starting points are sufficient for the study of small to immense molecular systems with a smaller scaling in terms of system size of $O(N^{3-4})$ [24, 48, 49, 179, 180].

4.7. Bethe-Salpeter Equation

The introduced GW scheme is not only a compelling method for calculating particle addition/removal energies but also its formulation based on MBPT can also be used to determine optical or neutral excitations [135]. In the original paper of Bethe and Salpeter [181] they considered a 4-point vertex function for representing two-particle correlated electron-hole amplitude, following the linear response method, called $L(1,2,3,4)$. This vertex function can be represented as:

$$L(1,2,3,4) = -i\frac{\delta G(1,2)}{\delta U(3,4)} \tag{4.36}$$

where U is a local external perturbation. Reducible polarizability can relate to this function via $\chi(1,2) = L(1,2,3,4)$ equation. By rewriting the above formulation of L function in a Dyson-like formalism similar to Eq. 4.21 one can reach to the famous Bethe-Salpeter Equation:

$$L(1,2,3,4) = L_0(1,2,3,4) + \int L_0(1,2,3,4)\ \Xi^{BSE}(3,5,4,6)\ L_0(7,8,3,4)\ d(5,6,7,8) \tag{4.37}$$

with $L_0(1,2,3,4) = \frac{\delta G_0(1,2)}{\delta U(3,4)} = G(1,4)G(2,3)$ being the noninteracting 4-point response function. The Ξ^{BSE} is the generalized BSE kernel that relates to the derivation of self-energy as:

$$\Xi^{BSE}(3,5,4,6) = v(5.7)\delta(5,6)\delta(7,8) + \frac{\delta\Sigma(5,6)}{\delta G(7,8)}. \tag{4.38}$$

To calculate the reducible polarizability χ, which is essential for optical absorption calculations, one needs to determine the self-energy via Ξ^{BSE}. A commonly used method for self-energy estimation is the screened Hartree-Fock, or the so-called GW approach with $\Sigma = iG(1,2)W(1,2,\omega)$. This GW/BSE combination is preferred over other approximations due to its more realistic definition of electron-hole interaction through the W parameter. The BSE kernel in the GW/BSE formalism is represented as:

$$\Xi^{BSE}(3,5,4,6) = v(5.7)\delta(5,6)\delta(7,8) - W(5,6)\delta(5,7)\delta(6,8) \tag{4.39}$$

where higher orders of W expansion have been neglected. In this formulation, W and self-energy are dynamic by means of their dependence on frequency ω. There are several ways to treat the frequency dependency in the BSE formalism. For instance, one can constrain the screened Coulomb interaction $W(\omega = 0)$, similar to the TDDFT approach, to obtain the standard static BSE approximation [182].

One can use a transition product basis $\phi_{i/a}$ in the response functions L to obtain a

generalized eigenvalue equation that is similar to the Casida formalism (Eq. 3.13) in TDDFT [121]. In this representation, the electron-hole eigenstates, or the transition densities of the Casida Hamiltonian, can be written as:

$$\gamma_n^{BSE}(\mathbf{r}_e, \mathbf{r}_h) = \sum_{ia} \left(X_n^{ia} + Y_n^{ia}\right) \phi_i(\mathbf{r}_e)\phi_a^*(\mathbf{r}_h) \tag{4.40}$$

where a/b and i/j are the occupied and virtual states, respectively, and n is the optical excitation number. What distinguishes the GW/BSE formalism from TDDFT is concealed in the definition of matrix elements A and B in Eq. 3.13. In GW/BSE method one uses QP eigenvalues, ε^{QP}, instead of generalized KS eigenstates, ε^{KS}. Furthermore, the kernel matrix element $K_{ia,jb}$ in TDDFT replaces with the definition of screened Coulomb interaction W. In GW/BSE the resonant transitions from occupied to unoccupied orbitals, A_{ia}^{jb}, and the coupling between resonant and antiresonant transition, B_{ia}^{jb}, represent as:

$$\begin{aligned} A_{ia}^{jb} = &(\varepsilon_a^{QP} - \varepsilon_i^{QP})\delta_{ij}\delta_{ab} \\ &+ \langle\phi_a(\mathbf{r})\phi_i(\mathbf{r})|v(\mathbf{r},\mathbf{r}')|\phi_b(\mathbf{r}')\phi_j(\mathbf{r}')\rangle \\ &- \langle\phi_a(\mathbf{r})\phi_i(\mathbf{r}')|W(\mathbf{r},\mathbf{r}',\omega)|\phi_b(\mathbf{r})\phi_j(\mathbf{r}')\rangle, \end{aligned} \tag{4.41}$$

$$\begin{aligned} B_{ia}^{jb} = &\langle\phi_a(\mathbf{r})\phi_i(\mathbf{r})|v(\mathbf{r},\mathbf{r}')|\phi_b(\mathbf{r}')\phi_j(\mathbf{r}')\rangle \\ &- \langle\phi_a(\mathbf{r})\phi_i(\mathbf{r}')|W(\mathbf{r},\mathbf{r}',\omega)|\phi_b(\mathbf{r})\phi_j(\mathbf{r}')\rangle \end{aligned} \tag{4.42}$$

while neglect of B and $-B^*$ blocks, or in other words the electron-hole interaction via screened Coulomb interaction, leads to Tamm-Dancoff approximation (TDA) [139]. As it has been illustrated before the GW/BSE calculations are performed as a post-processing step on top of a previous self-consistent DFT run. The (GKS) KS orbitals will be used to construct the Green's function and screen Coulomb interaction and finally, the excitation energies and related oscillator strength calculated from QP eigenvalues via A and B matrix block. Figure 4.1 show the usual workflow of perturbative GW/BSE calculations which connect the Green's function to the self-energy through introduced Hedin's equations. The GW/BSE method has a rich history, dating back to its first use in the study of organic molecules in 1990 [24]. However, it is only in the past two decades that this approximation has become more widely used as the *de facto* standard approach for accurate prediction of electronic structure and absorption spectra of a wide range of materials [156]. The fame of this method is attributed to several factors, including its favorable scaling with respect to system size, its ability to be combined with different theories or implemented in different frameworks, and most importantly, its potential for overcoming the well-known problems of TDDFT regarding non-locality features. As it is discussed in section 3.2, the standard TDDFT

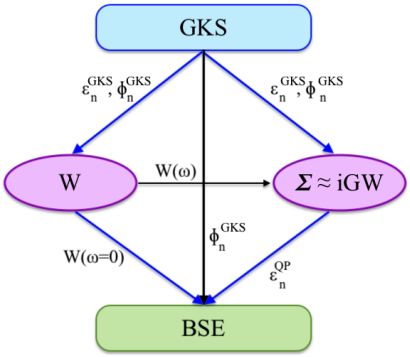

Figure 4.1: Workflow of perturbative GW and BSE calculations based on the original version in Ref. [135].

method fails to correctly describe charge-transfer excitation due to its incorrect asymptotic 1/R long-range behavior. However, in GW/BSE formalism the charge-transfer excitation energy:

$$E^{CT} = \varepsilon_a^{QP} - \varepsilon_i^{QP} - \langle \phi_a(\mathbf{r})\phi_i(\mathbf{r}')|W(\mathbf{r},\mathbf{r}',\omega)|\phi_b(\mathbf{r})\phi_j(\mathbf{r}')\rangle \tag{4.43}$$

has a correct decay as in long distances by reduction of screened Coulomb potential W to the bare Coulomb, the last term will not vanish and will keep the asymptotic 1/R behavior. Despite such success, continuous development and assessment of its accuracy for different types of molecular systems, in comparison with experiments or higher-level wavefunction approaches, remains a crucial task. Hope my work by benchmarking the performance of GW/BSE method for different types of BCL complexes can have a small contribution to this field of research.

Chapter 5

Numerical implementation

In addition to the importance of developing more advanced computational methods, the implementation of these approaches can have a crucial role in the ascertainment of efficiency and accuracy of the results. In practice for the translation of these theories to codes, one needs to employ scalable algorithms or apply further approximations and boundaries in numerical calculations. This chapter aims to provide key information on the fundamental approximations primarily implemented in different software packages. For all *GW*/BSE calculations in this thesis, the *MOLGW* software package [182] was employed. As the *MOLGW* software package is specifically designed for *GW*/BSE calculations, it is not well-suited for efficient parallelization in TDDFT calculations and may be time-consuming for large molecular systems. In this regard, except 6.3 that is focused on smaller BCL and Chl monomeric aggregates, we have done the TDDFT simulations through their implementation in two different codes, *TURBOMOLE* [183], and *Q-chem* [184]. It's important to note that certain software packages are better suited for specific tasks, and therefore the choice of software package can aid in the interpretation of results by providing access to different tools. For instance, *TURBOMOLE* is particularly efficient at calculating forces on nuclei, making it ideal for geometry relaxation of structures and vibrational normal mode analyses. However, to ensure the comparability of results, we maintained consistent computational setups and employed similar approximations in all of our simulations.

5.1. Basis set and related approximations

The one-particle wavefunction in the KS equation comprises a radial and an angular component. The KS equation can be solved through iterative numerical calculations, and the radial part of the wavefunction can be expanded using a set of mathematical functions referred to as basis functions or basis sets [185]. In this representation, the wavefunction is expressed as a linear combination of atomic orbitals $\phi_m(\mathbf{r})$, which are centered at each nucleus in the molecule:

$$\phi_m(\mathbf{r}) = \Sigma_m C_{mn} \varphi_m(\mathbf{r}) \tag{5.1}$$

where molecular orbital expansion coefficients C_{mn} is determined by arranging the KS equation in a diagonal matrix-eigenvalue form, known as the Roothaan-Hall equation:

$$H_{ks} C = S C \varepsilon_{ks} \tag{5.2}$$

that should solve self-consistency where S is the basis function overlap matrix $S_{\mu\nu} = \langle \varphi_\mu | \varphi_\nu \rangle$. The Gaussian [186], Slater [187], and plane-wave basis sets [188] are among the most commonly used representations of basis functions in various software packages. While the plane-wave basis set, which corresponds to the eigenstates of a homogeneous electron gas, is typically used within the solid-state community and exhibits superior performance for periodic systems, it generates a much larger Hamiltonian compared to local orbitals. In local orbital classification, Slater-type functions are hard to deal with in three- and four-center integrals such as repulsion integrals [185]. Gaussian-type orbital (GTO) functions are the most widely used basis sets in the quantum chemistry community for electronic structure calculations of finite-size systems due to their efficient integral evaluation. Consequently, all performed calculations in this thesis are based on the implementation of Cartesian Gaussian-type basis functions in *TURBOMOLE, Q-CHEM, and MOLGW* software packages following the representation below for the basis functions:

$$\varphi_m(\mathbf{r})^{GTO} = (x - x_0)^{n_x} \; (y - y_0)^{n_y} \; (z - z_0)^{n_z} \; \Sigma_b c_b e^{-\alpha(\mathbf{r} - A)^2} \tag{5.3}$$

where (n_x, n_y, n_z) and α are the angular momentum and decay rate, respectively, while the atom nucleus is located at coordinate $A = (x_0, y_0, z_0)$. The superiority of Slater-type orbitals over Gaussian-type orbitals is mainly due to the exponential part of the basis sets. Slater-type orbitals have an exponential decay behavior of the form $e^{-\alpha(\mathbf{r} - A)}$ that matches the shape of atomic orbitals. In contrast, Gaussian-type orbitals are flat and differentiable at the nucleus $\mathbf{r} = 0$ and have an incorrect behavior while also falling

off more quickly in further distances from the nucleus, $r = \infty$. The linear combination of primitive Gaussian functions mentioned above can help mitigate the issue with the decay behavior of Gaussian-type orbitals. Unfortunately using the Complete Basis Set (CBS) with an infinite number of primitive Gaussian functions ($b \to \infty$) is impossible. Hence, a finite combination of functions, known as contracted Gaussian, must be used instead. This limitation leads to a size-ranking representation of basis sets, where the basis sets are categorized based on the number and type of functions included in the set, as well as the determination of the angular component.

Minimal basis sets are the simplest sets that use only a single basis function for each atomic orbital in the atom and attempt to approximate Slater-type orbitals using n primitive Gaussian ($b = 1, .., n$). However, they lack the flexibility to adapt to different molecular environments, and therefore, are usually unsatisfactory for high-accuracy simulations. To improve accuracy, basis sets can include multiple basis functions corresponding to all atomic orbitals or only the valence space, which plays a more significant role in most molecular bonding. These basis sets are referred to as *split-valence basis sets*, and the number of basis functions considered in the basis set is distinguished by terms such as "double zeta" (DZ), "triplet zeta," and so on. The next level of increasing orbital flexibility is achieved by describing the polarization of the electron density of the atoms using higher order angular momentum functions such as d-type and p-type functions for heavier and lighter atoms (such as hydrogen and helium), respectively. These sets are called polarization functions and as the chemical bonds are generally polarized, consideration of these sets can be paramount for modeling the atomic bonding and consequently structural details. The next addition to the basis sets are diffuse basis functions that allow the description of electron density further from the nucleus by extending the tail portion of the atomic orbitals through the addition of small exponent α to the basis sets [189]. These functions improve the predicted properties of the anionic systems and EA energy. By convention, the basis sets including both polarization and diffuse functions considered balanced basis sets. Table 5.1 comprises a few of the most common basis functions in the quantum chemistry community that also has been used in my work.

The Pople basis sets [190], shown in the first row, are categorized as split-valence basis sets, which employ one contracted Gaussian function per core atomic orbital while using more than one atomic orbital to describe valence orbitals. The DZ group of Pople basis sets is commonly represented as $X-YZG$, where s and p functions share common exponents. Here, X represents the number of primitive Gaussian functions included in core atomic orbitals, and Y and Z indicate the number of primitive Gaussian functions comprising the first and second valence orbitals, respectively. The addition of polarization and diffuse functions to non-hydrogen atoms is denoted by the $*$ and $+$ notations

subclass	Basis set	
Pople	6-311G	6 primitives in the core and a triply split valence basis set
	6-311G**/6-311G(d,p)	polarization functions on all atoms
	6-311++G	diffuse functions on all atoms
correlation-consistent	cc-pVDZ	valence double zeta polarized
	cc-pVTZ	valence triple zeta polarized
	aug-cc-pVTZ	augmented versions of cc-pVTZ within diffuse functions
Karlsruhe	def2-SVP	split valence (double zeta) polarized
	def2-TZVP	valence triple zeta polarized
	def2-TZVPP	valence triple zeta heavily polarized

Table 5.1: Three subclasses of basis functions as has been introduced in the main text. For each subclass, a few basis sets along with illustrations of their initials are represented.

in the set, with the double notation indicating the addition of functions to all atoms. The second row is dedicated to correlation-consistent basis sets (*cc*) [191], which are optimized using extrapolation to correlated (CISD) wavefunctions. In this set, all functions within a set are chosen to yield similar atomic correlation energy as calculated by the correlated CISD method. The general form of these basis sets is $cc-pVXZ$, where $-pV$ refers to polarized and split-valence basis sets, and XZ can be DZ, TZ, and so on. The prefix *aug* signifies that one set of diffuse functions is included for every angular momentum present in the basis. Lastly, the second generation of default basis sets for the *TURBOMOLE* package developed by Ahlrichs group is represented in the last row, known as the Karlsruhe or def2 basis sets [192]. These basis sets are optimized for response properties and are designed to reproduce dipole polarizabilities computed by methods such as MP2, and are balanced basis sets. A detailed discussion on the differences between Gaussian-type basis sets and their performance is beyond the scope of this thesis, and interested readers are referred to Refs. [189, 193–195].

The choice of basis set has a significant impact on the accuracy and associated computational cost of the resulting data, particularly in GW/BSE calculations [196–198]. This highlights the importance of an optimization process to strike a balance between accuracy and performance prior to theoretical simulations. To achieve this, one can estimate the CBS result by systematically increasing the number of basis functions and extrapolating to an infinite-size basis set. Should be noted *MOLGW* software package offers such extrapolation to a trained linear regression automatically for each calculation [182, 198].

Regardless of the type of basis set used, increasing the number of atoms in the sys-

tem leads to a significant increase in the size of the basis set (N_{basis}), resulting in higher computational and memory costs. Hence, to reduce the runtime of simulations, further approximations such as the frozen-core approximation or resolution-of-the-identity (RI) method are often employed. In the frozen core approximation [199, 200], one assumes that the inner-shells or inactive core electrons do not change their states throughout the calculations, and thus, their corresponding orbitals can be excluded from the correlation. Numerous benchmark studies have confirmed the high accuracy and efficiency of this method [201, 202].

The resolution-of-the-identity (RI) method is another commonly used approach that allows the representation of two-electron four-center integrals (*e.g.* Eq. 3.12) in the form of two- and three-center ones [203, 204]. The RI method, in combination with DFT, is a useful tool for approximating the total electron density in terms of so-called auxiliary basis functions, in which the expansion coefficients C_{mn} can be determined by an optimum Coulomb metric. It is shown the RI-inaccuracy in calculations of DFT total energy is in order of meV [204, 205] while this method can scale downs the computational cost in the order of magnitude, usually $O(N^3)$ instead of $O(N^4)$ [206, 207]. In *GW* simulations, the RI error in predicting the HOMO and LUMO states can be slightly larger, but this error can be reduced by using a more comprehensive basis set [164, 167]. Hence, in many codes, the use of the RI method is strongly recommended, and in some cases, it is mandatory [208].

In addition to the choice of basis set and discussed approximations, the accuracy of DFT results is also strongly influenced by the selection of grid points in real space. The DFT potential will be evaluated on a radial grid and xc integrals will be calculated for each grid point. The number of grid points per atom is defined on vectors surrounding the molecule, and the accuracy of the results depends on the size of these grids. While many software packages have default values for grid size, it is suggested that the user may need to increase the grid size for certain types of simulations or in case of numerical integration problems. This is particularly important for simulations such as geometry optimization and frequency calculations, where the accuracy of the results can be more sensitive to the choice of grid size due to the specific framework of the method. It is recommended to specify the mesh range or the number of grid points in the setup of the calculations or to consult the software documentation to determine the appropriate grid size for a given simulation.

5.2. Technical implementation of GW/BSE formalism

This section will describe the technical details of G_0W_0/BSE formalism when a finite basis set is used following Ref. [156, 164, 182, 209]. Note that in the rest of this chapter, we will refer to electron repulsion integrals as below for the sake of simplicity:

$$\langle ia|jb\rangle = \int\int \phi_i(\mathbf{r})\phi_j(\mathbf{r}')\frac{1}{|\mathbf{r}-\mathbf{r}'|}\phi_a(\mathbf{r})\phi_b(\mathbf{r})\ d^3r d^3r' \tag{5.4}$$

Knowing the G_0 and W_0 formalism from Eq. 4.28 and 4.30, the next step would be calculating self-energy $\Sigma = iG_0W_0$ to obtain the QP eigenvalue ε_s^{QP} via Eq. 4.33. The diagonal matrix elements of the self-energy read as:

$$\Sigma(\omega) = \langle \phi_s^0 \mid \Sigma(\omega) \mid \phi_s^0 \rangle. \tag{5.5}$$

The self-energy includes the exchange term as $\langle \phi_s^0 \mid \Sigma(\omega)_x \mid \phi_s^0 \rangle = -\Sigma_i^{occ}\langle si|is\rangle$ and the real part of the correlation contribution can be written as:

$$\langle \phi_s^0 \mid \Sigma(\omega)_c \mid \phi_s^0 \rangle = \sum_{in} \frac{\rho_n^{si}(\mathbf{r})\rho_n^{si}(\mathbf{r}')}{\omega - \varepsilon_i + \Omega_n - i\eta} + \sum_{an} \frac{\rho_n^{sa}(\mathbf{r})\rho_n^{sa}(\mathbf{r}')}{\omega - \varepsilon_a - \Omega_n + i\eta} \tag{5.6}$$

where i and a are the occupied and virtual states, respectively, and s runs over all states. In this formalism the residues $\rho_n(\mathbf{r})$ are the transition densities as has been defined in Eq. 4.40. After diagonalization of Eq. 3.13, one can obtain eigenvalues Ω_n and the eigenvectors (X_n, Y_n), implemented in $\rho_n(\mathbf{r})$. Afterward, the self-energy and ε_s^{QP} should solve iteratively from the above equation and the diagonal quasi-particle Eq. 4.33. However, as the correlation part of self-energy is a complex term, most software packages use a few different techniques to prevent re-calculation of $\Sigma(\omega)_c$. In the linearized method, by assuming a comparatively small energy difference between ε_s^{QP} and ε_s^0 one uses the first-order Taylor expansion of the matrix elements $\Sigma(\omega)$ as [156]:

$$\varepsilon_s^{QP} = \varepsilon_s^0 + Z_s\ \langle \phi_s^0 | \Sigma^{GW}(\varepsilon_s^{QP}) - v_{xc}^{KS} | \phi_s^0 \rangle \tag{5.7}$$

where $Z_s = [1 - \langle \phi_s^0 | \frac{\partial \langle \phi_s^0 | \Sigma(\omega) | \phi_s^0 \rangle}{\partial \omega} |_{\omega=\varepsilon_s^0} | \phi_s^0 \rangle]^{-1}$ is the QP renormalization factors. This method is most accurate for the states near to HOMO and LUMO.

Another alternative method, known as the graphical solution, considers the crossing point of the straight line $\omega - \varepsilon_s^0 + v_{xc} - \Sigma_x$ and the correlation part of the self-energy Σ_c around ε_s^0 calculated for frequencies ω, as the possible solutions to quasi-particle Eq. 4.33. In *MOLGW* code both solutions to the quasi-particle equation are computed

and printed out in the output file.

The iterative self-energy solution is not the only parameter affecting the computational cost of *GW* calculations; the matrix size of self-energy is another crucial factor. The G_0 function has $N_{occ} + N_{virt}$ poles at eigenvalues $\varepsilon_{i/a}$, while W_0 has $2 \times N_{occ}N_{virt}$ poles within a transition space with a size of $N_{occ} \times N_{virt}$. Evaluating Σ requires summing over all these occupied and virtual states, resulting in $2 \times (N_{occ} + N_{virt})N_{occ}N_{virt}$ calculations, which is often the computational bottleneck in *GW* calculations [164]. Furthermore, systematic convergence studies have shown that QP energies converge slowly with respect to the system size and the number of virtual states [164, 208, 210]. Consequently, QP energies scale poorly with system size, making it more challenging to obtain accurate results for larger systems. Therefore, it is crucial to strike a balance between the accuracy of results and computational cost.

When considering a more complete basis set, constructing the coefficient matrix C_{mn} from Eq. 5.1 can also pose challenges. The *MOLGW* package offers several strategies for truncating virtual states or reducing the dimension of the C_{mn} matrix. One simple approach is to exclude higher-energy states from the summation of Green's function G_0 or screened Coulomb interaction W_0, resulting in a smaller N_{virt} size, by determining the exact number of considered states, N_{states}, in the calculations in which $N_{occ} + N_{virt} \leq N_{states}$. However, the convergence rate of HOMO-LUMO gap as a function of N_{states} in this method is very low, and cutting too many unoccupied states could lead to a significantly large deviation from the converged values. The second method for mitigating the matrix size issue is the use of the single-pole approximation [139]. In this approach, all matrix elements above a predefined N_{SPA} value are treated as diagonal in the RPA picture, eliminating the need for diagonalization of C_{mn} blocks above N_{SPA}.

The last strategy is the so-called optimized virtual orbital subspace method which simultaneously discards some high energy eigenstates and diminishes the C_{mn} matrix size [211]. This approach involves two types of basis sets, a larger and a smaller one, with total basis functions N_{large} and N_{small}, respectively, to describe the transition space. At first, the Hamiltonian matrix and eigenstate coefficients C_L will be determined from a previous converged SCF calculation using the larger basis set. Afterward, the $N_{occ} + N_{virt} = N_{large}$ space will be divided into three subsections as depicted in Figure. 5.1 and each section will be treated by a different basis set.

The first subspace, including all occupied and a few first virtual states above LUMO, is described by their expression in the large basis set using C_{Ln} coefficient matrix where $n \leq N_{S1}$. Index N_{S1} represents the total number of states considered in subspace one which can be defined manually by the user. The second subspace, N_{S2}, includes virtual states from $N_{S1} + 1$ up to N_{small} ($N_{S1} + 1 < n \leq N_{small}$) which will be optimized by

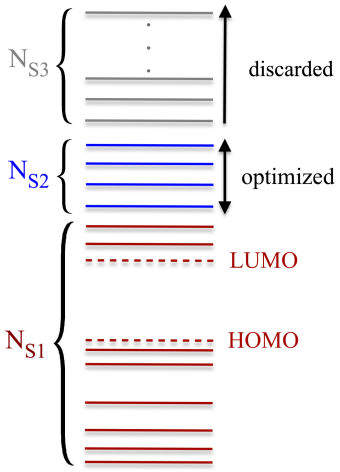

Figure 5.1: Diagrammatic representation of the various orbital subspaces. Each horizontal line indicates one electronic state and the color of the line specifies the type of subspaces. HOMO and LUMO states are shown with dash lines. Optimized subspace identified through a smaller basis set. Figure adapted from Ref. [211].

applying new eigenvectors coefficients $\tilde{C}'_{Ln}$, that is the projection of small basis set to the large basis set. It means to obtain the eigenvalues ε and eigenvectors, at first, the Roothaan-Hall equation introduced in Eq. 5.2, will be solved in the small subspace within C_{Sn}. Next, the coefficient matrix will be brought back to the original large basis with formalism:

$$\tilde{C}'_{Ln} = \sum_{OS} S_{LO}^{-1} S_{OS}^{cross} \tilde{C}_{sn} \tag{5.8}$$

where S_{LO} is the introduced overlap matrix and $S_{OS}^{cross} = \langle \phi_O \mid \phi_S \rangle$ is the projection matrix which connects the large basis set $|\phi_L\rangle$ to the small basis set $|\phi_S\rangle$. This approach helps to construct a much smaller coefficient matrix that should be solved in the self-consistent cycle. Finally, the virtual orbitals above N_{small}, $N_{small} < n \leq N_{large}$, will be deserted from the GW calculation [211]. This approach allows for a significant reduction in the size of the C_{mn} matrix while maintaining a complete basis set in the transition space. Additionally, it has been shown to improve the convergence rate of the QP energies as a function of the number of basis functions used [211].

Chapter 6

Introduction to the publications

6.1. Photosynthetic systems and their main features

In natural photosynthetic systems, a complex molecular mechanism involving various pigment-protein complexes is responsible for light harvesting and energy conversion [212]. In the first step, light-harvesting (LH) antennas absorb solar photons and transfer them to a photosynthesis reaction center (RC) with minimal energy loss. The charge separation initiated in the RC leads to the formation of chemical energy in the form of $NADPH^+$ and ATP synthase units. This electrochemical energy is consumed during the conversion of carbon dioxide to carbohydrates, which results in water splitting in oxygenic photosynthesis or oxidation of other molecules in anoxygenic photosynthesis [213]. While plants, algae, and cyanobacteria carry out oxygenic photosynthesis, other bacteria perform anoxygenic photosynthesis. Due to the highly symmetrical architecture of photosynthetic systems of purple bacteria, and easier growth conditions of some specific species such as *Rhodopseudomonas acidophila* and *Rhodopseudomonas sphaeroides*, these units have been studied extensively and their structural features are exceptionally well characterized [11–13]. Despite some disparities in bacterial structures, energy transduction follows similar principles in these systems. Accordingly, for the purpose of this thesis only the mechanism of *Rh. acidophila* and *Rh. sphaeroides* bacteria will be discussed here, however further information can be found in Ref. [214, 215].

Bacterial photosynthesis units generally consist of two main types of ring-shaped light-harvesting (LH) antenna systems, known as LHI and LHII, which are composed

of several chlorophyll (Chl) or bacteriochlorophyll (BCL) pigments and carotenoid molecules. These pigment molecules are tightly bound to surrounding proteins through non-covalent interactions. The photosynthesis membranes of purple bacteria absorb lower energy wavelengths above 500 nm. The protein environment surrounding the pigments tunes the absorption range, such that BCL molecules in LH systems absorb infra-red wavelengths above 800 nm, while carotenoids absorb green light around 500 nm [12, 13]. The LHII system consists of two rings of BCL molecules, B850 and B800, named after their maximum absorption wavelengths. To provide a better insight into the molecular arrangement in these aggregates the LHII system of *Rh. sphaeroides* is represented in Figure 6.1a. The BCL molecules in the inner ring B850 are strongly coupled, whereas due to the large distance between BCLs in B800 ring, these molecules are weakly interacting [174, 216]. The energy collected by the B800 ring is transferred to the B850 array and finally migrates to the LHI antenna, which surrounds the RC and is commonly referred to as the RC-LHI "core" complex. Although the structure of the LHI system is not as well characterized as that of LHII [12, 217], crystallography analyses show that it includes one ring of highly coupled BCL molecules with a structure similar to ring B850, and strong absorption at 875 nm [12].

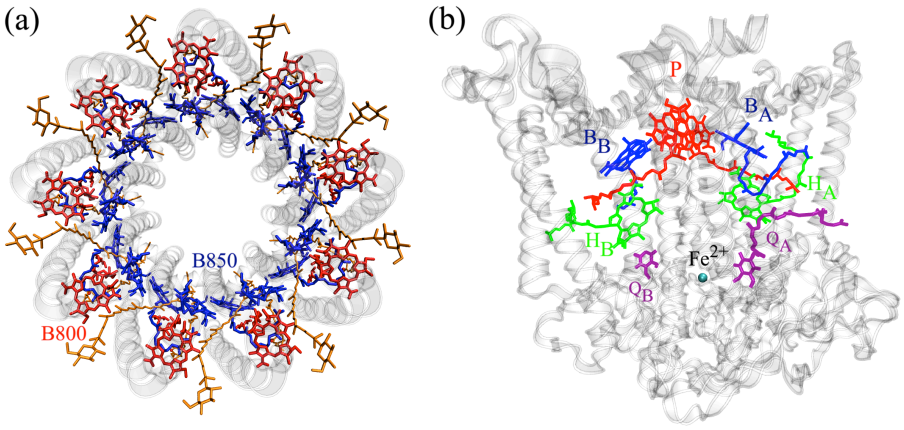

Figure 6.1: (a) Visual representation of LHII complex of *Rh. sphaeroides* consisting protein chains network that holds in place(in grey) and two rings of BCL units organized in an inner and outer shell called rings B850 (in blue) and B800 (in red), respectively. (b) Structural model of the RC of *Rh. sphaeroides* including the special pair (P in red), two accessory BCLs (B_A, B_B in blue), two bacteriopheophytines (H_A, H_B in green), two quinones (Q_A, Q_B in purple), and one Fe^{2+} metal ion. Protein chains are shown in transparent grey. Hydrogen atoms are omitted for clarity from both panels.

The energy transfer process ends successfully when the energy is trapped by RC and charge separation initiates. In the bacterial RC of *Rh. sphaeroides* the key molecular components include two centered strongly interacting BCLs, called special pair (P), followed by two accessory BCLs (B_A, B_B), two bacteriopheophytins (H_A, H_B),

two quinones (Q_A, Q_B), and one Fe^{2+} metal ion. These pigments are arranged along two branches, A- and B-branches, based on pseudo-C2 symmetry, with a carotenoid molecule located near the B_B aggregate. The structure of this system, held fixed by surrounding protein chains, is depicted in Figure 6.1b. During the last decades, crystallographic and spectroscopic studies on RC aggregates indicated that charge-transfer states in the A-branch are in much lower energies than those in the B-branch [122]. This finding suggests that the primary charge-transfer pathway occurs along the A-branch, which is also known as the active branch. This pathway leads to a final charge-separated state consisting of the oxidized special pair and the bacteriopheophytin anion, $P^+H_A^-$. Within ultrafast timescales of 200 ps and 100 μs, the electron transfers from the A-branch to the quinone molecules Q_A and Q_B, respectively, where the Q_B pigment leaves the protein to take part in the chemical reactions [218].

6.2. Visualization and quantification of charge-transfer character

In section 3.2 the definition of charge-transfer excitation is represented briefly, however, the quantification of (partial) charge-transfer from local or dark excitations in our theoretical calculations is not truly discussed yet. In this regard, here some details about the evaluation of excited-states character within the population analysis framework are provided. These information are essential for a better understanding of Publication III and Publication IV.

Two toolboxes have been used in my work based on the concept of the attachment/detachment analysis of the different densities and decomposition of transition densities. These can be derived from the frequency-dependent response of the density matrix within linear-response Casida formalism, Eq. 3.16 and 4.40. The density matrix contains a wealth of information that can help establish the direction of intermolecular electron transfer in the system and visualize density changes associated with an excitation.

In the electron-hole picture, the transition density is obtained as the diagonal part of the density matrix for a transition from the state n into an excited-state m as:

$$\rho_n(\mathbf{r}) = \gamma_{nm}(\mathbf{r}_e, \mathbf{r}_h). \tag{6.1}$$

Where for $n = m$ transition density reduces to state density. In the spirit of these analyses, the interaction strength of an electronic transition with light and the efficiency of excitation energy transfer can be determined [219]. The transition density

square, $|\rho_{0n}(\mathbf{r})|^2$ that represents the probability of finding the electron and hole at the same region, only has non-zero values whenever $\mathbf{r} = \mathbf{r}_e = \mathbf{r}_h$. By this means, the transition density vanishes for charge-transfer excitations in which the electron and hole are located on two different subunits and there is no overlap between the ground and excited-state. So the absence of transition density can distinguish charge-transfer excitations from neutral ones. However, only counting the diagonal part of the density might not give further information about the direction of charge-transfer or even lead to some miss interpretation of the results in symmetric systems [220]. For these reasons analyzing the whole matrix as has been suggested by Plasser [220] or using the concept of difference density matrix can be more useful for the recognition of these excitations and quantification of their character [219].

The difference between the ground-state density $\gamma_{00}(\mathbf{r}_e, \mathbf{r}_h)$ and the density of excited-state $\gamma_{nn}(\mathbf{r}_e, \mathbf{r}_h)$ can be defined as $\rho^{\Delta}_{0n}(\mathbf{r}) = \Delta_{0n}(\mathbf{r}_e, \mathbf{r}_h) = \gamma_{nn}(\mathbf{r}_e, \mathbf{r}_h) - \gamma_{00}(\mathbf{r}_e, \mathbf{r}_h)$. This subtraction has a nonvanishing value for charge-transfer excitations and allows the visualization of the change of density upon excitation of the system into excited-state n. It should be stressed out, in general, ρ_{0n} contains areas of positive and negative sign and its integral over all space has a zero value. Figure. 6.2 shows the visualization of transition density and different densities of a charge-transfer excitation for BCL dimer.

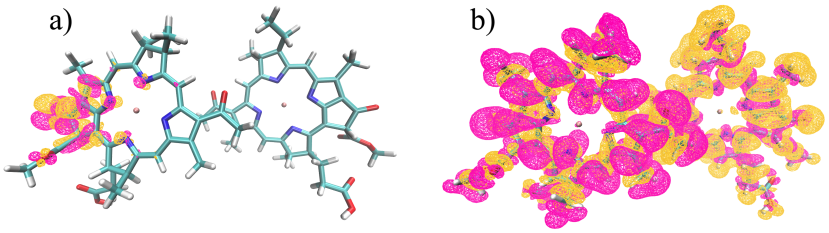

Figure 6.2: Schematic isosurface picture of the (a) transition density and (b) difference density of a charge-transfer excited-state. The pink and orange areas correspond to regions of positive and negative density, respectively.

6.3. Summary of publications

The transfer of charge and energy in LH and RC systems is strongly influenced by the relative distances and orientations of the BCL aggregates [221]. For this reason, understanding the mechanism and interaction of these chromophores with each other and with the surrounding proteins is not possible without the evaluation of their structural details and spectral properties. X-ray crystallography studies are typically the starting point for providing such information. BCL molecules found in LHI, LHII, and RC units

have a similar appearance, with small structural and more apparent orientational differences. The chemical structure of these molecules comprises a conjugated porphyrinic system plane with a Magnesium atom in the center, attached to four functional groups, namely FG1, FG2, FG3, and FG4, as shown in Figure 6.3. Previous studies have shown that the functional group FG2, which includes a Carbon chain called the phytyl tail, mainly has a structural role in fixing these aggregates in the protein environment, and its effects on excitation energies are negligible [123, 221]. Therefore, the phytyl tails are often truncated, and a hydrogen atom is used as a substitute to reduce computational costs.

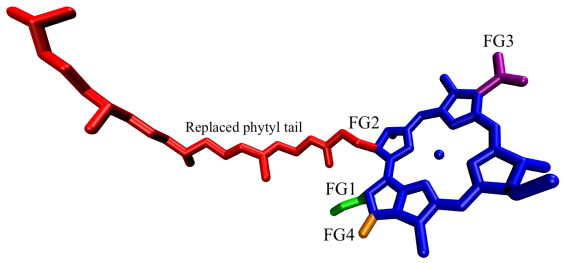

Figure 6.3: Structure of BCL molecule (P_A aggregate). The four functional groups FG_1 (in green), FG_2 (in red), FG_3 (in pink), and FG_4 (in orange) are highlighted. Hydrogen atoms are omitted for clarity.

The absorption spectra of BCL monomers, irrespective of their structure, exhibit two distinct bands known as the Q band and the B (or Soret) band. The Q band comprises of two bright excitations - Q_y and Q_x, which are located at lower energies, while the Soret band appears at energies around 3.0 eV, in the near-ultraviolet region. For multichromophoric systems, the excitation spectrum can be viewed on the basis of Frenkel-like exciton model, in which excitations are localized on single or two BCL molecules [15, 19]. In this model, the Hamiltonian of the system is expressed in terms of the excitations of individual molecules and the electronic coupling between any two chromophores in the system [16]. This approach allows for simplification compared to considering the larger system as a whole. In the beginning, many studies within semi-empirical models, constructed based on Frenkel-excitons Hamiltonians, have participated in the prediction of the excitation-energy and charge-transfer dynamics in large photosynthesis pigment-protein complexes [16, 222, 223].

However, it soon became evident that an accurate representation of the electronic coupling between BCL aggregates could only be achieved by including higher energy charge-transfer excitations and their coupling with local Frenkel excitations, which act as a mediator between localized excitations and the multiexcitonic ones [14, 16, 224, 225]. This indicates the importance of precise first-principles calculations for charge-transfer excitations and their electronic coupling [16, 226, 227]. Although, high-level

calculations of charge-transfer excitations are feasible, commonly applied approximations in the calculation of coupling terms in the effective Hamiltonian are often insufficient [228–230]. As a result, it is sometimes necessary to treat multichromophoric systems directly in a supermolecular manner without partitioning them into subunits.

Multi-reference and single-reference wavefunction-based methods have scarcely been employed in the case of smaller molecular systems. The first couple of lowest excitation energies of BCL and Chl units are calculated using RASPT2, an extension of the complete active space with second-order perturbation (CASPT2) [23, 231] or within second-order coupled cluster (CC2) method [232]. The dimeric system is investigated using configuration interaction single excitation (CIS) [233]. Suomivuori et al. applied algebraic diagrammatic construction (ADC) for the calculation of vertical excitation energy of monomeric, dimeric, and tetrameric complexes including nearest amino acid to the (BCL) Chl molecules [22, 234]. In their recent works [20, 235], Sirohiwal et al. utilized the wavefunction-based coupled cluster theory with single and double excitations (CCSD) to accurately determine the low-energy excited states of individual pigments. They compared their results with those obtained using different computational methods, including semiempirical approaches, CC2, ADC(2), and even TDDFT. Although these reports represent significant advances in the study of complex biological molecules, their computational efficiency is still an area of active research. The high formal scaling of wave function-based approaches ($O(N^{5-7})$) limits their applicability to low-lying excitation energies of single or dimer chromophore models, typically with relatively small basis sets or by consideration of different approximations such as scaled opposite spin (SOS) and reduced-virtual-space (RVS).

The *ab initio* TDDFT and GW/BSE methods offer a potential alternative to wavefunction-based approaches due to their much more suitable computational scaling of $O(N^{3-4})$. TDDFT with different types of functionals including RSH ones has been applied predominantly for the study of BCL and Chl molecular systems and the accuracy of its approximations and implementations in comparison with wavefunction-based methods or experiments has been tested tremendously for a variety of biochromophores [26, 27, 32, 148, 236]. In conjunction with model Hamiltonian, molecular dynamics (MD) and classical molecular mechanics (MM) this method become the most efficient approach for the simulation of large photosynthesis pigment-protein complexes including excitation spectrum of whole LHI and LHII systems by considering thermal and environmental effects [14, 15, 224, 225].

Computational modeling based on DFT and TDDFT has played a crucial role in unraveling the complex factors that influence charge-transfer excitations and their pathways in the RC. TDDFT, in combination with the polarizable continuum model (PCM), has been applied to investigate the effects of the protein environment on natu-

ral and charge-transfer excitations in dimeric, tetrameric, and hexameric model systems [237–240]. These studies have established the existence of locally distinct effective dielectric environments along the A- and B- branches, leading to spectral asymmetries in the RC and the occurrence of primary electron transfer along the A-branch. In a study conducted by Sirohiwal et al., the lowest charge-transfer state, strongly influenced by the protein electrostatic matrix, was identified as $B_A^+ H_A^-$ using TDDFT/MM calculations for a trimeric model system [28].

The use of molecular dynamics (MD) simulations based on (constrained) DFT has helped to shed light on the mechanism of primary electron transfer in photosynthetic systems. In particular, for a trimeric model system consisting of the special pair and one accessory BCL, nearby Histidines were found to play a crucial role in coupling two collective low-frequency vibrational modes with asymmetry electron density. Moreover, the displacement of protons was found to be coupled to the primary electron-transfer step from the special pair to the accessory BCL [124, 241]. The reasonable formal scaling of TDDFT also allows explicit consideration of parts of the protein environment and treating the model system directly in the QM level of theory. For example, the study of a model system consisting of the special pair and nearby residues has shown that protein-induced distortions of the special pair geometry lead to an asymmetric ground-state electron density [123]. Additionally, the excitation spectrum of the special pair, as well as tetrameric and hexameric model systems including some neighboring amino-acid residues, has been investigated for different types of purple bacteria, with a focus on the influence of nuclear motion on the relative energetic positions of different electronic excitations [27, 242]. Possible improved version:

As discussed previously, in principle the GW/BSE approach has some advantages over TDDFT and has shown great success, comparable to wavefunction-based methods, in predicting a large number of optical-electronic excitations [44, 48, 180, 243]. However, its accuracy and functionality still need to be tested for different variations of this method within diverse functionals and basis sets [168]. While this method has been used by a growing community of researchers in recent years, its application has been mainly focused on smaller gas phase organic molecules [48, 244, 245], and only a few larger molecular complexes have been studied [44, 49, 246]. In my earliest work, we employed this method for the first time on large monomeric models of LHII and assessed the performance of GW/BSE in comparison with state-of-the-art TDDFT and higher-order computational methods. By initiating this path, in favor of new implementations of GW/BSE formalism with lower formal scaling $O(N^3)$, today's study of larger biochromophoric systems, such as tetrameric and hexameric models are attainable [247]. In recent years the high-speed evaluation of this approach and its interface with different computational methods in software packages implies the promising future

of GW/BSE.

Publication I is dedicated to the systematic first-principles study of the electronic structure and excitations of seven members of the BCL and Chl family. Using several xc functionals we compared our TDDFT, G_0W_0/BSE, and $evGW$/BSE calculations with mentioned wavefunction-based methods [23, 235] and experimental literature results [248]. We showed the local LDA functional leads to a completely wrong description of the absorption spectrum, whereas an OT-RSH functional ωPBE yields a relatively accurate prediction of excitation energies for both TDDFT and G_0W_0/BSE methods. Using ωPBE as the starting point, we obtained G_0W_0/BSE results that are in good agreement with the more computationally demanding $evGW$/BSE method, with deviations of less than 40 meV, establishing the efficiency of G_0W_0@ωPBE/BSE in the prediction of the absorption spectrum. Furthermore, we illustrated the first bright excitation, Q_y, is overestimated by TDDFT regardless of the choice of xc functional, whereas the second bright excitation, Q_x, is predicted in the same energy range in all approaches. Finally, for the first three bright excitations of the entire family of BCL and Chls, GW/BSE provides slightly better agreement with experiment [248] and quantum-chemical methods [23, 235] as compared to TDDFT.

In Publication II, the $evGW$/BSE approach is applied to a different type of system based on our findings from the first paper. Methylene blue molecules are an important class of heterocyclic systems with an extensive range of light-assisted applications as sensitizers for photodynamic therapy, photoantimicrobials, and dye-sensitized solar cells [249, 250]. Same as BCL and Chl molecules, these applications are highly dependent on the accurate description of light absorption and electronic transitions of these systems in interaction with surrounding molecules. In the first step, the excited-state calculations were carried out within TDDFT, G_0W_0/BSE, and $evGW$/BSE using both LDA and ωPBE functionals. Our results followed the same pattern as observed in Publication I, where the use of the ωPBE functional led to more accurate predictions of excitation energies for both G_0W_0/BSE and $evGW$/BSE compared to TDDFT. The results followed the same pattern as observed in Publication I while G_0W_0@ωPBE/BSE and $evGW$@ωPBE/BSE calculations led to approximately the same description of excitation energies and a better agreement with experiment [251] compared to TDDFT with the ωPBE functional.

In the second step, we investigated the influence of solvent by adding nearby water molecules to the system. The presence of solvent caused the excitation energies to red-shift to lower energy, leading to values closer to experimental results. Notably, the optical gap difference between $evGW$/BSE and TDDFT using the ωPBE functional decreased from 0.3 eV to 0.1 eV in the solvated structure. This improvement in the performance of the TDDFT method with the ωPBE functional can be attributed to

the semilocal term of the functional dominating at larger distances, and dielectric screening being emulated by selecting the range separation parameter appropriately. This strategy could be generalized for studying similar systems at a relatively low computational cost, while still achieving acceptable accuracy within the TDDFT level of theory.

Turning back to photosynthesis aggregates, in Publication III and Publication IV the excitation spectrum of the dimeric system extracted from various parts of the photosynthetic system and a few specific tetrameric, and hexameric models from RC are investigated. Before demonstrating the main outcome of these simulations it would be helpful to first understand how to interpret the absorption spectra of a multichromophoric system. As a guide for the rest of the discussion, in Figure. 6.4 the excitation spectrum of monomeric, dimeric, tetrameric, and hexameric systems is represented. In a supermolecular system, the coupling of Q_y (Q_x) excitations from two individual BCL molecules leads to the appearance of a few bright excitations in the Q_y (Q_x) energy range. By convention, these excitations are referred to as Q_y (Q_x) coupled excitations. The energy range of these coupled excitations depends on the excitation energy of individual BCL aggregates, and the energy gap between the two types of bright excitations can differ based on the number of chromophores in the model system being considered.

The first panel of Figure 6.4 depicts the excitation spectrum of the P_A monomeric system within the Q_y and Q_x excitations. The BCL dimers are the smallest structural units in which intermolecular charge-transfer character can be observed, making them important for understanding charge-transfer behavior in these chromophores. When considering the special pair dimeric system, which includes P_A and P_B molecules, two coupled Q_y and Q_x excitations appear in a similar energy range to that of the monomeric system. The first two bright excitations at the beginning of the spectrum show the coupled Q_y excitations, where the second peak can be attributed to the P_A molecule.

Due to the large size of a BCL dimer, which features more than 300 electrons, the calculation of the *GW* self-energy which requires summation over virtual states is computationally demanding. Simulation of dimeric systems using the current implementation of *GW*/BSE method in the *MOLGW* code is on the edge of our computational limitation. In Publication III we investigated the effective factors on energy and character of charge-transfer excitations using diverse dimeric systems chosen from the LH2 complex and the RC of purple bacteria, with four different regimes of intermolecular coupling, ranging from very weak to strongly coupled. To further investigate the effects of intermolecular coupling on excited-state structures, we also constructed an artificial dimer inspired by these molecular aggregates, which allowed us to manually control a wide range of intermolecular coupling strengths.

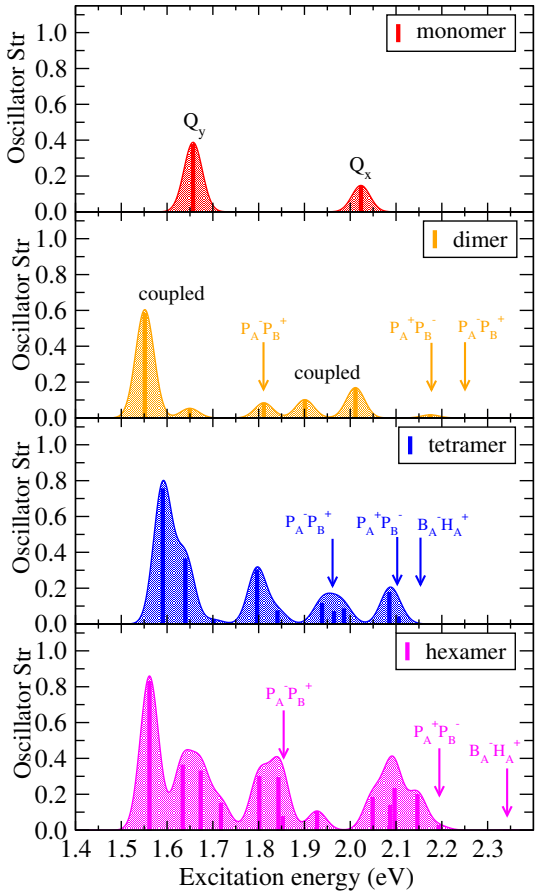

Figure 6.4: Excitation spectrum of P_A molecule, special pair dimer, A-branch tetramer structure including nearest amino acid molecules to each chromophore, and bare hexameric structure using TDDFT with ωPBE functional. For further information about structural details see main text. Arrows mark dark excitations with charge-transfer (CT) characters. The shaded areas are calculated by folding the excitation energies with Gaussian functions with a width of 0.08 eV as a guide to the eye.

Based on our results from the first two articles, the theoretical simulations were only performed by TDDFT and G_0W_0/BSE methods with the ωPBE functional warranting sufficient accuracy compared to *evGW*/BSE approach. The resulting data emulated the monomeric spectra by TDDFT systematically overestimating Q_y coupled excitations, compared to G_0W_0@ωPBE/BSE. However the charge-transfer excitations appeared at similar energies in both methods, indicating that the TDDFT method combined with the RSH functional is adequate for studying charge-transfer excitations in larger molecular systems such as the aggregates we investigated.

Among the different dimeric systems, the special pair dimer showed the lowest charge-transfer excitation energy, appearing before the coupled Q_x excitations, as demonstrated in Figure. 6.4. However, further analyses revealed that charge-transfer excitations were not solely dependent on intermolecular distances but also on the ori-

entation of functional groups and other carbon chains protruding from the porphyrin plane in the three-dimensional structure of the BCL molecule. The specific protein environment surrounding each branch defines the slightly different orientations of these functional groups, which can influence the charge-transfer excitation energy by up to ∼0.2 eV.

Such an effect can justify the preferred charge-transfer pathway in one of the branches in the RC compared to the other one. Furthermore, we identified the thermally-activated vibrational modes with pronounced effects on charge-transfer excitations of a relaxed dimeric system. The results indicated that the two lowest-frequency modes, which correspond to a rotational motion of the porphyrin planes of the BCL molecules, lead to substantial changes in all detected charge-transfer excitations. These significant effects in the order of ∼0.2 eV suggest that thermally-activated vibrational modes can mix the charge-transfer excitations with other delocalized and localized excitations of the system. In conclusion, while our results cannot directly infer charge-transfer mechanisms in photosynthetic systems, they provide valuable insights into the design rules for tailoring charge-transfer excitations in BCLs and similar photoactive molecules.

In the last publication a larger picture of these aggregates, more comparable to what we have in real photosynthetic systems, is considered. In purple bacteria of *Rhodobacter sphaeroides*, charge separation occurs in RCs comprising a hexameric aggregate consisting of a strongly coupled dimer of two BCL molecules dubbed the special pair (P), two accessory BCLs (B_A, B_B), and two bacteriopheophytines (H_A, H_B). These molecules, which are arranged along two pseudosymmetric branches, are tightly surrounded by several protein chains where the primary charge separation reaction only proceeds along the A-branch with a near-unity quantum efficiency [252–254]. Two-dimensional spectroscopic experiments indicate that charge-transfer starts with an excitation of the special pair P^* and leads to the charge-separated state $P^+H_A^-$ via an ultra-shortlived intermediate $P^+B_A^-$ [253, 255]. Although this assignment has been debated by proposing one or both accessory BCLs (B_A^* or B^*) as the initial point of charge separation pathway [256–259].

In Publication IV, we investigated the electronic and excited-state structure of the primary pigments in the RC of *Rhodobacter sphaeroides* using the first-principle TDDFT method with the ωPBE functional. Our aim was to understand charge-transfer in this reaction center by examining the effects of neighboring amino-acid residues on the system. However, due to the large size of the hexameric model, adding amino acids to this system would result in an impractically large number of excited-states that need to be calculated in order to observe charge-transfer, making it computationally infeasible. For this reason, we constructed two different types of tetrameric model systems to fully study the addition of amino acids. The first model consisted of the

central part of the RC, including the P, B_A, and B_B molecules, but it did not allow us to observe all relevant low-energy charge-transfer excitations along one branch due to the absence of H_A and H_B chromophores. In this regard, we created the second type of model systems, namely the A- and B-branch structures, including P, B_A, and H_A and P, B_B, and H_B, respectively. We demonstrated that these A- and B-branch models reproduced the main features of the hexameric model and probe the effect of adding amino acids to these models on the relevant charge-transfer states. To the best of our knowledge, this article constituted the first explicit TDDFT calculations on a reaction center model of this purple bacteria including hexameric and tetrameric model systems within parts of the environment.

To assess the influence of the environment on energy and charge-transfer excitations, we systematically added amino acids to our model systems, similar to the methodology described in Publication II. This approach enabled us to identify the specific amino acids that replicate the main (static) effects of the environment, which can be considered as a "reasonable minimal environment" for future calculations. The last two panels of Figure. 6.4 depict the excitation spectrum of A-branch structure including the nearest amino acids to each BCL molecule, referred to as model system A_2 in Publication IV and the bare hexameric model system without neighboring molecules. Adding more BCL aggregates to the model system almost completely eliminates the energy gap between Q-band excitations observed in the monomer and dimer models. Our analysis of transition and difference densities revealed that contrary to common assumptions, most of the coupled Q-band excitations are widely delocalized across several pigments, with some of them spreading over the entire RC model. In all supermolecular systems, regardless of the included BCL or amino acid molecules, the lowest internal charge-transfer excitation is attributed to the special pair $P_A^- P_B^+$ located in the middle of Q-band.

This article presents four main findings: Firstly, in bare model systems without any amino-acid environment, charge-transfer excitations are observed in the form of dark excitations that begin at ∼0.2 eV above the coupled Q_x excitations. Secondly, a forward charge-transfer into the A-branch is approximately 0.5 eV lower in energy compared to an equivalent excitation in the B-branch, which is consistent with the experimentally observed unidirectional charge-transfer along the A branch. Thirdly, the inclusion of the protein environment significantly redshifts the coupled Q_y and Q_x excitation energies. Finally, there is a significant redshift of the charge-transfer state into the A-branch, bringing this state to within 25 meV of the coupled Q_x excitations. This suggests that the addition of further parts of the protein environment, in combination with thermally-activated molecular vibrations, could result in the mixing of the charge-transfer excitations with the delocalized coupled Q_x excitations.

Our results suggested a mechanism for charge-transfer in this bacterial reaction center and pave the way for additional first-principles investigations into the interplay between delocalized excited-states, vibronic coupling, and the impact of the protein environment on this and other complex light-harvesting systems.

Glossary

B3LYP A hybrid xc functional, introduced by Becke and Lee, Yang and Par. 12

BLYP xc functional, the exchange part introduced by Becke and the correlation part proposed by Lee, Yang and Par. 12

BO Referring to Born-Oppenheimer approximation that separates the movement of nuclei from electrons in the system. 7, 34

DFT Density functional theory. 4–8, 12–15, 17–21, 23, 24, 26, 27, 31, 33, 37, 38, 41, 47, 56, 57

EA Electron affinity. 14–16, 19, 32, 45

GGA Generalized Gradient Approximation. 11–13, 29

GKS generalized Kohn-Sham scheme. 16, 18–20, 29, 41

HOMO Highest Occupied Molecular Orbital. 13, 15, 18–20, 39, 47–50

IP Ionization potential. 14, 16, 19, 32

KS Kohn-Sham, usually referring to the KS scheme, orbitals, eigenvalues, potential, or equation. 10, 15–19, 25–27, 29, 35, 37–39, 41, 44, 65

LDA Local Density Approximation. 11–13, 20, 29, 30, 58

LUMO Lowest Unoccupied Molecular Orbital. 15, 18–20, 39, 47–50

MBPT Many Body Perturbation Theory. 19, 32, 33, 39, 40

OT-RSH Optimally-tuned range separated hybrid xc functional. 13, 18–20, 29, 58

PBE xc functional of Perdew, Burke and Ernzerhof. 12, 13, 38

QM Quantum mechanic methods such as wavefunction-based methods or TDDFT and GW/BSE approaches. 2, 57

QP quasi-particle in *GW* approach. 35, 38, 39, 41, 48–50

RPA Random Phase Approximation. 36–38, 49

RSH Range separated hybrid xc functional. 13, 29, 56, 60

scGW Fully self-consistence GW method. 37–39

SIE Self-interaction error. 12, 16, 17, 29

TDDFT Time-dependent density functional theory. 3–5, 22, 24, 27, 29–32, 40, 41, 43, 56–62

xc exchange-correlation usually referring to functional. 9, 11–16, 18, 19, 24, 25, 27, 28, 38, 47, 58

References

[1] Nathan S Lewis and Daniel G Nocera. "Powering the planet: Chemical challenges in solar energy utilization". In: *Proceedings of the National Academy of Sciences* 103.43 (2006), pp. 15729–15735.

[2] Vincenzo Balzani, Alberto Credi, and Margherita Venturi. "Photochemical conversion of solar energy". In: *ChemSusChem: Chemistry & Sustainability Energy & Materials* 1.1-2 (2008), pp. 26–58.

[3] Derek Abbott. "Keeping the energy debate clean: How do we supply the world's energy needs?" In: *Proceedings of the IEEE* 98.1 (2009), pp. 42–66.

[4] Robert E Blankenship et al. "Comparing photosynthetic and photovoltaic efficiencies and recognizing the potential for improvement". In: *science* 332.6031 (2011), pp. 805–809.

[5] Aleksander W Roszak et al. "Crystal structure of the RC-LH1 core complex from Rhodopseudomonas palustris". In: *Science* 302.5652 (2003), pp. 1969–1972.

[6] Tõnu Pullerits and Villy Sundström. "Photosynthetic light-harvesting pigment-protein complexes: toward understanding how and why". In: *Accounts of Chemical Research* 29.8 (1996), pp. 381–389.

[7] James Barber. "Photosynthetic energy conversion: natural and artificial". In: *Chemical Society Reviews* 38.1 (2009), pp. 185–196.

[8] James H Alstrum-Acevedo, M Kyle Brennaman, and Thomas J Meyer. "Chemical approaches to artificial photosynthesis. 2". In: *Inorganic Chemistry* 44.20 (2005), pp. 6802–6827.

[9] Donald R Ort et al. “Redesigning photosynthesis to sustainably meet global food and bioenergy demand”. In: *Proceedings of the national academy of sciences* 112.28 (2015), pp. 8529–8536.

[10] Iain McConnell, Gonghu Li, and Gary W Brudvig. “Energy conversion in natural and artificial photosynthesis”. In: *Chemistry & biology* 17.5 (2010), pp. 434–447.

[11] YC Cheng and Robert J Silbey. “Coherence in the B800 ring of purple bacteria LH2”. In: *Physical review letters* 96.2 (2006), p. 028103.

[12] Xiche Hu et al. “Photosynthetic apparatus of purple bacteria”. In: *Quarterly reviews of biophysics* 35.1 (2002), pp. 1–62.

[13] Richard J Cogdell, Andrew Gall, and Jürgen Köhler. “The architecture and function of the light-harvesting apparatus of purple bacteria: from single molecules to in vivo membranes”. In: *Quarterly reviews of biophysics* 39.3 (2006), pp. 227–324.

[14] Xin Li et al. “An ab initio exciton model including charge-transfer excited states”. In: *Journal of chemical theory and computation* 13.8 (2017), pp. 3493–3504.

[15] Seogjoo J Jang and Benedetta Mennucci. “Delocalized excitons in natural light-harvesting complexes”. In: *Reviews of Modern Physics* 90.3 (2018), p. 035003.

[16] Carles Curutchet and Benedetta Mennucci. “Quantum chemical studies of light harvesting”. In: *Chemical reviews* 117.2 (2017), pp. 294–343.

[17] Felipe Cardoso Ramos et al. “The molecular mechanisms of light adaption in light-harvesting complexes of purple bacteria revealed by a multiscale modeling”. In: *Chemical Science* 10.42 (2019), pp. 9650–9662.

[18] Francesco Segatta et al. “Quantum chemical modeling of the photoinduced activity of multichromophoric biosystems: focus review”. In: *Chemical reviews* 119.16 (2019), pp. 9361–9380.

[19] Jacov Frenkel. “On the transformation of light into heat in solids. I”. In: *Physical Review* 37.1 (1931), p. 17.

[20] Abhishek Sirohiwal, Frank Neese, and Dimitrios A Pantazis. “How can we predict accurate electrochromic shifts for biochromophores? A case study on the photosynthetic reaction center”. In: *Journal of Chemical Theory and Computation* 17.3 (2021), pp. 1858–1873.

[21] J Linnanto, JEI Korppi-Tommola, and VM Helenius. "Electronic States, Absorption Spectrum and Circular Dichroism Spectrum of the Photosynthetic Bacterial LH2 Antenna of Rhodopseudomonas a cidophila as Predicted by Exciton Theory and Semiempirical Calculations". In: *The Journal of Physical Chemistry B* 103.41 (1999), pp. 8739–8750.

[22] Carl-Mikael Suomivuori et al. "Exploring the light-capturing properties of photosynthetic chlorophyll clusters using large-scale correlated calculations". In: *Journal of Chemical Theory and Computation* 12.6 (2016), pp. 2644–2651.

[23] André Anda, Thorsten Hansen, and Luca De Vico. "Multireference excitation energies for bacteriochlorophylls a within light harvesting system 2". In: *Journal of Chemical Theory and Computation* 12.3 (2016), pp. 1305–1313.

[24] Xavier Blase, Ivan Duchemin, and Denis Jacquemin. "The Bethe–Salpeter equation in chemistry: relations with TD-DFT, applications and challenges". In: *Chemical Society Reviews* 47.3 (2018), pp. 1022–1043.

[25] Erich Runge and Eberhard KU Gross. "Density-functional theory for time-dependent systems". In: *Physical review letters* 52.12 (1984), p. 997.

[26] Dage Sundholm. "A density-functional-theory study of bacteriochlorophyll b". In: *Physical Chemistry Chemical Physics* 5.19 (2003), pp. 4265–4271.

[27] Moritz Brutting, Johannes M Foerster, and Stephan Kummel. "Investigating Primary Charge Separation in the Reaction Center of Heliobacterium modesticaldum". In: *The Journal of Physical Chemistry B* 125.14 (2021), pp. 3468–3475.

[28] Abhishek Sirohiwal, Frank Neese, and Dimitrios A Pantazis. "Protein matrix control of reaction center excitation in photosystem II". In: *Journal of the American Chemical Society* 142.42 (2020), pp. 18174–18190.

[29] Zhi He, Villy Sundström, and Tõnu Pullerits. "Influence of the protein binding site on the excited states of bacteriochlorophyll: DFT calculations of B800 in LH2". In: *The Journal of Physical Chemistry B* 106.44 (2002), pp. 11606–11612.

[30] Stephan Kümmel. "Charge-Transfer Excitations: a challenge for time-dependent density functional theory that has been met". In: *Advanced Energy Materials* 7.16 (2017), p. 1700440.

[31] Meng-Sheng Liao, Yun Lu, and Steve Scheiner. "Performance assessment of density-functional methods for study of charge-transfer complexes". In: *Journal of computational chemistry* 24.5 (2003), pp. 623–631.

[32] Andreas Dreuw and Martin Head-Gordon. “Failure of time-dependent density functional theory for long-range charge-transfer excited states: the zincbacteriochlorin-bacteriochlorin and bacteriochlorophyll- spheroidene complexes”. In: *Journal of the American Chemical Society* 126.12 (2004), pp. 4007–4016.

[33] Neepa T Maitra et al. “Double excitations within time-dependent density functional theory linear response”. In: *The Journal of Chemical Physics* 120.13 (2004), pp. 5932–5937.

[34] David J Tozer and Nicholas C Handy. “Improving virtual Kohn–Sham orbitals and eigenvalues: Application to excitation energies and static polarizabilities”. In: *The Journal of chemical physics* 109.23 (1998), pp. 10180–10189.

[35] Tamar Stein, Leeor Kronik, and Roi Baer. “Reliable prediction of charge transfer excitations in molecular complexes using time-dependent density functional theory”. In: *Journal of the American Chemical Society* 131.8 (2009), pp. 2818–2820.

[36] Tamar Stein, Leeor Kronik, and Roi Baer. “Prediction of charge-transfer excitations in coumarin-based dyes using a range-separated functional tuned from first principles”. In: *The Journal of chemical physics* 131.24 (2009), p. 244119.

[37] Thiago B de Queiroz and Stephan Kümmel. “Charge-transfer excitations in low-gap systems under the influence of solvation and conformational disorder: Exploring range-separation tuning”. In: *The Journal of chemical physics* 141.8 (2014), p. 084303.

[38] Hao Li et al. “Comparison of LC-TDDFT and ADC (2) methods in computations of bright and charge transfer states in stacked oligothiophenes”. In: *Journal of chemical theory and computation* 10.8 (2014), pp. 3280–3289.

[39] Srijana Bhandari and Barry D Dunietz. “Quantitative accuracy in calculating charge transfer state energies in solvated molecular complexes using a screened range separated hybrid functional within a polarized continuum model”. In: *Journal of Chemical Theory and Computation* 15.8 (2019), pp. 4305–4311.

[40] Jeng-Da Chai and Martin Head-Gordon. “Systematic optimization of long-range corrected hybrid density functionals”. In: *The Journal of chemical physics* 128.8 (2008), p. 084106.

[41] Paul Boulanger et al. “Fast and accurate electronic excitations in cyanines with the many-body Bethe–Salpeter approach”. In: *Journal of Chemical Theory and Computation* 10.3 (2014), pp. 1212–1218.

[42] Fabio Caruso et al. “Benchmark of GW approaches for the GW 100 test set”. In: *Journal of chemical theory and computation* 12.10 (2016), pp. 5076–5087.

[43] Denis Jacquemin, Ivan Duchemin, and Xavier Blase. "Benchmarking the Bethe–Salpeter formalism on a standard organic molecular set". In: *Journal of chemical theory and computation* 11.7 (2015), pp. 3290–3304.

[44] Denis Jacquemin, Ivan Duchemin, and Xavier Blase. "0–0 energies using hybrid schemes: Benchmarks of TD-DFT, CIS (D), ADC (2), CC2, and BSE/GW formalisms for 80 real-life compounds". In: *Journal of chemical theory and computation* 11.11 (2015), pp. 5340–5359.

[45] Björn Baumeier, Denis Andrienko, and Michael Rohlfing. "Frenkel and charge-transfer excitations in donor–acceptor complexes from many-body green's functions theory". In: *Journal of Chemical Theory and Computation* 8.8 (2012), pp. 2790–2795.

[46] Huabing Yin et al. "Charge-transfer excited states in aqueous DNA: insights from many-body Green's function theory". In: *Physical Review Letters* 112.22 (2014), p. 228301.

[47] Sahar Sharifzadeh et al. "Low-energy charge-transfer excitons in organic solids from first-principles: The case of pentacene". In: *The Journal of Physical Chemistry Letters* 4.13 (2013), pp. 2197–2201.

[48] Denis Jacquemin, Ivan Duchemin, and Xavier Blase. "Is the Bethe–Salpeter formalism accurate for excitation energies? Comparisons with TD-DFT, CASPT2, and EOM-CCSD". In: *The journal of physical chemistry letters* 8.7 (2017), pp. 1524–1529.

[49] I Duchemin, T Deutsch, and X Blase. "Short-range to long-range charge-transfer excitations in the zincbacteriochlorin-bacteriochlorin complex: A Bethe-Salpeter study". In: *Physical review letters* 109.16 (2012), p. 167801.

[50] Katharina Krause and Wim Klopper. *Implementation of the Bethe- Salpeter equation in the TURBOMOLE program*. 2017.

[51] Richard M Martin. *Electronic structure: basic theory and practical methods*. Cambridge university press, 2020.

[52] David S Sholl and Janice A Steckel. *Density functional theory: a practical introduction*. John Wiley & Sons, 2022.

[53] Carlos Fiolhais, Fernando Nogueira, and Miguel AL Marques. *A primer in density functional theory*. Vol. 620. Springer Science & Business Media, 2003.

[54] NM Harrison. "An Introduction to Density Functional". In: *Computational materials science* 187 (2003), p. 45.

[55] Eberhard Engel and Reiner M Dreizler. "Density functional theory". In: *Theoretical and Mathematical Physics* (2011), pp. 351–399.

[56] Feliciano Giustino. *Materials modelling using density functional theory: properties and predictions*. Oxford University Press, 2014.

[57] Mike C Payne et al. "Iterative minimization techniques for ab initio total-energy calculations: molecular dynamics and conjugate gradients". In: *Reviews of modern physics* 64.4 (1992), p. 1045.

[58] Kurt Gottfried. *Quantum mechanics: fundamentals*. CRC Press, 2018.

[59] Walter Kohn. "Nobel Lecture: Electronic structure of matter—wave functions and density functionals". In: *Reviews of Modern Physics* 71.5 (1999), p. 1253.

[60] Max Born and W Heisenberg. "Zur quantentheorie der molekeln". In: *Original Scientific Papers Wissenschaftliche Originalarbeiten* (1985), pp. 216–246.

[61] Llewellyn H Thomas. "The calculation of atomic fields". In: *Mathematical proceedings of the Cambridge philosophical society*. Vol. 23. 5. Cambridge University Press. 1927, pp. 542–548.

[62] Pierre Hohenberg and Walter Kohn. "Inhomogeneous electron gas". In: *Physical review* 136.3B (1964), B864.

[63] Walter Kohn and Lu Jeu Sham. "Self-consistent equations including exchange and correlation effects". In: *Physical review* 140.4A (1965), A1133.

[64] David M Ceperley and Berni J Alder. "Ground state of the electron gas by a stochastic method". In: *Physical review letters* 45.7 (1980), p. 566.

[65] Cyrus J Umrigar and Xavier Gonze. "Accurate exchange-correlation potentials and total-energy components for the helium isoelectronic series". In: *Physical Review A* 50.5 (1994), p. 3827.

[66] Ulf Von Barth and Lars Hedin. "A local exchange-correlation potential for the spin polarized case. i". In: *Journal of Physics C: Solid State Physics* 5.13 (1972), p. 1629.

[67] Seymour H Vosko, Leslie Wilk, and Marwan Nusair. "Accurate spin-dependent electron liquid correlation energies for local spin density calculations: a critical analysis". In: *Canadian Journal of physics* 58.8 (1980), pp. 1200–1211.

[68] JP Perdew, ER McMullen, and Alex Zunger. "Density-functional theory of the correlation energy in atoms and ions: a simple analytic model and a challenge". In: *Physical Review A* 23.6 (1981), p. 2785.

[69] John P Perdew and Yue Wang. "Accurate and simple analytic representation of the electron-gas correlation energy". In: *Physical review B* 45.23 (1992), p. 13244.

[70] Stephan Kümmel and Leeor Kronik. “Orbital-dependent density functionals: Theory and applications”. In: *Reviews of Modern Physics* 80.1 (2008), p. 3.

[71] Wolfram Koch and Max C Holthausen. *A chemistś guide to density functional theory*. John Wiley & Sons, 2015.

[72] Kieron Burke. “Perspective on density functional theory”. In: *The Journal of chemical physics* 136.15 (2012), p. 150901.

[73] KEITH A BRUECKNER et al. “Correlation energy of an electron gas with a slowly varying high density”. In: *Physical Review* 165.1 (1968), p. 18.

[74] John P Perdew, P Ziesche, and H Eschrig. *Electronic structure of solids’ 91*. 1991.

[75] John P Perdew, Kieron Burke, and Matthias Ernzerhof. “Generalized gradient approximation made simple”. In: *Physical review letters* 77.18 (1996), p. 3865.

[76] Axel D Becke. “Density-functional exchange-energy approximation with correct asymptotic behavior”. In: *Physical review A* 38.6 (1988), p. 3098.

[77] Chengteh Lee, Weitao Yang, and Robert G Parr. “Development of the Colle-Salvetti correlation-energy formula into a functional of the electron density”. In: *Physical review B* 37.2 (1988), p. 785.

[78] Renato Colle and Oriano Salvetti. “Approximate calculation of the correlation energy for the closed shells”. In: *Theoretica chimica acta* 37.4 (1975), pp. 329–334.

[79] Viktor N Staroverov et al. “Comparative assessment of a new nonempirical density functional: Molecules and hydrogen-bonded complexes”. In: *The Journal of chemical physics* 119.23 (2003), pp. 12129–12137.

[80] Viktor N Staroverov et al. “Tests of a ladder of density functionals for bulk solids and surfaces”. In: *Physical Review B* 69.7 (2004), p. 075102.

[81] Axel D Becke. “A new mixing of Hartree–Fock and local density-functional theories”. In: *The Journal of chemical physics* 98.2 (1993), pp. 1372–1377.

[82] Olle Gunnarsson and Bengt I Lundqvist. “Exchange and correlation in atoms, molecules, and solids by the spin-density-functional formalism”. In: *Physical Review B* 13.10 (1976), p. 4274.

[83] Philippe Nozieres and David Pines. *The Theory of Quantum Liquids: Superfluid Bose Liquids*. CRC Press, 2018.

[84] John P Perdew, Matthias Ernzerhof, and Kieron Burke. “Rationale for mixing exact exchange with density functional approximations”. In: *The Journal of chemical physics* 105.22 (1996), pp. 9982–9985.

[85] Carlo Adamo and Vincenzo Barone. “Toward reliable density functional methods without adjustable parameters: The PBE0 model”. In: *The Journal of chemical physics* 110.13 (1999), pp. 6158–6170.

[86] Matthias Ernzerhof and Gustavo E Scuseria. “Assessment of the Perdew–Burke–Ernzerhof exchange-correlation functional”. In: *The Journal of chemical physics* 110.11 (1999), pp. 5029–5036.

[87] Narbe Mardirossian and Martin Head-Gordon. “Thirty years of density functional theory in computational chemistry: an overview and extensive assessment of 200 density functionals”. In: *Molecular Physics* 115.19 (2017), pp. 2315–2372.

[88] Philip J Stephens et al. “Ab initio calculation of vibrational absorption and circular dichroism spectra using density functional force fields”. In: *The Journal of physical chemistry* 98.45 (1994), pp. 11623–11627.

[89] Thierry Leininger et al. “Combining long-range configuration interaction with short-range density functionals”. In: *Chemical physics letters* 275.3-4 (1997), pp. 151–160.

[90] Hisayoshi Iikura et al. “A long-range correction scheme for generalized-gradient-approximation exchange functionals”. In: *The Journal of Chemical Physics* 115.8 (2001), pp. 3540–3544.

[91] Éric Brémond et al. “Range-separated hybrid density functionals made simple”. In: *The Journal of Chemical Physics* 150.20 (2019), p. 201102.

[92] Mary A Rohrdanz and John M Herbert. “Simultaneous benchmarking of ground- and excited-state properties with long-range-corrected density functional theory”. In: *The Journal of chemical physics* 129.3 (2008), p. 034107.

[93] Jeng-Da Chai and Martin Head-Gordon. “Long-range corrected double-hybrid density functionals”. In: *The Journal of chemical physics* 131.17 (2009), p. 174105.

[94] Leeor Kronik et al. “Excitation gaps of finite-sized systems from optimally tuned range-separated hybrid functionals”. In: *Journal of Chemical Theory and Computation* 8.5 (2012), pp. 1515–1531.

[95] Leeor Kronik and Stephan Kümmel. “Dielectric screening meets optimally tuned density functionals”. In: *Advanced Materials* 30.41 (2018), p. 1706560.

[96] Tamar Stein et al. “Fundamental gaps in finite systems from eigenvalues of a generalized Kohn-Sham method”. In: *Physical review letters* 105.26 (2010), p. 266802.

[97] Denis Jacquemin et al. “Performance of an optimally tuned range-separated hybrid functional for 0–0 electronic excitation energies”. In: *Journal of Chemical Theory and Computation* 10.4 (2014), pp. 1677–1685.

[98] Sivan Refaely-Abramson, Roi Baer, and Leeor Kronik. “Fundamental and excitation gaps in molecules of relevance for organic photovoltaics from an optimally tuned range-separated hybrid functional”. In: *Physical Review B* 84.7 (2011), p. 075144.

[99] Andreas Karolewski, Leeor Kronik, and Stephan Kümmel. “Using optimally tuned range separated hybrid functionals in ground-state calculations: Consequences and caveats”. In: *The Journal of chemical physics* 138.20 (2013), p. 204115.

[100] Haitao Sun, Cheng Zhong, and Jean-Luc Bredas. “Reliable prediction with tuned range-separated functionals of the singlet–triplet gap in organic emitters for thermally activated delayed fluorescence”. In: *Journal of chemical theory and computation* 11.8 (2015), pp. 3851–3858.

[101] Aron J Cohen, Paula Mori-Sánchez, and Weitao Yang. “Challenges for density functional theory”. In: *Chemical reviews* 112.1 (2012), pp. 289–320.

[102] Thilo Aschebrock. “Ultranonlocality in Density Functional Theory”. PhD thesis. 2019.

[103] Kyle R Bryenton et al. “Delocalization error: The greatest outstanding challenge in density-functional theory”. In: *Wiley Interdisciplinary Reviews: Computational Molecular Science* (2022), e1631.

[104] Thomas Körzdörfer. “Self-interaction and charge transfer in organic semiconductors”. In: (2009).

[105] James F Janak. “Proof that e n i= ε in density-functional theory”. In: *Physical Review B* 18.12 (1978), p. 7165.

[106] C-O Almbladh and Ulf von Barth. “Exact results for the charge and spin densities, exchange-correlation potentials, and density-functional eigenvalues”. In: *Physical Review B* 31.6 (1985), p. 3231.

[107] John P Perdew et al. “Understanding band gaps of solids in generalized Kohn–Sham theory”. In: *Proceedings of the national academy of sciences* 114.11 (2017), pp. 2801–2806.

[108] Aron J Cohen, Paula Mori-Sánchez, and Weitao Yang. “Fractional charge perspective on the band gap in density-functional theory”. In: *Physical Review B* 77.11 (2008), p. 115123.

[109] Paula Mori-Sánchez, Aron J Cohen, and Weitao Yang. “Localization and delocalization errors in density functional theory and implications for band-gap prediction”. In: *Physical review letters* 100.14 (2008), p. 146401.

[110] John P Perdew and Alex Zunger. “Self-interaction correction to density-functional approximations for many-electron systems”. In: *Physical Review B* 23.10 (1981), p. 5048.

[111] Tobias Schmidt and Stephan Kümmel. “One-and many-electron self-interaction error in local and global hybrid functionals”. In: *Physical Review B* 93.16 (2016), p. 165120.

[112] Aron J Cohen, Paula Mori-Sánchez, and Weitao Yang. “Insights into current limitations of density functional theory”. In: *Science* 321.5890 (2008), pp. 792–794.

[113] David J Tozer. “Relationship between long-range charge-transfer excitation energy error and integer discontinuity in Kohn–Sham theory”. In: *The Journal of chemical physics* 119.24 (2003), pp. 12697–12699.

[114] Matthew JP Hodgson et al. “How interatomic steps in the exact Kohn–Sham potential relate to derivative discontinuities of the energy”. In: *The journal of physical chemistry letters* 8.24 (2017), pp. 5974–5980.

[115] A Seidl et al. “Generalized Kohn-Sham schemes and the band-gap problem”. In: *Physical Review B* 53.7 (1996), p. 3764.

[116] Paula Sánchez-Friera and RW Godby. “Efficient total energy calculations from self-energy models”. In: *Physical Review Letters* 85.26 (2000), p. 5611.

[117] Tim Gould and Leeor Kronik. “Ensemble generalized Kohn–Sham theory: The good, the bad, and the ugly”. In: *The Journal of Chemical Physics* 154.9 (2021), p. 094125.

[118] Yuncai Mei et al. “Approximating quasiparticle and excitation energies from ground state generalized Kohn–Sham calculations”. In: *The Journal of Physical Chemistry A* 123.3 (2018), pp. 666–673.

[119] EJ Baerends, OV Gritsenko, and R Van Meer. “The Kohn–Sham gap, the fundamental gap and the optical gap: the physical meaning of occupied and virtual Kohn–Sham orbital energies”. In: *Physical Chemistry Chemical Physics* 15.39 (2013), pp. 16408–16425.

[120] Zeng-hui Yang et al. “More realistic band gaps from meta-generalized gradient approximations: Only in a generalized Kohn-Sham scheme”. In: *Physical review B* 93.20 (2016), p. 205205.

[121] Xavier Blase et al. “The Bethe–Salpeter equation formalism: From physics to chemistry”. In: *The Journal of Physical Chemistry Letters* 11.17 (2020), pp. 7371–7382.

[122] Fei Ma et al. “Both electronic and vibrational coherences are involved in primary electron transfer in bacterial reaction center”. In: *Nature communications* 10.1 (2019), p. 933.

[123] PK Wawrzyniak et al. “Acetyl group orientation modulates the electronic ground-state asymmetry of the special pair in purple bacterial reaction centers”. In: *Physical Chemistry Chemical Physics* 13.21 (2011), pp. 10270–10279.

[124] Thomas J Eisenmayer et al. “Mechanism and reaction coordinate of directional charge separation in bacterial reaction centers”. In: *The Journal of Physical Chemistry Letters* 3.6 (2012), pp. 694–697.

[125] Yuta Fujihashi, Masahiro Higashi, and Akihito Ishizaki. “Intramolecular vibrations complement the robustness of primary charge separation in a dimer model of the photosystem II reaction center”. In: *The Journal of Physical Chemistry Letters* 9.17 (2018), pp. 4921–4929.

[126] Yuanyuan Jing et al. “Theoretical Study of the Electronic–Vibrational Coupling in the Q y States of the Photosynthetic Reaction Center in Purple Bacteria”. In: *The Journal of Physical Chemistry B* 116.3 (2012), pp. 1164–1171.

[127] Karen Oda Hjorth Minde Dundas et al. “Harmonic infrared and Raman spectra in molecular environments using the polarizable embedding model”. In: *Journal of Chemical Theory and Computation* 17.6 (2021), pp. 3599–3617.

[128] Anthony P Scott and Leo Radom. “Harmonic vibrational frequencies: an evaluation of Hartree- Fock, Møller- Plesset, quadratic configuration interaction, density functional theory, and semiempirical scale factors”. In: *The Journal of Physical Chemistry* 100.41 (1996), pp. 16502–16513.

[129] Miguel AL Marques and Eberhard KU Gross. “Time-dependent density functional theory”. In: *Annual review of physical chemistry* 55.1 (2004), pp. 427–455.

[130] Robert Van Leeuwen. “Mapping from densities to potentials in time-dependent density-functional theory”. In: *Physical review letters* 82.19 (1999), p. 3863.

[131] Giovanni Onida, Lucia Reining, and Angel Rubio. “Electronic excitations: density-functional versus many-body Green’s-function approaches”. In: *Reviews of modern physics* 74.2 (2002), p. 601.

[132] EKU Gross and RM Dreizler. *Density Functional Theory, NATO ASI Series, Vol. B337*. 1995.

[133] Kieron Burke, Jan Werschnik, and EKU Gross. “Time-dependent density functional theory: Past, present, and future”. In: *The Journal of chemical physics* 123.6 (2005), p. 062206.

[134] Lorin X Benedict, Eric L Shirley, and Robert B Bohn. "Theory of optical absorption in diamond, Si, Ge, and GaAs". In: *Physical Review B* 57.16 (1998), R9385.

[135] Leeor Kronik and Jeffrey B Neaton. "Excited-state properties of molecular solids from first principles". In: *Annual review of physical chemistry* 67 (2016), pp. 587–616.

[136] ME Casida. "Recent developments and applications of modern density functional theory". In: *Theoretical and computational chemistry* 4 (1996), p. 391.

[137] Filipp Furche and Reinhart Ahlrichs. "Adiabatic time-dependent density functional methods for excited state properties". In: *The Journal of chemical physics* 117.16 (2002), pp. 7433–7447.

[138] So Hirata and Martin Head-Gordon. "Time-dependent density functional theory within the Tamm–Dancoff approximation". In: *Chemical Physics Letters* 314.3-4 (1999), pp. 291–299.

[139] Carsten A Ullrich. "Time-dependent density-functional theory: concepts and applications". In: (2011).

[140] Filipp Furche et al. "Circular dichroism of helicenes investigated by time-dependent density functional theory". In: *Journal of the American Chemical Society* 122.8 (2000), pp. 1717–1724.

[141] Miguel AL Marques et al. "Time-dependent density-functional approach for biological chromophores: the case of the green fluorescent protein". In: *Physical review letters* 90.25 (2003), p. 258101.

[142] Miguel AL Marques et al. *Time-dependent density functional theory*. Vol. 706. Springer Science & Business Media, 2006.

[143] Adele D Laurent and Denis Jacquemin. "TD-DFT benchmarks: a review". In: *International Journal of Quantum Chemistry* 113.17 (2013), pp. 2019–2039.

[144] Andreas Dreuw, Jennifer L Weisman, and Martin Head-Gordon. "Long-range charge-transfer excited states in time-dependent density functional theory require non-local exchange". In: *The Journal of chemical physics* 119.6 (2003), pp. 2943–2946.

[145] Fabio Della Sala and Andreas Görling. "Efficient localized Hartree–Fock methods as effective exact-exchange Kohn–Sham methods for molecules". In: *The Journal of Chemical Physics* 115.13 (2001), pp. 5718–5732.

[146] Dongwook Kim. "A Theoretical Analysis of the Excited State of Oligoacene Aggregates: Local Excitation vs. Charge-Transfer Transition". In: *Bulletin of the Korean Chemical Society* 36.9 (2015), pp. 2284–2289.

[147] Rika Kobayashi and Roger D Amos. "The application of CAM-B3LYP to the charge-transfer band problem of the zincbacteriochlorin–bacteriochlorin complex". In: *Chemical physics letters* 420.1-3 (2006), pp. 106–109.

[148] Ingo Schelter et al. "Assessing density functional theory in real-time and real-space as a tool for studying bacteriochlorophylls and the light-harvesting complex 2". In: *The Journal of Chemical Physics* 151.13 (2019), p. 134114.

[149] Roi Baer, Ester Livshits, and Ulrike Salzner. "Tuned range-separated hybrids in density functional theory". In: *Annual review of physical chemistry* 61 (2010), pp. 85–109.

[150] M Thiele and Stephan Kümmel. "Frequency dependence of the exact exchange-correlation kernel of time-dependent density-functional theory". In: *Physical Review Letters* 112.8 (2014), p. 083001.

[151] Ove Christiansen, Henrik Koch, and Poul Jörgensen. "The second-order approximate coupled cluster singles and doubles model CC2". In: *Chemical Physics Letters* 243.5-6 (1995), pp. 409–418.

[152] Ove Christiansen, Henrik Koch, and Poul Jo/rgensen. "Response functions in the CC3 iterative triple excitation model". In: *The Journal of chemical physics* 103.17 (1995), pp. 7429–7441.

[153] Lars Hedin. "New method for calculating the one-particle Green's function with application to the electron-gas problem". In: *Physical Review* 139.3A (1965), A796.

[154] Ferdi Aryasetiawan and Olle Gunnarsson. "The GW method". In: *Reports on Progress in Physics* 61.3 (1998), p. 237.

[155] Alexander L Fetter and John Dirk Walecka. *Quantum theory of many-particle systems*. Courier Corporation, 2012.

[156] Dorothea Golze, Marc Dvorak, and Patrick Rinke. "The GW compendium: A practical guide to theoretical photoemission spectroscopy". In: *Frontiers in chemistry* 7 (2019), p. 377.

[157] Christoph Friedrich and Arno Schindlmayr. "Many-body perturbation theory: the GW approximation". In: *NIC Series* 31 (2006), p. 335.

[158] Richard D Mattuck. *A guide to Feynman diagrams in the many-body problem*. Courier Corporation, 1992.

[159] Freeman J Dyson. "The radiation theories of Tomonaga, Schwinger, and Feynman". In: *Physical Review* 75.3 (1949), p. 486.

[160] LS Cederbaum, G Hohlneicher, and S Peyerimhoff. "Calculation of the vertical ionization potentials of formaldehyde by means of perturbation theory". In: *Chemical Physics Letters* 11.4 (1971), pp. 421–424.

[161] Julian Schwinger. "On gauge invariance and vacuum polarization". In: *Physical Review* 82.5 (1951), p. 664.

[162] Stephen L Adler. "Quantum theory of the dielectric constant in real solids". In: *Physical Review* 126.2 (1962), p. 413.

[163] Xinguo Ren et al. "Random-phase approximation and its applications in computational chemistry and materials science". In: *Journal of Materials Science* 47.21 (2012), pp. 7447–7471.

[164] Michiel J van Setten et al. "GW 100: Benchmarking G 0 W 0 for molecular systems". In: *Journal of chemical theory and computation* 11.12 (2015), pp. 5665–5687.

[165] Björn Baumeier et al. "Excited states of dicyanovinyl-substituted oligothiophenes from many-body Green's functions theory". In: *Journal of Chemical Theory and Computation* 8.3 (2012), pp. 997–1002.

[166] Xavier Blase, Claudio Attaccalite, and Valerio Olevano. "First-principles GW calculations for fullerenes, porphyrins, phtalocyanine, and other molecules of interest for organic photovoltaic applications". In: *Physical Review B* 83.11 (2011), p. 115103.

[167] Michiel J van Setten, Florian Weigend, and Ferdinand Evers. "The GW-method for quantum chemistry applications: Theory and implementation". In: *Journal of chemical theory and computation* 9.1 (2013), pp. 232–246.

[168] Fabien Bruneval and Miguel AL Marques. "Benchmarking the starting points of the GW approximation for molecules". In: *Journal of chemical theory and computation* 9.1 (2013), pp. 324–329.

[169] Tonatiuh Rangel et al. "Evaluating the GW approximation with CCSD (T) for charged excitations across the oligoacenes". In: *Journal of Chemical Theory and Computation* 12.6 (2016), pp. 2834–2842.

[170] Mark S Hybertsen and Steven G Louie. "Electron correlation in semiconductors and insulators: Band gaps and quasiparticle energies". In: *Physical Review B* 34.8 (1986), p. 5390.

[171] Conor Hogan et al. "Correlation effects in the optical spectra of porphyrin oligomer chains: Exciton confinement and length dependence". In: *The Journal of Chemical Physics* 138.2 (2013), 01B607.

[172] Noa Marom et al. “Benchmark of G W methods for azabenzenes”. In: *Physical Review B* 86.24 (2012), p. 245127.

[173] Maxim Shishkin and Georg Kresse. “Self-consistent G W calculations for semiconductors and insulators”. In: *Physical Review B* 75.23 (2007), p. 235102.

[174] Mark van Schilfgaarde, Takao Kotani, and Sergey Faleev. “Quasiparticle self-consistent g w theory”. In: *Physical review letters* 96.22 (2006), p. 226402.

[175] Cristiana Di Valentin, Silvana Botti, and Matteo Cococcioni. *First Principles Approaches to Spectroscopic Properties of Complex Materials*. Vol. 347. Springer, 2014.

[176] Joseph W Knight et al. “Accurate ionization potentials and electron affinities of acceptor molecules III: a benchmark of GW methods”. In: *Journal of chemical theory and computation* 12.2 (2016), pp. 615–626.

[177] Ferdinand Kaplan et al. “Quasi-particle self-consistent GW for molecules”. In: *Journal of chemical theory and computation* 12.6 (2016), pp. 2528–2541.

[178] Katharina Krause, Michael E Harding, and Wim Klopper. “Coupled-cluster reference values for the GW27 and GW100 test sets for the assessment of GW methods”. In: *Molecular Physics* 113.13-14 (2015), pp. 1952–1960.

[179] Adrian Stan, Nils Erik Dahlen, and Robert Van Leeuwen. “Levels of self-consistency in the GW approximation”. In: *The Journal of chemical physics* 130.11 (2009), p. 114105.

[180] Tonatiuh Rangel et al. “An assessment of low-lying excitation energies and triplet instabilities of organic molecules with an ab initio Bethe-Salpeter equation approach and the Tamm-Dancoff approximation”. In: *The Journal of Chemical Physics* 146.19 (2017), p. 194108.

[181] Edwin E Salpeter and Hans Albrecht Bethe. “A relativistic equation for bound-state problems”. In: *Physical Review* 84.6 (1951), p. 1232.

[182] Fabien Bruneval et al. “molgw 1: Many-body perturbation theory software for atoms, molecules, and clusters”. In: *Computer Physics Communications* 208 (2016), pp. 149–161.

[183] Reinhart Ahlrichs et al. “Electronic structure calculations on workstation computers: The program system turbomole”. In: *Chemical Physics Letters* 162.3 (1989), pp. 165–169.

[184] Yihan Shao et al. “Advances in molecular quantum chemistry contained in the Q-Chem 4 program package”. In: *Molecular Physics* 113.2 (2015), pp. 184–215.

[185] Karen L Schuchardt et al. “Basis set exchange: a community database for computational sciences”. In: *Journal of chemical information and modeling* 47.3 (2007), pp. 1045–1052.

[186] S Francis Boys. “Electronic wave functions-I. A general method of calculation for the stationary states of any molecular system”. In: *Proceedings of the Royal Society of London. Series A. Mathematical and Physical Sciences* 200.1063 (1950), pp. 542–554.

[187] John C Slater. “Analytic atomic wave functions”. In: *Physical Review* 42.1 (1932), p. 33.

[188] Conyers Herring. “A new method for calculating wave functions in crystals”. In: *Physical Review* 57.12 (1940), p. 1169.

[189] Ewa Papajak and Donald G Truhlar. “Efficient diffuse basis sets for density functional theory”. In: *Journal of chemical theory and computation* 6.3 (2010), pp. 597–601.

[190] Warren J Hehre, Robert Ditchfield, and John A Pople. “Self—consistent molecular orbital methods. XII. Further extensions of Gaussian—type basis sets for use in molecular orbital studies of organic molecules”. In: *The Journal of Chemical Physics* 56.5 (1972), pp. 2257–2261.

[191] Thom H Dunning Jr. “Gaussian basis sets for use in correlated molecular calculations. I. The atoms boron through neon and hydrogen”. In: *The Journal of chemical physics* 90.2 (1989), pp. 1007–1023.

[192] Florian Weigend and Reinhart Ahlrichs. “Balanced basis sets of split valence, triple zeta valence and quadruple zeta valence quality for H to Rn: Design and assessment of accuracy”. In: *Physical Chemistry Chemical Physics* 7.18 (2005), pp. 3297–3305.

[193] J Grant Hill. “Gaussian basis sets for molecular applications”. In: *International Journal of Quantum Chemistry* 113.1 (2013), pp. 21–34.

[194] Pierpaolo Morgante and Roberto Peverati. “The devil in the details: A tutorial review on some undervalued aspects of density functional theory calculations”. In: *International Journal of Quantum Chemistry* 120.18 (2020), e26332.

[195] Joost VandeVondele and Jürg Hutter. “Gaussian basis sets for accurate calculations on molecular systems in gas and condensed phases”. In: *The Journal of chemical physics* 127.11 (2007), p. 114105.

[196] Stig Rune Jensen et al. “The elephant in the room of density functional theory calculations”. In: *The journal of physical chemistry letters* 8.7 (2017), pp. 1449–1457.

[197] Chi Liu et al. “All-electron ab initio Bethe-Salpeter equation approach to neutral excitations in molecules with numeric atom-centered orbitals”. In: *The Journal of Chemical Physics* 152.4 (2020), p. 044105.

[198] Fabien Bruneval et al. “Extrapolating unconverged GW energies up to the complete basis set limit with linear regression”. In: *Journal of Chemical Theory and Computation* 16.7 (2020), pp. 4399–4407.

[199] L Pettersson and U Wahlgren. “An investigation of basis sets and basis set superposition error in transition metals using frozen core and frozen orbital techniques”. In: *Chemical Physics* 69.1-2 (1982), pp. 185–192.

[200] Juergen Hinze. “An overview of computational methods for large molecules”. In: *Adv. Chem. Phys* (1974), pp. 213–263.

[201] Victor Wen-zhe Yu, Jonathan Moussa, and Volker Blum. “Accurate frozen core approximation for all-electron density-functional theory”. In: *The Journal of Chemical Physics* 154.22 (2021), p. 224107.

[202] Kirk A Peterson. “Gaussian basis sets exhibiting systematic convergence to the complete basis set limit”. In: *Annual Reports in Computational Chemistry* 3 (2007), pp. 195–206.

[203] Jerry L Whitten. “Coulombic potential energy integrals and approximations”. In: *The Journal of Chemical Physics* 58.10 (1973), pp. 4496–4501.

[204] Karin Eichkorn et al. “Auxiliary basis sets for main row atoms and transition metals and their use to approximate Coulomb potentials”. In: *Theoretical Chemistry Accounts* 97 (1997), pp. 119–124.

[205] Florian Weigend. “Accurate Coulomb-fitting basis sets for H to Rn”. In: *Physical chemistry chemical physics* 8.9 (2006), pp. 1057–1065.

[206] Reinhart Ahlrichs. “Efficient evaluation of three-center two-electron integrals over Gaussian functions”. In: *Physical Chemistry Chemical Physics* 6.22 (2004), pp. 5119–5121.

[207] Yousung Jung et al. “Auxiliary basis expansions for large-scale electronic structure calculations”. In: *Proceedings of the National Academy of Sciences* 102.19 (2005), pp. 6692–6697.

[208] Xinguo Ren et al. “Resolution-of-identity approach to Hartree–Fock, hybrid density functionals, RPA, MP2 and GW with numeric atom-centered orbital basis functions”. In: *New Journal of Physics* 14.5 (2012), p. 053020.

[209] Fabien Bruneval. “Assessment of the linearized GW density matrix for molecules”. In: *Journal of Chemical Theory and Computation* 15.7 (2019), pp. 4069–4078.

[210] Fabien Bruneval. “Ionization energy of atoms obtained from GW self-energy or from random phase approximation total energies”. In: *The Journal of Chemical Physics* 136.19 (2012), p. 194107.

[211] Fabien Bruneval. “Optimized virtual orbital subspace for faster GW calculations in localized basis”. In: *The Journal of chemical physics* 145.23 (2016), p. 234110.

[212] Hohjai Lee, Yuan-Chung Cheng, and Graham R Fleming. “Coherence dynamics in photosynthesis: protein protection of excitonic coherence”. In: *Science* 316.5830 (2007), pp. 1462–1465.

[213] Tihana Mirkovic et al. “Light absorption and energy transfer in the antenna complexes of photosynthetic organisms”. In: *Chemical reviews* 117.2 (2017), pp. 249–293.

[214] Melih K Şener et al. “Atomic-level structural and functional model of a bacterial photosynthetic membrane vesicle”. In: *Proceedings of the National Academy of Sciences* 104.40 (2007), pp. 15723–15728.

[215] Melih Şener et al. “Förster energy transfer theory as reflected in the structures of photosynthetic light-harvesting systems”. In: *ChemPhysChem* 12.3 (2011), pp. 518–531.

[216] Juergen Koepke et al. “The crystal structure of the light-harvesting complex II (B800–850) from Rhodospirillum molischianum”. In: *Structure* 4.5 (1996), pp. 581–597.

[217] Kazutoshi Tani et al. “A previously unrecognized membrane protein in the Rhodobacter sphaeroides LH1-RC photocomplex”. In: *Nature communications* 12.1 (2021), p. 6300.

[218] Graham R Fleming and Rienk Van Grondelle. “The primary steps of photosynthesis”. In: *Physics Today* 47.2 (1994), pp. 48–57.

[219] Felix Plasser, Michael Wormit, and Andreas Dreuw. “New tools for the systematic analysis and visualization of electronic excitations. I. Formalism”. In: *The Journal of chemical physics* 141.2 (2014), p. 024106.

[220] Felix Plasser. “Entanglement entropy of electronic excitations”. In: *The Journal of Chemical Physics* 144.19 (2016), p. 194107.

[221] Andy Freer et al. “Pigment–pigment interactions and energy transfer in the antenna complex of the photosynthetic bacterium Rhodopseudomonas acidophila”. In: *Structure* 4.4 (1996), pp. 449–462.

[222] CP Van Der Vegte et al. “Atomistic modeling of two-dimensional electronic spectra and excited-state dynamics for a light harvesting 2 complex”. In: *The Journal of Physical Chemistry B* 119.4 (2015), pp. 1302–1313.

[223] Ana Damjanović, Thorsten Ritz, and Klaus Schulten. "Excitation transfer in the peridinin-chlorophyll-protein of Amphidinium carterae". In: *Biophysical journal* 79.4 (2000), pp. 1695–1705.

[224] Lorenzo Cupellini et al. "An ab initio description of the excitonic properties of LH2 and their temperature dependence". In: *The Journal of Physical Chemistry B* 120.44 (2016), pp. 11348–11359.

[225] Lorenzo Cupellini et al. "Coupling to charge transfer states is the key to modulate the optical bands for efficient light harvesting in purple bacteria". In: *The Journal of Physical Chemistry Letters* 9.23 (2018), pp. 6892–6899.

[226] Alexander A Voityuk. "Interaction of dark excited states. Comparison of computational approaches". In: *The Journal of Physical Chemistry B* 119.24 (2015), pp. 7417–7421.

[227] Xinle Liu and Joseph E Subotnik. "The variationally orbital-adapted configuration interaction singles (VOA-CIS) approach to electronically excited states". In: *Journal of Chemical Theory and Computation* 10.3 (2014), pp. 1004–1020.

[228] P López-Tarifa et al. "Coulomb couplings in solubilised light harvesting complex II (LHCII): challenging the ideal dipole approximation from TDDFT calculations". In: *Physical Chemistry Chemical Physics* 19.28 (2017), pp. 18311–18320.

[229] Souloke Sen et al. "Understanding the relation between structural and spectral properties of light-harvesting complex II". In: *The Journal of Physical Chemistry A* 125.20 (2021), pp. 4313–4322.

[230] Jan S Frähmcke and Peter J Walla. "Coulombic couplings between pigments in the major light-harvesting complex LHC II calculated by the transition density cube method". In: *Chemical physics letters* 430.4-6 (2006), pp. 397–403.

[231] André Anda, Thorsten Hansen, and Luca De Vico. "Q y and Q x absorption bands for bacteriochlorophyll a molecules from LH2 and LH3". In: *The Journal of Physical Chemistry A* 123.25 (2019), pp. 5283–5292.

[232] Nina OC Winter and Christof Hättig. "Scaled opposite-spin CC2 for ground and excited states with fourth order scaling computational costs". In: *The Journal of chemical physics* 134.18 (2011), p. 184101.

[233] Gregory D Scholes et al. "Ab initio molecular orbital calculations of electronic couplings in the LH2 bacterial light-harvesting complex of Rps. acidophila". In: *The Journal of Physical Chemistry B* 103.13 (1999), pp. 2543–2553.

[234] Carl-Mikael Suomivuori et al. "Absorption shifts of diastereotopically ligated chlorophyll dimers of photosystem I". In: *Physical Chemistry Chemical Physics* 21.13 (2019), pp. 6851–6858.

[235] Abhishek Sirohiwal et al. “Accurate computation of the absorption spectrum of chlorophyll a with pair natural orbital coupled cluster methods”. In: *The Journal of Physical Chemistry B* 124.40 (2020), pp. 8761–8771.

[236] Yihan Shao et al. “Benchmarking the performance of time-dependent density functional theory methods on biochromophores”. In: *Journal of chemical theory and computation* 16.1 (2019), pp. 587–600.

[237] Huseyin Aksu et al. “Explaining Spectral Asymmetries and Excitonic Characters of the Core Pigment Pairs in the Bacterial Reaction Center Using a Screened Range-Separated Hybrid Functional”. In: *The Journal of Physical Chemistry B* 123.42 (2019), pp. 8970–8975.

[238] Huseyin Aksu et al. “On the Role of the Special Pair in Photosystems as a Charge Transfer Rectifier”. In: *The Journal of Physical Chemistry B* 124.10 (2020), pp. 1987–1994.

[239] Terry J Frankcombe. “Explicit calculation of the excited electronic states of the photosystem II reaction centre”. In: *Physical Chemistry Chemical Physics* 17.5 (2015), pp. 3295–3302.

[240] Koji Mitsuhashi et al. “Nature of asymmetric electron transfer in the symmetric pathways of photosystem I”. In: *The Journal of Physical Chemistry B* 125.11 (2021), pp. 2879–2885.

[241] Thomas J Eisenmayer et al. “Proton displacements coupled to primary electron transfer in the Rhodobacter sphaeroides reaction center”. In: *The Journal of Physical Chemistry B* 117.38 (2013), pp. 11162–11168.

[242] Maeve A Kavanagh et al. “A TDDFT investigation of the Photosystem II reaction center: Insights into the precursors to charge separation”. In: *Proceedings of the National Academy of Sciences* 117.33 (2020), pp. 19705–19712.

[243] Fabien Bruneval, Samia M Hamed, and Jeffrey B Neaton. “A systematic benchmark of the ab initio Bethe-Salpeter equation approach for low-lying optical excitations of small organic molecules”. In: *The Journal of Chemical Physics* 142.24 (2015), p. 244101.

[244] Jeffrey C Grossman et al. “High accuracy many-body calculational approaches for excitations in molecules”. In: *Physical Review Letters* 86.3 (2001), p. 472.

[245] Murilo L Tiago et al. “Neutral and charged excitations in carbon fullerenes from first-principles many-body theories”. In: *The Journal of chemical physics* 129.8 (2008), p. 084311.

[246] Maurizia Palummo et al. “Ab initio electronic and optical spectra of free-base porphyrins: The role of electronic correlation”. In: *The Journal of chemical physics* 131.8 (2009), 08B607.

[247] Arno Förster and Lucas Visscher. “Quasiparticle Self-Consistent GW-Bethe–Salpeter Equation Calculations for Large Chromophoric Systems”. In: *Journal of chemical theory and computation* 18.11 (2022), pp. 6779–6793.

[248] Leenawaty Limantara et al. “Effects of nonpolar and polar solvents on the Qx and Qy energies of bacteriochlorophyll a and bacteriopheophytin a”. In: *Photochemistry and photobiology* 65.2 (1997), pp. 330–337.

[249] Alexandra B Ormond and Harold S Freeman. “Dye sensitizers for photodynamic therapy”. In: *Materials* 6.3 (2013), pp. 817–840.

[250] Zu-Sheng Huang, Herbert Meier, and Derong Cao. “Phenothiazine-based dyes for efficient dye-sensitized solar cells”. In: *Journal of Materials Chemistry C* 4.13 (2016), pp. 2404–2426.

[251] Jacob C Dean et al. “Broadband transient absorption and two-dimensional electronic spectroscopy of methylene blue”. In: *The Journal of Physical Chemistry A* 119.34 (2015), pp. 9098–9108.

[252] Colin A Wraight and Roderick K Clayton. “The absolute quantum efficiency of bacteriochlorophyll photooxidation in reaction centres of Rhodopseudomonas spheroides”. In: *Biochimica et Biophysica Acta (BBA)-Bioenergetics* 333.2 (1974), pp. 246–260.

[253] Fei Ma et al. “Vibronic coherence in the charge separation process of the Rhodobacter sphaeroides reaction center”. In: *The Journal of Physical Chemistry Letters* 9.8 (2018), pp. 1827–1832.

[254] Martin A Steffen, Kaiqin Lao, and Steven G Boxer. “Dielectric asymmetry in the photosynthetic reaction center”. In: *Science* 264.5160 (1994), pp. 810–816.

[255] Andrew Niedringhaus et al. “Primary processes in the bacterial reaction center probed by two-dimensional electronic spectroscopy”. In: *Proceedings of the National Academy of Sciences* 115.14 (2018), pp. 3563–3568.

[256] Marion E van Brederode et al. “On the efficiency of energy transfer and the different pathways of electron transfer in mutant reaction centers of Rhodobacter sphaeroides”. In: *Photosynthesis research* 55 (1998), pp. 141–146.

[257] Huilin Zhou and Steven G Boxer. “Probing excited-state electron transfer by resonance Stark spectroscopy. 1. Experimental results for photosynthetic reaction centers”. In: *The Journal of Physical Chemistry B* 102.45 (1998), pp. 9139–9147.

[258] Libai Huang et al. “Cofactor-specific photochemical function resolved by ultrafast spectroscopy in photosynthetic reaction center crystals”. In: *Proceedings of the National Academy of Sciences* 109.13 (2012), pp. 4851–4856.

[259] Su Lin et al. “Excitation wavelength dependent spectral evolution in Rhodobacter sphaeroides R-26 reaction centers at low temperatures: the Q Y transition region”. In: *The Journal of Physical Chemistry B* 102.20 (1998), pp. 4016–4022.

List of publications

Pub.1 *Assessment of the ab Initio Bethe–Salpeter Equation approach for the low-Lying excitation energies of Bacteriochlorophylls and Chlorophylls*
Zohreh Hashemi and Linn Leppert
The Journal of Physical Chemistry A, 125, 2163-2172 (2021)

Pub.2 *First principles theoretical spectroscopy of methylene blue: Between limitations of time-dependent density functional theory approximations and its realistic description in the solvent*
Thiago B. de Queiroz, Erick R. de Figueroa, Maurício D. Coutinho-Neto, Cleiton D. Maciel, Enrico Tapavicza, **Zohreh Hashemi**, and Linn Leppert
The Journal of Chemical Physics 154, 044106 (2021)

Pub.3 *Mapping Charge-Transfer Excitations in Bacteriochlorophyll Dimers from First Principles*
Zohreh Hashemi, Matthias Knodt, Mario R. G. Marques, and Linn Leppert
Electron. Struct, 5, 024006 (2023)

Pub.4 *Delocalized Electronic Excitations and their Role in Directional Charge Transfer in the Reaction Center of Rhodobacter Sphaeroides*
Sabrina Volpert, **Zohreh Hashemi**, Johannes M. Foerster, Mario R. G. Marques, Ingo Schelter, Stephan Kümmel, and Linn Leppert
The Journal of Chemical Physics A, 158, 195102 (2023)

Publication I

Assessment of the ab Initio Bethe–Salpeter Equation approach for the low-Lying excitation energies of Bacteriochlorophylls and Chlorophylls

Reprinted from

The Journal of Physical Chemistry A, 125, 2163-2172 (2021)

Zohreh Hashemi[1] and Linn Leppert[1,2]

1) Institute of Physics, University of Bayreuth, Bayreuth 95440, Germany

2) MESA+ Institute for Nanotechnology, University of Twente, 7500 AE Enschede, The Netherlands

My contribution

I was the lead contributor to the publication. I carried out all numerical calculations presented in this work using the GW+Bethe-Salpeter Equation (GW/BSE) approach and time-dependent density functional theory (TDDFT). The preparation of all figures, tables, and data in the supplementary information was done by me. I also

wrote the first draft of this manuscript and finalized the paper in collaboration with L. Leppert.

THE JOURNAL OF PHYSICAL CHEMISTRY A
A JOURNAL OF THE AMERICAN CHEMICAL SOCIETY

pubs.acs.org/JPCA

Article

Assessment of the *Ab Initio* Bethe–Salpeter Equation Approach for the Low-Lying Excitation Energies of Bacteriochlorophylls and Chlorophylls

Zohreh Hashemi and Linn Leppert*

Cite This: *J. Phys. Chem. A* 2021, 125, 2163–2172

Read Online

ACCESS | Metrics & More | Article Recommendations | Supporting Information

ABSTRACT: Bacteriochlorophyll and chlorophyll molecules are crucial building blocks of the photosynthetic apparatus in bacteria, algae, and plants. Embedded in transmembrane protein complexes, they are responsible for the primary processes of photosynthesis: excitation energy and charge transfer. Here, we use *ab initio* many-body perturbation theory within the *GW* approximation and Bethe–Salpeter equation (BSE) approach to calculate the electronic structure and optical excitations of bacteriochlorophylls *a*, *b*, *c*, *d*, and *e* and chlorophylls *a* and *b*. We systematically study the effects of the structure, basis set size, partial self-consistency in *GW*, and the underlying exchange–correlation approximation and compare our calculations with results from time-dependent density functional theory, multireference RASPT2, and experimental literature results. We find that optical excitations calculated with *GW*+BSE are in excellent agreement with experimental data, with an average deviation of less than 100 meV for the first three bright excitations of the entire family of (bacterio)chlorophylls. Contrary to state-of-the-art time-dependent density functional theory (TDDFT) with an optimally tuned range-separated hybrid functional, this accuracy is achieved in a parameter-free approach. Moreover, *GW*+BSE predicts the energy differences between the low-energy excitations correctly and eliminates spurious charge transfer states that TDDFT with (semi)local approximations is known to produce. Our study provides accurate reference results and highlights the potential of the *GW*+BSE approach for the simulation of larger pigment complexes.

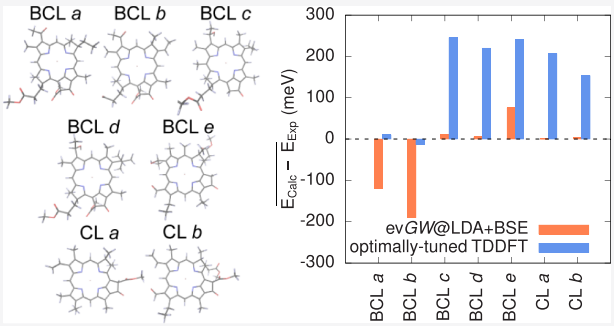

INTRODUCTION

Electronic excitations form the foundation of some of the most fundamental natural processes. In photosynthesis, plants, algae, and bacteria convert solar energy into chemical energy, utilizing a cascade of coupled energy and charge transfer excitations that are performed by pigment–protein complexes with high quantum efficiency. Bacteriochlorophyll (BCL) and chlorophyll (CL) molecules are among the most important building blocks of these pigment–protein complexes.[1] They are responsible for the absorption and transfer of excitation energy and for the charge separation necessary for establishing a proton gradient that eventually drives the synthesis of chemical energy in plants and bacteria.[2] Accurately calculating the electronic structure and excitations of these molecules from first principles is the prerequisite for understanding their interactions with each other and with the surrounding proteins and, consequently, energy and charge transfer in natural photosynthesis.

BCL and CL molecules constitute a family of substituted tetrapyrroles with varying absorption properties depending on conjugation and the number and nature of substitutions. CL *a* and *b* are present in plants and green algae, whereas green bacteria mostly rely on BCL *c*, *d*, and *e* for excitation energy transfer and BCL *a* for concentrating excitations close to the reaction center of the photosynthetic unit.[3] BCL *a* is also the main pigment in purple bacteria, whose light harvesting apparatus and reaction center are among the most thoroughly studied natural light-harvesting systems.[4] The optical excitation spectrum of these pigments possesses two characteristic absorption bands: (1) the Q band in the visible part of the spectrum, composed of excitations Q_y and Q_x with high- and low-oscillator strength, respectively and (2) the B (or Soret) band in the near ultraviolet.

In the field of finite organic and biological molecular systems, neutral excitations and optical spectra are predominantly calculated using time-dependent density functional theory (TDDFT). In conjunction with model Hamiltonian

Received: February 10, 2021
Revised: February 16, 2021
Published: March 3, 2021

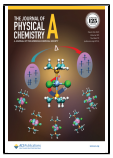

approaches, TDDFT has been employed for the simulation of large photosynthetic pigment−protein complexes.[5,6] The accuracy of its approximations and implementations has been tested for a variety of biochromophores.[7,8,47] However, TDDFT's standard approximations are inadequate for describing long-range charge transfer excitations[9] and high-energy Rydberg states[10] due to self-interaction errors and an incorrect asymptotic behavior. Exchange−correlation (xc) functionals that contain long-range exact exchange, such as optimally tuned range-separated hybrid functionals (OT-RSH), can be employed as a remedy in such cases,[11,12] but the use of such functionals requires a tedious per-system tuning procedure.

Multireference wavefunction-based methods have scarcely been used for molecules as large as BCL and CL. Vertical excitation energies of CL *a*, based on ADC(2) and different coupled cluster approaches show a spread of ∼0.4 eV, strongly depending on the method, basis set, and structural model used in these calculations.[13−15] In 2016 and 2019, Anda et al. reported multistate RASPT2/RASSCF excitation energies of several BCL units within the light-harvesting system 2 of a purple bacterium.[16,17] A RASPT2 approach was also combined with electrostatic embedding of fixed-point charges to simulate the effect of the protein environment on excitation energies of the same system by Segatta et al.[18] While these reports constitute important advances in the use of wavefunction-based methods for complex biological molecules, they were performed with relatively small basis sets and show a dependence on the choice of the restricted active space (RAS).

The *ab initio* Bethe−Salpeter equation (BSE) approach, when rigorously based on many-body Green's function theory, is an alternative method for describing neutral excitations of correlated many-electron systems.[19] It is based on a framework of charged excitation energies that correspond to electron addition and removal energies and that are most frequently calculated within the *GW* approximation. The *GW*+BSE approach has been shown to be successful in predicting the optical spectra of bulk solids[20,21] and low-dimensional materials.[22] In recent years, it has also begun to be applied to finite systems, such as small molecules,[23−25] and larger molecular complexes,[26−28] for which its accuracy has been shown to be comparable to single-reference wavefunction methods for both localized and charge transfer excitations,[29] at a substantially reduced computational cost.

In this article, we assess the accuracy of the *ab initio GW*+BSE approach for the Q_y, Q_x, and the first bright B excitation of several members of the BCL and CL family and the chemically closely related bacteriochlorin (BC) molecule. We compare two different approaches for approximating the electronic self-energy $\Sigma = iGW$: (1) G_0W_0, a one-shot method, in which the zeroth-order Green's function G_0 and screened Coulomb interaction W_0 are constructed from a DFT eigensystem and directly used to correct DFT eigenvalues perturbatively and (2) partially self-consistent *GW* (evG_nW_n), in which the corrected eigenvalues are used to iteratively recalculate G and/or W until self-consistency is reached. We compare our results to TDDFT calculations with the local density approximation (LDA), two global hybrids and an OT-RSH functional, with RASPT2 literature results,[16,17] and with experimental data.[30,31]

We find that the *GW*+BSE approach used in a partially self-consistent manner results in excitation energies in the visible and near-ultraviolet within less than 100 meV from experiment for the entire family of pigments studied here. Our results are almost completely independent of the DFT eigensystem used as an input for the *GW*+BSE calculations. In fact, even a simple and computationally inexpensive LDA starting point leads to excellent agreement with experiment and eliminates spurious charge transfer excitations between Q_y and Q_x that TDDFT with (semi)local functionals produces. Contrary to TDDFT, *GW*+BSE also correctly predicts the energy difference between the two *Q*-band excitations, a crucial prerequisite for understanding the coupling of excitations in systems consisting of more than one pigment. Finally, we show that differences between evG_nW_n+BSE and state-of-the-art TDDFT calculations using an OT-RSH functional can be explained almost entirely based on differences in how electron−hole interactions are described by the xc kernel of TDDFT and the BSE kernel, respectively. Eigenvalue differences as computed with evG_nW_n and DFT with an OT-RSH functional are almost identical.

The remainder of this article is structured as follows: we start by briefly reviewing the *GW*+BSE approach and report computational details and numerical convergence. We then show the effect of different DFT starting points and partial self-consistency on the excitation energies of the BC molecule. After this, we discuss our results for BCL *a*, *b*, *c*, *d*, and *e* and CL *a* and *b*, followed by a comparison with literature results and an in-depth discussion of differences between our *GW*+BSE and TDDFT results for BCL *a*.

METHODS

***GW*+BSE Approach.** In Green's function-based many-body perturbation theory, the calculation of charged excitations, corresponding to electron removal and addition energies, is based on knowledge of the exact interacting single-particle Green's function G, which can, in principle, be computed from a set of self-consistent integro-differential equations—Hedin's equations—linking G to the electronic self-energy Σ, the screened Coulomb interaction W, the irreducible polarizability χ, and the vertex function Γ.[32] The lowest-order expansion of Σ with respect to W leads to the *GW* approximation, in which the electronic self-energy $\Sigma = iGW$.[33] Quasiparticle (QP) eigenvalues can be obtained by solving

$$\left[-\frac{\hbar^2}{2m}\nabla^2 + V_{\text{ion}}(\mathbf{r}) + V_{\text{H}}(\mathbf{r})\right]\varphi_n^{\text{QP}}(\mathbf{r}) + \int d\mathbf{r}'\Sigma(\mathbf{r},\mathbf{r}';\varepsilon_n^{\text{QP}})\varphi_n^{\text{QP}}(\mathbf{r}') = \varepsilon_n^{\text{QP}}\varphi_n^{\text{QP}}(\mathbf{r}) \quad (1)$$

here, V_{ion} is the ionic potential, V_{H} is the Hartree potential, and $\varepsilon_n^{\text{QP}}$ and φ_n^{QP} are QP energies and wavefunctions, respectively.

To avoid the high computational cost of a self-consistent solution of eq 1, the *GW* approach is commonly used within a one-shot scheme, in which G_0 and W_0 are constructed from a (generalized) Kohn−Sham (gKS) eigensystem obtained from a preceding DFT calculation. We use the notation G_0W_0@gKS to refer to G_0W_0 based on the gKS eigensystem $(\varphi_n^{\text{gKS}};\varepsilon_n^{\text{gKS}})$ computed with the xc functional $E_{\text{xc}}^{\text{gKS}}$. In this approach, QP corrections are calculated to first order in Σ as

$$\varepsilon_n^{\text{QP}} = \varepsilon_n^{\text{gKS}} + \langle\varphi_n^{\text{gKS}}|\Sigma(\varepsilon_n^{\text{QP}}) - V_{\text{xc}}|\varphi_n^{\text{gKS}}\rangle \quad (2)$$

where V_{xc} is the xc potential, and it is assumed that $\varphi_n^{\text{QP}} \approx \varphi_n^{\text{gKS}}$.

While the G_0W_0 approach has been used with much success, in particular, for the calculation of band gaps and band structures of solids, a well-known and well-documented dependence on the gKS eigensystem used to construct G_0

https://dx.doi.org/10.1021/acs.jpca.1c01240
J. Phys. Chem. A 2021, 125, 2163−2172

and W_0 limits its predictive power.[34−36] Partial self-consistency in the QP eigenvalues can often mitigate this problem. In eigenvalue self-consistent *GW*, the gKS eigenvalues used to construct G and/or W are replaced with those from the output of a prior *GW* step; the self-energy corrections are then iterated until the QP eigenvalues converge. This approach, which we call evG_nW_n in the following (n refers to the number of iterations), has been shown to remove much of the starting point dependence for a range of different systems.[37,38]

The BSE is an equation for the two-particle electron−hole Green's function and allows for the calculation of the polarizability including electron−hole interactions through the screened Coulomb interaction W. In practice, the BSE is usually solved by neglecting the frequency dependence of W. Within this static approximation, it can be written in a form equivalent to Casida's equations of TDDFT

$$\begin{pmatrix} A & B \\ -B & -A \end{pmatrix} \begin{pmatrix} X^s \\ Y^s \end{pmatrix} = \Omega_s \begin{pmatrix} X^s \\ Y^s \end{pmatrix} \tag{3}$$

where Ω_s represents neutral excitation energies and (X^s, Y^s) the corresponding eigenvectors.[19] A and $-A$ represent resonant and antiresonant transitions that can be expressed as

$$A_{ia}^{jb} = (\varepsilon_a^{QP} - \varepsilon_i^{QP})\delta_{ij}\delta_{ab} - 2(ia|jb) + W_{ij}^{ab}(\omega = 0) \tag{4}$$

and that are coupled through B and $-B$, defined as

$$B_{ia}^{jb} = -2(ia|bj) + W_{ij}^{ab}(\omega = 0) \tag{5}$$

for singlet excitations. In these expressions, i and j are occupied and a and b are unoccupied states and $(ia|bj)$ stands for

$$(ia|bj) = \iint \mathrm{d}\mathbf{r}\mathrm{d}\mathbf{r}' \varphi_i^{QP}(\mathbf{r})\varphi_a^{QP}(\mathbf{r}) \frac{1}{|\mathbf{r} - \mathbf{r}'|} \varphi_j^{QP}(\mathbf{r}')\varphi_b^{QP}(\mathbf{r}') \tag{6}$$

Note that $\varphi_i^{QP} = \varphi_i^{gKS}$, whenever the G_0W_0 or evG_nW_n approaches are used to construct A and B.

Computational Details. Our calculations of charged and neutral excitations were performed using the *GW*+BSE and TDDFT implementation in the open-source MOLGW software package (version 2B), which relies on Gaussian basis functions.[39] We used the frozen-core approximation throughout, which changes excitation energies by less than 1 meV. We also employed the resolution-of-the-identity (RI) method, in order to reduce the calculation of four-center integrals to two- and three-center integrals. For BCL *a*, the RI changes the QP highest occupied molecular orbital (HOMO)−lowest unoccupied molecular orbital (LUMO) gap by less than 50 meV using a 6-31G basis set and BHLYP as a starting point, but we expect the effect of the RI to be even smaller for the larger basis sets used in the remainder of this article.[40] To further reduce the computational cost of the evaluation of the *GW* polarizability, we use the single-pole approximation (see the Supporting Information for details). The Tamm−Dancoff approximation, which corresponds to neglecting the B matrix elements in eq 3 is not used as it consistently increases both *GW*+BSE and TDDFT results by ∼0.3 eV, in agreement with previous findings.[6,27]

We tested the influence of the Gaussian basis set size on HOMO−LUMO gaps and Q_y and Q_x excitations of BCL *a* (using a structure from ref 16) with G_0W_0@BHLYP+BSE, considering seven different basis sets, namely, the Pople basis sets 6-31G, 6-311G, 6-311++G**, and 6-311++G(2d,2p), combined with the DeMon auxiliary basis set,[41] and the Karlsruhe basis sets def2-SVP, def2-TZVP, and def2-TZVPP and their corresponding auxiliary basis sets.[42]

Figures 1 and S2 show the convergence of the HOMO−LUMO gap and Q_y and Q_x excitation energies as a function of

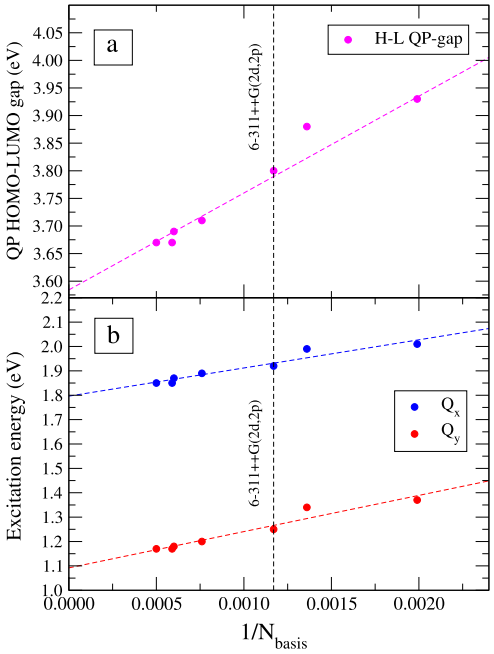

Figure 1. Convergence as a function of the number of basis functions $1/N_{basis}$ for (a) HOMO−LUMO gap and (b) Q_y and Q_x excitation energies, calculated with G_0W_0@BHLYP+BSE. Dashed lines represent a linear fit.

the inverse number of basis functions, $1/N_{basis}$ for *GW*+BSE and TDDFT, respectively (raw data are presented in Tables S1 and S2). We find that the HOMO−LUMO gap depends significantly more on $1/N_{basis}$ than Q_y and Q_x excitation energies and that TDDFT results are less sensitive to the choice of the basis set than *GW*+BSE. Based on these tests, we use the 6-311++G(2d,2p) basis set for all calculations reported in the following. We estimate the error in the *GW*(+BSE) HOMO−LUMO gap and the Q_y and Q_x excitation energies by linearly extrapolating to an infinite basis set. By excluding the very small 6-31G and 6-311G basis sets from these fits, we obtain extrapolated values of 3.57 eV for the HOMO−LUMO gap, 1.11 eV for Q_y, and 1.81 eV for Q_x. We conclude that using the 6-311++G(2d,2p) basis set for all further calculations, we likely overestimate *GW*(+BSE) HOMO−LUMO gaps and Q_y and Q_x excitation energies by ∼0.1 eV with respect to the complete basis set limit. Conversely, the use of the single-pole approximation leads to a similar underestimation of the HOMO−LUMO gap and the Q_y and Q_x excitations, resulting in a fortuitous cancellation of errors.

We test the effect of different xc functionals on our TDDFT and *GW*+BSE results. We use the LDA, two global hybrid functionals (B3LYP and BHLYP), and the range-separated hybrid (RSH) functional ωPBE. In RSH functionals, the Coulomb repulsion is separated into a short-range part and a long-range part, for numerical convenience expressed as

$$\frac{1}{r} = \frac{1 - \mathrm{erf}(\omega r)}{r} + \frac{\mathrm{erf}(\omega r)}{r} \tag{7}$$

https://dx.doi.org/10.1021/acs.jpca.1c01240
J. Phys. Chem. A 2021, 125, 2163−2172

where ω is called the range separation parameter. The ωPBE functional uses PBE exchange in the short range and the exact exchange energy in the long range, allowing for a self-interaction-free description at large electron−electron distances. We obtain the range separation parameter ω through the tuning procedure outlined in ref 43, in which ω is chosen such that the HOMO eigenvalue is as close as possible to the negative ionization potential both for the neutral and anionic system. Consequently, and by construction, the resulting HOMO−LUMO gap is a very good approximation to the fundamental gap of the neutral molecule. We use the Q-Chem code and a 6-31G(d,p) basis set for the tuning.[44] The tuned range separation parameters for all systems discussed in the following can be found in Table S3.

RESULTS AND DISCUSSION

Bacteriochlorin. To validate our methodological setup and investigate the starting point dependence of the G_0W_0 approach and the effect of eigenvalue self-consistency on our calculated HOMO−LUMO gaps and excitation energies, we start by examining the BC molecule, for which *GW*+BSE results have been reported in ref 27. We use a BC structure from ref 27 and denote the lowest energy excitations Q_x and Q_y, according to the direction of their transition dipole moments. Table 1 contains our calculated HOMO−LUMO gaps, Q_x and Q_y excitation energies, and oscillator strengths using TDDFT and several flavors of the *GW*+BSE approach. We find that, as expected, (generalized) Kohn−Sham HOMO−LUMO gaps show a large dependence on the xc functional, with LDA, B3LYP, and BHLYP leading to a significantly lower HOMO−LUMO gap and ωPBE leading to a HOMO−LUMO gap similar to the HOMO−LUMO gap calculated with G_0W_0 and eigenvalue-self-consistent evG_nW_n. In turn, Q_y and Q_x excitation energies from TDDFT are considerably less dependent on the xc functional than HOMO−LUMO gaps. In agreement with previous studies, we find that TDDFT overestimates the experimental values for Q_x and Q_y by up to ∼0.4 eV, depending on the xc functional.[27] TDDFT with the OT-RSH ωPBE is in best agreement with experiment, overestimating it by ∼0.2 eV for both excitations. We further find that G_0W_0@LDA+BSE underestimates Q_x by 0.4 eV and Q_y by 0.6 eV, whereas the use of a BHLYP and ωPBE starting point results in excitations within 0.1 eV of the experimental results. In accordance with prior studies, we observe that most of the starting point dependence of the G_0W_0+BSE results is inherited from the starting point dependence of the HOMO−LUMO gaps.[25]

Table 1. HOMO−LUMO Gaps, Q_x and Q_y Excitation Energies (in eV), and the Corresponding Oscillator Strengths, Γ_x and Γ_y, for BC Calculated with the 6-311++G(2d,2p) Basis Set

method	xc functional	H-L gap	Q_x	Γ_x	Q_y	Γ_y
TDDFT	LDA	1.38	2.04	0.18	2.39	0.03
	B3LYP	2.17	2.06	0.23	2.51	0.04
	BHLYP	3.27	1.93	0.28	2.55	0.04
	ωPBE	4.38	1.87	0.23	2.42	0.05
G_0W_0+BSE	LDA	4.15	1.21	0.09	1.67	0.04
	B3LYP	4.36	1.44	0.14	1.97	0.04
	BHLYP	4.56	1.67	0.19	2.23	0.05
	ωPBE	4.59	1.64	0.19	2.26	0.05
evG_nW_0+BSE	LDA	4.31	1.41	0.13	1.97	0.04
	B3LYP	4.43	1.54	0.16	2.12	0.05
	BHLYP	4.56	1.66	0.19	2.24	0.05
	ωPBE	4.57	1.62	0.18	2.27	0.04
evG_nW_n+BSE	LDA	4.42	1.51	0.17	2.21	0.05
	B3LYP	4.55	1.63	0.19	2.24	0.05
	BHLYP	4.60	1.69	0.20	2.27	0.05
	ωPBE	4.56	1.61	0.18	2.26	0.04
Exp[a]			1.60		2.30	

[a]Data for bacteriopheophorbide from refs.[31,27]

In order to investigate the effect of eigenvalue self-consistency in the *GW*+BSE approach, we tested the effect of updating the eigenvalues in the construction of G only (evG_nW_0) and of both G and W (evG_nW_n). Eigenvalue self-consistency in G alone only slightly changes the results as compared to G_0W_0. In contrast, full eigenvalue self-consistency largely eliminates the starting point dependence. In particular, using an LDA starting point results in excitation energies within 0.1 eV from experiment—similar to the ωPBE starting point, but at considerably reduced computational cost. In Table S4, we report similar results for the more complex pigment BCL *a*. In the remainder of this article, we therefore focus primarily on eigenvalue self-consistent results based on LDA and ωPBE starting points.

Excitation Energies of Bacteriochlorophylls and Chlorophylls. Next, we turn to reporting the vertical excitation energies of several members of the BCL and CL family of pigments. All structures were obtained from ref 45 and geometry-optimized using DFT as implemented in the Turbomole code with a def2-TZVP basis set and the B3LYP xc functional.[46] Atomic coordinates of all relaxed structures can be found in the Supporting Information. We used both LDA and ωPBE starting points for our evG_nW_n+BSE and ωPBE for our TDDFT calculations. Unlike the Q_x excitation of BCL *a* and *b*, which has significant oscillator strength, the Q_x excitation of BCL *c*−*e* is dark. Following ref 8, we therefore also compare our calculations with experimental results for the higher-energy B band.[31] We report the vertical excitation energies and corresponding oscillator strengths of the first six excitations of all pigments in Tables S6 and S7. In these calculations, we included a total of 20 excitations, in order to ensure that the higher lying excitations are well converged.

Table 2 demonstrates that evG_nW_n+BSE is in excellent agreement with experiment for the entire family of BCL and CL molecules. The MAE is about 50 meV for the Q_y and Q_x and between 100 and 200 meV for the *B* excitation. Our evG_nW_n+BSE results also accurately reflect the spectral shifts of the Q_y excitation when comparing different BCL pigments with each other. For example, the BCL *b* molecule differs from BCL *a* through an ethyliden side group, which shifts the Q_y excitation by 40 meV to the red. This red shift is perfectly reproduced in our *GW*+BSE calculations. This is the first main result of this study. The second one is that our results are essentially independent of the DFT eigensystem used as an input for the *GW*+BSE approach: a computationally inexpensive LDA starting point results in the same level of agreement with experiment as the more tedious ωPBE calculation that involves a system-dependent tuning procedure for the range separation parameter ω. This is in stark contrast to TDDFT. TD-LDA leads to spurious excitations with charge transfer character in between Q_y and Q_x, as well as slightly above Q_x, depending on the structure, as discussed below and in the literature.[47] TDDFT with the optimally tuned ωPBE

https://dx.doi.org/10.1021/acs.jpca.1c01240
J. Phys. Chem. A 2021, 125, 2163−2172

Table 2. Q_y, Q_x and First B Band Excitation Energy of BCLs and CLs Calculated Using a 6-311++G(2d,2p) Basis Set[a]

	GW@LDA+BSE			*GW*@ωPBE+BSE			TD-ωPBE			exp[b]		
molecule	Q_y	Q_x	*B*	Q_y	Q_x	*B*	Q_y	Q_x	*B*	Q_y	Q_x	*B*
BCL *a*	1.52	2.08	3.25	1.50	2.10	3.16	1.75	2.16	3.33	1.60	2.15	3.46
BCL *b*	1.48	2.07	2.95	1.45	2.09	3.05	1.69	2.15	3.19	1.56	2.14	3.37
BCL *c*	1.85	2.05	2.94	1.84	2.11	3.02	2.05	2.21	3.21	1.88		2.89
BCL *d*	1.90	2.15	2.94	1.89	2.21	3.05	2.08	2.29	3.19	1.90		2.93
BCL *e*	2.01	2.04	2.78	1.96	2.13	2.88	2.10	2.23	3.02	1.92		2.72
CL *a*	1.85	2.13	2.91	1.86	2.19	3.02	2.06	2.29	3.16	1.87	2.14	2.88
CL *b*	1.95	2.17	2.79	1.93	2.20	2.85	2.10	2.29	2.97	1.92	2.26	2.72
MAE	0.05	0.06	0.12	0.04	0.05	0.17	0.17	0.05	0.25			

[a]*GW*+BSE results are based on eigenvalue self-consistent evG_nW_n. [b]Experimental results in diethyl ether from ref 8.

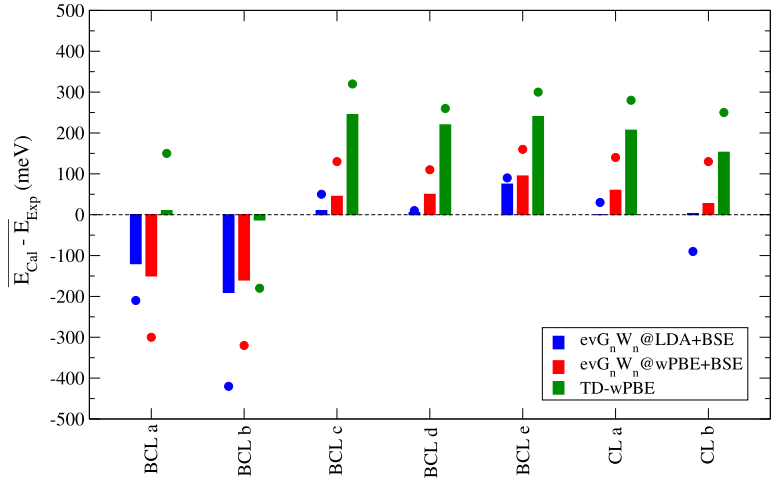

Figure 2. Colored bars denote the average difference between calculated and experimental excitation energies for evG_nW_n@LDA+BSE (blue), evG_nW_n@ωPBE+BSE (red), and TDDFT (green) with ωPBE. The dots represent the maximum deviation in each case.

results in good agreement with experiment for all three excitations, albeit with slightly higher MAEs of 170, 50, and 250 meV for Q_y, Q_x, and *B*, respectively.

In Figure 2, we plot the difference between our calculated results and experiment, averaged over all three excitations, to further highlight qualitative differences between evG_nW_n+BSE and TDDFT. For BCL *a* and BCL *b*, evG_nW_n+BSE, on average, underestimates experiment by ∼100 meV, whereas the average TDDFT deviation is close to zero, because TDDFT slightly overestimates the Q_y and Q_x excitations but underestimates the B excitation of these pigments. For all other BCL and the two CL molecules studied here, we consistently find that the average deviation of evG_nW_n+BSE is significantly smaller than that of TDDFT. Similar to our results for the BC molecule and to other benchmark studies of complex organic molecules,[6] TDDFT tends to overestimate all three excitations by between 200 and 300 meV. evG_nW_n+BSE is in much closer agreement with experiment for these pigments, on average, overestimating their excitation energies by less than 100 meV. We stress again that these results are independent of the DFT starting point, whereas our TDDFT results rely on a per-system tuning procedure.

Our results are in excellent agreement with correlated excited-state methods for those systems for which such studies have been reported, primarily CL *a* and BCL *a*. ADC(2) excitation energies of the first three excitations of CL *a* reported by Suomivuori et al. are 1.97, 2.11, and 2.95 eV, within ∼0.1 eV of our evG_nW_n@LDA+BSE results.[13] In another study by the same authors, the ADC(2) Q_y excitation energy of histidin-ligated BCL *a* was reported to be 1.46 eV, again within ∼0.1 eV of our results, although it should be noted that the structures of ligated and free-standing BCL *a* slightly differ, leading to excitation energy differences of 10−30 meV at the ADC(2) level.[14] Furthermore, Sirohiwal et al. used a pair-natural orbital coupled cluster approach to study CL *a* and reported Q_y and Q_x excitation energies of 1.75 and 2.24 eV, respectively, for CL *a*, also within ∼0.1 eV of our *GW*+BSE results for these excitations.[15]

Not only the absolute energies of Q_y and Q_x excitations are important for understanding and predicting excitation energy and charge transfer in photosynthetic systems but also their relative energy difference, $\Delta_{Q_x-Q_y}$, plays a role, in particular, in coupled systems of several pigment units. It is therefore reassuring that evG_nW_n+BSE predicts $\Delta_{Q_x-Q_y}$ in very good agreement with experiment, with a deviation of only 10 meV for BCL *a*, BCL *b*, and CL *a* and 120 meV for CL *b* for the LDA starting point and a slightly larger deviation of, on average, 60 meV for the ωPBE starting point. TDDFT based on ωPBE tends to underestimate $\Delta_{Q_x-Q_y}$, by, on average, 110 meV for these four pigments. For BCL *a*, we also show in Table 3 that $\Delta_{Q_x-Q_y}$ strongly depends on the xc functional used in the TDDFT calculations, primarily because of the strong dependence of the Q_x excitation on the amount of exact exchange, which can be seen by comparing the results based on the LDA (0% of exact exchange), B3LYP (∼23%), and BHLYP

https://dx.doi.org/10.1021/acs.jpca.1c01240
J. Phys. Chem. A 2021, 125, 2163−2172

Table 3. Difference between Q_x and Q_y Excitation Energies (in eV) Using TDDFT and evG_nW_n+BSE for BCL *a*

method	xc functional	$\Delta_{Q_x-Q_y}$
evG_nW_n+BSE	LDA	0.57
	B3LYP	0.54
	BHLYP	0.54
	ωPBE	0.59
TDDFT	LDA	0.25
	B3LYP	0.40
	BHLYP	0.64
	ωPBE	0.43
exp[8]		0.55

(50%). As before, evG_nW_n+BSE is in excellent agreement with experiment and almost independent of the underlying xc functional.

The experimental results reported in Tables 2 and 3 are based on measurements in diethyl ether, whereas our calculations are for gas-phase molecules. To approximately account for the effect of the solvent, we extracted experimental reference values for Q_y and Q_x excitations from a study by Limantara et al.,[30] in which electronic absorption spectroscopy was used to obtain Q_y and Q_x for a large number of nonpolar and polar solvents at room temperature. This study reports regression lines for Q_y and Q_x excitations of BCL *a* as a function of $R(n) = n^2 - 1/n^2 + 2$, where n is the refractive index of the solvent. The extrapolated values for $n = 1$ (vacuum) are 1.68 eV (nonpolar) and 1.67 eV (polar) for the Q_y and 2.25 eV (nonpolar) and 2.21 eV (polar) for the Q_x excitation. Based on these regression parameters, we estimate that the experimental reference values in Table 2 lie ∼50−70 meV below the gas-phase excitation energies. We also calculated the Q_y and Q_x excitation energies of BCL *a* with TDDFT (using ωPBE), approximating solvent effects with the COSMO approach as implemented in Turbomole. We used a dielectric constant of $4.33\varepsilon_0$ corresponding to the value in diethyl ether. COSMO red-shifts the Q_y and Q_x excitation energies by 70 and 50 meV, respectively, supporting our estimate. We conclude that solvent effects are small—within the numerical accuracy of our *GW*+BSE calculations—and do not change our main conclusions. Note that we also neglect the effects of temperature and the 0−0 vibrational energy contribution in our comparison with experimental results. Exact agreement of our calculated results with experiment is therefore not expected.

Bacteriochlorophyll *a*. In the remainder of this paper, we will use the BCL *a* molecule as a case study to compare to available computational literature results for this pigment, discuss the origin of differences between our evG_nW_n+BSE and TDDFT results, and comment on the effects of the choice of structure on excitation energies.

Comparison with RASPT2. For the Q_y and Q_x excitations of BCL *a*, we compare our *GW*+BSE and TDDFT calculations to multistate, second-order perturbation theory (RASPT2) calculations by Anda et al.[16,17] For this comparison, we use the molecular geometry reported in ref 16, which is a BCL *a* unit from the light-harvesting system LH2 of *Rhodoblastus acidophilus*. This structure was extracted from an experimental X-ray crystallographic structure of the LH2 complex (unit 302 within the structure 1NKZ in the RCSB Protein Data Bank).[48] The phytyl tail was truncated and replaced by a hydrogen atom, and no further geometry optimization was carried out. In the following, we will call this structure "A". Our geometry-optimized version of "A", which we relaxed using DFT as implemented in the Turbomole code with a def2-TZVP basis set and B3LYP,[46] will be called "R". A visual comparison between "A" and "R" is shown in Figure 3. The large differences that we observe between these two structures are unsurprising, given that we perform our geometry optimizations without taking into account the protein environment in which BCL *a* "A" is embedded *in vivo*. Table 4 shows our *GW*+BSE and TDDFT results for "A" in comparison with the RASPT2 excitation energies from refs.[16,17] We find, as before, that when eigenvalue self-consistency is used in *GW*, HOMO−LUMO gaps and Q_y and Q_x excitation energies differ by a maximum of 0.1 eV. Most notably, however, our *GW*+BSE excitation energies substantially differ from those calculated with RASPT2, with Q_y 0.4 eV and Q_x 0.5 eV lower than the RASPT2 result.

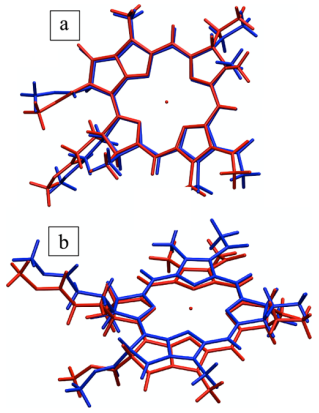

Figure 3. Overlay of structures "A" (red) and "R" (blue) in (a) top view and (b) side view.

Table 4. HOMO−LUMO Gaps and Q_y and Q_x Excitation Energies (in eV) for BCL *a* Structure "A"

method/basis set	xc functional	H-L gap	Q_y	Q_x
evG_nW_n+BSE/6-311++G(2d,2p)	LDA	3.62	1.17	1.90
	B3LYP	3.67	1.19	1.90
	BHLYP	3.72	1.23	1.92
	ωPBE	3.68	1.16	1.91
evG_nW_n+BSE/ANO-RCC-vDZP	LDA	3.76	1.38	2.18
TDDFT/6-311++G(2d,2p)	LDA	0.92	1.59	1.99
	B3LYP	1.60	1.64	2.17
	BHLYP	2.61	1.57	2.34
	ωPBE	3.70	1.48	2.02
RASPT2/ANO-RCC-vDZP			1.61	2.40

We find that about half of this difference can be traced back to the use of a smaller basis set (ANO-RCC-vDZP) in ref 16. Repeating our evG_nW_n@LDA+BSE calculation with the same basis, we obtain excitation energies of 1.38 eV for Q_y and 2.18 eV for Q_x. In line with previous studies, we also find that TDDFT with global hybrid functionals (B3LYP and BHLYP) results in similar excitation energies to RASPT2 for the Q_y excitation.[17,49] We hypothesize that this agreement is fortuitous. The optimally tuned RSH functional ωPBE has been shown to better describe singlet excitation energies of a

https://dx.doi.org/10.1021/acs.jpca.1c01240
J. Phys. Chem. A 2021, 125, 2163−2172

wide variety of organic compounds as compared to global hybrid functionals[50−52] and is more than 0.1 eV lower in energy than the RASPT2 Q_y excitation energy. Similar trends have also been shown for CL *a*, where DFT-based multireference CI, just as TDDFT with global hybrid functionals, tends to overestimate experiment by ∼0.2 eV for the Q_y and Q_x excitation.[53] All in all, given that comparisons with experimental data are complicated for an *in vivo* structure such as "A", we consider it most likely that our *GW*+BSE calculations underestimate the excitation energies of structure "A" by ∼0.1 eV, similar to our results for gas-phase BCL *a* (Table 2). The remaining deviations could be attributed to the multireference character of the Q_y excitation[16] and the choice of the RAS.

We also note that our *GW*+BSE results reproduce the energetic order and relative energy differences of the Q_y excitation of other BCL units within the LH2 ring that RASPT2 predicts, when using the ANO-RCC-vDZP basis set. However, the use of the significantly larger 6-311++G(2d,2p) basis leads to substantially larger excitation energy differences between these units (Table S7). Finally, it is worth mentioning that our *GW*+BSE calculations reproduce the relatively large energy difference $\Delta_{Q_x-Q_y} \approx 0.8$ eV that RASPT2 predicts, whereas TDDFT excitation energy differences are much less sensitive to details of the structure, with $\Delta_{Q_x-Q_y} \approx 0.5$ eV (using *ω*PBE) similar to the gas-phase structure of BCL *a*. We speculate that a geometry optimization of structure "A" within its protein environment would result in a smaller $\Delta_{Q_x-Q_y}$ for both RASPT2 and *GW*+BSE.

Role of the Electron−Hole Kernel. We find that the difference between *GW*+BSE and TDDFT excitation energies can be traced back almost entirely to differences in how electron−hole interactions are described in both schemes. The Q_y excitation is primarily (∼90%) a HOMO → LUMO transition, and the HOMO−LUMO gaps, as calculated with DFT-*ω*PBE and evG_nW_n@*ω*PBE, differ by only 0.02 meV (Table 3). In fact, the density of states (DOS) in the energy range relevant for both the Q_y and the Q_x excitations based on evG_nW_n@*ω*PBE and DFT-*ω*PBE eigenvalues are almost identical (see Figure 4). To further test our hypothesis, we construct the statically screened Coulomb interaction W_{ij}^{ab} (see eq 4) and solve the BSE based on a DFT-*ω*PBE eigensystem (instead of first computing QP eigenvalues using eq 2). We obtain values for the Q_y and Q_x excitation that are only 20 meV higher and 40 meV lower than the full *GW*+BSE solution, respectively, for structure "A". Similarly, for structure "R", the results are within less than 10 and 50 meV for the Q_y and Q_x excitation, respectively. This observation confirms that differences between the *GW*+BSE and TDDFT excitation energies are primarily due to differences in the xc and the BSE kernel. Generally, the overestimation of excitation energies that we observe with TDDFT is in line with results for other organic *π* chromophores such as rhodamine and rosamine[54] and of phenothiazine dyes,[55] for which it has been linked to an insufficient treatment of differential electron correlation between the ground and excited states by most TDDFT xc kernels.[56]

Charge Transfer Excitations with TD-LDA and G_nW_n@LDA+BSE. Finally, motivated by the excellent performance of evG_nW_n@LDA+BSE, we compare G_0W_0@LDA+BSE, ev*GW*LDA+BSE, and TD-LDA results for structures "A" and "R" of BCL *a*. Figure 5 shows the excitation spectrum calculated at

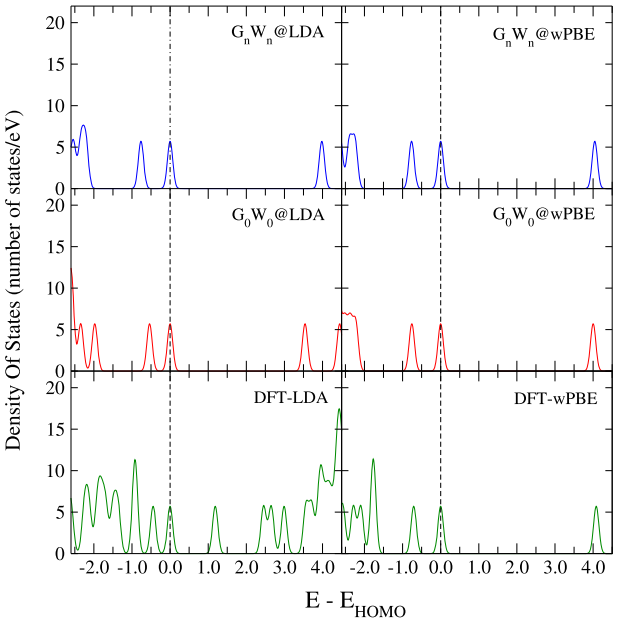

Figure 4. (Generalized) Kohn−Sham (green), G_0W_0 (red), and evG_nW_n (blue) DOS calculated using the LDA and *ω*PBE. The HOMO energies are aligned to zero.

these levels of theory. TD-LDA's severe underestimation of charge transfer excitations is well known[9] and leads to spurious excitations with charge transfer character at energies between Q_y and Q_x for BCL *a*.[47] Our comparison of structures "A" and "R" shows that while the energy of Q_y and Q_x is changing only slightly when TD-LDA is used, the relative position of these spurious low-oscillator strength excitations depends strongly on the structure. G_0W_0@LDA+BSE results in a very different, albeit no more reassuring, picture. For both structures, the first excitation already appears at energies below or around 1 eV and its oscillator strength is considerably lower than with TD-LDA; for structure "A", the oscillator strength of Q_y is even lower than that of Q_x. For structure "R", excitations 2, 3, and 4 have similar, very low, oscillator strength. However, already at the G_0W_0@LDA+BSE level, no charge transfer excitations are found between Q_y and Q_x—a consequence of the inherent nonlocality of the BSE kernel. Finally, for both structures, eigenvalue self-consistency pushes all excitations to significantly higher energies and results in a quantitatively correct description of Q_y and Q_x.

Inspection of the DOS calculated with DFT-xc, G_0W_0@xc, and G_nW_n@xc (xc = LDA, *ω*PBE) shown in Figure 4 is instructive for understanding the contribution of eigenvalue differences to the TDDFT and *GW*+BSE excitation energies. The G_0W_0@LDA DOS underestimates the HOMO−LUMO gap and the energy difference between the HOMO and HOMO − 1. In contrast, there is virtually no difference between the HOMO, HOMO − 1, and LUMO energies as calculated with DFT-*ω*PBE, G_0W_0@*ω*PBE, evG_nW_n@*ω*PBE, and evG_nW_n@LDA. As expected, the DFT-LDA DOS is markedly different, not only underestimating the HOMO−LUMO gap but also significantly underestimating the energy differences between the HOMO − 1, HOMO − 2, and HOMO − 3. Notably, the spurious dark states between Q_y and Q_x that TD-LDA predicts have significant contributions from transitions involving these lower occupied states.

https://dx.doi.org/10.1021/acs.jpca.1c01240
J. Phys. Chem. A 2021, 125, 2163−2172

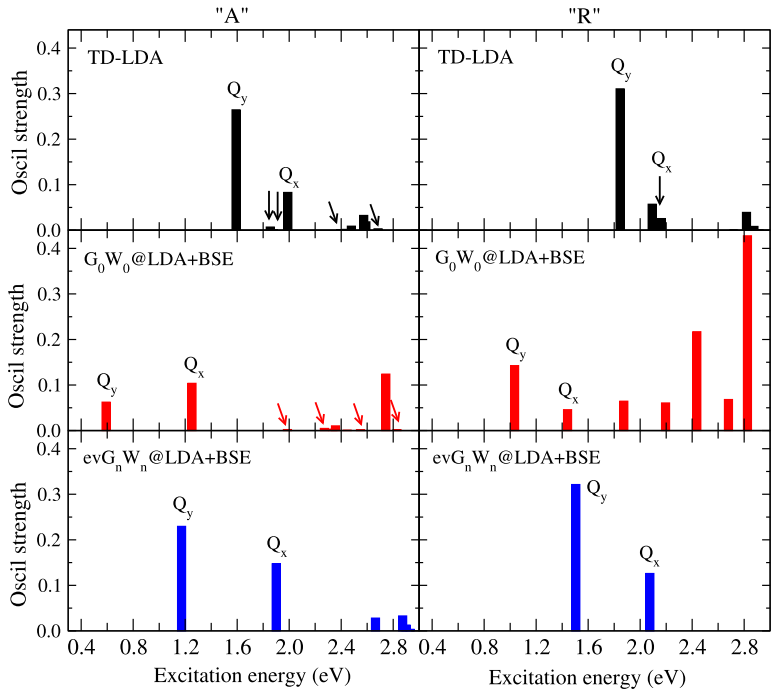

Figure 5. First excitations for structures "A" (left) and "R" (right) as calculated with TD-LDA (top), G_0W_0@LDA+BSE (center), and evG_nW_n@LDA+BSE (bottom). Arrows indicate excitations with very low oscillator strength.

CONCLUSIONS

In this article, we performed a systematic first-principles study of the electronic structure and excitations of seven members of the (bacterio)chlorophyll family, which we validated through comparison with calculated and experimental literature results. The *GW*+BSE approach, when used in a partially self-consistent fashion, is in excellent agreement with experiment for excitations in the visible and near-ultraviolet part of the spectrum. *GW*+BSE also correctly predicts the energy difference between the low-energy Q_y and Q_x excitations of these pigments, relevant for the description of the coupling between pigment complexes, present in the light harvesting units and reaction centers of plants and bacteria and crucial for excitation energy and charge transfer. Most importantly, our results are almost entirely independent of the DFT eigensystem used as an input for the *GW*+BSE calculations. A computationally inexpensive LDA starting point leads to similar results as a more involved optimally tuned ωPBE starting point.

It should be noted that the *GW* approach, despite its implementation using Gaussian basis functions and the use of the RI approximation in MOLGW and other codes, remains a major bottleneck of these calculations due to its $O(N^4)$ scaling with system size. Furthermore, our results highlight that the *GW* approach, more so than DFT, requires careful convergence with respect to the basis set size. This limits its applicability to systems with a few (B)CL pigments at most, until algorithms with better scaling become more widely available.[57−59] Our study joins a growing number of results, demonstrating that the *GW*+BSE approach can accurately predict neutral excitations of complex molecules without empirical parameters.[29] With new approaches for combining *GW*+BSE with large-scale molecular mechanics simulations[28] and polarizable continuum embedding[60] emerging, an accurate prediction of excitation energy and charge transfer in complex molecular environments is within reach.

ASSOCIATED CONTENT

Supporting Information

The Supporting Information is available free of charge at https://pubs.acs.org/doi/10.1021/acs.jpca.1c01240.

Atomic coordinates (ZIP)

Additional convergence data, tuned range-separation parameters, and excitation energies of all molecules discussed in the main manuscript (PDF)

AUTHOR INFORMATION

Corresponding Author

Linn Leppert − *MESA+ Institute for Nanotechnology, University of Twente, 7500 AE Enschede, The Netherlands; Institute of Physics, University of Bayreuth, Bayreuth 95440, Germany;* orcid.org/0000-0002-4361-4382; Email: l.leppert@utwente.nl

Author

Zohreh Hashemi − *Institute of Physics, University of Bayreuth, Bayreuth 95440, Germany*

Complete contact information is available at: https://pubs.acs.org/10.1021/acs.jpca.1c01240

Notes

The authors declare no competing financial interest.

ACKNOWLEDGMENTS

The authors are grateful for helpful discussions with C. Filippi. This work was supported by the Bavarian State Ministry of Science and the Arts through the Collaborative Research Network Solar Technologies go Hybrid (SolTech), the Elite

Network Bavaria (ENB), and through computational resources provided by the Bavarian Polymer Institute (BPI).

REFERENCES

(1) Blankenship, R. E. *Molecular Mechanisms of Photosynthesis*, 2nd ed.; Wiley Blackwell: Oxford, 2014.

(2) Hu, X.; Ritz, T.; Damjanović, A.; Autenrieth, F.; Schulten, K. Photosynthetic Apparatus of Purple Bacteria. *Q. Rev. Biophys.* **2002**, *35*, 1−62.

(3) Croce, R.; van Amerongen, H. Natural Strategies for Photosynthetic Light Harvesting. *Nat. Chem. Biol.* **2014**, *10*, 492−501.

(4) Cogdell, R. J.; Gall, A.; Köhler, J. The Architecture and Function of the Light-Harvesting Apparatus of Purple Bacteria: From Single Molecules to In Vivo Membranes. *Q. Rev. Biophys.* **2006**, *39*, 227−324.

(5) Jang, S.; Mennucci, B. Delocalized Excitons in Natural Light-Harvesting Complexes. *Rev. Mod. Phys.* **2018**, *90*, 035003.

(6) Shao, Y.; Mei, Y.; Sundholm, D.; Kaila, V. R. I. Benchmarking the Performance of Time-Dependent Density Functional Theory Methods on Biochromophores. *J. Chem. Theory Comput.* **2020**, *16*, 587−600.

(7) Sundholm, D. A Density-Functional-Theory Study of Bacteriochlorophyll b. *Phys. Chem. Chem. Phys.* **2003**, *5*, 4265−4271.

(8) Vokáčová, Z.; Burda, J. V. Computational Study on Spectral Properties of the Selected Pigments from Various Photosystems: Structure-Transition Energy Relationship. *J. Phys. Chem. A* **2007**, *111*, 5864−5878.

(9) Dreuw, A.; Head-Gordon, M. Failure of Time-Dependent Density Functional Theory for Long-Range Charge-Transfer Excited States: The Zincbacteriochlorin-Bacteriochlorin and Bacteriochlorophyll-Spheroidene Complexes. *J. Am. Chem. Soc.* **2004**, *126*, 4007−4016.

(10) Tozer, D. J.; Handy, N. C. Improving Virtual Kohn-Sham Orbitals and Eigenvalues: Application to Excitation Energies and Static Polarizabilities. *J. Chem. Phys.* **1998**, *109*, 10180−10189.

(11) Kuritz, N.; Stein, T.; Baer, R.; Kronik, L. Charge-Transfer-Like π -> π * Excitations in Time-Dependent Density Functional Theory: A Conundrum and Its Solution. *J. Chem. Theory Comput.* **2011**, *7*, 2408−2415.

(12) Kümmel, S. Charge-Transfer Excitations: A Challenge for Time-Dependent Density Functional Theory That Has Been Met. *Adv. Energy Mater.* **2017**, *7*, 1700440.

(13) Suomivuori, C.-M.; Fliegl, H.; Starikov, E. B.; Balaban, T. S.; Kaila, V. R. I.; Sundholm, D. Absorption Shifts of Diastereotopically Ligated Chlorophyll Dimers of Photosystem I. *Phys. Chem. Chem. Phys.* **2019**, *21*, 6851−6858.

(14) Suomivuori, C.-M.; Winter, N. O. C.; Hättig, C.; Sundholm, D.; Kaila, V. R. I. Exploring the Light-Capturing Properties of Photosynthetic Chlorophyll Clusters Using Large-Scale Correlated Calculations. *J. Chem. Theory Comput.* **2016**, *12*, 2644−2651.

(15) Sirohiwal, A.; Berraud-Pache, R.; Neese, F.; Izsák, R.; Pantazis, D. A. Accurate Computation of the Absorption Spectrum of Chlorophyll a with Pair Natural Orbital Coupled Cluster Methods. *J. Phys. Chem. B* **2020**, *124*, 8761−8771.

(16) Anda, A.; Hansen, T.; De Vico, L. Multireference Excitation Energies for Bacteriochlorophylls A within Light Harvesting System 2. *J. Chem. Theory Comput.* **2016**, *12*, 1305−1313.

(17) Anda, A.; Hansen, T.; De Vico, L. Q_y and Q_x Absorption Bands for Bacteriochlorophyll a Molecules from LH2 and LH3. *J. Phys. Chem. A* **2019**, *123*, 5283−5292.

(18) Segatta, F.; Cupellini, L.; Jurinovich, S.; Mukamel, S.; Dapor, M.; Taioli, S.; Garavelli, M.; Mennucci, B. A Quantum Chemical Interpretation of Two-Dimensional Electronic Spectroscopy of Light-Harvesting Complexes. *J. Am. Chem. Soc.* **2017**, *139*, 7558−7567.

(19) Onida, G.; Reining, L.; Rubio, A. Electronic Excitations: Density-Functional versus Many-Body Green's-Function Approaches. *Rev. Mod. Phys.* **2002**, *74*, 601.

(20) Albrecht, S.; Reining, L.; Del Sole, R.; Onida, G. Ab Initio Calculation of Excitonic Effects in the Optical Spectra of Semiconductors. *Phys. Rev. Lett.* **1998**, *80*, 4510.

(21) Rohlfing, M.; Louie, S. G. Electron-Hole Excitations and Optical Spectra from First Principles. *Phys. Rev. B: Condens. Matter Mater. Phys.* **2000**, *62*, 4927.

(22) Qiu, D. Y.; Da Jornada, F. H.; Louie, S. G. Optical Spectrum of MoS_2: Many-Body Effects and Diversity of Exciton States. *Phys. Rev. Lett.* **2013**, *111*, 216805.

(23) Grossman, J. C.; Rohlfing, M.; Mitas, L.; Louie, S. G.; Cohen, M. L. High Accuracy Many-Body Calculational Approaches for Excitations in Molecules. *Phys. Rev. Lett.* **2001**, *86*, 472−475.

(24) Tiago, M. L.; Kent, P. R. C.; Hood, R. Q.; Reboredo, F. A. Neutral and Charged Excitations in Carbon Fullerenes from First-Principles Many-Body Theories. *J. Chem. Phys.* **2008**, *129*, 084311.

(25) Bruneval, F.; Hamed, S. M.; Neaton, J. B. A Systematic Benchmark of the Ab Initio Bethe-Salpeter Equation Approach for Low-Lying Optical Excitations of Small Organic Molecules. *J. Chem. Phys.* **2015**, *142*, 244101.

(26) Palummo, M.; Hogan, C.; Sottile, F.; Bagalá, P.; Rubio, A. Ab Initio Electronic and Optical Spectra of Free-Base Porphyrins: The Role of Electronic Correlation. *J. Chem. Phys.* **2009**, *131*, 084102.

(27) Duchemin, I.; Deutsch, T.; Blase, X. Short-Range to Long-Range Charge-Transfer Excitations in the Zincbacteriochlorin-Bacteriochlorin Complex: A Bethe-Salpeter Study. *Phys. Rev. Lett.* **2012**, *109*, 167801.

(28) Wehner, J.; Brombacher, L.; Brown, J.; Junghans, C.; Çaylak, O.; Khalak, Y.; Madhikar, P.; Tirimbò, G.; Baumeier, B. Electronic Excitations in Complex Molecular Environments: Many-Body Green's Functions Theory in VOTCA-XTP. *J. Chem. Theory Comput.* **2018**, *14*, 6253−6268.

(29) Blase, X.; Duchemin, I.; Jacquemin, D. The Bethe-Salpeter Equation in Chemistry: Relations with TD-DFT, Applications and Challenges. *Chem. Soc. Rev.* **2018**, *47*, 1022−1043.

(30) Limantara, L.; Sakamoto, S.; Koyama, Y.; Nagae, H. Effects of Nonpolar and Polar Solvents on the Q_x and Q_y Energies of Bacteriochlorophyll a and Bacteriopheophytin a. *Photochem. Photobiol.* **1997**, *65*, 330−337.

(31) Scheer, H.; Inhoffen, H. *The Porphyrins*; Dolphi, Ed.; Academic Press: New York, 1978; Vol. II.

(32) Fetter, A.; Walecka, J. *Quantum Theory of Many-Particle Systems*; MacGraw-Hill: New York, 1971.

(33) Hedin, L. On Correlation Effects in Electron Spectroscopies and the GW Approximation. *J. Phys.: Condens. Matter* **1999**, *11*, R489.

(34) Jiang, H.; Gomez-Abal, R. I.; Rinke, P.; Scheffler, M. First-Principles Modeling of Localized d States with the GW@LDA+U Approach. *Phys. Rev. B: Condens. Matter Mater. Phys.* **2010**, *82*, 045108.

(35) Liao, P.; Carter, E. A. Testing Variations of the GW Approximation on Strongly Correlated Transition Metal Oxides: Hematite (α-Fe_2O_3) as a Benchmark. *Phys. Chem. Chem. Phys.* **2011**, *13*, 15189−15199.

(36) Marom, N.; Caruso, F.; Ren, X.; Hofmann, O. T.; Körzdörfer, T.; Chelikowsky, J. R.; Rubio, A.; Scheffler, M.; Rinke, P. Benchmark of GW Methods for Azabenzenes. *Phys. Rev. B: Condens. Matter Mater. Phys.* **2012**, *86*, 245127.

(37) Jacquemin, D.; Duchemin, I.; Blase, X. Benchmarking the Bethe-Salpeter Formalism on a Standard Organic Molecular Set. *J. Chem. Theory Comput.* **2015**, *11*, 3290−3304.

(38) Kaplan, F.; Weigend, F.; Evers, F.; Van Setten, M. J. Off-Diagonal Self-Energy Terms and Partially Self-Consistency in GW Calculations for Single Molecules: Efficient Implementation and Quantitative Effects on Ionization Potentials. *J. Chem. Theory Comput.* **2015**, *11*, 5152−5160.

(39) Bruneval, F.; Rangel, T.; Hamed, S. M.; Shao, M.; Yang, C.; Neaton, J. B. MOLGW 1: Many-Body Perturbation Theory Software for Atoms, Molecules, and Clusters. *Comput. Phys. Commun.* **2016**, *208*, 149−161.

https://dx.doi.org/10.1021/acs.jpca.1c01240
J. Phys. Chem. A 2021, 125, 2163−2172

(40) van Setten, M. J.; Caruso, F.; Sharifzadeh, S.; Ren, X.; Scheffler, M.; Liu, F.; Lischner, J.; Lin, L.; Deslippe, J. R.; Louie, S. G.; Yang, C.; Weigend, F.; Neaton, J. B.; Evers, F.; Rinke, P. GW100: Benchmarking G0W0 for Molecular Systems. *J. Chem. Theory Comput.* **2015**, *11*, 5665−5687.
(41) Godbout, N.; Salahub, D. R.; Andzelm, J.; Wimmer, E. Optimization of Gaussian-Type Basis Sets for Local Spin Density Functional Calculations. Part I. Boron Through Neon, Optimization Technique and Validation. *Can. J. Chem.* **1992**, *70*, 560−571.
(42) Zheng, J.; Xu, X.; Truhlar, D. G. Minimally Augmented Karlsruhe Basis Sets. *Theor. Chem. Acc.* **2011**, *128*, 295−305.
(43) Stein, T.; Eisenberg, H.; Kronik, L.; Baer, R. Fundamental Gaps in Finite Systems from Eigenvalues of a Generalized Kohn-Sham Method. *Phys. Rev. Lett.* **2010**, *105*, 266802.
(44) Shao, Y.; Gan, Z.; Epifanovsky, E.; Gilbert, A. T.; Wormit, M.; Kussmann, J.; Lange, A. W.; Behn, A.; Deng, J.; Feng, X.; et al. Advances in Molecular Quantum Chemistry Contained in the Q-Chem 4 Program Package. *Mol. Phys.* **2015**, *113*, 184−215.
(45) Oviedo, M. B.; Negre, C. F. A.; Sánchez, C. G. Dynamical Simulation of the Optical Response of Photosynthetic Pigments. *Phys. Chem. Chem. Phys.* **2010**, *12*, 6706−6711.
(46) *Turbomole*, V7.4 2019, a development of University of Karlsruhe and Forschungszentrum Karlsruhe GmbH, 2019. www.turbomole.org.
(47) Schelter, I.; Foerster, J. M.; Gardiner, A. T.; Roszak, A. W.; Cogdell, R. J.; Ullmann, G. M.; De Queiroz, T. B.; Kümmel, S. Assessing Density Functional Theory in Real-Time and Real-Space as a Tool for Studying Bacteriochlorophylls and the Light-Harvesting Complex 2. *J. Chem. Phys.* **2019**, *151*, 134114.
(48) Papiz, M. Z.; Prince, S. M.; Howard, T.; Cogdell, R. J.; Isaacs, N. W. The Structure and Thermal Motion of the B800-850 LH2 Complex from Rps. acidophila at 2.0 Å Resolution and 100 K: New Structural Features and Functionally Relevant Motions. *J. Mol. Biol.* **2003**, *326*, 1523−1538.
(49) List, N. H.; Curutchet, C.; Knecht, S.; Mennucci, B.; Kongsted, J. Toward Reliable Prediction of the Energy Ladder in Multi-chromophoric Systems: A Benchmark Study on the FMO Light-Harvesting Complex. *J. Chem. Theory Comput.* **2013**, *9*, 4928−4938.
(50) Kronik, L.; Stein, T.; Refaely-Abramson, S.; Baer, R. Excitation Gaps of Finite-Sized Systems from Optimally Tuned Range-Separated Hybrid Functionals. *J. Chem. Theory Comput.* **2012**, *8*, 1515−1531.
(51) Refaely-Abramson, S.; Baer, R.; Kronik, L. Fundamental and Excitation Gaps in Molecules of Relevance for Organic Photovoltaics from an Optimally Tuned Range-Separated Hybrid Functional. *Phys. Rev. B: Condens. Matter Mater. Phys.* **2011**, *84*, 075144.
(52) Jacquemin, D.; Moore, B.; Planchat, A.; Adamo, C.; Autschbach, J. Performance of an Optimally Tuned Range-Separated Hybrid Functional for 0-0 Electronic Excitation Energies. *J. Chem. Theory Comput.* **2014**, *10*, 1677−1685.
(53) Parusel, A. B. J.; Grimme, S. A Theoretical Study of the Excited States of Chlorophyllaand Pheophytina. *J. Phys. Chem. B* **2000**, *104*, 5395−5398.
(54) Moore, B.; Schrader, R. L.; Kowalski, K.; Autschbach, J. Electronic π-to-π^* Excitations of Rhodamine Dyes Exhibit a Time-Dependent Kohn-Sham Theory "Cyanine Problem". *ChemistryOpen* **2017**, *6*, 385−392.
(55) De Queiroz, T. B.; De Figueroa, E. R.; Coutinho-Neto, M. D.; Maciel, C. D.; Tapavicza, E.; Hashemi, Z.; Leppert, L. First Principles Theoretical Spectroscopy of Methylene Blue: Between Limitations of Time-Dependent Density Functional Theory Approximations and its Realistic Description in the Solvent. *J. Chem. Phys.* **2021**, *154*, 044106.
(56) Moore, B.; Autschbach, J. Longest-Wavelength Electronic Excitations of Linear Cyanines: The Role of Electron Delocalization and of Approximations in Time-Dependent Density Functional Theory. *J. Chem. Theory Comput.* **2013**, *9*, 4991−5003.
(57) Neuhauser, D.; Gao, Y.; Arntsen, C.; Karshenas, C.; Rabani, E.; Baer, R. Breaking the Theoretical Scaling Limit for Predicting Quasiparticle Energies: The Stochastic GW Approach. *Phys. Rev. Lett.* **2014**, *113*, 076402.
(58) Vlček, V.; Rabani, E.; Neuhauser, D.; Baer, R. Stochastic GW Calculations for Molecules. *J. Chem. Theory Comput.* **2017**, *13*, 4997−5003.
(59) Förster, A.; Visscher, L. Low-Order Scaling G_0W_0 by Pair Atomic Density Fitting. *J. Chem. Theory Comput.* **2020**, *16*, 7381−7399.
(60) Duchemin, I.; Guido, C. A.; Jacquemin, D.; Blase, X. The Bethe-Salpeter Formalism with Polarisable Continuum Embedding: Reconciling Linear-Response and State-Specific Features. *Chem. Sci.* **2018**, *9*, 4430−4443.

https://dx.doi.org/10.1021/acs.jpca.1c01240
J. Phys. Chem. A 2021, 125, 2163−2172

Supporting Information for Assessment of the *Ab Initio* Bethe-Salpeter Equation Approach for the Low-Lying Excitation Energies of Bacteriochlorophylls and Chlorophylls

Zohreh Hashemi[†] and Linn Leppert[*,‡,†]

[†]*Institute of Physics, University of Bayreuth, Bayreuth 95440, Germany*

[‡]*MESA+ Institute for Nanotechnology, University of Twente, 7500 AE Enschede, The Netherlands*

E-mail: l.leppert@utwente.nl

Convergence of Single Pole Approximation

In the single pole approximation (SPA), all matrix elements of the RPA polarizability larger than N_{SPA} are considered diagonal. Figure S1 a and b show the HOMO-LUMO gap and Q_y and Q_x excitation energies as a function of N_{SPA}. Dashed lines correspond to a fit with the function:

$$f(N_{SPA}) = \frac{a}{N_{SPA} - N_0} + b,$$

where a, b, and N_0 are fit parameters. Using this fit, we estimate the error due to using a finite N_{SPA} by identifying the asymptote b with the band gap extrapolated to infinite N_{SPA}. This leads to an underestimation of the HOMO-LUMO gap, the Q_y and the Q_x excitation by 40 meV, 10 meV, and 70 meV, respectively, using G_0W_0@BHLYP+BSE for structure 'A' (see Figure S1).

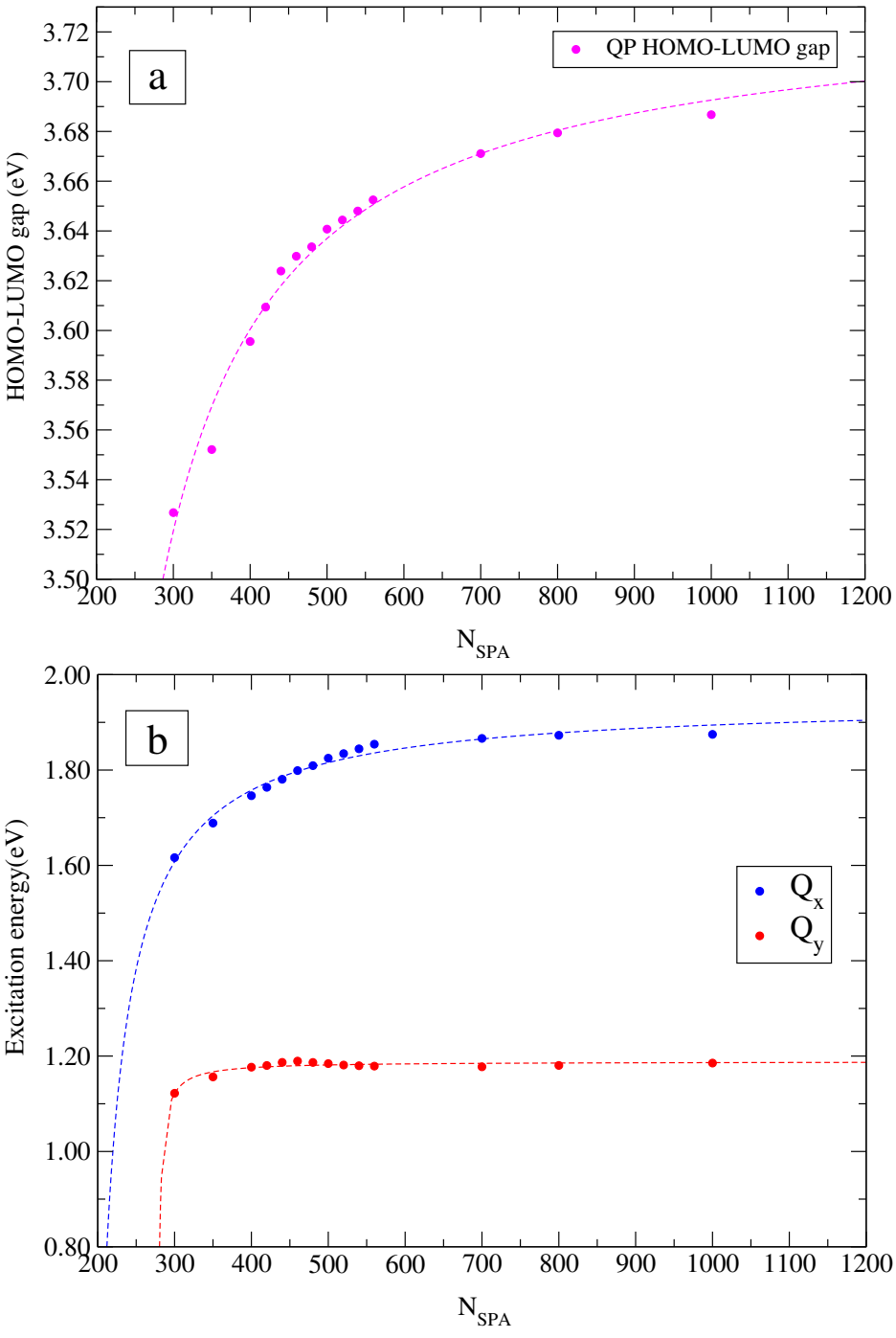

Figure S1: a) HOMO-LUMO gaps and b) Q_y and Q_x excitations energy (in eV) for BCL a structure 'A' calculated using the 6-311++G(2d,2p) basis set and G_0W_0@BHLYP+BSE as a function of the number of states explicitly used in the calculation of the polarizability.

Basis set convergence

Table S1: HOMO-LUMO gaps and Q_y and Q_y excitation energies (in eV) for BCL a structure 'A' calculated with G_0W_0@BHLYP+BSE for different basis sets.

Basis set	functions	aux. functions	HOMO-LUMO gap	Q_y	Q_x
6-31G	503	1728	3.93	1.37	2.01
6-311G	733	1728	3.88	1.34	1.99
ANO-RCC-vDZP	852	1728	3.78	1.26	1.95
def2-SVP	852	2784	3.80	1.25	1.92
6-311++G**	1308	1728	3.71	1.20	1.89
6-311++G(2d,2p)	1657	1728	3.69	1.18	1.87
def2-TZVP	1686	4158	3.67	1.17	1.85
def2-TZVPP	1990	4728	3.67	1.17	1.85

Table S2: HOMO-LUMO gaps and Q_y and Q_y excitation energies (in eV) for BCL a structure 'A' calculated with TD-BHLYP for different basis sets.

Basis set	functions	aux. functions	HOMO-LUMO gap	Q_y	Q_x
6-31G	503	1728	2.67	1.60	2.30
6-311G	733	1728	2.72	1.58	2.30
def2-SVP	852	2784	2.66	1.54	2.27
6-311++G**	1308	1728	2.61	1.57	2.35
6-311++G(2d,2p)	1657	1728	2.61	1.57	2.34
def2-TZVP	1686	4158	2.57	1.49	2.24
def2-TZVPP	1990	4728	2.61	1.51	2.28

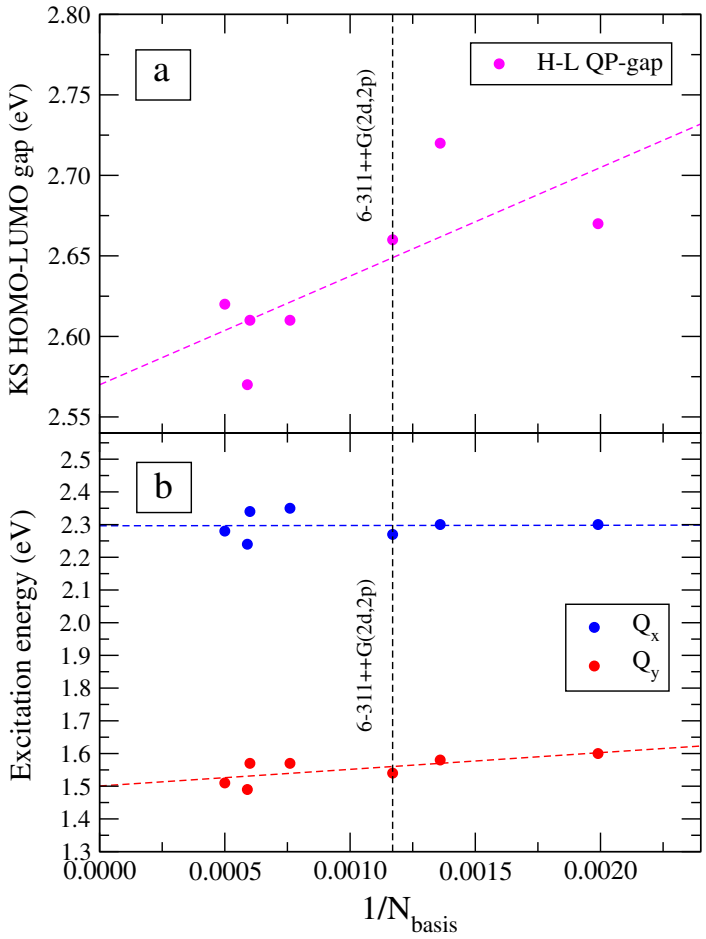

Figure S2: HOMO-LUMO gaps and Q_y and Q_y excitation energies (in eV) for BCL a structure 'A' calculated with TD-BHLYP for different basis sets.

Range separation parameters from optimal tuning procedure

Table S3: Optimized range separation parameters ω obtained from tuning procedure as outlined in Ref. 1.

molecule	ω (a_0^{-1})
BC	212
BCL a 'A'	163
BCL a 'R'	168
BCL b	166
BCL c	166
BCL d	162
BCL e	164
CL a	168
CL b	162

Calculated excitation energies of BCL *a* 'A'

Table S4: HOMO-LUMO gaps, Q_y and Q_x excitation energies (in eV) and oscillator strengths Γ_i for BCL a structure 'A' calculated with the 6-311++G(2d,2p) basis set.

Method	xc functional	HOMO-LUMO gap	Q_y	Γ_y	Q_x	Γ_x
G_0W_0+BSE	LDA	3.54	1.03	0.14	1.44	0.04
	B3LYP	3.81	1.30	0.22	1.77	0.09
	BHLYP	4.04	1.51	0.30	2.05	0.10
	ωPBE	4.00	1.46	0.29	2.06	0.10
evG_nW_n+BSE	LDA	3.98	1.50	0.32	2.07	0.12
	B3LYP	4.03	1.53	0.32	2.07	0.11
	BHLYP	4.08	1.55	0.32	2.09	0.11
	ωPBE	4.04	1.49	0.30	2.09	0.10
TDDFT	LDA	1.18	1.84	0.31	2.09	0.06
	B3LYP	1.91	1.89	0.38	2.29	0.11
	BHLYP	2.97	1.81	0.44	2.45	0.12
	ωPBE	4.08	1.75	0.37	2.18	0.10

Calculated excitation energies of BCL *a* – *e* and CL *a* and *b*

Table S5: Energies and oscillator strengths Γ_i of the first six excitations of BCLs and CLs calculate with TDDFT using ωPBE with ω as in Table S3.

Molecule	Q_1	Γ_1	Q_2	Γ_2	Q_3	Γ_3	Q_4	Γ_4	Q_5	Γ_5	Q_6	Γ_6
BCL a	1.75	0.34	2.16	0.10	2.98	0.00	3.02	0.00	3.17	0.00	3.33	0.20
BCL b	1.69	0.32	2.15	0.06	2.99	0.00	3.01	0.00	3.10	0.00	3.19	0.61
BCL c	2.05	0.16	2.21	0.05	3.03	0.00	3.21	0.62	3.31	0.09	3.35	0.17
BCL d	2.08	0.18	2.29	0.04	3.13	0.07	3.19	0.48	3.26	0.10	3.36	0.01
BCL e	2.10	0.10	2.23	0.02	3.02	0.61	3.05	0.53	3.06	0.20	3.15	0.00
ChL a	2.06	0.20	2.29	0.03	3.16	0.26	3.22	0.03	3.24	0.31	3.34	0.06
ChL b	2.10	0.14	2.29	0.00	2.97	0.50	3.07	0.75	3.10	0.09	3.16	0.01

Table S6: Energies and oscillator strengths Γ_i of the first six excitations of BCLs and CLs calculated with ev$G_n W_n$@ωPBE with ω as in Table S3.

Molecule	Q_1	Γ_1	Q_2	Γ_2	Q_3	Γ_3	Q_4	Γ_4	Q_5	Γ_5	Q_6	Γ_6
BCL a	1.50	0.29	2.10	0.11	3.16	0.10	3.25	0.42	3.29	0.00	3.37	0.00
BCL b	1.45	0.27	2.09	0.07	2.85	0.01	3.05	0.74	3.33	0.01	3.45	0.02
BCL c	1.84	0.18	2.11	0.03	3.02	0.82	3.21	0.75	3.23	0.00	3.41	0.01
BCL d	1.89	0.20	2.21	0.03	3.05	0.82	3.29	0.70	3.40	0.05	3.40	0.02
BCL e	1.96	0.13	2.13	0.01	2.88	0.76	2.95	0.67	3.11	0.00	3.31	0.00
ChL a	1.86	0.21	2.19	0.02	3.02	0.67	3.25	0.83	3.34	0.03	3.38	0.00
ChL b	1.93	0.18	2.20	0.00	2.85	0.71	2.98	0.72	3.28	0.01	3.30	0.00

Excitation energies of different BCL *a* units in the LH2 ring

Table S7: Q_y and Q_x excitation energies (in eV) for three BCL *a* units from the light harvesting 2 ring of *Rhodoblastus acidophilus*. RASPT2 results are taken from Ref. 2.

Method and basis	unit	Q_y	Q_x
evG_nW_n+BSE 6-311++G(2d,2p)	302	1.17	1.90
	303	1.31	2.01
	306	1.25	2.04
evG_nW_n+BSE ANO-RCC-vDZP	302	1.38	2.18
	303	1.44	2.16
	306	1.38	2.19
RASPT2 ANO-RCC-vDZP	302	1.61	2.40
	303	1.66	2.38
	306	1.61	2.38

References

(1) Stein, T.; Eisenberg, H.; Kronik, L.; Baer, R. Fundamental Gaps in Finite Systems from Eigenvalues of a Generalized Kohn-Sham Method. *Phys. Rev. Lett.* **2010**, *105*, 266802.

(2) Anda, A.; Hansen, T.; De Vico, L. Qy and Qx Absorption Bands for Bacteriochlorophyll a Molecules from LH2 and LH3. *J. Phys. Chem. A* **2019**, *123*, 5283–5292.

Publication II

First principles theoretical spectroscopy of methylene blue: Between limitations of time-dependent density functional theory approximations and its realistic description in the solvent

Reprinted from

The Journal of Chemical Physics 154, 044106 (2021)

Thiago B. de Queiroz[1], Erick R. de Figueroa[1], Maurício D. Coutinho-Neto[1], Cleiton D. Maciel[2], Enrico Tapavicza[3], **Zohreh Hashemi**[4], and Linn Leppert[4,5]

1) Centro de Ciencias Naturais e Humanas, Universidade Federal do ABC, Av. dos Estados 5001, 09510-580 Santo André-SP, Brazil

2) Instituto Federal de Educação, Ciência e Tecnologia de São Paulo, Campus Itaquaquecetuba, Avenida Primeiro de Maio, 500, 08571-050 Itaquaquecetuba-SP, Brazil

3) Department of Chemistry and Biochemistry, California State University, Long Beach, 1250 Bellflower Boulevard, Long Beach, California 90840, USA

4) Institute of Physics, University of Bayreuth, Bayreuth 95440, Germany

5) MESA+ Institute for Nanotechnology, University of Twente, 7500 AE Enschede, The Netherlands

My contribution

T. B. Queiroz is the first author and leads contributor to the article. This article is the outcome of cooperation between all authors. The excitation spectrum of the methylene blue molecule in the gas-phase and solvated within an explicit number of water molecules was studied in this work using TDDFT. We used the GW/BSE method as the reference value for the validation of TDDFT results. The TDDFT calculations along with vibration results were done by T. B. Queiroz, E. R. de Figueroa, M. D. Coutinho-Neto, C. D. Maciel, and E. Tapavicza. I performed all GW/BSE calculations and benchmarked the results using different functionals. T. B. Queiroz and L. Leppert commented on the GW/BSE results and helped with the direction of the simulations. Figures including both TDDFT and GW/BSE results in the main text and supplementary material were prepared by me. I wrote parts related to the GW/BSE calculations in the first draft. All authors were involved in the scientific discussions and worked on the final version of the article equally.

The Journal of Chemical Physics

First principles theoretical spectroscopy of methylene blue: Between limitations of time-dependent density functional theory approximations and its realistic description in the solvent

Cite as: J. Chem. Phys. **154**, 044106 (2021); https://doi.org/10.1063/5.0029727
Submitted: 15 September 2020 • Accepted: 01 January 2021 • Published Online: 26 January 2021

Thiago B. de Queiroz, Erick R. de Figueroa, Maurício D. Coutinho-Neto, et al.

The Journal of Chemical Physics ARTICLE scitation.org/journal/jcp

First principles theoretical spectroscopy of methylene blue: Between limitations of time-dependent density functional theory approximations and its realistic description in the solvent

Cite as: J. Chem. Phys. 154, 044106 (2021); doi: 10.1063/5.0029727
Submitted: 15 September 2020 • Accepted: 1 January 2021 •
Published Online: 26 January 2021

Thiago B. de Queiroz,[1,a] Erick R. de Figueroa,[1] Maurício D. Coutinho-Neto,[1,b] Cleiton D. Maciel,[2] Enrico Tapavicza,[3,a] Zohreh Hashemi,[4] and Linn Leppert[4,5,c]

AFFILIATIONS

[1]Centro de Ciências Naturais e Humanas, Universidade Federal do ABC, Av. dos Estados 5001, 09510-580 Santo André-SP, Brazil
[2]Instituto Federal de Educação, Ciência e Tecnologia de São Paulo, Campus Itaquaquecetuba, Avenida Primeiro de Maio, 500, 08571-050 Itaquaquecetuba-SP, Brazil
[3]Department of Chemistry and Biochemistry, California State University, Long Beach, 1250 Bellflower Boulevard, Long Beach, California 90840, USA
[4]Institute of Physics, University of Bayreuth, Bayreuth 95440, Germany
[5]MESA+ Institute for Nanotechnology, University of Twente, 7500 AE Enschede, The Netherlands

[a]Authors to whom correspondence should be addressed: thiago.branquinho@ufabc.edu.br and enrico.tapavicza@csulb.edu
[b]mauricio.neto@ufabc.edu.br
[c]l.leppert@utwente.nl

ABSTRACT

Methylene blue [3,7-Bis(di-methylamino) phenothiazin-5-ium chloride] is a phenothiazine dye with applications as a sensitizer for photodynamic therapy, photoantimicrobials, and dye-sensitized solar cells. Time-dependent density functional theory (TDDFT), based on (semi)local and global hybrid exchange-correlation functionals, fails to correctly describe its spectral features due to known limitations for describing optical excitations of π-conjugated systems. Here, we use TDDFT with a non-empirical optimally tuned range-separated hybrid functional to explore the optical excitations of gas phase and solvated methylene blue. We compute solvated configurations using molecular dynamics and an iterative procedure to account for explicit solute polarization. We rationalize and validate that by extrapolating the optimized range separation parameter to an infinite amount of solvating molecules, the optical gap of methylene blue is well described. Moreover, this method allows us to resolve contributions from solvent–solute intermolecular interactions and dielectric screening. We validate our results by comparing them to first-principles calculations based on the GW+Bethe–Salpeter equation approach and experiment. Vibronic calculations using TDDFT and the generating function method account for the spectra's subbands and bring the computed transition energies to within 0.15 eV of the experimental data. This methodology is expected to perform equivalently well for describing solvated spectra of π-conjugated systems.

I. INTRODUCTION

Phenothiazine dyes, such as methylene blue [MB, 3,7-Bis (di-methylamino) phenothiazin-5-ium chloride], are a technologically important class of π-conjugated heterocyclic molecules. They cover an extensive range of light assisted applications as sensitizers for photodynamic therapy,[1,2] photoantimicrobials,[3] and dye-sensitized solar cells.[4] These applications involve light absorption and

electronic transitions in the molecule, which are strongly influenced by surrounding molecules and the medium in which these molecules are solvated.[2,5] It is therefore important to describe the electronic structure and dynamics of this class of molecules in realistic environments accurately.[2]

Density functional theory (DFT) and time-dependent DFT (TDDFT) have been extensively employed for such studies since they are, in principle, exact theories while computationally efficient.[6–13] Low-lying valence states of organic compounds of intermediate size are usually well described by exchange-correlation (xc) functionals within the local density approximation (LDA)[7] and generalized gradient approximation (GGA, also called semilocal approximation)[14] as well as by their linear combination with nonlocal Fock-like exact exchange (EXX), the global hybrids[15,16] (see, for instance, Ref. 17). However, these "standard TDDFT approximations," i.e., LDA, GGA, and global hybrid xc-functionals, yield significant deviations for π–$\pi*$ valence transitions of some sets of π-conjugated systems in comparison to experimental and theoretical reference data,[18–24] which is a statement that is also valid for MB[25] and other related compounds.[26,27] The failure of standard TDDFT for intermediate or large π-conjugated systems has been the subject of an extensive number of studies.[18,21–23,28,29]

From the perspective of molecular topology, open chain π-conjugated systems can be categorized as either polyenes or polymethines.[18] Polyenes demonstrate π-density alternation in the bonds, but the structure is based on their σ-skeleton (alternating double and single bonds).[18,29] Polymethines, just as cyanine dyes, show similar alternating π-bonds but with the highest alternating density in the atomic positions.[18,29] MB can be regarded as a carbocyanine related compound. Additionally, MB is expected to present even higher electron delocalization of the π-electrons in the ground state, in comparison to other phenothiazine dyes, due to the presence of two strongly electron-donating dimethyl-amino groups located diametrically alongside the molecule.[5]

For polymethines, the lowest allowed excitation is composed of a single electronic configuration, well characterized by a single-particle HOMO–LUMO transition.[18,30] Yet, standard TDDFT substantially overestimates the transition energies.[18,31,32] These systems exhibit excited state charge densities that differ significantly from the ground state densities.[18,29] This error was later recast in terms of the very small magnitude of the exchange-correlation response kernel integrals.[33,34] This is a feature that is badly described by linear response TDDFT since the xc kernel is calculated as the functional derivative of the xc potential at the ground state density (in principle, an exact linear response formulation if time propagated, but time-independent in the adiabatic approximation).[35,36] Similarly to the polyene case, pure GGAs perform slightly better than their corresponding hybrids.[33]

Besides the errors caused by the approximations described above (as compared to reference calculation methods), there are also errors arising from the incorrect and unrealistic description of the medium (as compared to experimental data).[25] In fact, electron-hole interactions can be significantly weakened by the effect of dielectric screening on the Coulomb potential.[37] For instance, the correct prediction of the S_0–S_1 transition energy in azobenzene derivatives in comparison to experimental data from calculations with the GW and Bethe–Salpeter equation (GW + BSE) requires the consideration of solvent polarization effects (dielectric screening).[38] Intermolecular interactions also play a role. From the infrared absorption spectrum of MB in the gas phase in comparison to its hydrated crystalline state,[39] it was proposed that the functional group aside $N^+(CH_3)_2$ is H-bonding to a water molecule. Again, standard TDDFT approximations are ill-equipped for describing such effects since they can produce electron density delocalization errors and overestimate intermolecular interactions.[33,40] Finally, these approximations are not designed to appropriately describe the long-range dielectric screening,[41–43] scaling incorrectly at long distances [decaying faster than $-(1/R)$, where R is the electron–hole distance].[44–46]

More recently, (semi)local approximations have been combined with EXX using the error function [erf(ωr)] in the Coulomb operator. In these range-separated hybrid (RSH) functionals, a range separation parameter, ω, scales short- and long-range exchange terms such that (semi)local terms dominate at short range and EXX at long range [in this particular format, referred as the long-range corrected (LRC) functional].[47–49] This tempered mix of (semi)local and EXX takes advantage of the good performance of predominantly (semi)local hybrid functionals for describing valence transitions[15] while ensuring the correct asymptotic of the potential ($-1/R$), thereby improving preceding approximations in many respects.[47–51] The range separation parameter can be empirically optimized[47,52,53] or tuned from first principles, by choosing ω such that the eigenvalue of the Kohn–Sham frontier orbital located in the solute approaches the ionization energy.[54,55] The optimally tuned (OT) RSH functionals have been used with great success for the prediction of charge-transfer excitations for a variety of complex molecular systems,[56–58] intermolecular interactions,[59] and dielectric screening.[55,59] In fact, the introduction of the non-local EXX term at long range in the RSH seems to be appropriate for introducing the correct field-counteracting behavior due to the environment. For instance, polarizabilities and second hyperpolarizabilities are correctly predicted using this approach.[60]

In this article, we report first principles OT-RSH TDDFT calculations for the low-lying excited states of MB in vacuum and water, aiming to describe the system realistically while gaining insight into the limitations of state-of-the-art TDDFT. We employed the RSH functional ωPBE (PBE exchange at short range)[49] optimally tuned for MB optimized in vacuum and solvated by water molecules. We circumvent problems associated with RSH tuning for solvated molecules by analyzing the orbital localization involved in the functional tuning. Furthermore, we rationalize and demonstrate that the spectroscopic features of MB represented in its aqueous medium are well characterized by the OT-RSH functional. We show that this is a consequence of the increased short-to-long GGA/EXX interchange distance in solution (ω^{-1}), leading to higher weights of semilocal GGA exchange in the description of the MB molecule while treating the solvent by a balanced mix of semilocal and EXX at long range. Furthermore, we show that the zero-point vibrational energy shifts the spectrum to lower energies relative to vertical transitions and that vibronic contributions are responsible for a shoulder at higher energy (in comparison to the maximum absorption). As reference data, we use a partially self-consistent GW + BSE approach with the optimally tuned ωPBE as the starting point (as benchmarked in Refs. 61 and 62) in addition to experimental data. Thus, we present an inexpensive TDDFT methodology to describe accurately the absorption spectrum of this important organic dye in an aqueous solution, which can be extended to describe

excited states of other π-conjugated systems in a complex chemical environment.

II. METHODS

The details of the generation of the molecular configurations, molecular dynamics, calculation of vibrational spectrum, and calculation of excited states with TDDFT and GW + BSE and the data obtained are listed in the supplementary material. We also discuss our strategy for optimally tuning the RSH in explicit solvated systems, basis set convergence, and starting point issues in the GW + BSE calculations in the supplementary material.

The geometries and vibronic spectrum were obtained from DFT/B3LYP/def2-SV(P) calculations (theory/xc-approximation/basis set) followed by molecular dynamics simulations [isothermal–isobaric (NPT) ensemble with T = 298 K and P = 1 atm]. The ground and excited state vibrational spectra were computed using analytical and numerical second derivatives.[63,64] The structures for excited state calculations were obtained from MD frames and labeled according to their MD step after reaching thermal equilibrium and the number of solvating water molecules (in parenthesis), namely, MB-01(20), MB-13(20), MB-19(13), MB-27(20), MB-31(23), MB-38(26), and MB-46(21). These structures were generated with a solvation cutoff of 3.2 Å, where solvation cutoff is the maximum distance between an MB atom and an atom in the water molecule selected for the calculations. The structure MB-31 was taken as a representative structure and progressively solvated with additional cutoffs of 3.8 Å, 4.0 Å, 4.2 Å, 4.4 Å, 4.5 Å, 4.6 Å, 4.8 Å, 5.0 Å, 5.2 Å, and 5.4 Å, corresponding to 46, 58, 59, 67, 70, 71, 76, 84, 93, and 101 water molecules, respectively. The excited states were calculated from (i) TDDFT calculations with the functionals $xPBE_x + (1 - x)$ EXX + PBE_c, $0 \le x \le 1$, with the 6-31G(d,p) as basis set, (ii) TDDFT with the ωPBE and 6-31G(d,p) as functional and basis set, and (iii) eigenvalue self-consistent G_nW_n + BSE/ωPBE/6-311++(2d,2p) (method/starting point/basis set).

III. RESULTS

A. Ground state properties

MB and solvent configurations were obtained using an iterative procedure to account for solute polarization described in detail in the supplementary material. We employ a protocol to induce the solvent perturbation on the solute by generating an average solvent electrostatic potential (ASEP) developed initially by Sánchez and co-workers.[65,66] We follow a sequential QM/MM iterative procedure similar to the one proposed by Coutinho *et al.*[67,68] to generate converged solvent configurations in equilibrium with induced solute polarization for fixed solute geometries. In their procedure, solvent effects are included using point changes whose configurations come from Metropolis Monte Carlo simulations while solute charges are computed using the CHELPG algorithm.[69] An iterative procedure is used, where at each iteration a new set of solute CHELPG charges is obtained at distinct sampled solvent configurations. They have applied their method for the calculation of condensed phase spectra of several systems with encouraging results.[70–72]

Solvated MB displays a strong increase in dipole moment in the water when compared to vacuum, going from 2.55 D to 4.23 D as computed by our iterative procedure. A strong charge separation matches the increase of the dipole moment of the molecule, where the central nitrogen acquires a strongly negative charge compared to its vacuum value. CHELPG values increase from $-0.60e$ to $-0.91e$. As expected, solute–solvent interactions are affected, resulting in a larger number of hydrogen bonds between the central nitrogen and water. These interactions are present in most configurations sampled from molecular dynamics and in the configurations selected for spectroscopic studies.

B. Excited states of the isolated MB by exploring global hybrid functionals: Assignment of the failures and the OT-RSH proposal

As we expect that standard TDDFT cannot describe the optical gap of MB well, we try to map possible error sources by calculating the first excited state transitions (S_0–S_1 and S_0–T_1), adding EXX stepwise in the hybrid functional. Figure 1 shows the S_1 and T_1 excitation energies calculated with TDDFT as a function of EXX/PBE_x admixture for MB-31(0), as well as calculated from the G_nW_n + BSE method [$\Delta E(S_0–S_1)$ = 2.25 eV and $\Delta E(S_0–T_1)$ = 1.00 eV] and the experimental maximum absorption of MB in water (1.87 eV).[73] The experimental value taken in water does not represent the optical gap of the molecule in the gas phase, but solvent effects are not expected to exceed 0.1 eV–0.4 eV (see below). Thus, the optical gap of the molecule in the gas phase should be around 2.0 eV–2.3 eV, suggesting that G_nW_n + BSE can be regarded as the reference data (also rationalized in Refs. 61 and 62). The S_0–S_1 transition energy approaches the G_nW_n + BSE and the experimental values as the

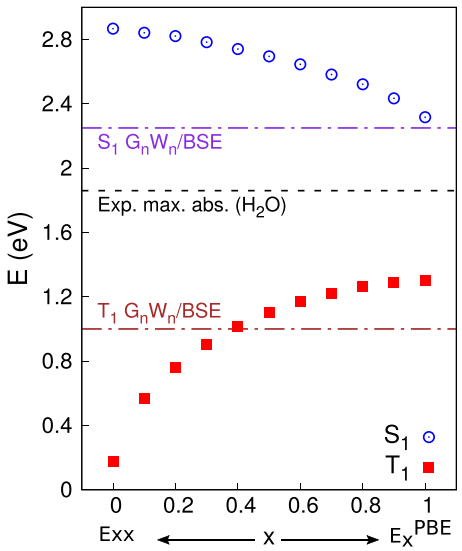

FIG. 1. S_0–S_1 and S_0–T_1 transition energies for MB-31(0) as a function of PBE exchange and exact Fock exchange admixture in the TDDFT approximation [E_x = $xPBE_x$ + (1-x)EXX] and in comparison to G_nW_n + BSE calculations and the experimental maximum absorption of MB in water.

GGA portion increases, going from 2.87 eV when E_x = EXX to 2.32 eV when E_x = PBE$_x$. Simultaneously, S_0–T_1 increases from the unrealistic value of ≈0.1 eV when E_x = EXX to the reasonable value of ≈1.2 eV when E_x = PBE$_x$. Yet, either TDDFT or GW + BSE estimates for the S_0–T_1 transition are considerably underestimated, in comparison with reference data (1.75 eV using CASPT2),[74] due to triplet instabilities.[75–78]

The superior performance of pure GGAs over HF indicates that charge transfer is not a dominant feature and that the transition could be of double excitation character (when error cancellations occur for GGAs).[23] However, the overestimation of the optical gap resembles the case of the cyanine dyes,[18,33,34] when the dynamical correlation is important, as well as the fact that the pure GGAs outperform their associated hybrids.[33] We could calibrate the global hybrid functional with high portions of GGA and proceed further to study the influence of the solvent in the optical gap of MB. However, besides the lack of generality of such procedure, from previous studies, we learn that the optimally tuned RSH can describe well intermolecular interactions[59,79] and dielectric screening,[55] differently from global hybrids.[59] Furthermore, short-contact intermolecular interactions with solvent molecules could lead to an increase in the charge-transfer character of the first excited state, another feature that is well described by RSH functionals in contrast to hybrid functionals,[79] especially if constructed with large portions of GGA.

Figure 2 shows the electron–hole pair of the natural transition orbitals (NTOs) of MB-31(0) for the S_0–S_1 transition from TDDFT/ωPBE calculations. The transition is almost entirely represented by a HOMO–LUMO transition (> 90%) and described by the electron migration from the whole molecule to the central sulfur and nitrogen atoms, an apparent valence excitation with little intramolecular charge transfer character. The TDDFT/ωPBE calculations estimate the S_0–S_1 and S_0–T_1 transitions at 2.54 eV and 1.22 eV, respectively. These transitions are off by ≈0.3 eV in comparison with G_nW_n + BSE, slightly worse than the pure PBE and desired accuracy (within ≈0.1 eV).

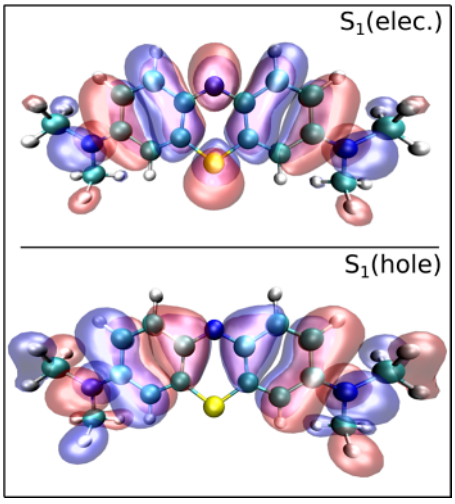

FIG. 2. NTO isosurface densities of the most significant electron–hole pair (⩾ 90%) of S_1 for MB-31(0). Carbon atoms are represented in green, nitrogen in blue, sulfur in yellow, and hydrogen in white.

We anticipate that the inferior performance of the OT-RSH with respect to the GGA will be attenuated or removed when inserting solvent effects. The optimal ω for the solvated structures tends to be smaller since the frontier orbitals tend to be more delocalized.[43] Thus, the distance where the fraction of EXX is larger than the PBE exchange increases, such that a larger contribution to the energy of MB comes from the GGA exchange potential.[43] For instance, according to the optimal ω values, the GGA/EXX interchange distance for the isolated molecule is at 1.3 Å and for the fully solvated system at 1.7 Å [taken from erf($\omega_{opt} r_0$) = 1/2, see ω optimization below]. Furthermore, the OT-RSH is indicated for explicitly solvated systems because GGAs tend to overestimate electron density delocalization while EXX tends to underestimate it, such that the OT-RSH temper these limits showing small delocalization errors.[33]

C. Excited states from TDDFT/ωPBE and the contributions from intermolecular interactions and dielectric screening

Table I lists the TDDFT/ωPBE transition energies of the first excited states with respective oscillator strengths for singlets of all configurations (note that triplet transitions are forbidden in our calculations due to the lack of spin–orbit coupling). Figure 3 illustrates the transitions in comparison with the experimental data. The excited states with strong oscillator strength (~0.5) are always localized in MB, topologically similar to the transition of the isolated molecule, as noted by their electron–hole pair from the NTOs [see representative NTOs in Fig. 4-left for MB-31(101)]. The singlet transitions with low oscillator strength are of a mixed charge transfer character, described by the electron donation from a water molecule nearby the sulfur atom of MB [represented in Fig. 4-right for MB-31(101)]. For most of the configurations, this excitation is about 0.1 eV–0.4 eV distant from the excitation localized in MB, and its oscillator strength is limited to 10^{-2}. Interestingly, for the configuration MB-31(23), this excitation is the lowest one and shows increased oscillator strength, 0.07, and it is much closer, in energy, to the one located in MB (ΔE = 0.036 eV). This indicates that there might be a coupling between S_1 and S_2, such that S_1 increases in oscillator strength, pulling the absorption band to lower energies (similar to the coupling reported in Ref. 80). Note that by taking into consideration the structures generated with a solvent cutoff of 3.2 Å with 20–21 solvent molecules, the dispersion in the optical gap is about 0.3 eV, which is related to small molecular distortions and distinct solvent configurations (similarly to the configurational variances when collecting the experimental data, but here limited to a small number of sampling configurations).

After looking at the optical gap dispersion of MB due to distinct molecular arrangements and a variation of intermolecular interactions, we look at MB-31 as a representative configuration to investigate the influence of intermolecular interaction and dielectric screening in the first excited states. Thus, structures with various distance cutoffs with respect to solvent molecules were generated and the optimization parameter was calculated as a function of the

TABLE I. First excited states and oscillator strengths (O.S.) for MB structures as calculated by the TDDFT/ωPBE method. Note that ω_{EA} is used for all calculations except for MB-31(101), in which ω^{ext}_{solv} was used instead, which is the optimal ω extrapolated to a completely solvated system.

Molecule	ω_{opt} ($\times 10^{-3}$ a_0^{-1})	S_1 (eV)	O.S.$_{S_1}$	S_2 (eV)	O.S.$_{S_2}$	T_1 (eV)	T_2 (eV)
MB-01(20)	182	1.6316	0.0008	2.3508	0.4767	1.0563	1.6293
MB-13(20)	182	2.3099	0.7991	2.4412	0.0181	0.9131	1.6807
MB-19(13)	191	2.3813	0.8285	2.5467	0.0014	0.9977	1.8134
MB-27(20)	182	2.5791	0.8002	2.6941	0.0056	1.2580	1.9027
MB-38(26)	179	2.2398	0.6958	2.3912	0.0009	0.8197	1.6489
MB-46(21)	179	1.9670	0.0055	2.3705	0.7052	1.0959	1.6642
MB-31(0)	203	2.5432	0.8694	2.7871	0.0063	1.2233	1.9838
MB-31(23)	179	2.1800	0.0701	2.2160	0.6484	0.7460	1.7490
MB-31(101)	150	2.1527	0.7135	2.3240	0.0079	0.8199	1.6509

number of solvent molecules. The optimization parameter could be represented by a mono-exponential decay as the number of solvent molecules (n) increases, described as $\omega(n) = \omega_0 \exp(-n/\delta) + \omega^{ext}_{solv}$, where ω_0 is the optimal ω of the bare structure, δ is a system dependent fitting parameter, and ω^{ext}_{solv} is the optimal ω when extrapolating the optimization to the fully solvated structure ("bulk" water).[55] Interestingly, the exponential decay of the parameter ω as a function of the solvation shell number is not only observed for weakly intermolecular interacting systems, as demonstrated in Ref. 55 but also for a system of polar molecules prone to intermolecular interaction.

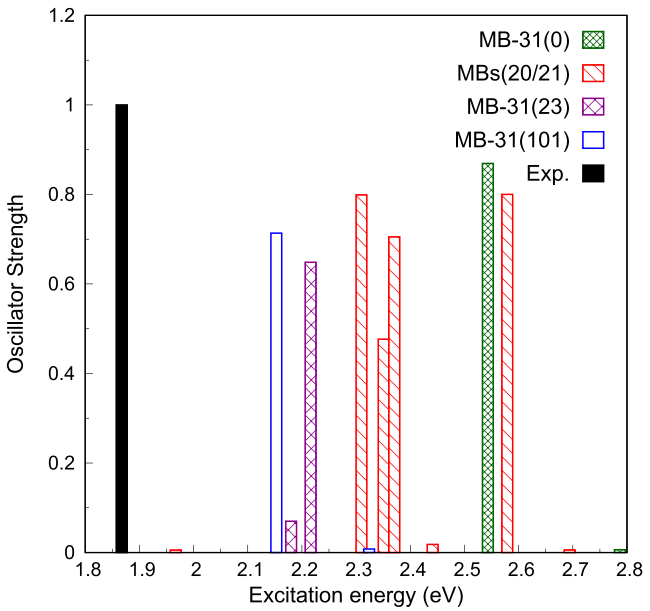

FIG. 3. Excited state spectra for MB-31(0), in green; MB-01(20), MB-13(20), MB-27(20), and MB-46(21), in red; MB-31(23), in magenta; and MB-31(101), in blue, as calculated by the TDDFT/ωPBE method, and experimental data, in black.

Using ω^{ext}_{solv} in TDDFT/ωPBE calculations, one can account for the long-range dielectric screening of the media in the description of the excited states.[55,81] Figure 5 shows a good agreement between the approximate curve and the ΔSCF-calculated $\omega(n)$, which resulted in an ω^{ext}_{solv} value of 0.150 a_0^{-1}.

The comparison between the optical gap of MB as calculated from the G_nW_n + BSE and TDDFT/ωPBE methodologies is illustrated in Fig. 6. The S_0–S_1 transition of MB-31(23) from the G_nW_n + BSE calculation is at 2.05 eV, indicating a decrease in 0.2 eV due to intermolecular interactions and local screening. TDDFT/ωPBE predicts the S_0–S_1 transition of MB-31(23) at 0.36 eV below the transition for the isolated molecule. The OT-RSH is more influenced by the explicit solvation because the range separating parameter decays rapidly by including the first coordination shell, and the lowering of the parameter emulates long-range dielectric screening.[55] For instance, ω decays from 0.203 to 0.179 a_0^1 by including the first coordination shell (88% of ω_0), reaching 0.150 a_0^1 when the parameter is extrapolated to fully solvated structure (74% of ω_0).

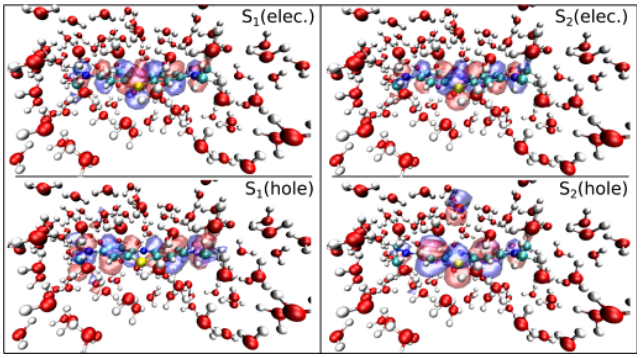

FIG. 4. NTO isosurface densities of the most significant electron–hole pair (≥90%) of the S_1 and S_2 transitions for MB-31(101) as calculated by the TDDFT/ωPBE method. Carbon atoms are represented in green, nitrogen in blue, sulfur in yellow, oxygen in red, and hydrogen in white.

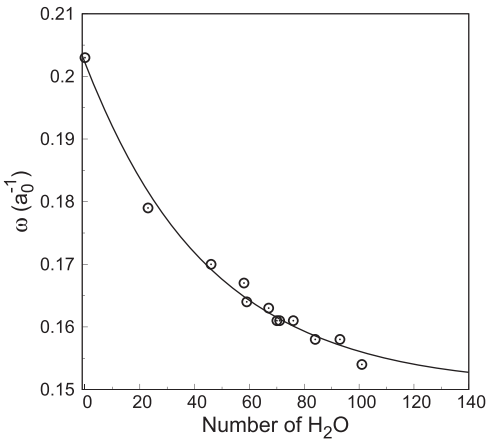

FIG. 5. Optimal ω as a function of the number of water solvent molecules surrounding MB-31 and exponential decay fits.

Moving to the fully solvated structure, one notes an additional shift to the lower energy of about 0.03 eV, with all results indicating a modest contribution from long-range dielectric screening in the first excited singlet state. This is expected since MB is considered a dye with a small solvatochromic shift.[5,82] Note that the calculation of MB-31(101) results in a S_0–S_1 with a deviation of 0.28 eV to higher energies in comparison to experimental data. Vibronic and zero point corrections shift this value further down, as described in Sec. III D.

The performance of TDDFT for cyanine dyes has been previously analyzed as follows:[33] An electronic transition with a strong HOMO–LUMO character in the adiabatic approximation is approximately given by the HOMO–LUMO gap (ε_L–ε_H), added by the Coulomb electron–electron repulsion term and xc kernel integrals.[33] For instance, for the two-level model HOMO–LUMO transition in the Tamm–Dancoff approximation,[33]

$$E_{S1}^{TDDFT} = (\varepsilon_L - \varepsilon_H) + 2[LH|r_{12}^{-1}|LH] + [LH|f_{xc}^{\alpha\alpha} + f_{xc}^{\alpha\beta}|LH], \quad (1)$$

where the second term on the right-hand side of the equation is a two-electron repulsion integral and the third term is the xc linear response kernel (f_{xc}) integral (L and H refer to the HOMO and LUMO Kohn–Sham orbitals, respectively, and α and β are spin labels). The HOMO–LUMO gap is the dominant positive term, the electron–electron Coulomb repulsion term is typically small but positive, and the xc kernel integrals are generally negative.

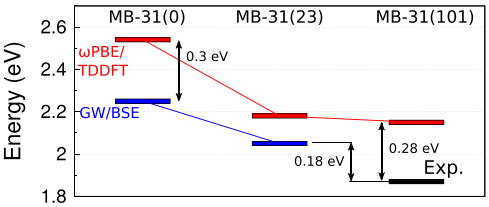

FIG. 6. Diagram of the first excited state for MB-31(0) and MB-31(23) as calculated from the G_nW_n + BSE and TDDFT/ωPBE methods, in addition to the TDDFT/ωPBE calculation for MB-31(101), and experimental data.

The HOMO–LUMO gap for MB-31(0) as calculated from DFT/ωPBE is 4.5 eV (similar to the other configurations). Thus, the last term of the above equation, the xc kernel integrals, should be sufficiently large (and negative) in order to lower the optical gap in the direction of the reference data (E_{S1}^{GW+BSE} = 2.25 eV). The fact that the TDDFT/ωPBE results are generally overestimating those of the G_nW_n + BSE is similar to what has been observed for cyanine dyes, and has been attributed to too small contributions of the xc response kernel integrals.[33,34]

D. Vibronic contributions

Another question regarding the absorption spectrum of MB is related to the shape of the envelope, in particular the cause of the line broadening and the shoulder between 625 nm and 606 nm (1.98 eV and 2.04 eV, or 16 000 cm^{-1} and 16 500 cm^{-1}, respectively) (Fig. 7). Within the generating function method,[83,84] the 0–0 transition occurs at

$$\Delta E_{0-0} = \Delta E_{adia} - E_{ZPV}^{0} + E_{ZPV}^{1}, \quad (2)$$

where ΔE_{adia} is the adiabatic excitation energy, and the last two terms are the zero-point vibrational energy (ZPV) in the ground

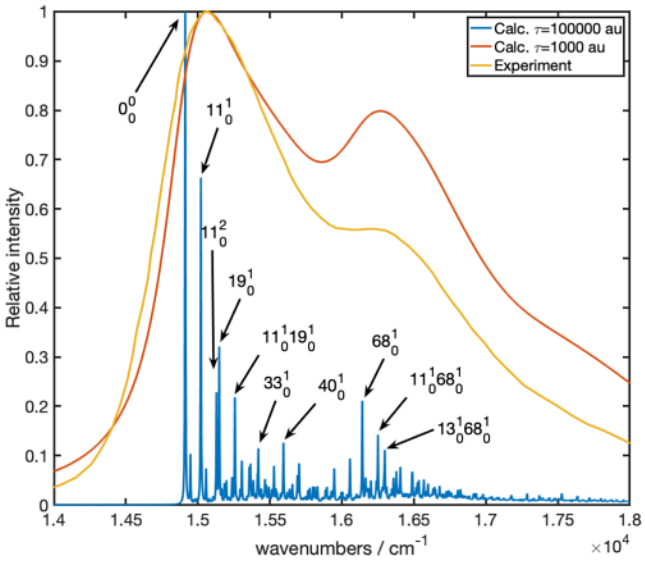

FIG. 7. Comparison between the calculated vibronic absorption spectrum in the gas phase and the experimentally measured spectrum in water.[73] Computed spectra have been downshifted by 0.5 eV (4046 cm^{-1}) to align the main band of the broad spectrum with the experimental λ_{max} value. 0_0^0 denotes the 0–0 transition. In the other peak assignments, the mode number according to Table S2 (supplementary material) is given with subscripts indicating its ground state vibrational quantum number and superscripts indicating its excited state vibrational quantum number of the transition; all other modes have both zero as initial and final quantum numbers.

and excited states, respectively. The 0–0 transition (denoted 0_0^0 in Fig. 7) serves as the reference point for the vibronic structure. Since the excited state ZPV energy (8.458 eV) is smaller than the ground state ZVP (8.532 eV), the 0–0 transition (2.351 eV) lies 0.16 eV below the TDDFT/B3LYP/def2-SVP adiabatic excitation energy of 2.424 eV. When applying a line broadening with a lifetime of 1000 au (red in Fig. 7), the peak maximum is shifted 0.019 eV to the blue, relative to the 0–0 transition using a lifetime of 100 000 au (blue in Fig. 7). In general, line broadening could be caused by conformational isomers[85,86] or by vibronic bands.[83] Our vibronic spectra calculations, including Duschinsky effects, show that both line broadening and the dominant shoulder are due to the vibronic effects. Furthermore, the line broadening is mainly caused by three vibrational modes, mode 11, mode 19, and mode 40, shown in Fig. 8 (Multimedia view)—(Table S2 lists all vibrational transitions in the supplementary material). By assigning modes 11 and 19 as the main causes for the broadening, our calculations are partially consistent with previous calculations of Franck–Condon factors by Dean and co-workers based on the displaced harmonic oscillator model; however, mode 40 was not identified by their work.[73] In addition, several peaks with minor intensity (<0.1 in Fig. 7) contribute to broadening and were not included in previous spectral simulations.[73] Regarding the dominant shoulder above 625 nm (16 000 cm^{-1}), our calculations show that it is mainly due to mode 68 and its combinations with modes 11 and 13 (Fig. 7).

We also computed the vibronic spectrum using the ωPBE xc-functional [6-31G(d,p) basis set and $\omega = 0.203 a_0^{-1}$] but within the displaced harmonic oscillator approximation because we could not determine the full Duschinsky matrix from the output. However, since the Duschinsky matrix for MB is close to unity, the approximation made is small. The ωPBE vibronic spectrum compares well to the TD-B3LYP spectrum (see the supplementary material).

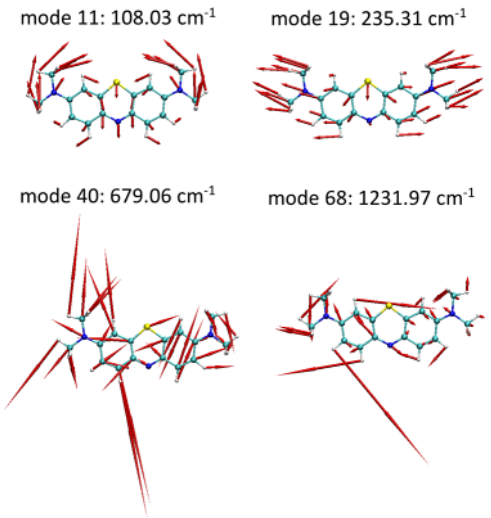

FIG. 8. Dominant excited state vibrational normal modes and their frequencies calculated by TDDFT/B3LYP/def2-SVP. Multimedia views: https://doi.org/10.1063/5.0029727.1; https://doi.org/10.1063/5.0029727.2; https://doi.org/10.1063/5.0029727.3; https://doi.org/10.1063/5.0029727.4

As expected, the vibrational features are relatively insensitive to the xc-functional approximation. In addition, we computed the TD-B3LYP/TDA vibronic spectrum. Vibrational frequencies in the excited state are very similar in TD-B3LYP and TD-B3LYP/TDA, but some peak intensities are different in the two spectra due to differences in the Duschinsky matrix (see the supplementary material). This shows that the TDA affects the computation of the vibrational modes in the excited state.

IV. CONCLUSIONS

We present a strategy to predict the optical gap of MB in water using an optimally tuned range-separated hybrid functional for fully solvated structures within TDDFT. The addition of a realistic solvent environment, dielectric screening effects, and vibronic corrections are essential for bringing the results close to experiments. Solvation effects, which we take into account explicitly, are responsible for lowering the optical gap by about 0.2 eV–0.4 eV, resulting in an overestimation of the experimental data by 0.2 eV–0.3 eV depending on the structure used. Vibronic effects and zero-point corrections shift the adiabatic value down in energy by 0.16 eV, as estimated by TDDFT/B3LYP calculations. The overestimation then decreases to only ~0.15 eV with respect to experimental data. Vibronic calculations also show that in-plane mode 68, with a large component in ring CH bending, and mode 11 are responsible for the vibronic subband that is very characteristic of MB's UV spectra in solution.

The optical gap difference between G_nW_n + BSE and TDDFT/ωPBE is reduced from 0.3 eV to 0.1 eV by going from the isolated MB to the solvated structure. The improvement in the performance of TDDFT/ωPBE for the solvated structure occurs because the semilocal term of the functional takes over at larger distances, and dielectric screening is emulated by choosing the range separation parameter appropriately.[55] Since semilocal functionals are reported to treat better π-conjugated systems (although due to error cancellations),[20,23,33] we expect that such a strategy might be generalized, permitting to study these important systems at relatively low computational cost and with acceptable accuracy. The combination of the methodologies employed in this study is going to be relevant for the description of the absorption spectra of π-conjugated systems, especially in solution or in other chemical environments.

SUPPLEMENTARY MATERIAL

See the supplementary material for details about molecular configurations, vibronic spectra calculations and illustrative movies of the relevant vibrational modes, optimal tuning of the RSH functional and TDDFT calculations, GW + BSE calculations: starting point dependence and basis set convergence, and tables with data obtained in the optimal tuning of the RSH functional and GW + BSE calculations, and the vibronic modes.

ACKNOWLEDGMENTS

T.B.d.Q. acknowledges the support of CNPq (Universal Grant No. 404951/2016-3). Z.H. and L.L. acknowledge the support of the

Bavarian State Ministry of Science and the Arts through the Collaborative Research Network Solar Technologies go Hybrid (SolTech), the Elite Network Bavaria (ENB), and computational resources provided by the Bavarian Polymer Institute (BPI). M.D.C.-N. acknowledges the support of FAPESP (Grant No. 12/50680-5). This study was financed, in part, by the Coordenação de Aperfeiçoamento de Pessoal de Nível Superior–Brasil (CAPES), Finance Code 001. The authors are thankful to the University of Bayreuth-Theoretical Physics IV for computational time and Professor Stephan Kümmel for valuable discussions.

DATA AVAILABILITY

The data that support the findings of this study are available from the corresponding author upon reasonable request.

REFERENCES

[1] A. Ormond and H. Freeman, Materials **6**, 817 (2013).
[2] J. C. Dean, D. G. Oblinsky, S. Rafiq, and G. D. Scholes, J. Phys. Chem. B **120**, 440 (2016).
[3] M. Wainwright, J. Braz. Chem. Soc. **26**, 2390 (2015).
[4] Z.-S. Huang, H. Meier, and D. Cao, J. Mater. Chem. C **4**, 2404 (2016).
[5] C. Párkányi, C. Boniface, J. J. Aaron, and M. Maafi, Spectrochim. Acta A **49**, 1715 (1993).
[6] P. Hohenberg and W. Kohn, Phys. Rev. **136**, B864 (1964).
[7] W. Kohn and L. J. Sham, Phys. Rev. **140**, A1133 (1965).
[8] E. Runge and E. K. U. Gross, Phys. Rev. Lett. **52**, 997 (1984).
[9] D. Rappoport and F. Furche, J. Am. Chem. Soc. **126**, 1277 (2004).
[10] K. Burke, J. Werschnik, and E. K. U. Gross, J. Chem. Phys. **123**, 062206 (2005).
[11] J. Schirmer and A. Dreuw, Phys. Rev. A **75**, 022513 (2007).
[12] N. T. Maitra, R. van Leeuwen, and K. Burke, Phys. Rev. A **78**, 056501 (2008).
[13] J. Schirmer and A. Dreuw, Phys. Rev. A **78**, 056502 (2008).
[14] J. P. Perdew, K. Burke, and M. Ernzerhof, Phys. Rev. Lett. **77**, 3865 (1996).
[15] C. Adamo and V. Barone, J. Chem. Phys. **110**, 6158 (1999).
[16] J. P. Perdew, M. Ernzerhof, and K. Burke, J. Chem. Phys. **105**, 9982 (1996).
[17] D. Jacquemin, E. A. Perpète, G. E. Scuseria, I. Ciofini, and C. Adamo, J. Chem. Theory Comput. **4**, 123 (2008).
[18] M. Schreiber, V. Buß, and M. P. Fülscher, Phys. Chem. Chem. Phys. **3**, 3906 (2001).
[19] J. Fabian, Theor. Chem. Acc. **106**, 199 (2001).
[20] C.-P. Hsu, S. Hirata, and M. Head-Gordon, J. Phys. Chem. A **105**, 451 (2001).
[21] S. Grimme and M. Parac, ChemPhysChem **4**, 292 (2003).
[22] M. Parac and S. Grimme, Chem. Phys. **292**, 11 (2003).
[23] J. H. Starcke, M. Wormit, J. Schirmer, and A. Dreuw, Chem. Phys. **329**, 39 (2006).
[24] J. Fabian, Dyes Pigm. **84**, 36 (2010).
[25] S. Di Tommaso, D. Bousquet, D. Moulin, F. Baltenneck, P. Riva, H. David, A. Fadli, J. Gomar, I. Ciofini, and C. Adamo, J. Comput. Chem. **38**, 998 (2017).
[26] B. Calitree, D. J. Donnelly, J. J. Holt, M. K. Gannon, C. L. Nygren, D. K. Sukumaran, J. Autschbach, and M. R. Detty, Organometallics **26**, 6248 (2007).
[27] T. Lazarides, T. M. McCormick, K. C. Wilson, S. Lee, D. W. McCamant, and R. Eisenberg, J. Am. Chem. Soc. **133**, 350 (2011).
[28] S. Grimme and F. Neese, J. Chem. Phys. **127**, 154116 (2007).
[29] A. E. Masunov, Int. J. Quantum Chem. **110**, 3095 (2010).
[30] C. M. Marian and N. Gilka, J. Chem. Theory Comput. **4**, 1501 (2008).
[31] B. Champagne, M. Guillaume, and F. Zutterman, Chem. Phys. Lett. **425**, 105 (2006).
[32] B. Le Guennic and D. Jacquemin, Acc. Chem. Res. **48**, 530 (2015).
[33] B. Moore and J. Autschbach, J. Chem. Theory Comput. **9**, 4991 (2013).
[34] H. Zhekova, M. Krykunov, J. Autschbach, and T. Ziegler, J. Chem. Theory Comput. **10**, 3299 (2014).
[35] M. Petersilka, U. J. Gossmann, and E. K. U. Gross, Phys. Rev. Lett. **76**, 1212 (1996).
[36] M. E. Casida, "Time-dependent density functional response theory for molecules," in *Recent Advances in Density Functional Methods*, edited by P. Chong (World Scientific, Singapore, 1995), pp. 155–192.
[37] S. R. Yost and T. Van Voorhis, J. Phys. Chem. C **117**, 5617 (2013).
[38] A. R. Kshirsagar, G. D'Avino, X. Blase, J. Li, and R. Poloni, J. Chem. Theory Comput. **16**, 2021 (2020).
[39] O. V. Ovchinnikov, A. V. Evtukhova, T. S. Kondratenko, M. S. Smirnov, V. Y. Khokhlov, and O. V. Erina, Vib. Spectrosc. **86**, 181 (2016).
[40] A. J. Cohen, P. Mori-Sánchez, and W. Yang, Science **321**, 792 (2008).
[41] J. J. Eriksen, S. P. A. Sauer, K. V. Mikkelsen, O. Christiansen, H. J. A. Jensen, and J. Kongsted, Mol. Phys. **111**, 1235 (2013).
[42] A. Eilmes, Theor. Chem. Acc. **133**, 1538 (2014).
[43] T. B. de Queiroz and S. Kümmel, J. Chem. Phys. **141**, 084303 (2014).
[44] D. J. Tozer, J. Chem. Phys. **119**, 12697 (2003).
[45] A. Dreuw and M. Head-Gordon, J. Am. Chem. Soc. **126**, 4007 (2004).
[46] T. Stein, L. Kronik, and R. Baer, J. Am. Chem. Soc. **131**, 2818 (2009).
[47] T. Yanai, D. P. Tew, and N. C. Handy, Chem. Phys. Lett. **393**, 51 (2004).
[48] Y. Tawada, T. Tsuneda, S. Yanagisawa, T. Yanai, and K. Hirao, J. Chem. Phys. **120**, 8425 (2004).
[49] T. M. Henderson, B. G. Janesko, and G. E. Scuseria, J. Chem. Phys. **128**, 194105 (2008).
[50] S. Kümmel, Adv. Energy Mater. **7**, 1700440 (2017).
[51] J.-D. Chai and M. Head-Gordon, J. Chem. Phys. **128**, 084106 (2008).
[52] O. A. Vydrov and G. E. Scuseria, J. Chem. Phys. **125**, 234109 (2006).
[53] O. A. Vydrov, J. Heyd, A. V. Krukau, and G. E. Scuseria, J. Chem. Phys. **125**, 074106 (2006).
[54] R. Baer, E. Livshits, and U. Salzner, Annu. Rev. Phys. Chem. **61**, 85 (2010).
[55] T. B. de Queiroz and S. Kümmel, J. Chem. Phys. **143**, 034101 (2015).
[56] S. Refaely-Abramson, R. Baer, and L. Kronik, Phys. Rev. B **84**, 075144 (2011).
[57] A. Karolewski, T. Stein, R. Baer, and S. Kümmel, J. Chem. Phys. **134**, 151101 (2011).
[58] V. Ziaei and T. Bredow, ChemPhysChem **18**, 579 (2017).
[59] D. Raithel, S. Baderschneider, T. B. de Queiroz, R. Lohwasser, J. Köhler, M. Thelakkat, S. Kümmel, and R. Hildner, Macromolecules **49**, 9553 (2016).
[60] H. Sekino, Y. Maeda, M. Kamiya, and K. Hirao, J. Chem. Phys. **126**, 014107 (2007).
[61] P. Boulanger, D. Jacquemin, I. Duchemin, and X. Blase, J. Chem. Theory Comput. **10**, 1212 (2014).
[62] C. Azarias, I. Duchemin, X. Blase, and D. Jacquemin, J. Chem. Phys. **146**, 034301 (2017).
[63] P. Deglmann, F. Furche, and R. Ahlrichs, Chem. Phys. Lett. **362**, 511 (2002).
[64] P. Deglmann and F. Furche, J. Chem. Phys. **117**, 9535 (2002).
[65] M. L. Sánchez, M. A. Aguilar, and F. J. O. del Valle, J. Comput. Chem. **18**, 313 (1997).
[66] M. L. Sánchez, M. E. Martín, M. Aguilar, and F. Olivares del Valle, J. Comput. Chem. **21**, 705 (2000).
[67] K. Coutinho and S. Canuto, *Advances in Quantum Chemistry* (Elsevier, 1997), Vol. 28, pp. 89–105.
[68] K. Coutinho, H. C. Georg, T. L. Fonseca, V. Ludwig, and S. Canuto, Chem. Phys. Lett. **437**, 148 (2007).
[69] C. M. Breneman and K. B. Wiberg, J. Comput. Chem. **11**, 361 (1990).
[70] V. Ludwig, K. Coutinho, and S. Canuto, Phys. Chem. Chem. Phys. **9**, 4907 (2007).

[71] R. C. Barreto, K. Coutinho, H. C. Georg, and S. Canuto, Phys. Chem. Chem. Phys. **11**, 1388 (2009).
[72] V. Manzoni, M. L. Lyra, R. M. Gester, K. Coutinho, and S. Canuto, Phys. Chem. Chem. Phys. **12**, 14023 (2010).
[73] J. C. Dean, S. Rafiq, D. G. Oblinsky, E. Cassette, C. C. Jumper, and G. D. Scholes, J. Phys. Chem. A **119**, 9098 (2015).
[74] J. J. Nogueira, M. Oppel, and L. González, Angew. Chem., Int. Ed. **54**, 4375 (2015).
[75] D. Jacquemin, I. Duchemin, A. Blondel, and X. Blase, J. Chem. Theory Comput. **13**, 767 (2017).
[76] X. Gui, C. Holzer, and W. Klopper, J. Chem. Theory Comput. **14**, 2127 (2018).
[77] D. Jacquemin, I. Duchemin, and X. Blase, J. Phys. Chem. Lett. **8**, 1524 (2017).
[78] T. Rangel, S. M. Hamed, F. Bruneval, and J. B. Neaton, J. Chem. Phys. **146**, 194108 (2017).
[79] D. Niedzialek, I. Duchemin, T. B. de Queiroz, S. Osella, A. Rao, R. Friend, X. Blase, S. Kümmel, and D. Beljonne, Adv. Funct. Mater. **25**, 1972 (2015).
[80] I. Schelter, J. M. Foerster, A. T. Gardiner, A. W. Roszak, R. J. Cogdell, G. M. Ullmann, T. B. de Queiroz, and S. Kümmel, J. Chem. Phys. **151**, 134114 (2019).
[81] L. Kronik and S. Kümmel, Adv. Mater. **30**, 1706560 (2018).
[82] A. G. Gilani, M. Salmanpour, and T. Ghorbanpour, J. Mol. Liq. **179**, 118 (2013).
[83] E. Tapavicza, F. Furche, and D. Sundholm, J. Chem. Theory Comput. **12**, 5058 (2016).
[84] E. Tapavicza, J. Phys. Chem. Lett. **10**, 6003 (2019).
[85] C. Cisneros, T. Thompson, N. Baluyot, A. C. Smith, and E. Tapavicza, Phys. Chem. Chem. Phys. **19**, 5763 (2017).
[86] E. Tapavicza, T. Thompson, K. Redd, and D. Kim, Phys. Chem. Chem. Phys. **20**, 24807 (2018).

First principles theoretical spectroscopy of Methylene Blue: Between limitations of time-dependent density functional theory approximations and its realistic description in the solvent - Supplementary Material.

Thiago B. de Queiroz,* Erick R. de Figueroa, and Maurício D. Coutinho-Neto†
Centro de Ciências Naturais e Humanas, Universidade Federal do ABC, Av. dos Estados 5001, 09510-580, Santo André-SP, Brazil

Cleiton D. Maciel
Instituto Federal de Educação, Ciência e Tecnologia de São Paulo, Campus Itaquaquecetuba, Avenida Primeiro de Maio, 500, 08571-050, Itaquaquecetuba-SP, Brazil

Enrico Tapavicza
Department of Chemistry and Biochemistry, California State University, Long Beach, 1250 Bellflower Boulevard, Long Beach, California 90840, United States

Zohreh Hashemi
Institute of Physics, University of Bayreuth, Bayreuth 95440, Germany

Linn Leppert‡
MESA+ Institute for Nanotechnology, University of Twente, 7500 AE Enschede, The Netherlands and Institute of Physics, University of Bayreuth, Bayreuth 95440, Germany

* thiago.branquinho@ufabc.edu.br
† mauricio.neto@ufabc.edu.br
‡ l.leppert@utwente.nl

S1. Methods

A. Molecular configurations

We have used molecular dynamics simulations in the isothermical-isobaric (NPT) ensemble with T = 298 K and P = 1 atm to generate solvent configurations. In order to enhance solvent sampling and reduce the number of QM calculations, we used multiple solvent geometries at each sequential QM/MM step. In our procedure, solvent molecules of the system are represented by point charges superposed around the solute scaled by 1/n with respect to their original values. We have used in our procedure n=8, that is, eight superposed solvent configurations collected every 200 ps at each QM iteration. Because the solvent configurations are statistically uncorrelated, a relatively small number of iterations is sufficient to give convergent results for the atomic charges, dipole and solvent distribution.

The simulated system consisted of a cubic cell containing MB plus an anion chloride (Cl-) immersed in 4000 water molecules. The water molecule was represented by simple point charge (SPC) potential.[1] Parameters for MB are taken from the Gromos 53a6 force field.[2] All MD calculations were performed using GROMACS package version 4.5.[3, 4] using velocity rescaling[5] and Parrinello-Rahman schemes[6] for keeping temperature and pressure constant. Long range electrostatic was treated using Particle Mesh Ewald.[7]

At each iterative step, the system was allowed to equilibrate for 5 ns before the collection of solvent configurations. All QM calculations for determining CHELPG charges were performed using the Orca code version 3.0.3[8] the B3LYP functional and def2-TZVP basis set.[9] The solvent configurations (MD frames) used for computing the spectra were generated in a final simulation after obtaining converged solute (MB) dipole and charges. After a 10 ns equilibration, individual MD frames were collected every 500 ps for a total of 50 frames. From this sampling, we sorted 7 MD frames for the spectroscopic studies.

B. Vibronic Spectra Calculations

All vibronic spectra calculations were carried out with TURBOMOLE V7.3.[10] Ground and excited states equilibrium structures were optimized using the B3LYP functional and the def2-SVP basis set, within the Tamm-Dancoff approximation (TDA) and full linear response (discussed in the manuscript). The ground and excited state vibrational spectra were computed using analytical and numerical second derivatives, respectively, as implemented in the aoforce and Numforce modules.[11, 12] Based on the ground and excited state structures and their vibrational spectra (Adiabatic Hessian model), the vibronic absorption spectrum was computed within the harmonic approximation, using the full Duschinsky matrix to obtain the vibronic fine structure of the absorption spectrum using the radless module [13–15]. For vibronic spectra, the generating function was propagated for about 10000 au in time. To obtain similar line widths as in the experimental spectrum, a lifetime broadening of 1000 was applied. For the assignment of vibronic transition a lifetime of 100000 au was used to resolve the vibrational fine structure of the spectrum. Illustrative movies of the vibronic modes 11, 19, 40, and 68 are also available. We also performed these calculations with the ωPBE/6-31G(d,p) ($\omega = 0.203 a_0^{-1}$); here we employed the displaced harmonic oscillator approximation, in which the Duschinsky matrix is set to unity. This was necessary, because we could not determine the Duschinsky matrix from the Qchem output. However, since the Duschinsky matrix for MB is close to unity, the approximation made is small.

C. Optimal tuning of the RSH functional and TDDFT calculations

Ground state and excited state calculations were performed by solving the (generalized) Kohn-Sham DFT equations self-consistently and from linear-response TDDFT by solving the Casida equations,[16, 17] respectively, with the 6-31G(d,p) basis set for all atoms (the selected basis set provides transition energies within less than 0.1 eV in comparison to the complete basis set, as illustrated in Fig. S3). Some calculations were performed using the Generalized Gradient Approximation (GGA) xc functional of the energy as derived by Perdew, Burke, and Ernzerhof (PBE)[18] combined with some portion of EXX, as conceived for global hybrid functionals.[19, 20] The xc energy (and their associated functionals) is chosen as E_{xc} = xPBE$_x$ + (1-x)EXX + PBE$_c$, $0 \leq x \leq 1$ (note that for x = 1 the functional is equivalent to the PBE, for x = 0.75 is equivalent to the PBE0,[19, 20] and for x = 0 it is given by EXX + PBE$_c$).

In addition, the calculations were performed with the RSH functional ωPBE,[21] which contains PBE$_x$ at short range, EXX at long range, and PBE$_c$ at all ranges. The optimal range separation parameter (ω) was initially determined for each system following the established tuning procedure[22–24] of choosing ω such that the calculated first ionization energies ($IP(i)$) and the HOMO eigenvalues ($\epsilon^i_{\mathrm{HOMO}}$) of the cationic (i=N-1 electrons) and the neutral (i=N electrons) species agree in modulus as closely as possible (recall that MB is a cation in its most stable form with

a chloride as counter ion). The first ionization energies, i.e, ionization potential (IP) and electron affinity (EA), are calculated from the total energy differences (ΔSCF). We have demonstrated that for conventional organic systems the optimal ω values are practically equal for both constraints ($-\epsilon^{N-1}_{\rm HOMO}$ = IP or $-\epsilon^{N}_{\rm HOMO}$ = EA),[25–27] but for explicitly solvated systems there might be occasions where the frontier Kohn-Sham orbitals are located at different molecules.[28] In particular, one of these orbitals could be located in the target molecule (the solute) and the other in one of the solvent molecules.[28] In that case, the RSH functional is tuned to correctly describe the excited states of the solvent or the solute, depending on which criterion is applied ($-\epsilon^{N-1}_{\rm HOMO}$ = IP or $-\epsilon^{N}_{\rm HOMO}$ = EA). Fig. S1 shows the functions $J_2^{IP}(\omega)$ = IP(ω) + $\epsilon^{N-1}_{\rm HOMO}(\omega)$ and $J_2^{EA}(\omega)$ = EA(ω)+$\epsilon^{N}_{\rm HOMO}(\omega)$ for the structures MB-13(20), MB-46(21), MB-31(23), and MB-31(101). For MB-13(20) both functions converge similarly to equivalent optimal ω values: ω_{IP} = 0.171 a_0^{-1} and ω_{EA} = 0.181 a_0^{-1} when the difference functions are minimal. This is characteristic for an ω optimization in solvated systems when only one molecule is inspected, i.e., HOMO(N-1) and HOMO(N) are both located in one specific molecule. In this case, the orbitals are located in the target molecule of the study, MB, and not in one of the solvent molecules, as noted in Fig. S2a) (note that generally HOMO(N) can be represented by LUMO(N-1)). For MB-46(21), $J_2^{IP}(\omega)$ and $J_2^{EA}(\omega)$ behave differently, resulting in quite different optimized ω values: ω_{IP} = 0.201 a_0^{-1} and ω_{EA} = 0.179 a_0^{-1}. This inconsistent tuning is associated to Kohn-Sham frontier orbitals of completely different nature. Indeed, the HOMO(N-1) of MB-46(21) structure is located in a water molecule while LUMO(N-1) is located mostly on MB, as noted in Fig. S2b). Same statements are valid by comparing the results of the structures MB-31(23) and MB-31(101), as noted in Fig. S1c) contrasted to Fig. S2c) and Fig. S1d) contrasted to Fig. S2d). Interestingly, this fluctuation in the HOMO(N-1) localization is not only noted between structures of different MD frames, but it also depends on the solvation shell size. In order to circumvent possible tuning ambiguities we have previously employed the concept of the Absolutely Localized Molecular Orbitals (ALMO),[28–30] but this strategy is not appropriate for systems with significant solvent-solute interactions. Thus, we are taking advantage of the permanent localization of the LUMO(N-1) in MB for all structures (not shown) to use the minimization of the $J_2^{EA}(\omega)$ as the only optimization criterion. Table S1 in the Supplementary Material lists the optimal ω and quantities of comparison in the RSH functional optimization, i.e., $\epsilon^{N-1}_{\rm HOMO}$, IP(N-1), $\epsilon^{N}_{\rm HOMO}$, and IP(N) when ω=ω_{EA}.

These calculations were performed requesting singlet and triplet transitions in the Q-Chem chemistry package.[31] All isosurface densities were plotted using molden[32] and vmd[33] plotting packages, with a density factor of 0.015.

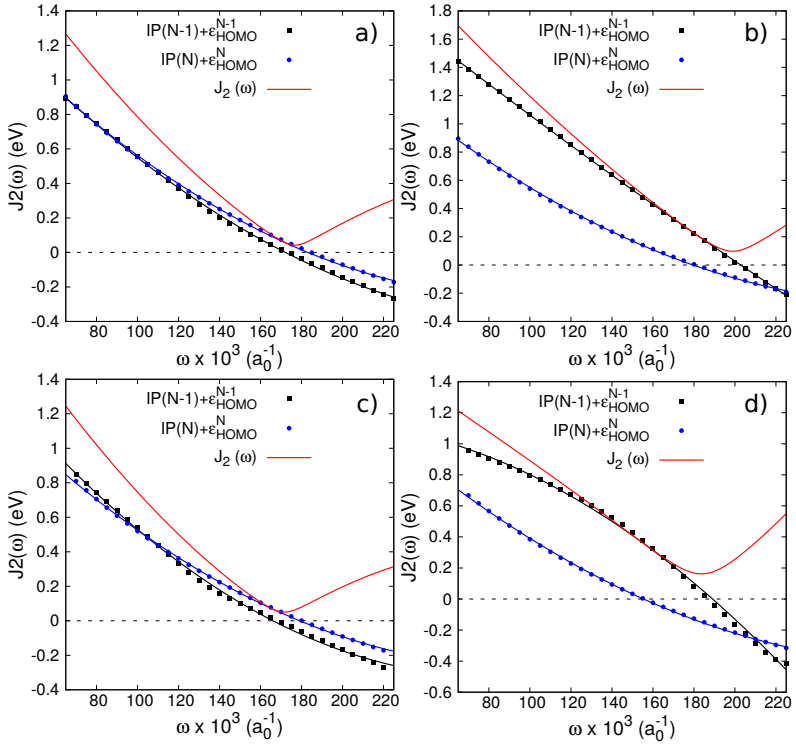

FIG. S1. Difference functions J_2^{IP} = IP + $\epsilon^{N-1}_{\rm HOMO}$, J_2^{EA} = EA + $\epsilon^{N}_{\rm HOMO}$, and global difference function ($J_2(\omega) = [J_2^{IP}(\omega)^2 + J_2^{EA}(\omega)^2]^{1/2}$) for the structures a) MB-13(20), b) MB-46(21), c) MB-31(23), and d) MB-31(101).

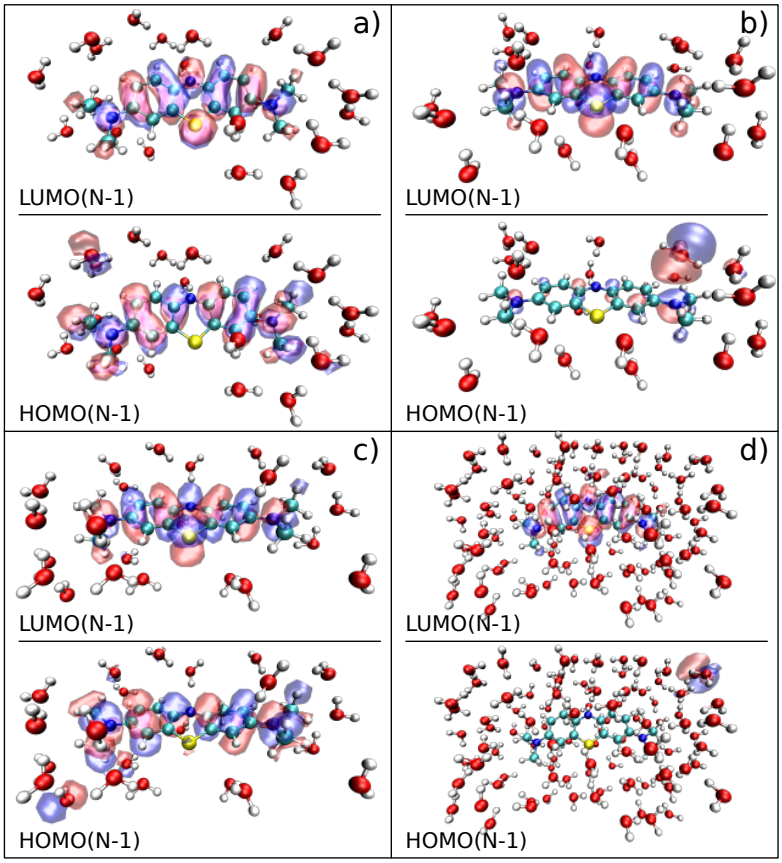

FIG. S2. Isosurface densities of the HOMO^{N-1} and LUMO^{N-1} for the structures a) MB-13(20), b) MB-46(21), c) MB-31(23), and d) MB-31(101). Only for these calculations ω tuning was obtained from the minimization of the global difference function ($J_2(\omega) = [J_2^{IP}(\omega)^2 + J_2^{EA}(\omega)^2]^{1/2}$). Carbon atoms are represented in green, nitrogen in blue, sulfur in yellow, oxygen in red, and hydrogen in white.

D. GW+BSE calculations: starting point dependence and basis set convergence

We calculated the excitation spectrum of MB using first principles Green's function-based many-body perturbation theory within the GW+BSE approach as a reference for our TDDFT calculations. We start by using a one-shot G_0W_0 approach in which the electronic self energy $\Sigma_0 = iG_0W_0$, where G_0, the zeroth-order one-particle Green's function, and W_0, the zeroth-order screened Coulomb interaction, are constructed from a generalized Kohn-Sham (gKS) eigensystem. G_0W_0 quasiparticle (QP) eigenvalues are then calculated as a perturbative correction to the xc potential used in the preceding DFT calculations using $\varepsilon_i^{\mathrm{QP}} = \varepsilon_i^{\mathrm{gKS}} + \langle\varphi_i^{\mathrm{gKS}}|\Sigma_0(\varepsilon_i^{\mathrm{QP}}) - v_{xc}|\varphi_i^{\mathrm{gKS}}\rangle$. In this approximation, it is assumed that $\varphi_i^{\mathrm{QP}} \approx \varphi_i^{\mathrm{gKS}}$. Neutral excitations are then calculated by solving the Bethe-Salpeter equation (BSE). For details on the GW and BSE approaches, the reader is referred to Ref. 34 and 35. We performed these calculations using an implementation of the GW+BSE approach in the MOLGW software package.[36] MOLGW relies on local atomic orbital basis sets and makes use of the resolution-of-the-identity approximation, which results in errors of less than 10 meV when a sufficiently large basis set is employed.[37] We further use the frozen core approximation, which changes excitation energies by less than 1 meV. The first excitation is converged to within 0.1 meV when accounting for the first ten excitations in our BSE calculations.

GW+BSE calculations are sensitive to the choice of basis set. We show the convergence of the S_0-S_1 excitation of MB-31(0) in Fig. S3, and observe a shift of more than 0.1 eV when going from the 6-311G to the 6-311++(2d,2p) basis set. Using the quadruple basis set def-QZVP changes the S_0-S_1 excitation by less than 10 meV. All further GW+BSE calculations were therefore performed with the 6-311++(2d,2p) basis set.

The G_0W_0 approach suffers from a well-documented dependence on the gKS eigensystem used to construct Σ_0.[38–40] We show that this is the case for MB in Fig. S4, where we compare the S_0-S_1 excitation of MB-31(0) using G_0W_0@LDA and G_0W_0@ωPBE. G_0W_0@LDA results in a S_0-S_1 excitation with far too low oscillator strength, that

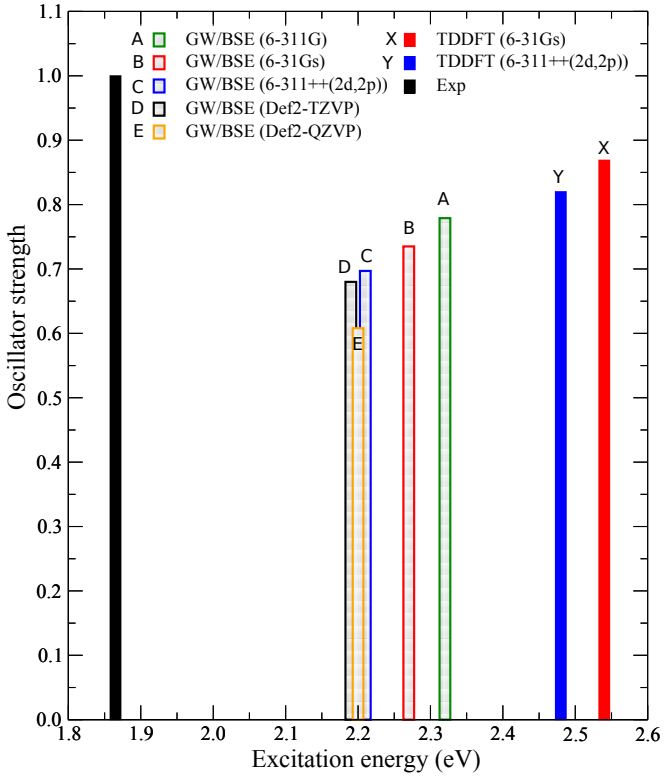

FIG. S3. G_0W_0@ωPBE+BSE calculations of the first excited state for the MB-31(0) molecule using different basis sets compared to experimental data.

underestimates the experimental value by almost 0.4 eV, whereas G_0W_0@ωPBE overestimates experiment by ∼0.3 eV. In contrast, the TDDFT results based on the LDA and ωPBE, respectively, differ by only ∼0.2 eV, although it should be noted that the TDLDA result underestimates the oscillator strength of the S_0-S_1 excitation considerably. The starting point problem of G_0W_0 has been shown to be mitigated for many systems by using the QP eigenvalues to update G and W self-consistently and re-calculate $\varepsilon_i^{\mathrm{QP}}$ until self-consistency has been reached. In the following, we call this eigenvalue self-consistent approach G_nW_n. Fig. S4 demonstrates that eigenvalue selfconsistency drastically changes the result based on the LDA, but only slightly affects the ones based on ωPBE. Using the G_nW_n approach, these excitations differ by less than 0.1 eV. In the following we use G_nW_n@ωPBE results as reference for our TDDFT calculations.

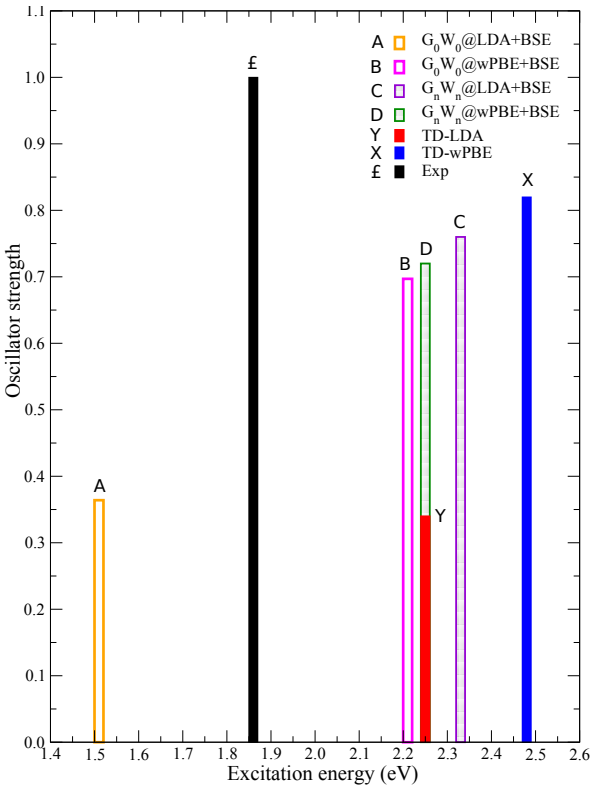

FIG. S4. First excited state of the MB-31(0) molecule using TDDFT, G_0W_0/BSE, and G_nW_n/BSE methods for two different functionals, LDA and ωPBE compare to experimental data. In all the calculations, 6-311++(2d,2p) basis set has been used based on following discussion.

S2. Tables with data obtained in the optimal tuning of the RSH functional and GW+BSE calculations, and the vibronic modes using different methods.

TABLE S1. HOMO eigenvalues, first ionization energies, and differences between these quantities for the the optimal ω for solvated MB structures. The structures are labeled according to the MD frame step and number of solvating water molecules (in brackets). Note that the difference between HOMO eigenvalues and ionization energies are written in meV. The optimal ω is chosen by enforcing only -$\epsilon^N_{\mathrm{HOMO}}$ = EA.

Molecule	ω_{opt} (x10^{-3} a_0^{-1})	$\epsilon^{N-1}_{\mathrm{HOMO}}$ (eV)	IP(N-1) (eV)	$\lvert\Delta^{N-1}_{IP+\epsilon}\rvert$ (meV)	$\epsilon^{N}_{\mathrm{HOMO}}$ (eV)	IP(N) (eV)	$\lvert\Delta^{N}_{IP+\epsilon}\rvert$ (meV)
MB-01(20)	182	-8.6980	8.9623	264	-4.2310	4.2327	2
MB-13(20)	182	-9.3015	9.2451	56	-4.5858	4.5923	6
MB-19(13)	191	-9.3524	9.3425	10	-4.5353	4.5342	1
MB-27(20)	182	-9.2676	9.4642	196	-4.7299	4.7333	3
MB-38(26)	179	-8.9219	8.8796	42	-4.3210	4.3239	3
MB-46(21)	179	-8.4908	8.7295	239	-4.0014	4.0051	4
MB-31(0)	203	-10.011	9.9721	39	-4.858	4.8592	1
MB-31(23)	179	-8.6811	8.6081	73	-4.1113	4.1128	1
MB-31(46)	170	-8.3439	8.4497	106	-4.1822	4.1782	4
MB-31(58)	167	-7.6637	8.3225	659	-4.0826	4.0807	2
MB-31(59)	164	-7.8935	8.2740	380	-4.0321	4.0343	2
MB-31(67)	163	-7.8085	8.2852	477	-4.0526	4.0451	7
MB-31(70)	161	-8.0577	8.3177	260	-4.0393	4.0431	4
MB-31(71)	161	-7.9478	8.3160	368	-4.0572	4.0590	2
MB-31(76)	161	-8.0625	8.3102	248	-4.0478	4.0456	2
MB-31(84)	158	-7.5994	8.2847	685	-4.0894	4.0939	4
MB-31(93)	158	-7.7610	8.1080	347	-3.8389	3.8346	4
MB-31(101)	154	-7.7717	8.1385	367	-3.9021	3.9074	5
			GW+BSE				
MB-31(0)	203	-9.7958	—	—	-4.6186	—	—
MB-31(23)	179	-8.7970	—	—	-4.1129	—	—

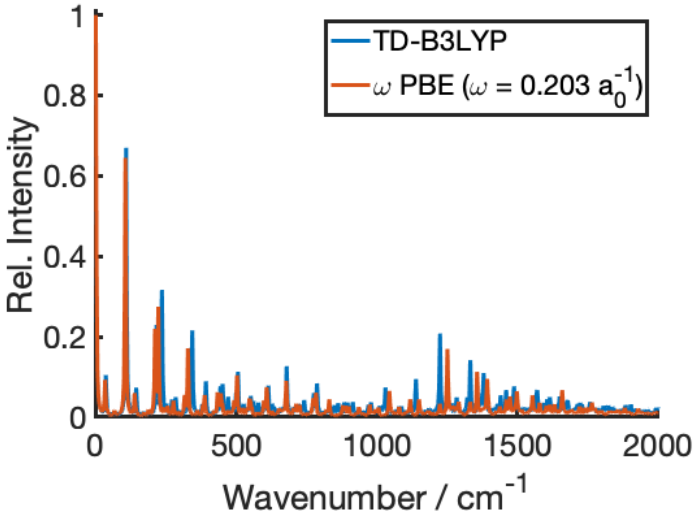

FIG. S5. Comparison between vibronic spectra computed by TD-B3LYP and ωPBE ($\omega = 0.203 a_0^{-1}$). The ωPBE spectrum was computed using the displaced harmonic oscillator approximation, since the Duschinsky matrix could not be determined. The 0-0 band was shifted to zero; intensities are given relative to the intensities of their respective 0-0 band.

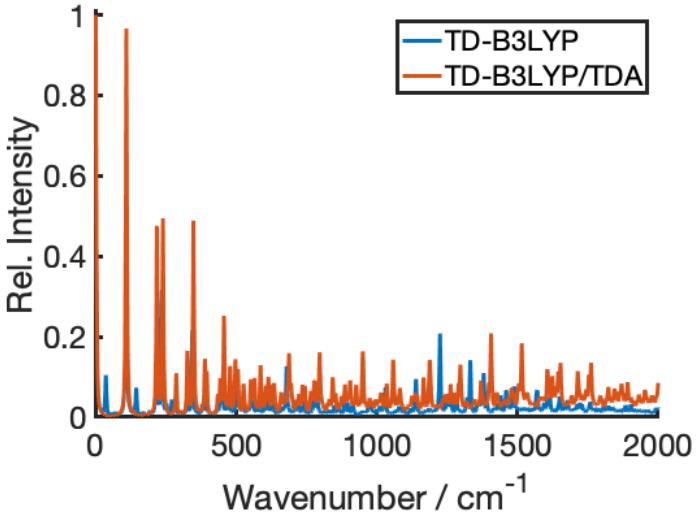

FIG. S6. Comparison between vibronic spectra computed by TD-B3LYP and TD-B3LYP/TDA. The 0-0 band was shifted to zero; intensities are given relative to the intensities of their respective 0-0 band.

Ground state						Excited state					
Mode number	waven. cm^{-1}	intensity km/mol	Mode number	waven. cm^{-1}	intensity km/mol	Mode number	waven. cm^{-1}	intensity km/mol	Mode number	waven. cm^{-1}	intensity km/mol
7	32.62	2.49444	61	1145.97	0.05276	7	35.93	2.18636	61	1139.27	251.70709
8	48.48	0.00174	62	1146.30	0.04520	8	60.37	1.33764	62	1140.61	18.76891
9	64.88	0.00115	63	1164.46	214.18245	9	69.52	1.67171	63	1144.79	0.09102
10	72.00	0.00128	64	1172.85	1.60115	10	82.95	2.77010	64	1168.29	1.27271
11	107.61	1.80565	65	1198.10	100.31962	11	108.03	2.78140	65	1170.22	27.57472
12	126.48	0.11593	66	1201.21	1.60391	12	128.67	1.80126	66	1199.30	12.89473
13	133.96	1.58656	67	1264.89	89.79430	13	151.93	0.48959	67	1224.36	35.21499
14	145.92	0.01246	68	1265.39	33.77028	14	172.85	2.14338	68	1231.97	35.59200
15	147.37	0.00687	69	1272.00	145.03768	15	177.36	5.09230	69	1254.96	35.34025
16	160.21	0.03303	70	1299.97	1.20312	16	185.77	0.51109	70	1267.41	16.61986
17	194.32	0.00931	71	1339.41	0.01409	17	192.79	2.23800	71	1284.16	24.58755
18	200.06	0.01252	72	1369.99	1208.23423	18	219.61	1.69389	72	1321.44	33.42083
19	218.84	1.11502	73	1388.32	202.87967	19	235.31	4.15622	73	1352.88	187.46696
20	243.55	0.03635	74	1398.52	8.41905	20	239.91	0.05023	74	1362.10	53.82935
21	264.51	0.00170	75	1428.65	10.02048	21	270.03	3.98374	75	1379.61	47.79040
22	284.82	0.94924	76	1440.20	202.46864	22	284.48	8.04489	76	1391.92	10.39520
23	305.72	9.12996	77	1442.64	3.40780	23	300.72	12.85729	77	1424.84	2.47289
24	359.75	0.01710	78	1451.24	863.89536	24	356.63	3.34779	78	1439.73	2.35686
25	360.74	0.48146	79	1469.05	0.09104	25	372.90	0.73856	79	1442.86	5.33164
26	395.63	11.41958	80	1469.08	0.00911	26	391.41	0.17387	80	1451.75	4.54267
27	447.47	1.61742	81	1477.06	8.70909	27	423.92	0.13914	81	1460.47	107.73978
28	448.74	4.98582	82	1480.40	146.57744	28	442.87	5.55212	82	1465.46	8.45670
29	457.73	25.45765	83	1482.53	21.28475	29	443.57	4.59288	83	1465.64	41.51534
30	475.99	0.52319	84	1482.64	37.11102	30	447.47	1.73573	84	1468.43	24.94209
31	477.26	0.00058	85	1484.99	316.82385	31	462.05	13.56093	85	1478.87	30.81844
32	496.99	0.06894	86	1486.34	4.65228	32	492.99	2.72720	86	1480.95	27.38900
33	508.10	0.04605	87	1494.97	98.88641	33	505.67	16.44133	87	1481.54	33.31572
34	530.41	2.05891	88	1508.12	3.60847	34	526.13	3.07028	88	1492.37	21.49054
35	556.31	22.16259	89	1520.64	1.35109	35	560.89	2.45015	89	1495.49	21.45472
36	608.85	2.24517	90	1524.96	8.48848	36	599.32	4.84580	90	1504.54	16.49147
37	629.47	0.00101	91	1535.11	1263.65194	37	602.05	1.34125	91	1511.81	1.87962
38	645.41	5.23614	92	1535.81	52.15088	38	623.42	4.96509	92	1520.22	23.80514
39	684.25	40.44541	93	1570.02	46.12627	39	672.68	5.51344	93	1544.66	478.64768
40	685.91	0.11705	94	1579.19	62.45484	40	679.06	5.61251	94	1570.79	153.17464
41	760.96	0.00036	95	1663.37	1138.54255	41	715.74	0.52238	95	1606.32	194.54461
42	782.19	2.06854	96	1687.96	27.31605	42	764.16	0.50359	96	1650.19	171.53217
43	790.10	0.04582	97	3010.24	15.82116	43	775.32	2.92744	97	2987.79	12.12868
44	806.40	21.72491	98	3010.38	38.21927	44	803.39	1.99044	98	2999.02	8.24824
45	848.40	15.10732	99	3018.52	128.52852	45	832.09	10.93994	99	2999.44	40.13544
46	849.32	0.95068	100	3019.16	18.85811	46	850.53	10.06292	100	3012.82	22.95651
47	872.61	3.30036	101	3081.04	8.94260	47	858.28	37.24984	101	3052.98	16.25365
48	877.57	76.48977	102	3081.31	8.90397	48	862.15	0.94813	102	3061.06	13.78649
49	879.48	0.02195	103	3089.61	10.48404	49	878.30	23.62913	103	3066.45	16.38538
50	903.47	188.43333	104	3090.16	10.69693	50	901.55	52.13532	104	3079.65	12.18481
51	974.92	3.55134	105	3151.85	0.29548	51	976.01	21.03951	105	3148.84	4.44016
52	976.05	25.71580	106	3152.61	0.28630	52	979.60	2.41438	106	3153.02	0.10226
53	1018.98	0.00086	107	3164.32	11.26620	53	1004.92	1.05524	107	3160.88	17.62976
54	1019.58	0.00002	108	3164.75	10.09953	54	1012.31	1.33702	108	3165.58	6.45796
55	1051.14	33.18246	109	3207.17	0.36917	55	1030.69	8.14196	109	3202.38	0.22325
56	1078.18	23.79465	110	3207.44	0.21888	56	1079.97	5.40183	110	3207.96	6.09447
57	1078.63	23.08644	111	3218.40	1.75007	57	1081.51	26.54792	111	3212.27	7.27758
58	1085.04	0.04023	112	3218.45	0.22316	58	1082.88	6.77970	112	3223.87	12.47266
59	1125.59	0.00152	113	3236.38	1.14525	59	1107.92	0.01935	113	3231.28	1.30047
60	1125.98	0.00091	114	3236.89	1.13779	60	1127.17	13.73492	114	3241.26	3.64280

TABLE S2. Vibrational frequencies computed by TDB3LYP/def2-SVP.

Ground state						Excited state					
Mode number	waven. cm^{-1}	intensity km/mol	Mode number	waven. cm^{-1}	intensity km/mol	Mode number	waven. cm^{-1}	intensity km/mol	Mode number	waven. cm^{-1}	intensity km/mol
7	28.65	2.57100	61	1115.33	0.04900	7	33.15	2.93800	61	1118.35	0.02700
8	47.32	0.00100	62	1115.34	0.24200	8	42.00	0.00000	62	1118.36	0.13900
9	59.40	0.09800	63	1146.96	375.98400	9	64.37	0.10000	63	1141.58	618.38500
10	60.50	0.04500	64	1156.04	1.34200	10	71.84	0.00000	64	1156.56	1.22000
11	104.01	1.74600	65	1177.20	132.86300	11	105.36	1.59500	65	1177.74	177.54300
12	109.77	0.07000	66	1181.41	0.21900	12	118.46	0.00500	66	1182.83	0.05200
13	115.67	2.82900	67	1254.66	304.53800	13	126.17	3.70400	67	1250.82	579.37800
14	132.81	0.40600	68	1259.65	20.18200	14	146.72	0.00800	68	1268.36	14.59500
15	145.56	0.00200	69	1260.71	8.76400	15	158.01	0.00000	69	1271.12	32.84200
16	159.32	0.38900	70	1278.94	2.72600	16	169.55	0.18200	70	1279.93	8.38500
17	187.96	0.00600	71	1319.43	0.12400	17	187.67	0.02000	71	1291.27	1.23800
18	192.96	0.01700	72	1348.73	2049.80400	18	201.70	0.00600	72	1332.11	3685.26200
19	215.74	1.55500	73	1374.82	8.86600	19	222.56	1.63900	73	1372.96	337.24800
20	239.52	0.05400	74	1388.05	8.35300	20	238.64	0.06600	74	1382.19	0.11400
21	250.50	0.00000	75	1416.21	283.08000	21	255.49	0.00100	75	1392.24	14.50900
22	276.10	1.09400	76	1417.52	3.48700	22	275.89	1.10300	76	1409.97	0.97700
23	283.91	10.19800	77	1420.09	3.65100	23	287.07	9.58700	77	1420.76	2.20700
24	336.62	0.00600	78	1424.35	1476.61600	24	346.47	0.01400	78	1420.85	31.64500
25	351.73	1.23800	79	1455.39	5.05300	25	350.49	3.20100	79	1451.35	220.79000
26	387.54	16.83400	80	1456.50	0.21600	26	387.16	19.64500	80	1456.14	0.13300
27	424.84	0.71700	81	1456.63	0.87100	27	439.98	1.10900	81	1456.20	0.65400
28	440.83	4.48500	82	1461.04	182.41500	28	441.74	3.95800	82	1457.08	6.86800
29	450.65	33.94000	83	1467.54	331.14100	29	449.62	37.45200	83	1457.61	188.72100
30	456.78	0.00000	84	1470.81	29.81000	30	463.56	0.00300	84	1467.35	1.75800
31	459.27	1.23200	85	1471.00	6.48200	31	470.46	0.77400	85	1470.31	8.04900
32	487.14	0.01600	86	1471.51	14.43200	32	487.02	0.00800	86	1470.36	39.38800
33	500.10	0.01200	87	1478.42	214.81900	33	502.52	0.01800	87	1479.02	53.22500
34	517.03	1.68700	88	1494.34	0.76400	34	521.15	1.14900	88	1486.34	0.81300
35	544.50	37.65200	89	1508.73	8.77200	35	545.62	43.70100	89	1499.23	38.85700
36	597.46	0.03400	90	1512.65	11.34500	36	597.69	1.54300	90	1501.41	5.80000
37	597.80	1.89600	91	1521.25	1196.99700	37	598.57	0.00100	91	1515.38	84.82000
38	618.11	4.24900	92	1527.91	9.78400	38	620.86	4.09300	92	1536.40	19.62900
39	673.93	50.86400	93	1565.83	125.09800	39	675.18	39.38300	93	1544.27	337.89100
40	674.78	0.07100	94	1573.55	62.06900	40	677.73	0.07500	94	1553.03	56.64100
41	714.00	0.00000	95	1653.67	1352.27600	41	714.31	0.00000	95	1632.00	1626.55200
42	743.34	0.61700	96	1678.87	35.60800	42	745.73	0.78900	96	1659.59	38.02600
43	773.85	1.38000	97	3003.47	13.91600	43	773.80	1.32900	97	2991.22	16.16300
44	801.45	25.85600	98	3003.58	41.14400	44	799.15	29.31600	98	2991.35	43.94400
45	808.81	0.43500	99	3011.92	142.64800	45	809.28	0.31300	99	3000.49	149.64300
46	811.61	0.00900	100	3012.38	1.77600	46	811.59	0.00500	100	3000.97	1.98700
47	830.06	112.60800	101	3074.77	3.30100	47	830.38	0.43700	101	3057.63	7.10300
48	830.15	3.02600	102	3074.77	13.24600	48	830.53	115.03400	102	3057.64	11.37900
49	862.63	2.76700	103	3085.38	7.90700	49	866.09	2.18900	103	3069.34	6.78800
50	886.72	317.36200	104	3085.52	8.89600	50	887.89	259.62300	104	3069.38	11.78500
51	967.75	0.61700	105	3139.49	0.51100	51	974.38	4.30500	105	3138.42	0.33900
52	968.24	13.80500	106	3139.58	0.52600	52	974.40	6.43800	106	3138.43	0.44000
53	976.07	0.28200	107	3149.08	8.30700	53	975.14	0.36000	107	3147.75	13.41000
54	976.57	0.00100	108	3149.18	5.99300	54	975.58	0.00100	108	3147.77	2.53100
55	1038.49	156.74400	109	3180.73	0.77500	55	1044.36	200.60800	109	3179.31	0.96100
56	1061.00	21.06800	110	3180.90	0.66700	56	1067.85	25.56500	110	3179.46	0.76300
57	1061.13	17.19900	111	3191.14	1.31200	57	1067.92	12.61200	111	3187.45	1.54800
58	1076.09	0.05900	112	3191.24	0.25700	58	1079.44	0.17500	112	3187.50	0.02800
59	1100.62	0.19100	113	3205.16	0.93200	59	1105.36	0.14400	113	3204.73	0.85200
60	1100.67	0.09000	114	3205.38	0.84900	60	1105.41	0.05100	114	3204.76	0.70300

TABLE S3. Vibrational frequencies computed by ωPBE/6-31G(d,p) ($\omega = 0.203 a_0^{-1}$).

Excited state					
Mode number	waven. cm^{-1}	intensity km/mol	Mode number	waven. cm^{-1}	intensity km/mol
7	38.84	1.85149	61	1136.77	275.12760
8	66.71	0.26478	62	1147.20	0.00072
9	78.04	0.12484	63	1149.43	0.00299
10	88.75	0.05248	64	1157.68	88.49210
11	108.59	3.86044	65	1169.24	54.74580
12	131.61	0.30637	66	1188.05	62.44944
13	153.64	0.01551	67	1205.15	3.62013
14	179.63	1.10763	68	1239.08	1.89099
15	185.29	1.72916	69	1261.93	90.54299
16	190.98	0.06877	70	1269.13	0.62355
17	194.12	0.09149	71	1289.93	4.25036
18	236.09	0.14158	72	1307.66	2.60590
19	238.78	0.68574	73	1362.24	314.90506
20	263.99	0.29484	74	1368.24	191.88322
21	266.48	0.00496	75	1392.85	3.72158
22	285.89	2.56904	76	1406.43	0.70205
23	303.13	9.56485	77	1435.42	13.76488
24	355.31	0.22019	78	1442.26	3.55033
25	369.69	0.02935	79	1447.91	16.97764
26	387.96	0.88582	80	1453.96	3.01010
27	420.24	0.05837	81	1457.64	204.34114
28	436.31	4.29935	82	1465.27	0.00738
29	442.82	21.31266	83	1470.77	3.40197
30	449.00	0.01845	84	1472.05	22.84521
31	466.21	9.53510	85	1477.96	24.24084
32	493.98	4.16556	86	1479.95	47.21093
33	505.50	8.51089	87	1485.71	8.41641
34	526.23	3.94858	88	1491.03	0.45420
35	556.86	1.65936	89	1503.03	167.45052
36	591.21	3.30674	90	1504.27	1.06986
37	598.83	0.30066	91	1517.38	12.42691
38	611.94	5.73389	92	1521.56	2.23913
39	657.23	3.42401	93	1548.64	404.07686
40	685.26	0.28920	94	1594.75	259.81368
41	687.46	0.37513	95	1605.91	764.50423
42	757.31	0.50372	96	1653.03	77.03806
43	777.71	7.42674	97	2988.33	18.64282
44	800.18	11.97069	98	2998.30	7.40754
45	831.26	3.76585	99	3003.84	27.64394
46	842.42	2.88004	100	3013.70	70.43175
47	847.00	35.56174	101	3049.89	6.36440
48	851.40	17.39089	102	3059.98	14.64360
49	877.39	24.73482	103	3070.63	11.33010
50	900.79	98.48625	104	3081.34	12.21993
51	948.88	22.87369	105	3150.88	0.66556
52	976.89	25.41785	106	3154.37	1.76040
53	990.68	1.37810	107	3162.67	12.87123
54	1002.26	0.47071	108	3165.53	9.40334
55	1010.34	0.01933	109	3199.94	0.14141
56	1077.82	4.59158	110	3207.72	0.41638
57	1086.44	34.52656	111	3213.01	1.54738
58	1087.08	9.54707	112	3225.88	2.97900
59	1123.16	0.00778	113	3232.33	3.44001
60	1131.59	0.00547	114	3243.39	7.93598

TABLE S4. Vibrational frequencies computed by TD-B3LYP/TDA/def2-SVP.

[1] H. J. Berendsen, J. P. Postma, W. F. van Gunsteren, and J. Hermans, in *Intermolecular forces* (Springer, 1981) pp. 331–342.
[2] C. Oostenbrink, A. Villa, A. E. Mark, and W. F. Van Gunsteren, J. Comput. Chem. **25**, 1656 (2004).
[3] H. Berendsen, B. Hess, E. Lindahl, D. Van Der Spoel, A. Mark, and G. Groenhof, J. Comput. Chem **26**, 1701 (2005).
[4] D. Spoel and B. Hess, Wiley Interdisciplinary Reviews: Computational Molecular Science **1**, 710 (2011).
[5] G. Bussi, D. Donadio, and M. Parrinello, J. Chem. Phys. **126**, 014101 (2007).
[6] M. Parrinello and A. Rahman, Journal of Applied physics **52**, 7182 (1981).
[7] T. Darden, D. York, and L. Pedersen, J. Chem. Phys. **98**, 10089 (1993).
[8] F. Neese, Wiley Interdisciplinary Reviews: Computational Molecular Science **2**, 73 (2012).
[9] A. Schäfer, H. Horn, and R. Ahlrichs, J. Chem. Phys. **97**, 2571 (1992).
[10] S. G. Balasubramani, G. P. Chen, S. Coriani, M. Diedenhofen, M. S. Frank, Y. J. Franzke, F. Furche, R. Grotjahn, M. E. Harding, C. Hattig, A. Hellweg, B. Helmich-Paris, C. Holzer, U. Huniar, M. Kaupp, A. Marefat Khah, S. Karbalaei Khani, T. Muller, F. Mack, B. D. Nguyen, S. M. Parker, E. Perlt, D. Rappoport, K. Reiter, S. Roy, M. Ruckert, G. Schmitz, M. Sierka, E. Tapavicza, D. P. Tew, C. van Wullen, V. K. Voora, F. Weigend, A. Wodynski, and J. M. Yu, J. Chem. Phys. **152**, 184107 (2020).
[11] P. Deglmann, F. Furche, and R. Ahlrichs, Chem. Phys. Lett. **362**, 511 (2002).
[12] P. Deglmann and F. Furche, J. Chem. Phys. **117**, 9535 (2002).
[13] E. Tapavicza, F. Furche, and D. Sundholm, J. Chem. Theory Comput. **12**, 5058 (2016).
[14] E. Tapavicza, J. Phys. Chem. Lett. **10**, 6003 (2019).
[15] I. Benkyi, E. Tapavicza, H. Fliegl, and D. Sundholm, Phys. Chem. Chem. Phys. **21**, 21094 (2019).
[16] W. Kohn and L. J. Sham, Phys. Rev. **140**, A1133 (1965).
[17] M. E. Casida, "Time-dependent density functional response theory for molecules," in *Recent Advances in Density Functional Methods*, edited by P. Chong (World Scientific, Singapore, 1995) pp. 155–192, https://doi.org/10.1142/9789812830586_0005.
[18] J. P. Perdew, K. Burke, and M. Ernzerhof, Phys. Rev. Lett. **77**, 3865 (1996).
[19] J. P. Perdew, M. Ernzerhof, and K. Burke, J. Chem. Phys. **105**, 9982 (1996), https://doi.org/10.1063/1.472933.
[20] C. Adamo and V. Barone, J. Chem. Phys. **110**, 6158 (1999).
[21] O. A. Vydrov and G. E. Scuseria, J. Chem. Phys. **125**, 234109 (2006).
[22] T. Stein, L. Kronik, and R. Baer, J. Am. Chem. Soc. **131**, 2818 (2009).
[23] T. Stein, L. Kronik, and R. Baer, J. Chem. Phys. **131**, 244119 (2009).
[24] A. Karolewski, T. Stein, R. Baer, and S. Kümmel, J. Chem. Phys. **134**, 151101 (2011).
[25] D. Niedzialek, I. Duchemin, T. B. de Queiroz, S. Osella, A. Rao, R. Friend, X. Blase, S. Kümmel, and D. Beljonne, Adv. Funct. Mater. **25**, 1972 (2015).
[26] D. Raithel, S. Baderschneider, T. B. de Queiroz, R. Lohwasser, J. Köhler, M. Thelakkat, S. Kümmel, and R. Hildner, Macromolecules **49**, 9553 (2016), http://dx.doi.org/10.1021/acs.macromol.6b02077.
[27] I. Schelter, J. M. Foerster, A. T. Gardiner, A. W. Roszak, R. J. Cogdell, G. M. Ullmann, T. B. de Queiroz, and S. Kümmel, J. Chem. Phys. **151**, 134114 (2019), https://doi.org/10.1063/1.5116779.
[28] T. B. de Queiroz and S. Kümmel, J. Chem. Phys. **143**, 034101 (2015).
[29] H. Stoll, G. Wagenblast, and H. Preuß, Theor. Chim. Acta **57**, 169 (1980).
[30] R. Z. Khaliullin, M. Head-Gordon, and A. T. Bell, J. Chem. Phys. **124**, 204105 (2006).
[31] Y. Shao, L. F. Molnar, Y. Jung, J. Kussmann, C. Ochsenfeld, S. T. Brown, A. T. Gilbert, L. V. Slipchenko, S. V. Levchenko, D. P. O'Neill, R. A. DiStasio Jr, R. C. Lochan, T. Wang, G. J. Beran, N. A. Besley, J. M. Herbert, C. Yeh Lin, T. Van Voorhis, S. Hung Chien, A. Sodt, R. P. Steele, V. A. Rassolov, P. E. Maslen, P. P. Korambath, R. D. Adamson, B. Austin, J. Baker, E. F. C. Byrd, H. Dachsel, R. J. Doerksen, A. Dreuw, B. D. Dunietz, A. D. Dutoi, T. R. Furlani, S. R. Gwaltney, A. Heyden, S. Hirata, C.-P. Hsu, G. Kedziora, R. Z. Khalliulin, P. Klunzinger, A. M. Lee, M. S. Lee, W. Liang, I. Lotan, N. Nair, B. Peters, E. I. Proynov, P. A. Pieniazek, Y. Min Rhee, J. Ritchie, E. Rosta, C. David Sherrill, A. C. Simmonett, J. E. Subotnik, H. Lee Woodcock III, W. Zhang, A. T. Bell, A. K. Chakraborty, D. M. Chipman, F. J. Keil, A. Warshel, W. J. Hehre, H. F. Schaefer III, J. Kong, A. I. Krylov, P. M. W. Gill, and M. Head-Gordon, Phys. Chem. Chem. Phys. **8**, 3172 (2006).
[32] G.Schaftenaar and J. Noordik, J. Comput.-Aided Mol. Design **14**, 123 (2000).
[33] W. Humphrey, A. Dalke, and K. Schulten, Journal of Molecular Graphics **14**, 33 (1996).
[34] D. Golze, M. Dvorak, and P. Rinke, Frontiers in Chemistry **7** (2019), 10.3389/fchem.2019.00377, arXiv:1912.04893.
[35] X. Blase, I. Duchemin, and D. Jacquemin, Chemical Society Reviews **47**, 1022 (2018).
[36] F. Bruneval, T. Rangel, S. M. Hamed, M. Shao, C. Yang, and J. B. Neaton, Comput. Phys. Comm. **208**, 149 (2016).
[37] M. J. van Setten, F. Caruso, S. Sharifzadeh, X. Ren, M. Scheffler, F. Liu, J. Lischner, L. Lin, J. R. Deslippe, S. G. Louie, *et al.*, J. Chem. Theory Comput. **11**, 5665 (2015).
[38] H. Jiang, R. I. Gomez-Abal, P. Rinke, and M. Scheffler, Phys. Rev. B **82**, 045108 (2010).
[39] P. Liao and E. a. Carter, Phys. Chem. Chem. Phys. **13**, 15189 (2011).
[40] N. Marom, F. Caruso, X. Ren, O. T. Hofmann, T. Körzdörfer, J. R. Chelikowsky, A. Rubio, M. Scheffler, and P. Rinke, Phys. Rev. B **86**, 245127 (2012).

Publication III

Mapping Charge-Transfer Excitations in Bacteriochlorophyll Dimers from First Principles

Accepted by Electronic Structure journal and reprinted from

Electron. Struct, 5, 024006 (2023)

Zohreh Hashemi[1], Matthias Knodt[1], Mario R. G. Marques[1], and Linn Leppert[1,2]

1) Institute of Physics, University of Bayreuth, Bayreuth 95440, Germany

2) MESA+ Institute for Nanotechnology, University of Twente, 7500 AE Enschede, The Netherlands

My contribution

I am the first author and the lead contributor to the publication. L. Leppert and I conceived the theoretical study on the absorption spectra of the dimeric systems from

photosynthetic aggregates. I performed all numerical calculations based on the *ab-initio* TDDFT and GW/BSE approaches. Furthermore, for this paper, I implemented the calculation of the GW/BSE transition density in the MOLGW software package. M. Knodt wrote a script for creating artificial dimers based on the distance and orientations of the molecules' transition dipole moments. I used this script to construct artificial dimers similar to *real* dimeric systems (as found in the photosynthetic apparatus of purple bacteria) and calculated their spectra. M. R. G. Marques computed and analyzed the vibrational spectra of the molecules. I repeated these calculations under the supervision of M. R. G. Marques with higher accuracy and these values were reported in the final version of the article. L. Leppert was involved in scientific discussions with all authors. I prepared all figures and tables in the main draft and wrote the first version of the manuscript and the supplementary material. All authors worked on the final version of the article.

Mapping charge-transfer excitations in Bacteriochlorophyll dimers from first principles

Electronic Structure

PAPER

Mapping charge-transfer excitations in Bacteriochlorophyll dimers from first principles

Zohreh Hashemi[1], **Matthias Knodt**[1], **Mario R G Marques**[1] **and Linn Leppert**[1,2,*]

[1] Institute of Physics, University of Bayreuth, Bayreuth 95440, Germany
[2] MESA+ Institute for Nanotechnology, University of Twente, 7500 AE Enschede, The Netherlands
* Author to whom any correspondence should be addressed.

E-mail: l.leppert@utwente.nl

Keywords: charge-transfer excitations, time-dependent density functional theory, GW+Bethe-Salpeter equation approach, Bacteriochlorophylls, excited states, first principles

Supplementary material for this article is available online

OPEN ACCESS

RECEIVED
6 January 2023

REVISED
8 April 2023

ACCEPTED FOR PUBLICATION
4 May 2023

PUBLISHED
16 May 2023

Abstract

Photoinduced charge-transfer excitations are key to understand the primary processes of natural photosynthesis and for designing photovoltaic and photocatalytic devices. In this paper, we use Bacteriochlorophyll dimers extracted from the light harvesting apparatus and reaction center of a photosynthetic purple bacterium as model systems to study such excitations using first-principles numerical simulation methods. We distinguish four different regimes of intermolecular coupling, ranging from very weakly coupled to strongly coupled, and identify the factors that determine the energy and character of charge-transfer excitations in each case. We also construct an artificial dimer to systematically study the effects of intermolecular distance and orientation on charge-transfer excitations, as well as the impact of molecular vibrations on these excitations. Our results provide design rules for tailoring charge-transfer excitations in Bacteriochloropylls and related photoactive molecules, and highlight the importance of including charge-transfer excitations in accurate models of the excited-state structure and dynamics of Bacteriochlorophyll aggregates.

1. Introduction

Photoinduced charge-transfer excitations are of central importance to the primary processes of natural photosynthesis and for photovoltaic and photocatalytic applications [1, 2]. In organic semiconductors, charge-transfer excitations are believed to be important intermediates between excited states localized on donor molecules and charge-separated electron–hole states on acceptor and donor units, respectively, even though the exact mechanism of charge-separation is debated [3–12]. In photosynthesis, the efficient conversion of solar energy into chemical energy is achieved by structurally complex aggregates of Bacteriochlorophylls (BCL), Chlorophylls, and other pigment molecules embedded in transmembrane proteins that modulate their structure and function. These pigment-protein complexes form light-harvesting complexes and reaction centers (RCs) that are responsible for photon absorption, excitation-energy transfer, and charge-separation. Their main operating principles are well-understood due to a wealth of crystallographic and spectroscopic studies complemented by numerical modeling using semi-empirical and first-principles approaches [13–22].

In purple bacteria, charge separation occurs in RCs comprising a hexameric aggregate of four BCLs and two Bacteriopheophytins, tightly surrounded by several protein chains [23–25]. The primary four BCL molecules of this RC are shown in figure 1(a), highlighting the so-called *special pair*, a strongly-coupled dimer of BCLs called P_A—P_B in the following. Charge separation in the bacterial RC is initiated by a series of energy- and charge-transfer excitations that involve the special pair and proceed along the *A branch*, the photoactive of the two pseudo-symmetric branches the RC consists of [19, 26–28]. In figure 1(b), we have highlighted the A-branch dimer P_A—B_A that has been speculated to be involved in the primary

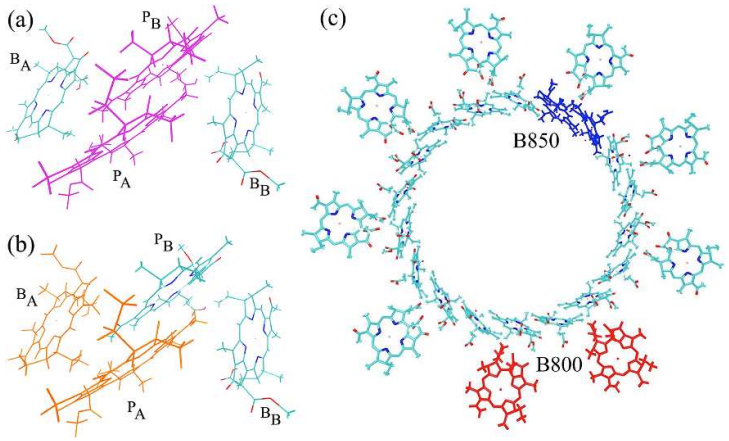

Figure 1. Crystal structure of BCL aggregates in the RC and light-harvesting II (LHII) complex of the purple bacteria *Rhodobacter sphaeroides* and *Rhodoblastus acidophilus*, respectively. Dimers of BCLs are highlighted in color using (a) pink for the *special pair* P_A—P_B, (b) orange for the A branch dimer P_A—B_A, (c) red for a dimer from the B800 and blue for a dimer from the B850 ring of the LHII complex. Hydrogen atoms are omitted for clarity.

charge-separation step, although this assignment is debated in the literature [29–32]. Excitation energy reaches the RC through a cascade of excitation-energy transfer processes that are initiated in the light harvesting II (LHII) complex, consisting of two rings of BCL molecules dubbed B850 and B800, respectively, and shown in figure 1(c). Neighboring BCLs in the B800 ring are only weakly coupled and excitation-energy transfer is well-described by Förster dipole-dipole coupling [33]. In the B850 ring, neighboring BCL molecules are closer and intermediate between the weakly coupled B800 and the strongly coupled special-pair BCLs.

The excited states that are believed to be responsible for excitation-energy transfer in and between the light-harvesting complexes and the RC, are commonly thought of as Frenkel-like excitons that are spatially relatively localized on one or two BCL molecules [34]. Semi-empirical models based on Frenkel-exciton Hamiltonians have played an important role in modeling the excitation-energy and charge-transfer dynamics in large photosynthetic pigment-protein complexes [35–37]. However, for a reliable and predictive representation of the electronic coupling between adjacent pigments, charge-transfer excitations need to be included in these model Hamiltonians [36, 38–41], calling for accurate first-principles calculations of such excitations.

For computationally efficient first-principles methods such as time-dependent density functional theory (TDDFT), charge-transfer excitations were long considered a major challenge due to their inherently nonlocal nature, i.e., the spatial separation of the occupied and virtual orbitals contributing to these excitations [42]. TDDFT with optimally-tuned range-separated hybrid functionals is a viable solution to this problem, and has been used to predict excited states of molecular systems and solids with great success [43–49]. In these exchange-correlation functionals, the presence of long-range exact exchange leads to asymptotically correct potentials. Additionally, a parameter controlling the length scales of exact and semilocal exchange can be used to tune the energies of the highest occupied and the lowest unoccupied orbitals to correspond to the negative of the ionization potentials and the electron affinity, respectively, within the conceptual framework of generalized Kohn–Sham theory [50]. Both conditions are crucial for accurately capturing charge-transfer excitations within linear-response TDDFT [51] and have been extended to solvated molecular systems [47, 52] and solids [49].

An alternative approach for calculating charge-transfer excitations of is the *GW*+Bethe-Salpeter equation (*GW*+BSE) approach [53, 54]. While this method was initially primarily applied to solids, recent years have witnessed a multitude of studies that have demonstrated the accuracy and predictive power of the *GW*+BSE method for small molecules [55–57] and larger molecular complexes [58–62]. In particular, we [63] and others [62] benchmarked the accuracy of the *GW*+BSE approach against experiment and wavefunction-based methods and found excellent agreement for the Q_y and Q_x excitations of a range of BCL and Chlorophyll molecules. We showed that eigenvalue self-consistent *GW* calculations and *one-shot* G_0W_0 calculations where the zeroth-order single-particle Green's function G_0 and screened Coulomb interaction W_0 were constructed from a DFT eigensystem obtained with an optimally-tuned range-separated hybrid functional lead to the best results. TDDFT with an optimally-tuned hybrid-functional performed slightly worse and tended to overestimate the energy of the Q_y excitations, in agreement with previous studies [58].

In this article, we report a systematic first-principles study of charge-transfer excitations in BCL dimers—the smallest structural units in which excitations with intermolecular charge-transfer character can be observed. Two types of BCL dimers constitute our model systems in this study: The first class of dimers (discussed in section 3.1) are extracted from the LHII complex and RC of purple bacteria. We note that the excitation energies that we calculate for these systems will be different from those *in vivo*, where electrostatic and dielectric effects of the protein environment and coupling with other pigments leads to different excitations and affects locally excited and charge-transfer states differently [34, 64–66]. Our goal is to elucidate the factors that determine the energy and character of these excitations, in particular their mixing with the coupled Q_y and Q_x excitations of the dimers. We treat these dimers as representative of four different regimes of intermolecular coupling resulting in distinct charge-transfer properties: 1. The B800 dimer is very weakly coupled with Q_y and Q_x excitations resembling those of the monomeric units and high-energy charge-transfer excitations due to vanishing orbital overlap. 2. The A-branch dimer is more strongly coupled and exhibits one charge-transfer excitation corresponding to electron transfer from P_A to B_A. We use the notation $P_A^+ B_A^-$ to indicate the direction of charge-transfer in the following. This charge-transfer excitation is ∼0.4 eV higher in energy than the coupled Q_x excitations. 3. The B850 dimer is even more strongly coupled. The lowest-energy charge-transfer excitation mixes with the coupled Q_x excitations and another charge-transfer state appears at slightly higher energies. 4. Finally, the special pair is the most strongly coupled case with three charge-transfer excitations mixing with the coupled Q_x excitations. Additionally, we construct an artificial BCL dimer and systematically study the effects of intermolecular distance and orientation on charge-transfer excitations. We also estimate the effect of molecular vibrations on charge-transfer excitations. We do this by calculating the vibrational normal modes of a dimeric system and determining the change of excitation energies for structures distorted along normal modes. This allows us to identify vibrational modes with pronounced effects on charge-transfer excitations. Finally, we comment on differences and similarities between TDDFT with an optimally-tuned range separated hybrid functional and the *GW*+BSE approach.

2. Computational methods

2.1. First-principles methods and computational details

For all calculations reported in this article, we used TDDFT as implemented in TURBOMOLE version 7.5 [67] and the *GW*+BSE approach as implemented in MOLGW version 3.0 [68]. Briefly, in the linear-response formulation of both methods the excitation energies Ω_n can be obtained by solving the matrix eigenvalue equation $C\mathbf{Z} = \Omega_n^2 \mathbf{Z}$, where C is

$$C_{ij\sigma,kl\tau} = (\varepsilon_{i\sigma} - \varepsilon_{j\sigma})^2 \delta_{ij}\delta_{jl}\delta_{\sigma\tau} + 2\sqrt{\varepsilon_{i\sigma} - \varepsilon_{j\sigma}}\sqrt{\varepsilon_{k\tau} - \varepsilon_{l\tau}} K_{ij\sigma,kl\tau} \quad (1)$$

and the indices i, k refer to occupied, j, l to virtual orbitals and σ, τ to spin-indices. Differences between TDDFT and the *GW*+BSE approach enter equation (1) in two distinct ways: 1. Through the differences between virtual and occupied orbital energies $\varepsilon_{i\sigma} - \varepsilon_{j\sigma}$ which are obtained from a (generalized) Kohn–Sham calculation in TDDFT and from the *GW* approach in *GW*+BSE. 2. Through the kernel matrix element $K_{ij\sigma,kl\tau}$, which depends on the exchange-correlation kernel $f_{xc,\sigma}$—the functional derivative of the exchange-correlation potential—in TDDFT, and on the screened Coulomb interaction W, typically evaluated in the random phase approximation and at zero frequency, in the BSE approach [69–72].

Here we use the optimally-tuned range-separated hybrid functional ωPBE for our TDDFT calculations. We use a range-separation parameter $\omega = 0.171\ a_0^{-1}$, based on tuning for a single BCL *a* molecule performed by Schelter *et al* [73]. The optimal-tuning procedure follows the recipe by Stein *et al* and ensures that the HOMO eigenvalue corresponds to the ionization potential and the LUMO eigenvalue corresponds to the electron affinity of the molecule [74]. We do not perform a new tuning procedure for the dimers for general reasons: Using the same ω for each dimer allows us to compare the electronic and excited state structure of these systems on the same footing. Furthermore, optimal tuning of conjugated systems of increasing size leads to artificially low values of ω and, thus, a dominance of semilocal exchange at long range, which deteriorates the description of charge-transfer excitations [47, 75].

For our *GW*+BSE calculations we use a 'one-shot' G_0W_0 approach in which we construct the zeroth-order single-particle Green's function G_0 and the screened Coulomb interaction W_0 from DFT eigenvalues and eigenfunctions calculated using the same ωPBE as described above. This approach leads to excellent agreement with experimental excitation energies and reference values from wavefunction-based methods for a range of BCL and Chlorophyll molecules [63]. Range-separated hybrid functionals have been shown to lead to accurate charge-transfer excitations for larger molecular complexes as well [58, 76]. In all calculations we used a def2-TZVP basis set, and the frozen core and resolution-of-the-identity

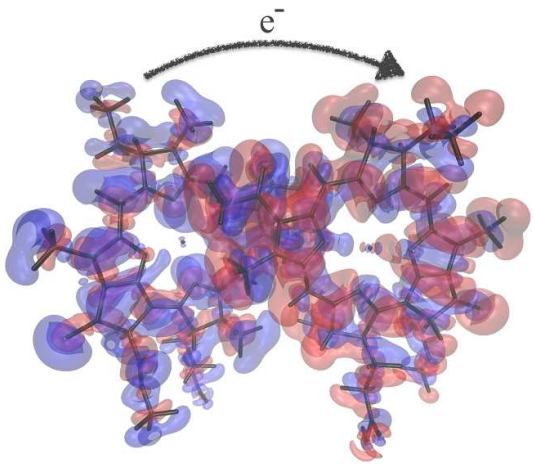

Figure 2. Schematic isosurface picture of the difference density of an excited state. The red and blue areas correspond to regions of positive and negative density, respectively. We integrate the difference density over volumes associated with each molecule to quantify how much charge is transferred as a result of the excitation (see main text).

approximations (with the DeMon auxiliary basis set [77]). We did not apply the Tamm-Dancoff approximation in any of the results reported in this paper. In our G_0W_0 calculations, we used the optimized virtual subspace method by Bruneval with an aug-cc-pVDZ basis set for the reduced virtual orbital subspace [78]. With these settings, our excitation energies are converged to within 40 meV. Further details on our convergence tests can be found in section 2.2 and in the Supplemental Material (SM).

For evaluating the character of the excited states, we calculated their transition and difference densities which are both derived from the density matrix $\gamma^{ii}(r,r') = N\int \Psi^i(r,r_2,r_3,\ldots,r_n)\Psi^i(r',r_2,r_3,\ldots,r_n)dr_2\ldots dr_n$, where N is the number of electrons and Ψ^i is the generalized Kohn–Sham excited-state wavefunction, here constructed from a sum of Slater determinants of generalized Kohn–Sham orbitals with coefficients from linear-response TDDFT or the BSE. The ground state density is $n^0(r) = \gamma^{00}(r,r')$. The density of excited state i is $n^i(r) = \gamma^{ii}(r,r')$. The difference density is obtained by subtracting n^i from n^0, and allows to visualize the change of density upon excitation of the system into excited state i, as schematically shown in figure 2. The transition density is obtained as the diagonal part of the density matrix for a transition from the ground state into an excited state i *as* $\rho^{0i}(r) = \gamma^{0i}(r,r')$, and is particularly useful for determining the interaction strength of electronic transitions with light and efficiencies of excitation energy transfer. For charge-transfer excitations there is no overlap between ground and excited state, thus the transition density vanishes. We therefore use the difference density for visualizing charge-transfer excitations and quantifying their charge-transfer character [79]. Note that for the identification of charge-resonance excitations, i.e., excitations without a net charge transfer which can be described as linear combinations of forward and backward charge transfers of equal weight, direct analysis of the transition density matrix is a more useful tool [80]. In the following, we define charge-transfer excitations as those with a net shift of charge with respect to the ground state.

To quantify the magnitude of charge transfer we integrated over subsystem difference densities. For this purpose, we subdivided the volume containing the difference densities of the dimer into subsystem volumes, each containing one pigment. Our aim is to assign each grid point of the difference-density grid to its closest pigment molecule. For achieving this, we used the distances between grid points and each molecule's atomic coordinates (including hydrogen atoms), as previously done in [64].

Finally, to obtain a mode-resolved picture of the effect of thermally-activated vibrations (section 3.3), we relaxed a dimer structure using the B3LYP approximation for the exchange-correlation functional and def2-TZVP basis set, and evaluated its normal modes and frequencies. Using the harmonic approximation, we related the amplitude of these normal modes with the thermal energy of a molecule. Thus, we distorted the dimer structure along its lowest-frequency normal modes at a temperature of 300 K. In this manner, we generated 60 distortions of the dimer, that we then studied using TDDFT calculations using the ωPBE functional. All these calculations were performed using the tools provided in the TURBOMOLE package.

2.2. Convergence of G_0W_0+BSE calculations

We carefully tested that our GW+BSE results are converged. Due to the large size of a BCL dimer, featuring more than 300 electrons, the calculation of the GW self-energy which requires summation over virtual states is computationally demanding. We therefore used the optimized virtual subspace method implemented in

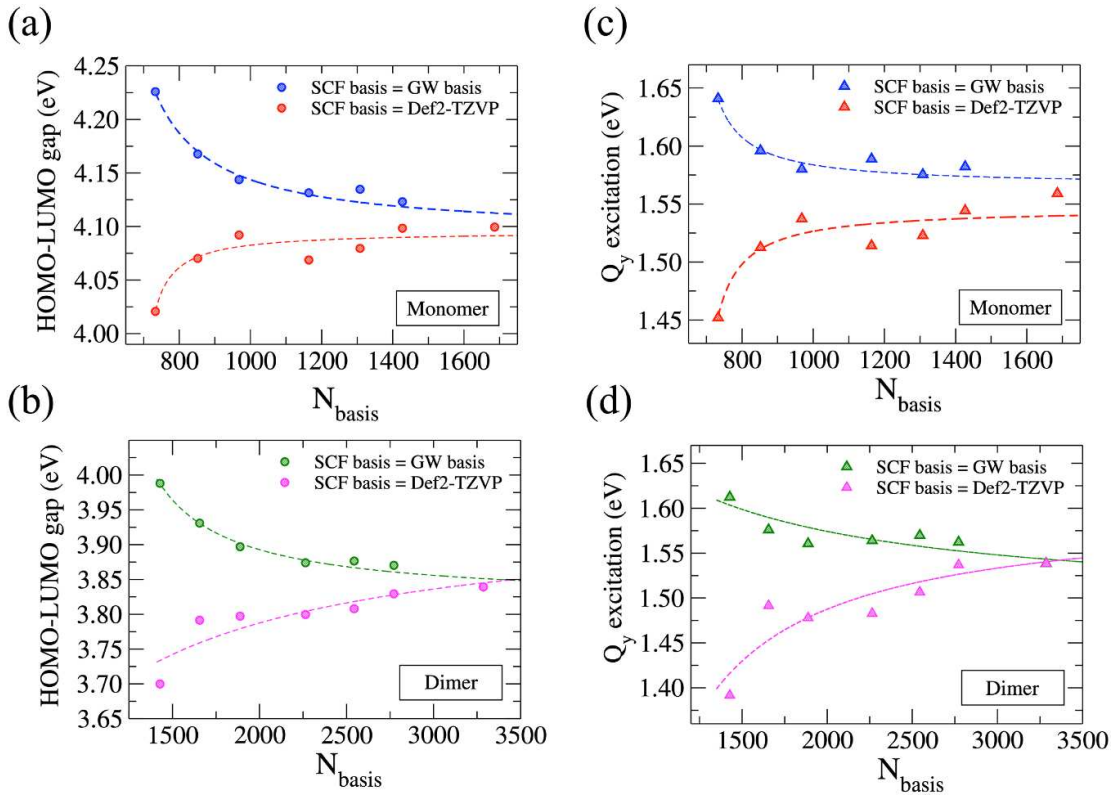

Figure 3. Convergence of *GW* (a) HOMO-LUMO gap and (c) energy of the first excited state of BCL *a* monomer as a function of the number of basis functions. Blue data points correspond to calculations in which the same basis set is used for the occupied orbitals and the virtual subspace. Red points correspond to calculations using the optimized virtual subspace method. Lines are fits to these data points. Convergence of the HOMO-LUMO gap and energy of the first excited state is shown in panel (b) and (d) for the B850 dimer, respectively. Here, green corresponds to using the same basis set for the occupied orbitals and the virtual subspace and pink to calculations using the optimized virtual subspace method.

the MOLGW code, in which a reduced virtual orbital subspace represented by a comparably small basis set is used to evaluate the *GW* self-energy [78].

We start by testing the convergence of the HOMO-LUMO gap, and the Q_y and Q_x excitations of a BCL *a* monomer with respect to basis set size without the optimized virtual subspace method (table S1). In agreement with our previous results [63], we find that the def2-TZVP basis set deviates by less than 10 meV from the considerably larger aug-cc-pVTZ basis. We proceeded by calculating the convergence of the Q_y and Q_x excitations of the BCL monomer as a function of the number of virtual orbitals N_{virt} included in the evaluation of the *GW* self-energy using the def2-TZVP basis (figure S1). We find that for $N_{virt} = 500$ both excitations are converged to within 80 meV from the limit of infinite N_{virt}. Based on these findings we continued by evaluating the effect of using a smaller basis set for the virtual subspace [78]. The results for the HOMO-LUMO gap and the Q_y excitation are plotted in figures 3(a) and (c), and show that the optimized virtual subspace method leads to an underestimation of the HOMO-LUMO gap and the Q_y excitation energy as compared to the *conventional* method in which the same basis set is used for all orbitals. We find that using the aug-ccpVDZ basis for the optimized virtual subspace in conjunction with $N_{virt} = 500$ leads to a fortuitous error cancellation and results in a HOMO-LUMO gap and Q_y and Q_x excitation energies that are within less than 50 meV of the results obtained with the conventional method and $N_{virt} \to \infty$ (figure S2).

For the dimer, we therefore chose $N_{virt} = 1000$ and the same strategy for determining the optimized virtual subspace. We find very similar results for the convergence of the HOMO-LUMO gap and the first bright coupled Q_y excitation shown in figures 3(b) and (d). All *GW*+BSE results reported in this paper are therefore based on calculations using the def2-TZVP basis set for the occupied orbitals and the aug-ccpVDZ basis for the optimized virtual subspace.

2.3. Construction of the model systems

We constructed our model systems from the x-ray crystallographic structures of the purple bacteria *Rhodobacter sphaeroides* (structure ID 1*M3X* in the Protein Data Base) [81], *Rhodoblastus acidophilus* (structure ID 1 *NKZ* [82]). In all structures, we replaced the phytyl tail with hydrogen. Hydrogen atoms not resolved in the experimental crystal structure were added using AVOGADRO and their positions were optimized

while keeping the rest of the structure fixed. These geometry optimizations were performed using TURBOMOLE and the B3LYP exchange-correlation functional. The RC dimers P_A—P_B and P_A—B_A (figures 1(a) and (b)) were constructed using structure 1*M3X* while the B800 and B850 ring dimers (figure 1(c)) were extracted from 1 *NKZ*. These molecules correspond to ID numbers *BCL*307 and *BCL*309 for the B800, and *BCL*302 and *BCL*303 for the B850 ring. Note that the resolution of x-ray crystal structures of protein complexes is often not high enough to resolve the internal structure of the chromophores. Therefore, internal coordinates (such as bond lengths) can be unreliable, and care should be taken when comparing calculations to experiment [83]. We illustrate this effect in figure S3, where we compare TDDFT spectra based on the x-ray crystal structures with those based on constrained relaxations of the B800 and the B850 dimers. Geometry optimization leads to significant changes in the excitation energies, in particular a blueshift of the Q_y excitation and charge-transfer states. Nonetheless, in section 3.1, we present results based on unrelaxed crystal structures, since qualitatively the results are the same.

To study the effect of structure in more detail, we additionally constructed an artificial dimer consisting of two exactly equivalent relaxed BCL *a* molecules (using molecule P_A) that we initially oriented in the same way as the special-pair dimer P_A—P_B by aligning their transition dipole moments (as calculated with TDDFT) with those of P_A and P_B, respectively. We are providing all relevant structure files necessary to reproduce the results of this article in the SM.

3. Discussion and results

3.1. Charge-transfer excitations in RC and LHII dimers

We start by comparing the excitation spectrum of the four dimeric systems shown in figures 1(a)–(c) using TDDFT and *GW*+BSE. The energies and oscillator strengths of the first 15 excitations of each system can be found in table S3 and S4. The spectra are shown in figures 4(a) and (b), respectively, and allow for several observations. First, we find that TDDFT and *GW*+BSE predict qualitatively very similar spectra. The most striking difference appears for the B800 dimer, for which the coupled Q_y excitations calculated with TDDFT are ∼0.3 eV higher in energy than with *GW*+BSE while all other excitations are at similar energies. This observation is consistent with our results for single BCL *a* molecules for which TDDFT with optimally-tuned ωPBE consistently overestimates the Q_y excitation energy by ∼0.3 eV [63] and therefore leads to an underestimation of the Q_y—Q_x energy difference as compared to experiment. Interestingly, this overestimation as compared to *GW*+BSE, while still present, is less pronounced for the other three dimers and seems to decrease with increasing intermolecular coupling. Our results are in qualitative agreement with previous calculations (see table S5), but a comparison is complicated by the use of different structural models, exchange-correlation functionals and basis sets.

Second, we find several dark excitations for all four systems, predicted at very similar energies with TDDFT and the *GW*+BSE approach. We analyze the charge-transfer character of these excitations by calculating their difference densities and integrating over subsystem difference densities as described in section 2.1. The energy and character of these dark excitations considerably differs for our four dimers. For the B800 dimer, we find three dark excitations, E_5, E_6, and E_7, ∼0.7 eV above the coupled Q_x excitations which are almost degenerate. The difference densities (figure S4 and table 1) do not indicate any charge-transfer character for these excitations—their charge distribution is primarily localized on only one BCL in each excitation, and looks similar to those of the monomeric system. Charge-transfer excitations can be found at around 3.0 eV, consistent with the large distance of 20 Å between the B800 molecules, measured as the distance between their centers of masses.

The molecules P_A and B_A of the A-branch dimer are ∼13 Å apart, leading to stronger intermolecular coupling and the appearance of a charge-transfer state in the energy range considered here. Figure 4 shows that for this system the coupled Q_y and Q_x excitations are split and the first dark excitation is ∼0.3 eV higher in energy than the second coupled Q_x excitation. Contrary to the B800 dimer, this dark excitation has clear charge-transfer character (table 1) and corresponds to $P_A^+B_A^-$. The character of the two following dark states is unchanged as compared to B800 apart from a redshift.

In the B850 dimer with ∼11 Å distance, the stronger intermolecular coupling leads to a further redshift of the dark excitations. We find that a dark state mixes with the coupled Q_x excitations leading to charge-transfer character in E_3. The second charge-transfer excitation, E_6, appears ∼0.2 eV above the first one, in the vicinity but energetically well-separated from the coupled Q_x excitations.

The excitation spectrum of the special-pair dimer is yet different. Due to the strong intermolecular coupling of the two molecules which are only 9 Å apart, three charge-transfer excitations appear at relatively low energies. The first one is lower in energy than the first coupled Q_x excitation and corresponds to $P_A^+P_B^-$, whereas the other two are above the coupled Q_x excitations and correspond to $P_A^-P_B^+$ and $P_A^+P_B^-$, respectively. Note that due to the overestimation of the coupled Q_y excitations by TDDFT, *GW*+BSE predicts the energy

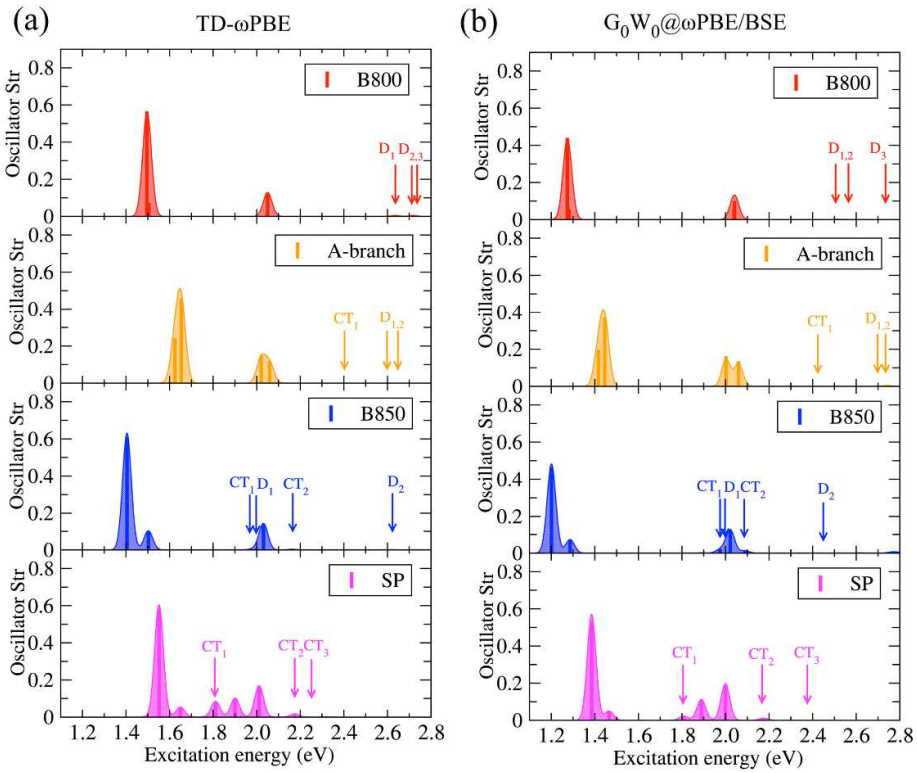

Figure 4. Excitation spectrum of B800, A-branch, B850, and SP dimers using (a) TDDFT with ωPBE and (b) the G_0W_0@ωPBE+BSE approach. Arrows mark dark excitations without (D) and with (CT) charge-transfer character. The shaded areas are calculated by folding the excitation energies with Gaussian functions with a width of 0.08 eV as a guide to the eye.

Table 1. Difference density integrated over subsystem volumes. The first two excitations, i.e. E_1 and E_2, are not included since their difference densities integrate to zero in all studied systems.

		Charge distribution				
Dimer	Molecule label	E_3	E_4	E_5	E_6	E_7
B800	B307	0	0	0	0	0
	B309	0	0	0	0	0
A-branch	P_A	0	0	−0.97	0	0
	B_A	0	0	0.97	0	0
B850	B302	−0.83	0	0	0.86	0
	B303	0.83	0	0	−0.86	0
SP	P_A	−0.69	0	0	0.83	−0.76
	P_B	0.69	0	0	−0.83	0.76

gap between the coupled Q_y excitations and CT_1 to be twice as large as TDDFT. Nonetheless, since the qualitative features of all four excitation spectra and the charge-transfer character of all excitations is similar, we use TDDFT for all further calculations and report *GW*+BSE results in the SM.

3.2. Charge-transfer excitations in artificial dimer

The dimeric systems extracted from the RC and LHII crystal structures discussed in section 3.1, differ in their distance, relative orientation, and the structural details of the two molecular subunits comprising the dimer. To disentangle these effects, we therefore proceeded by performing TDDFT calculations for an artificial dimeric system constructed as discussed in section 2. The structural parameters that define the distance and relative orientations of this dimer are shown in figure 5. We measure the distance between the molecules r as the distance between their centers of masses $\mathbf{R}_1$ and $\mathbf{R}_2$, i.e. $r = |\mathbf{r}| = |\mathbf{R}_1 - \mathbf{R}_2|$. Their relative orientation is defined by three angles α, β, and γ. The first angle, α, is a rotation around the normal vector of the plane spanned by the Q_y and Q_x transition dipole moments of a single molecule, i.e. it is approximately perpendicular to the porphyrin-ring plane. The second rotation axis, associated with β, corresponds to

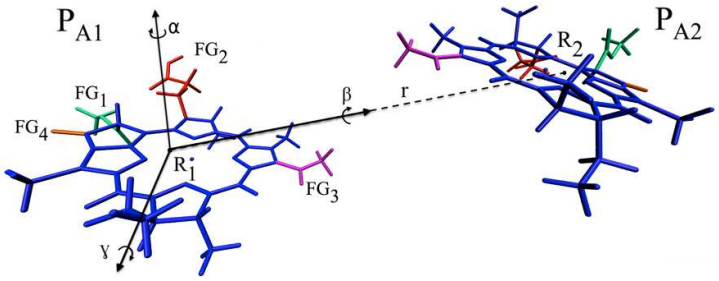

Figure 5. Structure of artificial dimer based on two identical P_A molecules. We highlight four functional groups FG_1 (in green), FG_2 (in red), FG_3 (in pink), and FG_4 (in orange). Hydrogen atoms are omitted for clarity.

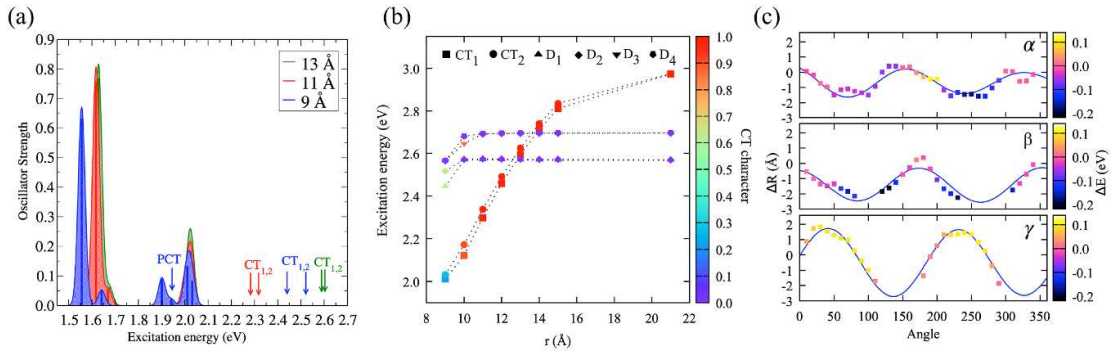

Figure 6. (a) Absorption spectra of artificial dimer with $r = 9$ Å (blue), $r = 11$ Å (red), and $r = 13$ Å (green). Arrows mark excitations with charge-transfer character. The shaded areas are calculated by folding the excitation energies with Gaussian functions with a width of 0.08 eV as a guide to the eye. (b) The excitation energy of the first two charge-transfer (CT_1 and CT_2) excitations and the first four dark states (D_1–D_4) as a function of r. The color scale represents the charge-transfer character of each excitation based on the absolute value of the integrated subsystem difference densities. (c) ΔR (see main text) as a function of the rotation angle α (top), β (middle), and γ (bottom). Blue lines are periodic fits and serve as a guide to the eye. The color scale corresponds to the change in energy ΔE of CT_1 as compared to the unrotated reference structure.

$\mathbf{r} = \mathbf{R}_1 - \mathbf{R}_2$. The third rotation, γ, is around the axis given by the cross product of $\mathbf{r}$ and the normal vector of the Q_y—Q_x plane. For our further discussion, we also distinguish between the four functional groups FG_1, FG_2, FG_3, and FG_4, highlighted in figure 5.

We start by investigating the effect of changing the distance r between the molecules P_{A1} and P_{A2}, fixing the relative orientation of the molecules such that it corresponds to the one found in the special-pair dimer. Figure 6(a) shows the excitation spectra of dimers separated by 9, 11, and 13 Å, corresponding to the center-of-mass difference found in the special pair, the B850 dimer, and the A-branch dimer of section 3.1, respectively. Note that distances smaller than 9 Å are not possible for the artificial dimer due to overlap between the FG_3 functional groups. Decreasing the center-of-mass difference leads to a redshift and splitting of the coupled Q_y excitations accompanied by a redistribution of oscillator strength between the two excitations, in accordance with expectations from Kasha's exciton theory [84]. The effect on the coupled Q_x excitations cannot be discussed without also considering the higher-energy charge-transfer excitations. The latter are redshifted when going from 13 to 11 Å, and mix with the coupled Q_x excitations at 9 Å, similar to the situation in the special-pair dimer. The corresponding charge distributions based on subsystem integrals of difference densities are shown in table 2 and demonstrate that for the system at $r = 9$ Å, all excitations in the energy-range of the coupled Q_x excitations and the higher energy dark states exhibit charge-transfer character. We classify E_4, which is in the energy range of the coupled Q_x excitations and corresponds to transfer of half an electron from P_{A1} to P_{A2} as a partial charge-transfer state in figure 6(a). Our results are qualitatively similar when using the GW+BSE approach, as shown in figure S6 and consistent with our discussion in section 3.1.

These trends are even more apparent in figure 6(b), where we plot the energy of all dark excitations as a function of distance and indicate their charge-transfer character in color. In the energy range considered here, there are four dark excitations without charge-transfer character which are essentially independent of distance and are only redshifted and acquire substantial charge-transfer character at relatively small r. The two charge-transfer states exhibit a significant distance dependence and are red-shifted by almost 1 eV with

Table 2. Charge distribution on each molecule in the artificial dimer upon excitation as calculated by integration over subsystem difference densities. The first two excitations, i.e. E_1 and E_2, are not included since their subsystem difference densities integrate to zero.

		Charge distribution				
r (Å)	Molecule	E_4	E_5	E_6	E_7	E_8
9	P_{A1}	−0.48	0.21	0.28	−0.62	−0.63
	P_{A2}	0.48	−0.21	−0.28	0.62	0.63
11	P_{A1}	0	−0.96	0.96	0	0
	P_{A2}	0	0.96	−0.96	0	0
13	P_{A1}	0	0	0	−0.99	0.99
	P_{A2}	0	0	0	0.99	−0.99

decreasing r but lose some of their charge-transfer character at the smallest distance where they start mixing with the coupled Q_x excitations.

For investigating the effect of the relative orientation of the two molecules, we fixed the intermolecular distance at 13 Å. Shorter distances were not possible due to overlap of functional groups for some orientations. Since rotations around the angles α, β, and γ do not commute, we treat them separately from each other, i.e. we first consider rotations around α for fixed β and γ, then rotations around β for fixed α and γ, and finally rotations around γ for fixed α and β. For each structure, we determine the smallest intermolecular distance between every two individual atoms in P_{A1} and P_{A2}, R. The difference between R in the reference (unrotated) structure from each rotated structure, $\Delta R = R_{ref} - R_{rot}$, as a function of rotation angle, is shown in figure 6(c). Since charge-transfer excitations CT_1 and CT_2 follow similar trends, we only show the change in energy of CT_1 upon rotation in figure 6(c). Negative (positive) values of $\Delta E^{CT_1} = E^{CT_1}_{ref} - E^{CT_1}_{rot}$ correspond to a redshift (blue-shift) of the excitation energy.

Rotations around α and β correspond to orientations with smaller R than in the reference structure. Consequently, we observe increased intermolecular coupling and hence a redshift of the charge-transfer state by up to ∼0.2 eV. For the structure for which we observe the largest effect (corresponding to a β rotation of 120 degrees), it is primarily the relative orientation and distance of carbon chains determining the intermolecular coupling (figure S8(a)). For many of the other structures that show pronounced redshifts, we find that the functional groups of the two BCLs highlighted in figure 5 are in close spatial proximity (see figure S8(b) for an example). In contrast, the rotation around the angle γ results primarily in structures with positive ΔR and a blueshift of the charge-transfer excitation by up to ∼0.1 eV. We note that in the majority of structures rotated around γ, the functional groups FG_1, FG_2, and FG_4 are far apart from the second BCL. However, for some structures, overlap between FG_2 and the second BCL molecule led to unrealistic structures that were excluded from figure 6(c). Overall, the γ rotation primarily leads to geometries with weaker intermolecular coupling and an overall blueshift in energy of the charge-transfer excitation.

3.3. Vibrational effects on charge-transfer excitations

Excitations of different spatial localization and character are known to be affected in different ways by molecular vibrations [85]. Our goal here is to provide a mode-resolved picture of excitation energy changes in a BCL dimer due to thermally-activated vibrations, following earlier work by Hele *et al* [86]. For this purpose, we started from the crystal structure of the special-pair dimer and performed a full geometry optimization using the def2-TZVP basis set and B3LYP exchange-correlation functional. In the absence of the protein environment and other co-factors, no external force fixes P_A and P_B in the parallel configuration they have *in vivo*. Consequently, the relaxed structure differs considerably from the special-pair structure, and is more akin to the A-branch dimer. Since our aim is to provide a qualitative picture, we proceed with this structure which is dynamically stable, i.e. without imaginary frequencies. We note, however, that the excitation spectrum of the relaxed dimer, shown in figure 7(a), differs from the spectra discussed so far. In particular, the spectrum displays a charge-transfer state CT_1 at ∼1.6 eV (see also table S9). This state mixes with the coupled Q_y excitations and corresponds to the transfer of 0.78 of an electron from P_A to P_B (see table S10). A second charge-transfer state CT_2 mixes with the coupled Q_x excitations, while the third one, CT_3, is energetically well-separated from the Q-band excitations at ∼2.7 eV.

We calculate the vibrational normal modes of the relaxed dimer using the same basis set and exchange-correlation functional but with a very fine grid for the quadrature of the exchange-correlation energy. We then generate 60 structures by distorting the relaxed reference structure along each of the 60 lowest-frequency normal modes. We assume a classical distribution to approximate the amplitude of these distortions at $T = 300$ K and generate one distorted structure per mode corresponding to a positive distortion amplitude. The excitation spectrum of each distorted structure is then calculated with TDDFT as before, i.e. with ωPBE with $\omega = 0.171\ a_0^{-1}$. We define the excitation energy change of excitation n as

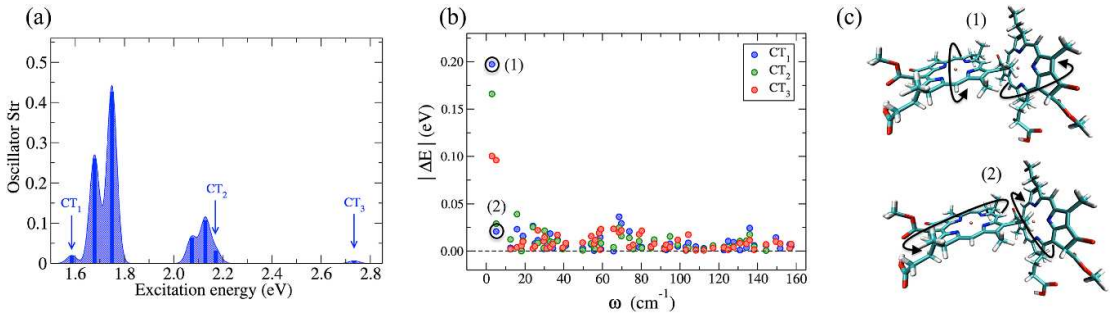

Figure 7. (a) Absorption spectrum of relaxed dimer. Arrows mark the first three charge-transfer excitations. (b) Excitation-energy change $|\Delta E|$ as a function of normal-mode frequency for CT_1, CT_2, and CT_3. (c) Visualization of the first two normal modes which correspond to intermolecular rotations (see main text).

$\Delta E^n = E^n_{ref} - E^n_{dis}$. Here we focus on how molecular vibrations affect charge-transfer excitations, but note that ΔE for the coupled Q_y and Q_x excitations can also be substantial as shown in figure S9.

While ΔE can be either positive or negative, depending on the direction of the distortion mode, we show $|\Delta E|$ of the charge-transfer excitations CT_1, CT_2, and CT_3 in figure 7(b). We find that high-frequency modes correspond to intramolecular vibrations such as C–C and C–H stretch modes, which are not thermally activated and only have a small effect on the energy of the three charge-transfer states. In contrast, low-frequency modes correspond to intermolecular vibrations that change the orbital overlap between neighboring molecules and thus have a more substantial impact. In particular, we find that the two lowest-frequency modes lead to substantial changes in all three charge-transfer states. Both modes correspond to a rotational motion of the porphyrin planes of the BCL molecules with respect to each other as indicated in figure 7(c). The first mode leads to a redshift of all three excitations which is with ∼0.2 eV most pronounced for CT_1, the second one leads to a smaller blueshift of CT_1 and CT_3 and a slight redshift of CT_2. These results qualitatively agree with our results in section 3.2, suggesting that thermally-activated vibrational modes can significantly affect the energy of charge-transfer excitations affecting their charge-transfer character and mixing with other delocalized and localized excitations of the system.

4. Summary and conclusions

In summary, we have presented a systematic first-principles study of charge-transfer excitations in BCL dimers. Our model systems are inspired by molecular aggregates found in the LHII complex and RC of purple bacteria and cover a wide range of intermolecular coupling strengths, and consequently, excited-state structures. Charge-transfer excitations can be found in a wide range of energies, primarily depending on intermolecular distance and orientation. BCL molecules have a complex three-dimensional structure with several functional groups, a long phytyl tail, and other carbon chains protruding out of the porphyrin plane. *In vivo*, i.e. within the evolutionary-optimized protein networks of the photosynthetic apparatus, the protein environment determines the distance, orientation, and structural details of these aggregates. Furthermore, the protein environment indirectly affects the excited state structure and dynamics of BCL aggregates through dielectric screening and electrostatic effects [64, 87–95]. Therefore our results can not directly be used to infer charge-transfer mechanisms in photosynthetic systems. Nonetheless, they provide an intuitive understanding and design rules for tailoring charge-transfer excitations in BCLs and similar photoactive molecules. Furthermore, they explicitly confirm the importance of charge-transfer excitations for a correct description of the *Q*-band excitations of BCL aggregates [40]. We hope that our results inspire future calculations of the excited-state structure and dynamics of pigment-protein complexes and chromophore aggregates based on model Hamiltonians, that include charge-transfer excitations.

Furthermore, we have compared our results based on TDDFT with the optimally-tuned ωPBE functional to calculations using the *GW*+BSE approach. While charge-transfer excitations appear at very similar energies with both approaches, coupled Q_y excitations are systematically overestimated by TDDFT as compared to the *GW*+BSE approach. Previous studies suggest that Q_y excitation energies from *GW*+BSE are in better agreement with wavefunction-based methods and experiment than TDDFT with ωPBE [62, 63]. However, accurate benchmarks for larger molecular aggregates are missing and we therefore do not think that a clear recommendation for using *GW*+BSE instead of TDDFT is warranted. Nonetheless, with advances in code implementation [68, 96, 97] and in the combination of *GW*+BSE with discrete and polarizable continuum models [98, 99] and other QM/MM methods [100], *GW*+BSE calculations of large

molecular aggregates are becoming computationally feasible, demonstrated in a recent study by Förster *et al* [62]. Further study of the accuracy and predictive power of TDDFT, with exchange-correlation functionals that capture the nonlocal nature of charge-transfer excitations for such aggregates is necessary.

Data availability statement

All data that support the findings of this study are included within the article (and any supplementary files).

Acknowledgments

This work was supported by the Bavarian State Ministry of Science and the Arts through the Elite Network Bavaria (ENB) and through computational resources provided by the Bavarian Polymer Institute (BPI).

ORCID iD

Linn Leppert https://orcid.org/0000-0002-4361-4382

References

[1] Wahadoszamen M, Margalit I, Ara A M, van Grondelle R and Noy D 2014 *Nat. Commun.* **5** 5287
[2] Zoppi L and Baldridge K K 2018 *Int. J. Quantum Chem.* **118** e25413
[3] Muntwiler M, Yang Q, Tisdale W A and Zhu X Y 2008 *Phys. Rev. Lett.* **101** 196403
[4] Ohkita H *et al* 2008 *J. Am. Chem. Soc.* **130** 3030–42
[5] Pensack R D and Asbury J B 2009 *J. Am. Chem. Soc.* **131** 15986–7
[6] Lee J, Vandewal K, Yost S R, Bahlke M E, Goris L, Baldo M A, Manca J V and Van Voorhis T 2010 *J. Am. Chem. Soc.* **132** 11878–80
[7] Bakulin A A, Rao A, Pavelyev V G, van Loosdrecht P H M, Pshenichnikov M S, Niedzialek D, Cornil J, Beljonne D and Friend R H 2012 *Science* **335** 1340–4
[8] Caruso D and Troisi A 2012 *Proc. Natl Acad. Sci.* **109** 13498–502
[9] Murthy D H K, Gao M, Vermeulen M J W, Siebbeles L D A and Savenije T J 2012 *J. Phys. Chem.* C **116** 9214–20
[10] Yost S R and Van Voorhis T 2013 *J. Phys. Chem.* C **117** 5617–25
[11] Jakowetz A C, Böhm M L, Zhang J, Sadhanala A, Huettner S, Bakulin A A, Rao A and Friend R H 2016 *J. Am. Chem. Soc.* **138** 11672–9
[12] Lee D, Forsuelo M A, Kocherzhenko A A and Whaley K B 2017 *J. Phys. Chem.* C **121** 13043–51
[13] Jordanides X J, Scholes G D and Fleming G R 2001 *J. Phys. Chem.* B **105** 1652–69
[14] Camara-Artigas A, Brune D and Allen J P 2002 *Proc. Natl Acad. Sci.* **99** 11055–60
[15] Jonas D M, Lang M J, Nagasawa Y, Joo T and Fleming G R 1996 *J. Phys. Chem.* **100** 12660–73
[16] Schlau-Cohen G S, Re E D, Cogdell R J and Fleming G R 2012 *J. Phys. Chem. Lett.* **3** 2487–92
[17] Rancova O, Jankowiak R, Kell A, Jassas M and Abramavicius D 2016 *J. Phys. Chem.* B **120** 5601–16
[18] Mirkovic T, Ostroumov E E, Anna J M, Van Grondelle R and Scholes G D 2017 *Chem. Rev.* **117** 249–93
[19] Niedringhaus A, Policht V R, Sechrist R, Konar A, Laible P D, Bocian D F, Holten D, Kirmaier C and Ogilvie J P 2018 *Proc. Natl Acad. Sci.* **115** 3563–8
[20] Kawashima K and Ishikita H 2018 *Chem. Sci.* **9** 4083–92
[21] Kavanagh M A, Karlsson J K, Colburn J D, Barter L M and Gould I R 2020 *Proc. Natl Acad. Sci.* **117** 19705–12
[22] Cupellini L, Bondanza M, Nottoli M and Mennucci B 2020 *Biochim. Biophys. Acta (BBA)-Bioenerg.* **1861** 148049
[23] Wraight C A and Clayton R K 1974 *Biochim. Biophys. Acta (BBA)-Bioenerg.* **333** 246–60
[24] Kirmaier C, Holten D and Parson W W 1985 *Biochim. Biophys. Acta (BBA)-Bioenerg.* **810** 49–61
[25] Zinth W and Wachtveitl J 2005 *ChemPhysChem* **6** 871–80
[26] Ma F, Romero E, Jones M R, Novoderezhkin V I and van Grondelle R 2018 *J. Phys. Chem. Lett.* **9** 1827–32
[27] Ma F, Romero E, Jones M R, Novoderezhkin V I and van Grondelle R 2019 *Nat. Commun.* **10** 933
[28] Policht V R, Niedringhaus A, Willow R, Laible P D, Bocian D F, Kirmaier C, Holten D, Mančal T and Ogilvie J P 2022 *Sci. Adv.* **8** eabk0953
[29] van Brederode M E, Ridge J P, van Stokkum I H M, van Mourik F, Jones M R and van Grondelle R 1998 *Photosynth. Res.* **55** 141–6
[30] Zhou H and Boxer S G 1998 *J. Phys. Chem.* B **102** 9139–47
[31] Lin S, Jackson J, Taguchi A K W and Woodbury N W 1998 *J. Phys. Chem.* B **102** 4016–22
[32] Huang L, Ponomarenko N, Wiederrecht G P and Tiede D M 2012 *Proc. Natl Acad. Sci.* **109** 4851–6
[33] Fassioli F, Dinshaw R, Arpin P C and Scholes G D 2014 *J. R. Soc. Interface* **11** 20130901
[34] Jang S J and Mennucci B 2018 *Rev. Mod. Phys.* **90** 35003
[35] van der Vegte C P, Prajapati J D, Kleinekathöfer U, Knoester J and Jansen T L C 2015 *J. Phys. Chem.* B **119** 1302–13
[36] Curutchet C and Mennucci B 2016 *Chem. Rev.* **117** 294–343
[37] Thyrhaug E, Tempelaar R, Alcocer M J P, Žídek K, Bína D, Knoester J, Jansen T L C and Zigmantas D 2018 *Nat. Chem.* **10** 780–6
[38] Voityuk A A 2014 *J. Chem. Phys.* **140** 244117
[39] Voityuk A A 2015 *J. Phys. Chem.* B **119** 7417–21
[40] Li X, Parrish R M, Liu F, Kokkila Schumacher S I and Martínez T J 2017 *J. Chem. Theory Comput.* **13** 3493–504
[41] Sen S, Mascoli V, Liguori N, Croce R and Visscher L 2021 *J. Phys. Chem.* A **125** 4313–22
[42] Dreuw A and Head-Gordon M 2004 *J. Am. Chem. Soc.* **126** 4007–16
[43] Refaely-Abramson S, Baer R and Kronik L 2011 *Phys. Rev.* B **84** 075144
[44] Refaely-Abramson S, Sharifzadeh S, Govind N, Autschbach J, Neaton J B, Baer R and Kronik L 2012 *Phys. Rev. Lett.* **109** 226405
[45] Körzdörfer T and Marom N 2012 *Phys. Rev.* B **86** 041110
[46] Refaely-Abramson S, Sharifzadeh S, Jain M, Baer R, Neaton J B and Kronik L 2013 *Phys. Rev.* B **88** 081204

[47] De Queiroz T B and Kümmel S 2014 *J. Chem. Phys.* **141** 084303
[48] Manna A K, Refaely-Abramson S, Reilly A M, Tkatchenko A, Neaton J B and Kronik L 2018 *J. Chem. Theory Comput.* **14** 2919–29
[49] Wing D, Ohad G, Haber J B, Filip M R, Gant S E, Neaton J B and Kronik L 2020 *Proc. Natl Acad. Sci.* **118** e2104556118
[50] Seidl A, Görling A, Vogl P, Majewski J A and Levy M 1996 *Phys. Rev.* B **53** 3764–74
[51] Kümmel S 2017 *Adv. Energy Mater.* **7** 1700440
[52] Bhandari S, Cheung M S, Geva E, Kronik L and Dunietz B D 2018 *J. Chem. Theory Comput.* **14** 6287–94
[53] Rohlfing M and Louie S G 1998 *Phys. Rev. Lett.* **81** 2312–5
[54] Rohlfing M and Louie S G 2000 *Phys. Rev.* B **62** 4927
[55] van Setten M J *et al* 2015 *J. Chem. Theory Comput.* **11** 5665–87
[56] Bruneval F, Hamed S M and Neaton J B 2015 *J. Chem. Phys.* **142** 244101
[57] Rangel T, Hamed S M, Bruneval F and Neaton J B 2017 *J. Chem. Phys.* **146** 194108
[58] Duchemin I, Deutsch T and Blase X 2012 *Phys. Rev. Lett.* **109** 167801
[59] Duchemin I and Blase X 2013 *Phys. Rev.* B **87** 245412
[60] Sharifzadeh S, Darancet P, Kronik L and Neaton J B 2013 *J. Phys. Chem. Lett.* **4** 2197
[61] Blase X, Duchemin I and Jacquemin D 2018 *Chem. Soc. Rev.* **47** 1022–43
[62] Förster A and Visscher L 2022 *J. Chem. Theory Comput.* **18** 6779–93
[63] Hashemi Z and Leppert L 2021 *J. Phys. Chem.* A **125** 2163–72
[64] Volpert S, Hashemi Z, Foerster J M, Marques M R G, Schelter I, Kümmel S and Leppert L 2023 *J. Chem. Phys.* accepted (https://doi.org/10.1063/5.0139691)
[65] Aksu H, Schubert A, Geva E and Dunietz B D 2019 *J. Phys. Chem.* B **123** 8970–5
[66] Sirohiwal A, Neese F and Pantazis D A 2020 *J. Am. Chem. Soc.* **142** 18174–90
[67] Ahlrichs R, Bär M, Häser M, Horn H and Kölmel C 1989 *Chem. Phys. Lett.* **162** 165–9
[68] Bruneval F, Rangel T, Hamed S M, Shao M, Yang C and Neaton J B 2016 *Comput. Phys. Commun.* **208** 149–61
[69] Onida G, Reining L and Rubio A 2002 *Rev. Mod. Phys.* **74** 601
[70] Blase X, Duchemin I and Jacquemin D 2018 *Chem. Soc. Rev.* **47** 1022–43
[71] Blase X, Duchemin I, Jacquemin D and Loos P F 2020 *J. Phys. Chem. Lett.* **11** 7371–82
[72] Marques M A and Gross E K 2004 *Annu. Rev. Phys. Chem.* **55** 427–55
[73] Schelter I, Foerster J M, Gardiner A T, Roszak A W, Cogdell R J, Ullmann G M, de Queiroz T B and Kümmel S 2019 *J. Chem. Phys.* **151** 134114
[74] Stein T, Eisenberg H, Kronik L and Baer R 2010 *Phys. Rev. Lett.* **105** 266802
[75] Körzdörfer T, Sears J S, Sutton C and Brédas J L 2011 *J. Chem. Phys.* **135** 204107
[76] Baumeier B, Andrienko D and Rohlfing M 2012 *J. Chem. Theory Comput.* **8** 2790–5
[77] Godbout N, Salahub D R, Andzelm J and Wimmer E 1992 *Can. J. Chem.* **70** 560–71
[78] Bruneval F 2016 *J. Chem. Phys.* **145** 234110
[79] Plasser F, Wormit M and Dreuw A 2014 *J. Chem. Phys.* **141** 024106
[80] Plasser F and Lischka H 2012 *J. Chem. Theory Comput.* **8** 2777–89
[81] Camara-Artigas A, Brune D and Allen J 2002 *Proc. Natl Acad. Sci.* **99** 11055–60
[82] Papiz M Z, Prince S M, Howard T, Cogdell R J and Isaacs N W 2003 *J. Mol. Biol.* **326** 1523–38
[83] Dreuw A, Harbach P H, Mewes J M and Wormit M 2010 *Theor. Chem. Account.* **125** 419–26
[84] Kasha M, Rawls H R and El-Bayoumi M A 1965 *Pure Appl. Chem.* **11** 371–92
[85] Alvertis A M, Pandya R, Muscarella L A, Sawhney N, Nguyen M, Ehrler B, Rao A, Friend R H, Chin A W and Monserrat B 2020 *Phys. Rev.* B **102** 081122
[86] Hele T J H, Monserrat B and Alvertis A M 2021 *J. Chem. Phys.* **154** 244109
[87] Stanley R J, King B and Boxer S G 1996 *J. Phys. Chem.* **100** 12052–9
[88] Steffen M A, Lao K and Boxer S G 1994 *Science* **264** 810–6
[89] Hiyama M and Koga N 2011 *Photochem. Photobiol.* **87** 1297–307
[90] Lockhart D J, Kirmaier C, Holten D and Boxer S G 1990 *J. Chem. Phys.* **94** 6987–95
[91] Alden R G, Parson W W, Chu Z T and Warshel A 1995 *J. Am. Chem. Soc.* **117** 12284–98
[92] Gunner M R, Nicholls A and Honig B 1996 *J. Phys. Chem.* **100** 4277–91
[93] Saggu M, Fried S D and Boxer S G 2019 *J. Phys. Chem.* B **123** 1527–36
[94] Tamura H, Saito K and Ishikita H 2021 *Chem. Sci.* **12** 8131–40
[95] Brütting M, Foerster J M and Kümmel S 2021 *J. Phys. Chem.* B **125** 3468–75
[96] Förster A and Visscher L 2020 *J. Chem. Theory Comput.* **16** 7381–99
[97] Duchemin I and Blase X 2021 *J. Chem. Theory Comput.* **17** 2383–93
[98] Duchemin I, Jacquemin D and Blase X 2016 *J. Chem. Phys.* **144** 164106
[99] Duchemin I, Guido C A, Jacquemin D and Blase X 2018 *Chem. Sci.* **9** 4430–43
[100] Wehner J, Brombacher L, Brown J, Junghans C, Çaylak O, Khalak Y, Madhikar P, Tirimbò G and Baumeier B 2018 *J. Chem. Theory Comput.* **14** 6253–68

Supplementary Material - Mapping Charge-Transfer Excitations in Bacteriochlorophyll Dimers from First Principles

Zohreh Hashemi[1], **Matthias Knodt**[1], **Mario R. G. Marques**[1], **Linn Leppert**[1,2]

[1)]Institute of Physics, University of Bayreuth, Bayreuth 95440, Germany,
[2)]MESA+ Institute for Nanotechnology, University of Twente, 7500 AE Enschede, The Netherlands

E-mail: l.leppert@utwente.nl

1. Convergence Studies

1.1. Basis Set Convergence

We tested the convergence of our results with respect to the basis set size by calculating the first 15 excitations of a BCL *a* monomer using 8 different basis sets. The HOMO-LUMO gap and Q_y and Q_x excitation energies as a function of basis set size are listed in Table S1 and Table S2 for G_0W_0@ωPBE+BSE and TDDFT with the ωPBE exchange-correlation functional, respectively. The HOMO-LUMO gap and Q_y and Q_x excitation energies calculated with the def2-TZVP basis set differ by less than 10 meV from the more complete aug-cc-pVTZ basis set.

Basis set	# basis functions	HOMO-LUMO gap	Q_y	Q_x
6-311G	733	4.21	1.62	2.20
cc-pVDZ	852	4.10	1.53	2.11
6-311G*	968	4.09	1.52	2.11
TZVP	1164	4.07	1.52	2.10
6-311++G**	1308	4.07	1.52	2.10
def2-TZVP	1686	4.06	1.51	2.09
cc-pVTZ	1946	4.06	1.52	2.08
aug-cc-pVTZ	3040	4.05	1.51	2.10

Table S1: HOMO-LUMO gaps and Q_y and Q_x excitation energies (in eV) for BCL *a* monomer calculated with the G_0W_0@ωPBE+BSE method for different basis sets.

Basis set	# basis functions	HOMO-LUMO gap	Q_y	Q_x
6-311G	733	4.16	1.83	2.23
cc-pVDZ	852	4.10	1.78	2.20
6-311G*	968	4.09	1.77	2.19
TZVP	1164	4.07	1.76	2.18
6-311++G**	1308	4.06	1.74	2.17
def2-TZVP	1686	4.06	1.73	2.16
cc-pVTZ	1946	4.07	1.74	2.17
aug-cc-pVTZ	3040	4.06	1.73	2.16

Table S2: HOMO-LUMO gaps and Q_y and Q_x excitation energies (in eV) for BCL *a* monomer calculated with TDDFT using the ωPBE exchange-correlation functional for different basis sets.

1.2. Convergence With Respect To Virtual Orbital Subspace

We reduced the computational cost of our G_0W_0+BSE calculations by excluding the high-energy virtual states in the calculation of the *GW* self-energy. Figure S1 shows the convergence of the Q_y and Q_x excitation energies of the BCL *a* monomer as a function of the number of virtual states (N_{virt}) G_0W_0+BSE method and using the def2-TZVP basis set. Dashed lines correspond to a fit with the function $f(N_{virt}) = \frac{a}{N_{virt}+b} + c$, where a, b, and c are fit parameters. Using these fit parameters we estimated extrapolated values of the Q_y and Q_x excitations for $N_{virt} \to \infty$. The Q_y and Q_x excitation energies at $N_{virt} = 1000$ are within less than 20 meV from the extrapolated values at $N_{virt} \to \infty$. For $N_{virt} = 500$, the excitation energies are overestimating the extrapolated values by ∼80 meV.

Figure S2 demonstrates the error cancellation between using $N_{virt} = 500$ and the optimized virtual subspace scheme (see main text) with the def2-TZVP basis set for the occupied orbital subspace and 6-31G, 6-311G, TZV, 6-311++G**, TZVP and aug-ccpVDZ basis sets for the reduced virtual subspace used for the evaluation of the *GW* self-energy.

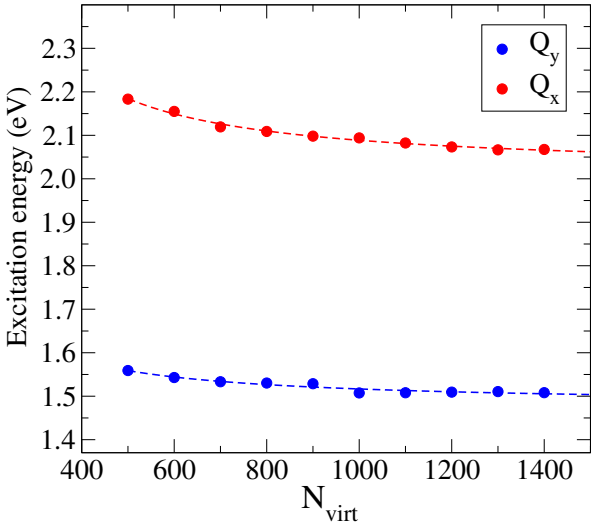

Figure S1: Q_y and Q_x excitation energies (in eV) for BCL *a* monomer calculated using the def2-TZVP basis set and G_0W_0@ωPBE+BSE as a function of the number of states explicitly used in the calculation of the *GW* polarizability.

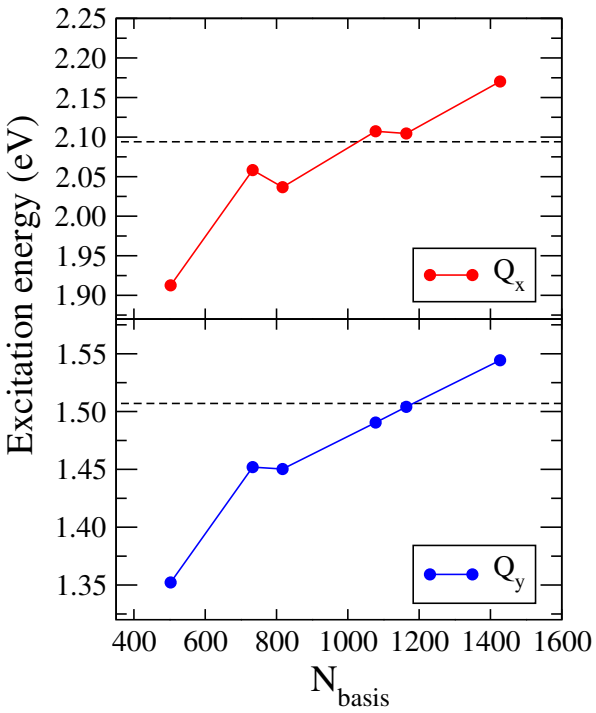

Figure S2: Q_y and Q_x excitation energies (in eV) for BCL *a* using G_0W_0@ωPBE+BSE, $N_{virt} = 500$, and the def2-TZVP basis set for the occupied orbital subspace as a function of different basis sets describing the virtual orbital subspace. The dashed line corresponds to values obtained with $N_{virt} = 1000$ and without the optimized virtual subspace scheme.

2. Additional Data

2.1. Comparison with Literature

Comparison of the first two low-lying bright excitation energies obtained in this work with previous data sets are presented in Table S5.

2.2. Additional GW/BSE and TDDFT Data for Artificial Dimer

Figure S6 depicts the excitation spectra of the artificial dimer with $r = 9, 11, 13$ Å calculated using the G_0W_0@ωPBE+BSE method. The excitation energies of the first 15 excitations for these systems using TDDFT with ωPBE and G_0W_0@ωPBE+BSE are reported in Table S6 and Table S7 along with their oscillator strengths.

2.3. Effect of Structural Relaxation

Structural relaxation can have significant effects on excitation energies. We demonstrate this in Figure S3 by comparing the TDDFT spectra calculated using a def2-TZVP basis and the ωPBE functional based on X-ray crystal structures of the B800 and B850 dimers without

	B800	A-branch	B850	SP
#	Energy (eV)	Energy (eV)	Energy (eV)	Energy (eV)
1	1.495 (0.56)	1.624 (0.23)	1.404 (0.61)	1.551 (0.58)
2	1.504 (0.06)	1.653 (0.45)	1.502 (0.10)	1.649 (0.05)
3	2.049 (0.01)	2.020 (0.14)	1.967 (0.00)	1.811 (0.08)
4	2.050 (0.12)	2.059 (0.11)	1.996 (0.00)	1.900 (0.09)
5	2.636 (0.00)	2.421 (0.00)	2.030 (0.12)	2.011 (0.16)
6	2.717 (0.00)	2.608 (0.00)	2.163 (0.00)	2.174 (0.01)
7	2.743 (0.00)	2.634 (0.00)	2.610 (0.00)	2.319 (0.00)
8	2.756 (0.00)	2.722 (0.00)	2.710 (0.00)	2.556 (0.00)
9	2.988 (0.00)	2.759 (0.00)	2.746 (0.00)	2.619 (0.00)
10	2.999 (0.00)	2.764 (0.00)	2.786 (0.00)	2.630 (0.00)
11	3.067 (0.00)	2.963 (0.02)	2.809 (0.00)	2.674 (0.00)
12	3.069 (0.00)	2.982 (0.00)	2.833 (0.00)	2.739 (0.00)
13	3.070 (0.00)	2.995 (0.00)	2.884 (0.00)	2.883 (0.02)
14	3.100 (0.34)	2.997 (0.00)	2.940 (0.00)	2.966 (0.01)
15	3.110 (0.86)	3.026 (0.01)	3.023 (0.01)	2.987 (0.01)

Table S3: Energies and oscillator strengths (in brackets) of the first 15 excitations of the B800, A-branch, B850 and SP dimers calculated using TDDFT with ωPBE.

and with constrained optimization of the structure. We tested two types of constrained optimization, in both cases using a def2-TZVP basis set and the B3LYP exchange-correlation functional: In the first optimization, we fixed the central Mg and neighboring N atoms, and in the second one the central Mg and the functional group FG2, which corresponds to the phytyl tail of BCL. Both constraints lead to very similar structures and thus excitation spectra, shown in panels (a) and (b) in Figure S3 for the B800 and the B850 dimer, respectively.

These constrained optimizations show that, as expected, the excitation energies differ quantitatively from our results for the unrelaxed crystal structures. However, structural relaxation does not change the main message of our paper: The B850 dimer is representative of an intermediate coupling regime, where charge-transfer excitations appear in the vicinity of the coupled Qx excitations and may mix with those depending on details of structure (and additional environment and temperature effects in vivo).

3. Difference Densities

The difference densities of the first 10 excitations are shown in Figure S7. Table S8 lists the integrals over subsystem difference densities as described in the main text.

	B800	A-branch	B850	SP
#	Energy (eV)	Energy (eV)	Energy (eV)	Energy (eV)
1	1.273 (0.43)	1.416 (0.19)	1.200 (0.46)	1.385 (0.52)
2	1.281 (0.05)	1.445 (0.36)	1.286 (0.07)	1.465 (0.04)
3	2.039 (0.05)	2.002 (0.16)	1.894 (0.00)	1.807 (0.02)
4	2.041 (0.09)	2.059 (0.13)	1.975 (0.02)	1.889 (0.10)
5	2.506 (0.00)	2.413 (0.00)	2.021 (0.12)	1.999 (0.18)
6	2.550 (0.00)	2.695 (0.00)	2.088 (0.01)	2.174 (0.01)
7	2.777 (0.00)	2.741 (0.00)	2.620 (0.00)	2.397 (0.00)
8	2.796 (0.01)	2.760 (0.00)	2.765 (0.00)	2.644 (0.00)
9	2.807 (0.00)	2.771 (0.00)	2.798 (0.00)	2.679 (0.00)
10	2.987 (0.15)	2.832 (0.00)	2.822 (0.00)	2.711 (0.00)
11	2.994 (1.09)	2.893 (0.00)	2.852 (0.00)	2.725 (0.00)
12	3.042 (0.00)	2.944 (0.00)	2.898 (0.02)	2.767 (0.00)
13	3.046 (0.00)	3.037 (0.02)	2.970 (0.25)	2.910 (0.00)
14	3.048 (0.00)	3.053 (0.00)	3.005 (0.17)	3.012 (0.01)
15	3.065 (0.00)	3.273 (0.52)	3.021 (0.07)	3.078 (0.00)

Table S4: Energies and oscillator strengths (in brackets) of the first 15 excitations of the B800, A-branch, B850, and SP dimers calculated using the $G_0W_0@\omega$PBE+BSE approach.

Dimer	G_0W_0@ωPBE+BSE		TD-ωPBE		literature	
	E_1	E_2	E_1	E_2	E_1	E_2
B800	1.27	1.28	1.49	1.50	1.40[a], 1.89[b]	1.41[a], 1.90[b]
B850	1.20	1.29	1.40	1.50	1.32[a], 1.80[b]	1.43[a], 1.98[b]
SP	1.39	1.47	1.55	1.65	1.53[c], 1.87[d]	1.62[c], 1.92[d]

Table S5: Comparison of the first two excitation energies (in eV) of our calculations and literature results for dimeric systems extracted from B800, B850 and SP. Our own GW/BSE and TDDFT excitation energies are calculated using a def2-TZVP basis and the ωPBE functional as a starting point for G_0W_0 and in TDDFT, respectively, while literature values are calculated at different levels of theory.

[a]Results from Ref. [1], starting from the same crystal structure as we used (PBD id: 1NKZ), but relaxed and thermalized using molecular dynamics. Excitation energies are calculated using QM/MMPOL calculations with TDDFT/CAM-B3LYP/6-31G(d) for the QM part.

[b]Results from Ref. [2], using the crystal structure without optimization, and calculated using the CIS approach and a 3-21G* basis set.

[c]Results from Ref. [3]. Suomivuori and et al. calculated excitation energy of SP and the coordinating Histidine residues using a crystal structure from Rhodobacter sphaeroides (PBD id: 3I4D) at RVS-LT-SOS-ADC2/def2-TZVP level of theory.

[d]Results from Ref. [4] using TDDFT with ωPBE (ω=0.15) and 6-31G** basis set in combination with polarizable continuum model (PCM). The structure of the SP dimer is relaxed by employing the ωB97X-D functional and the 6-31G** basis set with PCM.

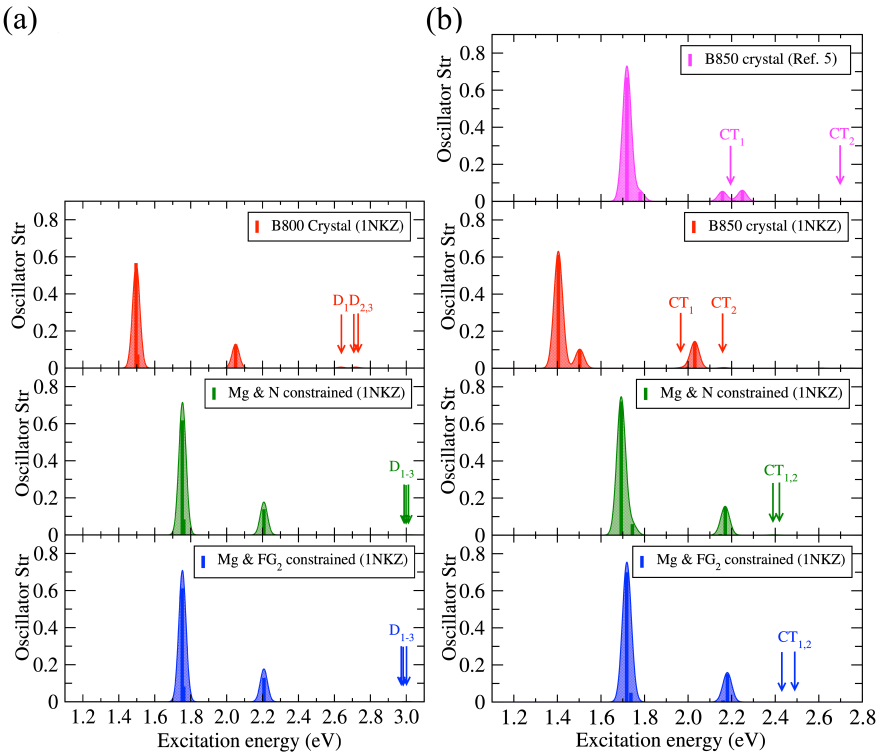

Figure S3: (a) TDDFT spectra of B800 dimer using the crystal structure with PDB id 1NKZ (red) and after constrained optimization (green and blue), (b) TDDFT spectra of B850 using a crystal structure from Ref. [5] (magenta), the 1NKZ crystal structure (red), and after constrained optimization (green and blue).

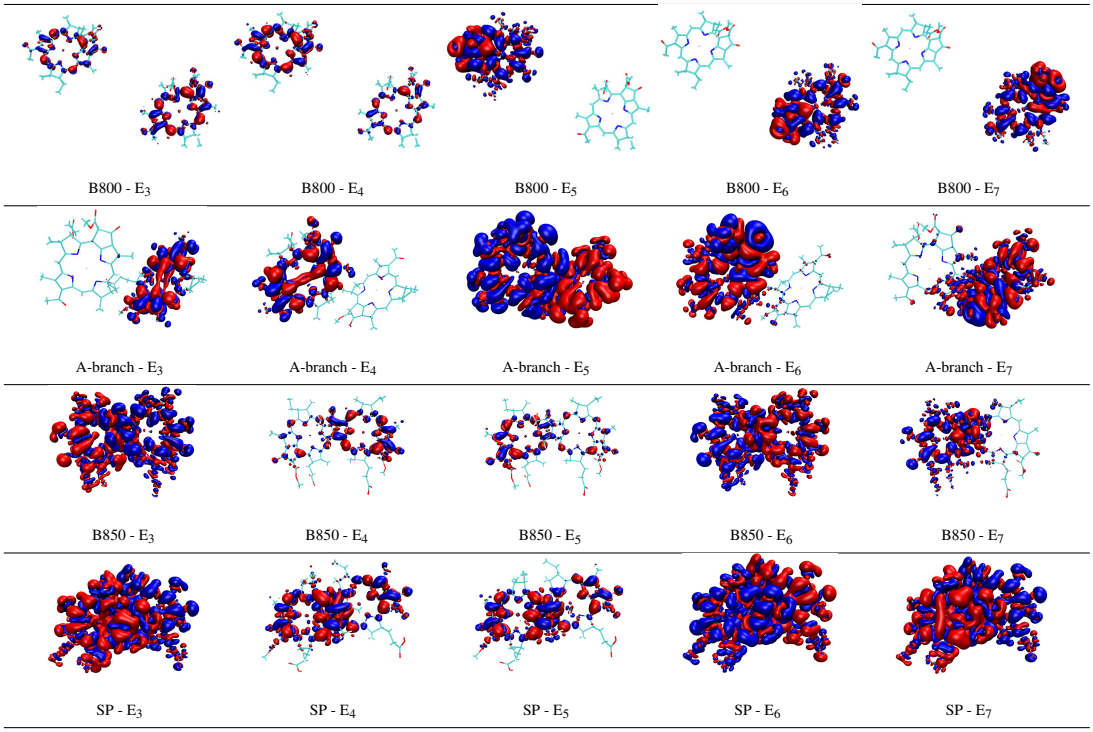

Figure S4: Difference densities of excitations E_3 – E_7 calculated using TDDFT with ωPBE for B800, A-branch, B850 and SP dimers. Here and in the following, positive isovalues (blue) correspond to areas of decreased electron density (holes) and negative isovalues (red) correspond to areas of increased electron density (electrons).

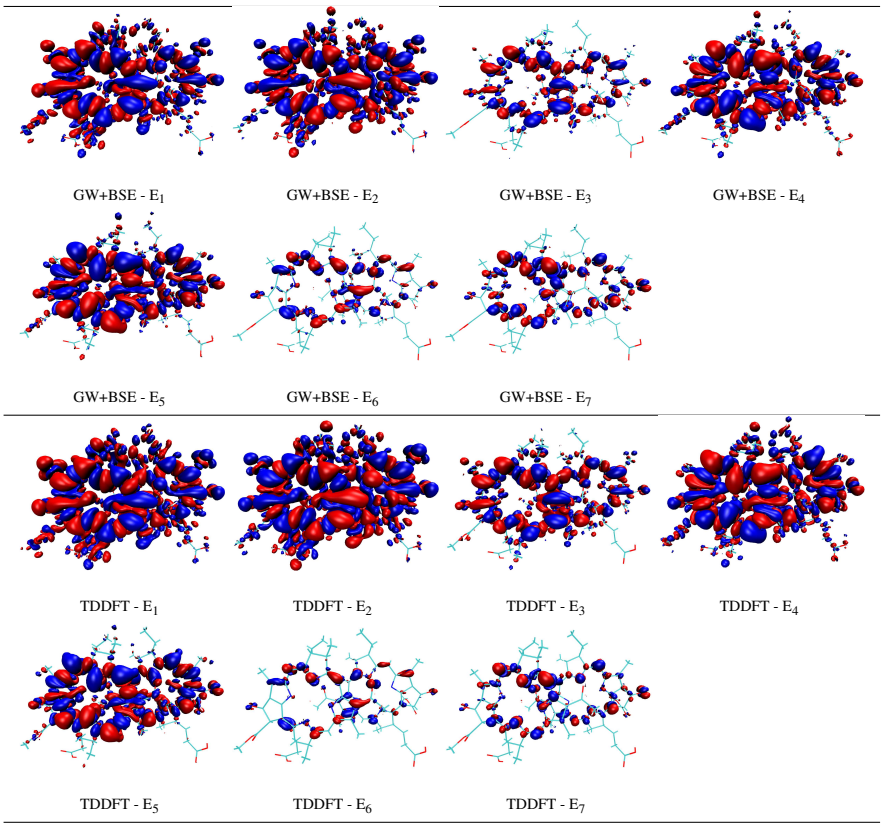

Figure S5: Transition densities of excitations $E_1 - E_7$ for SP dimer calculated using G_0W_0@ωPBE+BSE and TDDFT with ωPBE, respectively.

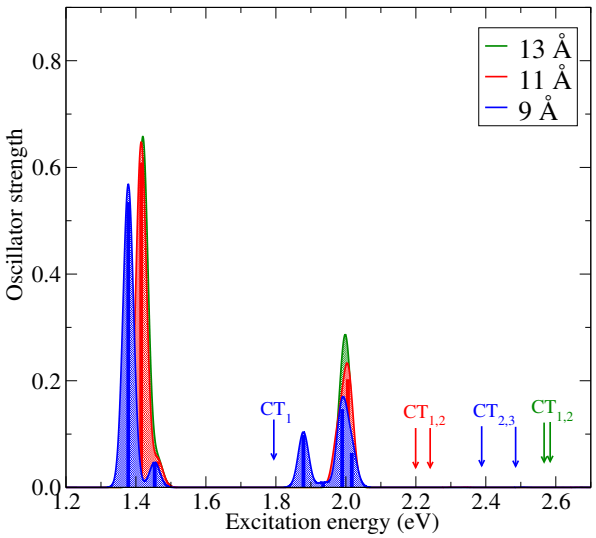

Figure S6: Absorption spectra of artificial dimers with $r = 9, 11, 13$ Å calculated using the G_0W_0@ωPBE+BSE approach. Arrows mark excitations with charge-transfer characters. The shaded areas are calculated by folding the eigenvalues with Gaussian functions with a width of 0.08 eV as a guide to the eye.

	9 Å	11 Å	13 Å
#	Energy (eV)	Energy (eV)	Energy (eV)
1	1.555 (0.63)	1.617 (0.75)	1.628 (0.76)
2	1.641 (0.04)	1.668 (0.05)	1.674 (0.06)
3	1.901 (0.08)	1.999 (0.07)	2.012 (0.07)
4	1.941 (0.02)	2.025 (0.18)	2.026 (0.19)
5	2.011 (0.13)	2.297 (0.00)	2.568 (0.00)
6	2.031 (0.08)	2.337 (0.00)	2.572 (0.00)
7	2.444 (0.00)	2.569 (0.00)	2.594 (0.00)
8	2.516 (0.00)	2.573 (0.00)	2.624 (0.00)
9	2.564 (0.00)	2.689 (0.00)	2.692 (0.00)
10	2.565 (0.00)	2.691 (0.00)	2.694 (0.00)
11	2.659 (0.00)	2.842 (0.00)	2.974 (0.01)
12	2.679 (0.00)	2.886 (0.00)	2.974 (0.01)
13	2.900 (0.01)	2.980 (0.03)	2.990 (0.01)
14	2.968 (0.01)	2.984 (0.01)	2.992 (0.00)
15	3.008 (0.00)	3.022 (0.00)	3.163 (0.00)

Table S6: Excitation energies and oscillator strengths (in brackets) of the first 15 excitations of the artificial dimer with $r = 9, 11, 13$ Å calculated using TDDFT with ωPBE.

	9 Å	11 Å	13 Å
#	Energy (eV)	Energy (eV)	Energy (eV)
1	1.419 (0.61)	1.415 (0.60)	1.419 (0.61)
2	1.462 (0.04)	1.462 (0.04)	1.462 (0.04)
3	1.985 (0.08)	1.977 (0.08)	1.985 (0.08)
4	2.001 (0.21)	2.006 (0.20)	2.001 (0.21)
5	2.590 (0.00)	2.297 (0.00)	2.590 (0.00)
6	2.620 (0.00)	2.339 (0.00)	2.620 (0.00)
7	2.672 (0.00)	2.659 (0.00)	2.672 (0.00)
8	2.673 (0.00)	2.667 (0.00)	2.673 (0.00)
9	2.710 (0.01)	2.703 (0.01)	2.710 (0.01)
10	2.712 (0.01)	2.708 (0.01)	2.712 (0.01)
11	2.953 (0.00)	2.801 (0.00)	2.953 (0.00)
12	2.961 (0.00)	2.922 (0.00)	2.961 (0.00)
13	3.147 (0.01)	2.948 (0.00)	3.147 (0.01)
14	3.198 (0.01)	2.981 (0.00)	3.198 (0.01)
15	3.224 (0.00)	3.296 (0.04)	3.224 (0.00)

Table S7: Excitation energies and oscillator strengths (in brackets) of the first 15 excitations of the artificial dimer with $r = 9, 11, 13$ Å calculated using the G_0W_0@ωPBE+BSE approach.

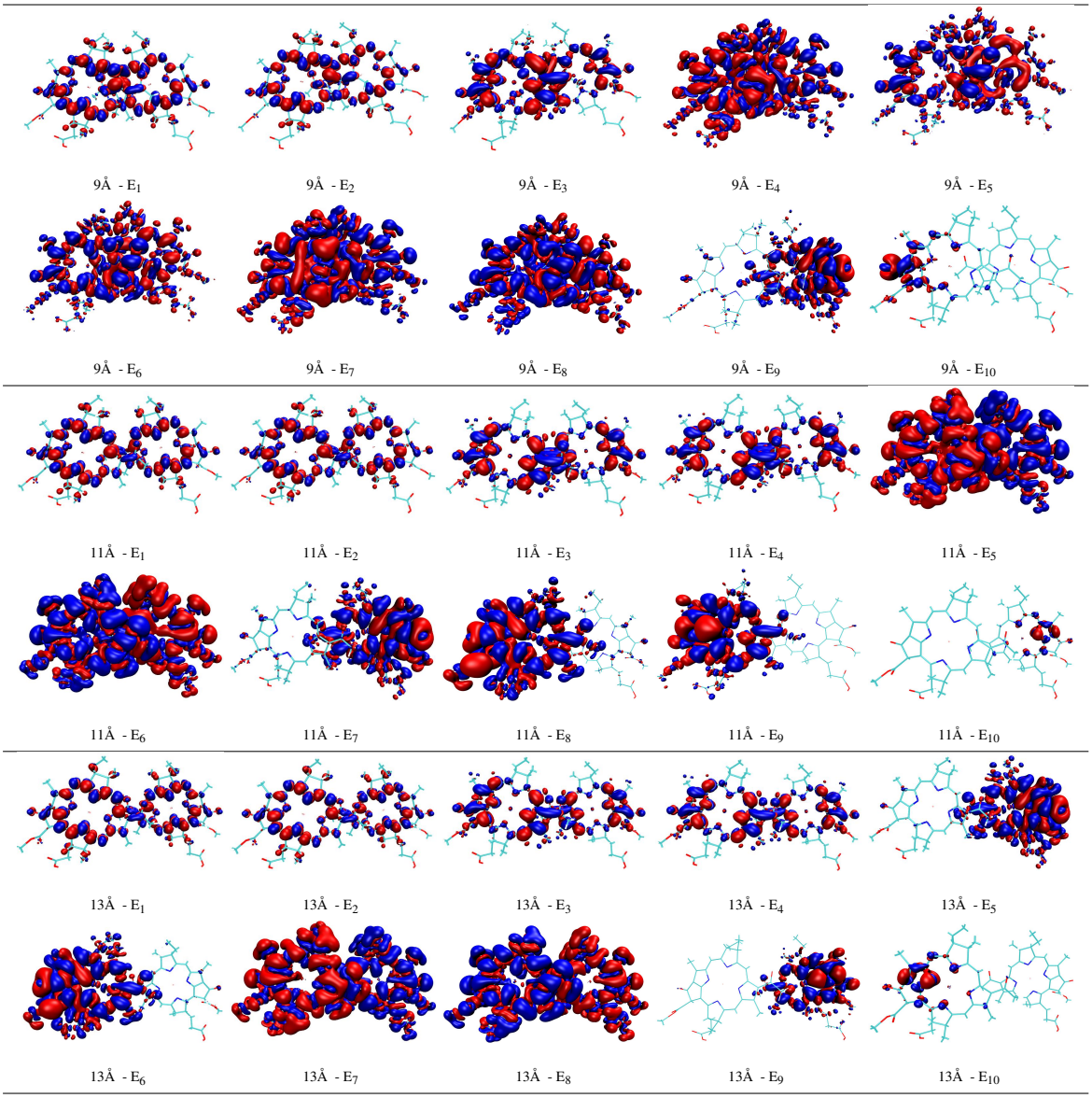

Figure S7: Difference densities of the first 10 excitations of artificial dimers with $r = 9, 11, 13$ Å calculated using TDDFT with ωPBE.

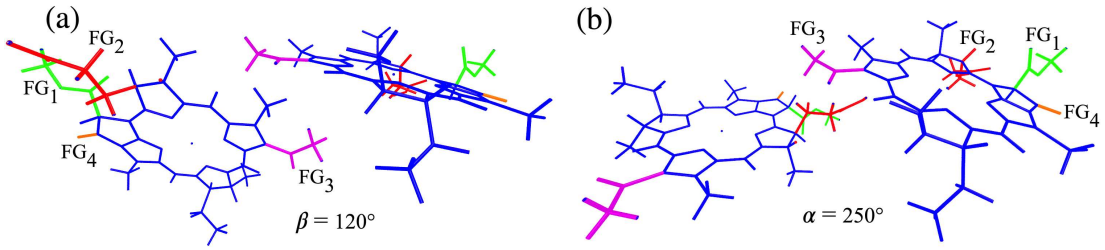

Figure S8: Artificial dimer with rotation angles (a) β=120° and (b) α=250° that lead to the first and second largest red shift in the excitation energy of CT_1, respectively.

r (Å)	molecule	charge distribution						
		E_4	E_5	E_6	E_7	E_8	E_9	E_{10}
9	P_{A1}	-0.48	0.21	0.28	-0.62	-0.63	0	0
	P_{A2}	0.48	-0.21	-0.28	0.62	0.63	0	0
10	P_{A1}	0	-0.89	0.90	0	0	-0.85	0
	P_{A2}	0	0.89	-0.90	0	0	0.85	0
11	P_{A1}	0	-0.96	0.96	0	0	0	0
	P_{A2}	0	0.96	-0.96	0	0	0	0
12	P_{A1}	0	-0.98	0.98	0	0	0	0
	P_{A2}	0	0.98	-0.98	0	0	0	0
13	P_{A1}	0	0	0	-0.99	0.99	0	0
	P_{A2}	0	0	0	0.99	-0.99	0	0
14	P_{A1}	0	0	0	0	0	-0.99	0.99
	P_{A2}	0	0	0	0	0	0.99	-0.99
15	P_{A1}	0	0	0	0	0	-0.99	0.99
	P_{A2}	0	0	0	0	0	0.99	-0.99
21	P_{A1}	0	0	0	0	0	-0.99	0.99
	P_{A2}	0	0	0	0	0	0.99	-0.99

Table S8: Difference densities of E_4 – E_{10} integrated over subsystem volumes calculated using TDDFT with ωPBE for artificial dimer as a function of r.

#	Energy (eV)
1	1.585 (0.02)
2	1.678 (0.25)
3	1.748 (0.42)
4	2.074 (0.06)
5	2.128 (0.10)
6	2.171 (0.03)
7	2.734 (0.00)
8	3.010 (0.00)
9	3.041 (0.00)
10	3.066 (0.00)
11	3.146 (0.00)
12	3.167 (0.00)
13	3.203 (0.11)
14	3.227 (0.00)
15	3.244 (0.03)

Table S9: Energies and oscillator strengths (in brackets) of the first 15 excitations of relaxed dimer calculated using TDDFT with ωPBE.

dimer	molecule	charge distribution						
		E_1	E_2	E_3	E_4	E_5	E_6	E_7
SP	P_A	0.78	0	0	0	0	-0.63	0.88
	P_B	-0.78	0	0	0	0	0.63	-0.88

Table S10: Difference density integrated over subsystem volumes of the charge-transfer excitations of relaxed dimer calculated using TDDFT with ωPBE.

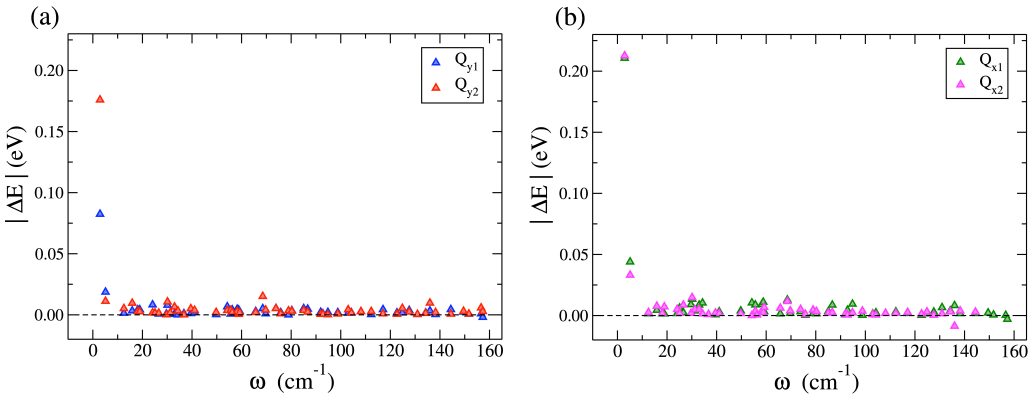

Figure S9: Excitation energy change, $|\Delta E|$, as a function of normal mode frequency for the coupled (a) Q_y and (b) Q_x excitations.

[1] Cupellini L, Jurinovich S, Campetella M, Caprasecca S, Guido C A, Kelly S M, Gardiner A T, Cogdell R and Mennucci B 2016 *The Journal of Physical Chemistry B* **120** 11348–11359
[2] Scholes G D, Gould I R, Cogdell R J and Fleming G R 1999 *The Journal of Physical Chemistry B* **103** 2543–2553
[3] Suomivuori C M, Winter N O, Hättig C, Sundholm D and Kaila V R 2016 *Journal of Chemical Theory and Computation* **12** 2644–2651
[4] Aksu H, Schubert A, Bhandari S, Yamada A, Geva E and Dunietz B D 2020 *The Journal of Physical Chemistry B* **124** 1987–1994
[5] Schelter I, Foerster J M, Gardiner A T, Roszak A W, Cogdell R J, Ullmann G M, de Queiroz T B and Kümmel S 2019 *The Journal of Chemical Physics* **151** 134114

Publication IV

Delocalized Electronic Excitations and their Role in Directional Charge Transfer in the Reaction Center of Rhodobacter Sphaeroides

Reprinted from

The Journal of Chemical Physics A, 158, 195102 (2023)

Sabrina Volpert[1], **Zohreh Hashemi**[1], Johannes M. Foerster[1], Mario R. G. Marques[1], Ingo Schelter[1], Stephan Kümmel[1], and Linn Leppert[1,2]

1) Institute of Physics, University of Bayreuth, Bayreuth 95440, Germany

2) MESA+ Institute for Nanotechnology, University of Twente, 7500 AE Enschede, The Netherlands

My contribution

S. Volpert is the lead contributor to this publication. S. Volpert and J. M. Foerster were involved in the molecular structure preparation. I. Schelter designed tools for the data analyses such as scripts for calculating the excited states difference densities based on output from Q-CHEM. M. R. G. Marques performed the vibrational calculations. S. Kümmel and L. Leppert supervised the study. The main results included in this publication are presented in three sections. The computational study presented in section B was carried out by S. Volpert. S. Volpert also produced preliminary results for section C. All simulations that are presented in the final version of the manuscript were produced by me. I also prepared all figures and tables in the main text, some based on an earlier draft of the paper by S. Volpert, and the majority of the supplementary material. L. Leppert, S. Volpert, and I wrote the first draft of the article, and all authors were involved in scientific discussions and finalizing the manuscript.

The Journal of Chemical Physics

RESEARCH ARTICLE | MAY 15 2023

Delocalized electronic excitations and their role in directional charge transfer in the reaction center of *Rhodobacter sphaeroides*

Special Collection: 2023 JCP Emerging Investigators Special Collection

Sabrina Volpert; Zohreh Hashemi; Johannes M. Foerster; ... et. al

J. Chem. Phys. 158, 195102 (2023)
https://doi.org/10.1063/5.0139691

The Journal of Chemical Physics ARTICLE scitation.org/journal/jcp

Delocalized electronic excitations and their role in directional charge transfer in the reaction center of *Rhodobacter sphaeroides*

Cite as: J. Chem. Phys. **158**, 195102 (2023); doi: 10.1063/5.0139691
Submitted: 22 December 2022 • Accepted: 16 March 2023 •
Published Online: 15 May 2023

View Online Export Citation CrossMark

Sabrina Volpert,[1] Zohreh Hashemi,[1] Johannes M. Foerster,[1] Mario R. G. Marques,[1] Ingo Schelter,[1] Stephan Kümmel,[1] and Linn Leppert[1,2,a)]

AFFILIATIONS

[1] Institute of Physics, University of Bayreuth, 95440 Bayreuth, Germany
[2] MESA+ Institute for Nanotechnology, University of Twente, 7500 AE Enschede, The Netherlands

Note: This paper is part of the 2023 JCP Emerging Investigators Special Collection.
[a)] Author to whom correspondence should be addressed: l.leppert@utwente.nl

ABSTRACT

In purple bacteria, the fundamental charge-separation step that drives the conversion of radiation energy into chemical energy proceeds along one branch—the A branch—of a heterodimeric pigment–protein complex, the reaction center. Here, we use first principles time-dependent density functional theory (TDDFT) with an optimally-tuned range-separated hybrid functional to investigate the electronic and excited-state structure of the six primary pigments in the reaction center of *Rhodobacter sphaeroides*. By explicitly including amino-acid residues surrounding these six pigments in our TDDFT calculations, we systematically study the effect of the protein environment on energy and charge-transfer excitations. Our calculations show that a forward charge transfer into the A branch is significantly lower in energy than the first charge transfer into the B branch, in agreement with the unidirectional charge transfer observed experimentally. We further show that the inclusion of the protein environment redshifts this excitation significantly, allowing for energy transfer from the coupled Q_x excitations. Through analysis of transition and difference densities, we demonstrate that most of the Q-band excitations are strongly delocalized over several pigments and that both their spatial delocalization and charge-transfer character determine how strongly affected they are by thermally-activated molecular vibrations. Our results suggest a mechanism for charge-transfer in this bacterial reaction center and pave the way for further first-principles investigations of the interplay between delocalized excited states, vibronic coupling, and the role of the protein environment in this and other complex light-harvesting systems.

I. INTRODUCTION

In natural photosynthesis, the energy of sunlight is converted into chemical energy in highly efficient excitation- and charge-transfer processes.[1] Absorption of light happens primarily in antenna complexes, which funnel the excitation energy toward the reaction center (RC), where a charge-separation step initiates a cascade of electron-transfer processes resulting in a proton gradient that drives the biochemical reactions of photosynthesis. In purple bacteria such as *Rhodobacter sphaeroides*, the fundamental design principles of these pigment-protein complexes are well understood due to a wealth of experimental and computational techniques that give access to detailed structural and spectroscopic information.[2–9] In this respect, the bacterial RC can also be understood as a model system for the RC of more complex photosynthetic organisms because its structure is highly conserved across bacteria, algae, and plants.[10] Its main building blocks, shown in Fig. 1, are arranged along two pseudosymmetric branches A and B and consist of a strongly coupled dimer of two bacteriochlorophyll (BCL) molecules dubbed the special pair (P), two accessory BCLs (B_A, B_B), two bacteriopheophytins (H_A, H_B), and two quinones (Q_A, Q_B) embedded in a transmembrane protein matrix.

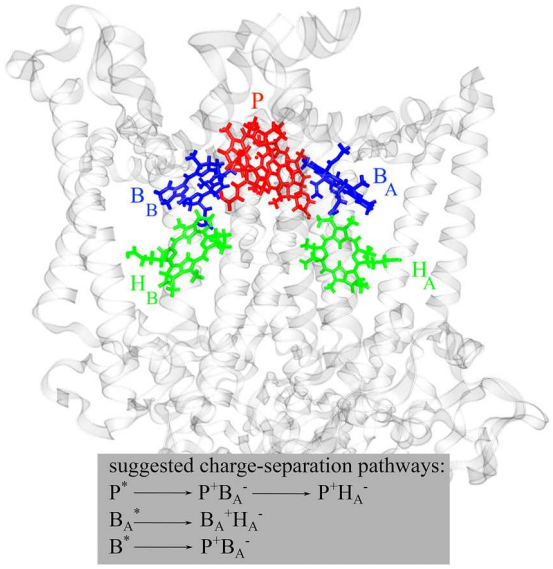

FIG. 1. Proposed charge-separation pathways[7,15,19–22] and structural model of the RC of *Rhodobacter sphaeroides*, including the special pair (*P* in red), two accessory BCLs (B_A, B_B in blue), and two bacteriopheophytins (H_A, H_B in green). Protein chains are shown in transparent gray. Hydrogen atoms are omitted for clarity.

Despite the similar, but not exactly symmetric, structure of the *A* and *B* branches, it is well-established that the primary charge separation reaction only proceeds along the *A* branch with near-unity quantum efficiency.[11–13] The ultrafast timescales on which the primary energy- and charge-transfer processes occur in the RC, in combination with broad overlapping absorption peaks originating from the coupling of multiple pigments and their protein environments, have posed significant challenges to spectroscopic techniques. Two-dimensional electronic spectroscopy (2DES) has become one of the primary experimental techniques for studying the bacterial RC[7,14–16] and other photosynthetic systems.[17,18] For the RC of *Rhodobacter sphaeroides* and similar RCs, 2DES has been used to propose models for the kinetics of the primary charge separation. In these models, it is usually assumed that charge separation is initiated through the excitation of *P* (denoted as P^*), leading to a charge-transfer intermediate $P_A^- P_B^+$, which is followed by a charge-separated state $P^+H_A^-$ via an ultra-shortlived intermediate $P^+B_A^-$;[7,15] however, alternative charge-separation pathways have been suggested as well, for example, starting from an excitation localized on one or both accessory BCLs, i.e., B_A^* or B^*[19–22] (Fig. 1).

Computational modeling has played an important role in helping to unravel the intricate factors affecting excitation and charge transfer in the antenna complexes and the RC. Calculations based on model Hamiltonians and advances in the semiempirical modeling of long- and short-range coupling between chromophores have allowed for the simulation of excitation processes in large pigment-protein complexes.[23–25] However, also computationally more demanding first-principles calculations, primarily based on (time-dependent) density functional theory (TDDFT), have been employed to study systems of growing complexity and size. The focus of many studies has been the origin of the unidirectionality of the charge-separation process in bacterial RCs and photosystem II of plants.

For the RC of photosystem II, a large model system was used by Frankcombe, including four (truncated) chlorophyll molecules, two pheophytin molecules, and two plastoquinone molecules using TDDFT and a polarizable continuum model (PCM) to account for effects of the protein environment.[26] Later, Sirohiwal *et al.* reported TDDFT calculations using a range-separated hybrid functional on chlorophyll monomers, dimers, and trimers of the photosystem II RC showing that the lowest-energy charge-transfer excitation corresponds to $B_A^+H_A^-$ and is strongly affected by protein electrostatics.[27] Low-energy charge-transfer excitations were also reported by Kavanagh *et al.* in TDDFT calculations using a hexameric model of the photosystem II RC, which included parts of the protein environment explicitly. Similarly, Förster *et al.* observed an excitation with a partial $B_A^+H_A^-$ charge-transfer character using the *GW* + Bethe-Salpeter Equation approach.[28]

For the RC of *Rhodobacter sphaeroides*, (TD)DFT calculations including the special pair and some of its neighboring amino-acid residues were reported in 2011 by Wawrzyniak *et al.* and indicated that protein induced distortions of the special pair geometry lead to an asymmetric ground-state electron density.[29] A similar model system was employed by Eisenmayer *et al.*, who performed molecular dynamics simulations based on constrained DFT and showed that the electron-density asymmetry is dynamical and coupled to a low-frequency vibrational mode related to the rotation of a histidine residue close to B_A.[30] Later, Eisenmayer *et al.* included the B_A in their constrained DFT simulations showing the coupling of proton displacements to the primary electron-transfer step from *P* to B_A.[31] Aksu *et al.* combined TDDFT with a tuned range-separated hybrid functional with PCM and showed that spectral asymmetries arise from locally different dielectric environments along the *A* and *B* branches.[32] The initial charge-transfer excitations of *P* were also studied by Aksu *et al.*, employing the same methodology.[33] (TD)DFT calculations by Mitsuhashi *et al.*, in which the environment of *P* together with either B_A or B_B was represented using a QM/MM/PCM scheme, further indicated that the lowest unoccupied molecular orbital (LUMO) of B_A is lower in energy than the LUMO of B_B, suggesting that B_A is the primary electron acceptor.[34] Another study, in which some of the same authors used a diabatization scheme to evaluate electronic couplings between *P* and B_A and B_B, respectively, pointed to the particular importance of a tyrosine residue close to B_A as being responsible for the directionality of charge transfer.[35] Brütting *et al.* investigated the primary charge separation step in the quasi-symmetric reaction center of *Heliobacterium* modesticaldum, with an emphasis on revealing the influence of nuclear motion on the relative energetic positions of different electronic excitations.[36]

To the best of our knowledge, explicit TDDFT calculations on a reaction center model of *Rhodobacter sphaeroides*, including all six primary pigments and parts of the environment, have not been reported yet. Furthermore, while previous studies have provided detailed insight into the effects of the protein environment and molecular vibrations on excited states, little attention has been directed at the delocalized, correlated multi-particle nature of these excitations. One may wonder whether these characteristics can be

properly captured by TDDFT, as the wave functions obtained in TDDFT have no rigorous physical meaning. We here show, however, that one can analyze the excitations reliably based on transition densities and difference densities, i.e., quantities that have a solid foundation in TDDFT.

To this end, we use TDDFT with an optimally-tuned range-separated hybrid functional to study a hexameric model of the RC, including the primary pigments, i.e., the special pair P, the accessory BCLs B_A and B_B, and the bacteriopheophytins H_A and H_B. We also explicitly model the effect of close-lying amino-acid residues on the excited states by including them in our TDDFT calculations. We clarify which amino acids are responsible for significant changes in excited-state energies and compare our results with QM/MM calculations. Our calculations show that a distinction between localized excitations on the one hand and charge-transfer excitations on the other hand is of limited usefulness to understand the excited state structure of this system of strongly coupled pigments. Instead, we find excitations without charge-transfer character that are delocalized across several pigments and that cannot readily be classified as coupled excitations of individual monomeric units. Partial charge-transfer states between the special pair pigments $(P_A^- P_B^+)$ are low in energy, mix with these delocalized states, and are a consequence of the strong coupling between the pigments. The lowest-energy charge-transfer state that transfers an electron into the A branch can clearly be classified as $B_A^- H_A^+$ and is significantly lower in energy than charge-transfer into the B branch. This is in agreement with previous first-principles calculations on the photosystem II reaction center but not in line with experimental reports suggesting charge-transfer through an intermediate $P^+ B_A^-$ state. The $B_A^- H_A^+$ excitation is ~20 meV higher in energy than the highest-energy Q-band excitations. Although we cannot rule out that including further parts of the environment might lower its energy further, such a small energetic separation suggests that the vibrational modes of the pigments and/or the environment could couple this charge-transfer state to the delocalized Q-band excitations.

II. COMPUTATIONAL METHODS

A. Structure of model systems

All our calculations are based on the experimental crystal structure of the wild-type RC of *Rhodobacter sphaeroides* with Protein Data Bank file ID 1M3X.[3] The pigment–protein complex has two main protein chains called L- and M-chains, which form the backbone of the A and B branches, respectively. We are interested in the primary charge-transfer process and, therefore, have included P, B_A, B_B, H_A, and H_B in all our computational models. For approximating the effect of the protein environment on energy- and charge-transfer excitations, we added amino-acid residues explicitly to our model structures, as described in more detail in Sec. III B. Hydrogen atoms are not resolved in the experimental crystal structure and are, therefore, added with the module HBUILD in CHARMM[37] and energetically optimized using the CHARMM force field[38] as described in Ref. 39. In all model systems, we cropped the phytyl tails of the BCL molecules and saturated the carboxyl group with a hydrogen atom. Using a methyl group to saturate the phytyl tail does not change the main conclusions of this paper, as shown in Fig. S1 of the supplementary material. Furthermore, we cut the bonds between the amino-acid residues and the polypeptide chains between C_α and C_β and saturated them with hydrogen atoms.

B. TDDFT calculations

We performed linear-response TDDFT (LR-TDDFT) calculations using Q-CHEM, version 5.2.2.[40] Vibrational normal modes were calculated with TURBOMOLE version 7.5[41,42] and QM/MM simulations with ORCA version 5.0.2.[43] We used the Pople basis set 6-31G(d,p) for which the Q_y and Q_x excitation energies of a single BCL a molecule are converged to within 50 meV.[39] We also tested the accuracy of the basis set for the special pair P, as discussed in the supplementary material (Table S1). The exchange-correlation energy is approximated using the optimally-tuned ωPBE functional,[44] which has been shown to properly capture the coupling between BCLs[39] and to be *on par* with Green's function-based many-body perturbation theory for a wide range of single chromophores.[45,46] Range-separated hybrid functionals have also been demonstrated to accurately describe electrochromic shifts due to the protein environments of various biochromophores in an extensive benchmark of DFT approximations by Sirohiwal *et al.*[47] In the optimally-tuned ωPBE functional, the range–separation parameter determines the length scale at which short-range semilocal exchange goes over into exact long-range exchange. Such functionals significantly improve the description of charge-transfer excitations[48] and lead to excellent agreement with experimental photoemission spectroscopy for a broad range of systems, from molecules to solids.[49–55] In the optimal-tuning procedure, the range–separation parameter ω is varied such that the difference between the HOMO eigenvalue ε_{HOMO} and the negative ionization potential of both the neutral and the anionic system is minimized.[56] Here, we use $\omega = 0.171 a_0^{-1}$ based on tuning for one BCL a performed by Schelter *et al.*[39] We confirmed that the deviation of the ionization potentials from $-\varepsilon_{HOMO}$ of P and of a single BCL a with coordinating histidine is negligible, and we do not perform a separate tuning procedure for each of our model systems. This approach is also supported by more general arguments: Using the same ω for each model system allows us to compare the electronic and excited state structures of our model systems on the same footing. Furthermore, optimal tuning of conjugated systems of increasing size leads to artificially low values of ω and, thus, a dominance of semilocal exchange at long range, which deteriorates the description of charge-transfer excitations,[53,57] as shown for model structures of increasing size in Fig. S2. For our LR-TDDFT calculations, we used the Casida approach and did not make the Tamm–Dancoff approximation (TDA) unless otherwise noted. We provide further information regarding the numerical convergence of our calculations in the supplementary material. Details of our QM/MM LR-TDDFT calculations with ORCA can also be found in the supplementary material.

C. Classification of charge-transfer excitations

Since the transition density vanishes for charge-transfer states, we calculated the difference density $\Delta n_i = n_i - n_0$ between the excited (n_i) and the ground-state density (n_0) for every excitation i. The excited-state density n_i is calculated as the diagonal part of the excited state density matrix $\gamma^{ii}(r, r') = N \int \Psi^i(r, r_2, r_3, \ldots, r_N) \Psi^i(r', r_2, r_3, \cdots, r_N) dr_2 \ldots dr_N$, where N is

the number of electrons and Ψ^i is the approximate excited-state wavefunction that consists of a sum of Slater determinants of generalized Kohn–Sham orbitals with coefficients obtained from LR-TDDFT.[58] There is no formal guarantee that this wavefunction is equal to the exact excited-state wavefunction. However, it has been shown that eigenvalues and orbitals from accurate exchange-correlation potentials are an ideal basis for describing molecular excitations,[59] and the Kohn–Sham Slater determinant can be rigorously interpreted as the zeroth-order approximation to the true wavefunction in Görling–Levy perturbation theory.[60] For organic molecular systems, it has been found that approximating the true wavefunction by the Kohn–Sham Slater determinant is often justified. This is seen, e.g., in the successful interpretation of photoemission data using Kohn–Sham wavefunctions[61,62] and the great success of the concept of natural transition orbitals.[63] To quantify the magnitude of charge transfer, we integrated over subsystem difference densities. For this purpose, we subdivided the volume containing the difference densities of our full model systems into subsystem volumes, each containing one pigment. Note that P is separated into P_A and P_B to enable the characterization of internal charge-transfer states of type $P_A^+P_B^-$. Our aim is to assign each grid point of the difference-density grid to its closest pigment molecule. To achieve this, we tested two methods for assigning grid points to subsystem volumes: In method 1, we used the distances between grid points and each molecule's atomic coordinates (including hydrogen atoms). In method 2, we used distances between grid points and each molecule's geometrical center of gravity. Both methods result in the same trends, although the absolute values of the integrated subsystem densities differ slightly.

III. RESULTS AND DISCUSSION

In the following discussion, our aim is to elucidate a mechanism for charge-transfer in the RC of *Rhodobacter sphaeroides* and to probe the effect of explicitly including amino-acid residues in the vicinity of the primary pigments. We start with a hexameric model system in Sec. III A consisting of P, B_A, B_B, H_A, and H_B. If amino acids are added to this system, the number of excited states that needs to be calculated to observe charge-transfer is too large to be computationally feasible. We, therefore, use two different types of model systems to study the addition of amino acids: in Sec. III B, we construct a tetrameric model system consisting of P, B_A, and B_B. We systematically add amino acids to establish the minimal model necessary to account for the static effects of the protein environment. However, this model does not include the bacteriopheophytins H_A and H_B and, therefore, does not allow us to observe all relevant low-energy charge-transfer excitations. In Sec. III C, we, therefore, use models of the A and B branches, including P, B_A, H_A, and P, B_B, H_B, respectively. We show that the A and B branch structures reproduce the main features of the hexameric model (Sec. III A) and probe the effect of adding amino acids to these models on the relevant charge-transfer states.

Since our goal is to isolate the direct electronic effects of the amino-acid environment on the excited states, we do not perform geometry optimizations for each model system. In other words, differences between the excitation spectra of our model systems can be fully attributed to the electronic effects of the amino-acid environment and are not related to additional structural effects.

A. Absorption spectrum and excited state character of the bare hexameric RC model

We start our discussion by inspecting the absorption spectrum of a hexameric model of the RC based on the crystal structure as described in Sec. II A and without including any parts of the environment, as shown in Fig. 2(a). For this model, we were able to calculate 16 excitations, which correspond to the energy range depicted in Fig. 2(a). This energy range is dominated by Q-band excitations, i.e., excited states that originate from the coupling of the Q_y and Q_x excitations of the individual BCL and bacteriopheophytin molecules. However, because of the spatial proximity of these pigments in the RC, not all excitations can clearly be classified as coupled Q_y or Q_x, as

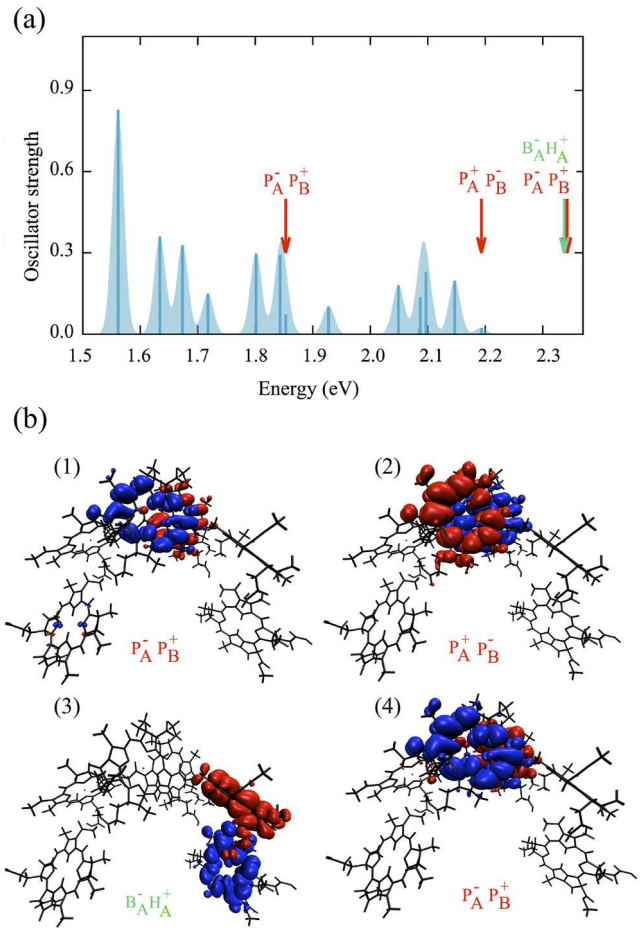

FIG. 2. (a) LR-TDDFT absorption spectrum of the bare hexameric RC model. Arrows mark excitations with low/vanishing oscillator strength and (partial) charge-transfer character. The shaded areas are calculated by folding the excitation energies into Gaussian functions with a width of 80 meV as a guide to the eye. (b) Difference densities of the four charge-transfer excitations in this energy range. Isosurface values correspond to $-0.0001a_0^{-3}$ (red) and $0.0001a_0^{-3}$ (blue), respectively.

apparent from their transition densities shown in Fig. S3. These transition densities also show that the majority of Q-band excitations are spatially strongly delocalized across several pigments, with some of them spreading over the entire RC model. This is the first main result of our study. A list of excitation energies, oscillator strengths, and spatial character as determined from the transition densities (and difference densities in the case of charge-transfer excitations) can be found in Table I. In this table and in the rest of the text, the notation $(PBH)^*$ corresponds to an excitation delocalized across P, B_A, B_B, H_A, and H_B, while $P_A^+P_B^-$ denotes a charge-transfer excitation from P_A to P_B.

We find four excitations with charge-transfer character in this energy range. The difference densities of these excitations are depicted in Fig. 2(b) (all other difference densities for this structural model can be found in Fig. S4). Here and in the following, positive difference density values indicate a region of space in which the electron density (i.e., negative charge density) increases as a consequence of the excitation (shown in blue), whereas negative values indicate regions of space in which the electron density decreases (shown in red). Numerical values based on the integration of difference densities as described in Sec. II C are listed in Table S3. The three charge-transfer excitations within the special pair, corresponding to $P_A^+P_B^-$ and $P_A^-P_B^+$ arise as a consequence of the strong coupling of P_A and P_B. In particular, the first $P_A^-P_B^+$ excitation mixes strongly with other excitations at ~1.85 eV and, therefore, exhibits partial charge-transfer character, in which 0.69 of an electron is transferred from P_A to P_B. Strikingly, we also find a charge-transfer excitation from B_A to H_A in this energy range. This is the lowest-energy pure charge-transfer state we find in our calculations (0.99 of an electron is transferred from B_A to H_A). The second main result of our study is that the appearance of this charge-transfer state at ~2.3 eV is a consequence of the spatial arrangement of the pigments in the bacterial RC alone. We will discuss how the energy of this state is affected by including environmental effects in Sec. III C.

TABLE I. Excitation energies (in eV), oscillator strengths, and spatial delocalization/charge-transfer character of the first 16 excitations of the bare hexameric RC model structure.

No.	Energy	Oscillator strength	Character
1	1.56	0.83	$(PBH)^*$
2	1.63	0.36	$(PBH_B)^*$
3	1.67	0.33	$(PBH)^*$
4	1.71	0.15	$(PBH)^*$
5	1.80	0.30	$(BH_B)^*$
6	1.84	0.29	$(PB_AH)^*$
7	1.85	0.07	$P_A^-P_B^+$
8	1.92	0.10	$(PBH)^*$
9	2.04	0.18	$(PBH)^*$
10	2.08	0.02	$(P_BBH_B)^*$
11	2.08	0.13	$(PBH)^*$
12	2.09	0.23	$(PBH_A)^*$
13	2.14	0.20	$(PBH_B)^*$
14	2.19	0.02	$P_A^+P_B^-$
15	2.33	0.00	$B_A^-H_A^+$
16	2.34	0.00	$P_A^-P_B^+$

B. Effect of the protein environment on a tetrameric RC model

The importance of the protein environment and its impact on charge transfer were recognized already in early studies of the bacterial RC.[64–66] Proposals for how the surrounding proteins affect charge transfer in the RC have primarily included asymmetries in the dielectric environment and in the protein electrostatic fields that A and B branch cofactors experience.[65,67–70] Our goal here is to explicitly include parts of the protein environment in our LR-TDDFT calculations to elucidate which amino-acid residues electronically couple to the primary RC pigments. For this purpose, we start by studying tetrameric models of the RC, including the special pair P and the accessory BCLs B_A and B_B, and systematically increase the number of amino-acid residues in our calculations.

We construct four model systems, as shown in Fig. 3(a): model system M_1 consists of the four BCL molecules P_A, P_B, B_A, and B_B. For a direct analysis of the influence of the closest lying amino acids, the histidine molecules that coordinate each of the BCLs (HIS M202, HIS M182, HIS L173, and HIS L153) were included in model system M_2. Our largest model system, M_4, contains *all* amino acids in a radius of 3 Å around the BCLs. These 32 amino acids were determined by constructing spheres with a radius of 3 Å around each atom of the four BCL molecules (excluding hydrogen atoms and the phytyl tail). A complete list (Table S4) and all structure files can be found in the supplementary material. We calculated the electronic density of states (DOS) of these model systems and found two occupied states localized on amino acids TRP M157 and MET L248, respectively, energetically close to the highest occupied molecular orbital of M_4 (see Figs. S5 and S6). However, a model system M_3^* consisting of the four primary BCL molecules, the coordinating histidines, and these two amino acids features an electronic DOS distinctly different from that of M_4 (Fig. S7). We therefore additionally included the two main symmetry breaking amino acids PHE M197 and HIS L168 as suggested by Eisenmayer *et al.*[31] to construct model system M_3 with a DOS in very good agreement with the DOS of M_4 in the relevant energy range.

The LR-TDDFT Q-band spectra of M_1–M_4 comprising the ten lowest-energy excitations are shown in Fig. 3(b) and Tables S5 and S6. The first four excitations of these model systems can be seen as arising from a coupling of the Q_y excitations of P, B_A, and B_B. We provide a detailed analysis of the origin of these excitations in the supplementary material (Figs. S9–S11). Inspection of their transition densities (Fig. S9) shows that only the first excitation is localized on P, while excitations 2–4 are coupled Q_y excitations spread across all four BCLs. Among the following six excitations of M_1, 5, 6, and 7 can clearly be assigned to P. Two of these excitations (6 and 7) have coupled Q_x character; excitation 5 has Q_y character, but integration over the difference density corresponding to this state also shows substantial charge-transfer character. States 8 and 9 of M_1 are Q_x excitations associated with B_A and B_B. Excitation 10 of M_1 is nearly dark and corresponds to a $P_A^+P_B^-$ charge-transfer state.

Inclusion of the histidines in M_2 hardly affects the first four excitations. Only when further amino-acid residues are added do we observe a noticeable redshift: the first excitation of M_4 is 40 meV lower in energy than that of M_1. The character of these excitations is not changed by the environment. The average difference density

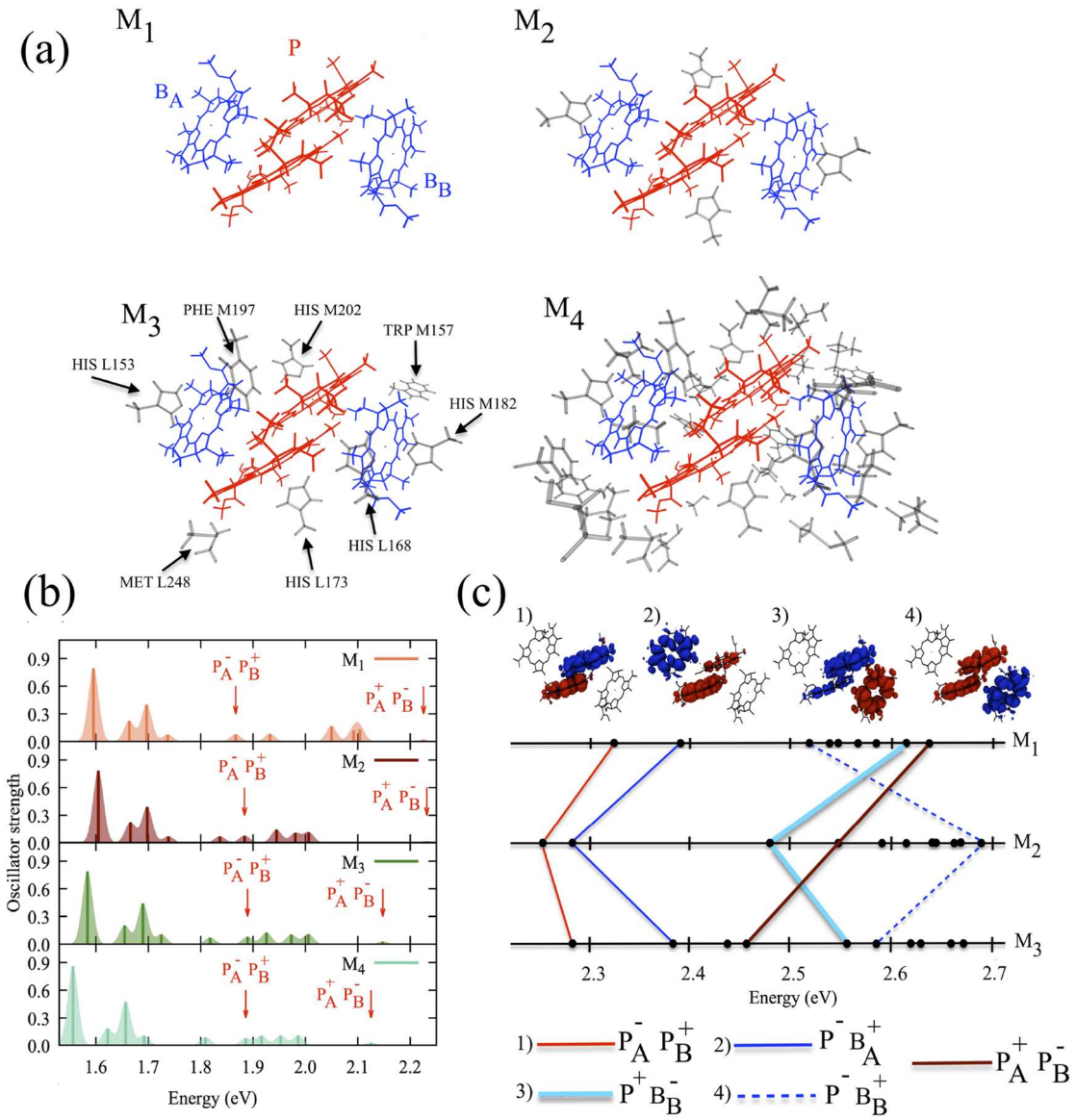

FIG. 3. (a) Representation of model systems M_1, M_2, M_3, and M_4 as described in the main text. (b) Absorption spectra of $M_1 - M_4$ in the energy region where coupled Q_y and Q_x excitations are expected. Red arrows mark excitations with charge-transfer character. (c) Energy of dark excitations (zero oscillator strength) of $M_1 - M_3$ and difference densities of selected charge-transfer excitations of M_1. The red surface of the difference density shows the isovalue $-0.0001a_0^{-3}$ and the blue surface shows $0.0001a_0^{-3}$.

of excitations 1–4 is barely affected by the addition of the environment, as shown in Fig. S12. We observe more significant energy differences for the next six excitations. Excitations with Q_x character are redshifted by ~100 meV through addition of the coordinating histidines, and the coupled Q_x excitations of P are redshifted by another 20 meV for model system M_3, while the Q_x excitations of the accessory BCLs are stable. We note that the significance of the coordinating histidines for these excitations can also be seen in the difference density (Fig. S12). In systems M_2–M_4, there is a clear transfer of positive charge from P to the coordinating histidines.

The energy of the (partial) charge-transfer excitations 5 and 10 of M_1 is also affected by adding the protein environment. Excitation 5 of M_1 is redshifted by ~60 meV and becomes excitation 6 in M_4, and excitation 10 is redshifted by ~100 meV. The magnitude of charge transfer is only slightly affected by the addition of the environment. The amount of charge transferred from P_A to P_B in

excitation 5 of M_1 decreases slightly when adding the environment while in excitation 10 it remains the same. Overall, the character of excitations 5–10 is only slightly affected by the amino-acid environment, as can be seen in Fig. S13, which shows the average difference density of excitations 5–10 for systems M_1–M_4. Importantly, Fig. 3(b) demonstrates that the spectrum of M_4 is very similar to that of M_3 with the same order of states and only a small global redshift as compared to M_3. We, therefore, conclude that the eight amino acids considered in M_3 reproduce the main (static) effects of the amino-acid environment. Therefore, they constitute a "reasonable minimal environment" that should be explicitly included in future calculations.

At energies above the Q-band and below the Soret band, which starts at ~3 eV,[10] we observe a range of dark states with charge-transfer character. Here, we only discuss five states in this energy region that lead to a clear charge transfer between different BCL molecules. The energy and difference densities of these states are shown in Fig. 3(c). (Integrated) difference densities of all states are shown in Fig. S14 and Table S7. Due to the large size of M_4, we only calculated 12 excitations with high numerical accuracy for this system. Since the effects of the environment are well-represented by M_3, as shown before, we do not discuss the charge-transfer excitations of M_4 in detail. However, Tables S5 and S6 show that the energies of the charge-transfer excitations 11 and 12 of M_3 and M_4 are in very good agreement.

In similarity to the findings for our hexameric model of the RC, we find a $P_A^- P_B^+$ excitation in M_1-M_3 (excitation 11). The addition of the histidines redshifts this state by 80 meV, while the additional amino acids in M_3 lead to a blueshift of 26 meV. The 12th excitation corresponds to $P^- B_A^+$. This state is redshifted by 120 meV through the addition of histidines, while further amino acids blueshift the excitation back by 110 meV. The energy gap between $P^- B_A^+$ and the next charge-transfer excitation is substantial: ~130 meV in M_1, ~210 meV in M_2, and 85 meV in M_3. In the 13th excitation of M_1, we observe a backward charge transfer from the B branch corresponding to $P^+ B_A^-$. The first forward charge transfer into the B branch ($P^+ B_B^-$) occurs at ~2.6 eV, i.e., at significantly higher energies than $P^- B_A^+$. The addition of amino acids affects this excitation in a similar way as $P^- B_A^+$. These calculations show that the inclusion of a (static) protein environment in the system studied here changes excitation energies substantially but hardly affects the character and spatial delocalization of states. For our tetrameric model systems, addition of the protein environment also does not lead to a mixing of Q-band excitations and experimentally relevant charge-transfer states.

To probe the effect of structural fluctuations on the energy of the excited states, we also calculated the normal mode spectrum of model system M_1 in TURBOMOLE using the B3LYP functional and def2-SVP basis sets. We then distorted the structure along each of the normal modes with a distortion amplitude corresponding to 300 K and calculated the LR-TDDFT excitation spectra in QCHEM with ωPBE as before. The high-frequency modes of M_1 correspond to intramolecular vibrations such as C–C and C–H stretch modes, which are not thermally activated and only have a small effect on the energy of the delocalized excitations that we are interested in here. We, therefore, only calculated the effect of normal mode distortions on excitation energies for wavenumbers below 85 cm^{-1}. Low-frequency modes correspond to intermolecular vibrations that change the orbital overlap between neighboring BCL molecules and are thus expected to have a more substantial effect on the excitation energies of delocalized and charge-transfer excitations.[71]

Our results, shown in Fig. S15, confirm this intuitive picture: The first excitation, corresponding to a coupled Q_y excitation of P, exhibits mode-dependent energy changes of up to 20 meV, while excitations 2–4 are much less sensitive to these distortions with energy changes of $\lesssim$10 meV in line with their spatial delocalization across B_A and B_B, which are far apart. A similar observation holds for the coupled Q_x excitations of P, B_A, and B_B. On the other hand, excitations with (partial) charge-transfer character between neighboring molecules are highly sensitive to low-frequency vibrations, exhibiting excitation-energy changes of up to 30 meV for charge transfer between P_A and P_B and up to 50 meV for charge transfer between P and B_A or B_B. These excitation-energy changes can result in both red- and blueshifts, as shown in Fig. S15. Nonetheless, our analysis indicates that the inclusion of inter- and intramolecular vibrations does not change our overall result that, in a tetrameric model of the bacterial RC, charge-transfer excitations into the A-branch are energetically well-separated from the Q-band excitations. A more complete picture of the effect of thermal fluctuations could be obtained through a statistical analysis of the excitation spectra of structure "snapshots" from molecular dynamics simulations. Such simulations were performed for the RC of *Heliobacterium modesticaldum* in Ref. 36. There, it was found that the excitation energies changed quantitatively, but the conclusions about the relative ordering of the excitations based on the ensemble-averaged excitation spectrum agreed with the conclusions that were drawn based on a single spectrum.

Finally, we tested whether the inclusion of further parts of the protein environment through a QM/MM scheme would change our main conclusions. Figures S16 and S17 show the full LR-TDDFT spectrum and the TDA spectrum of M_1 with and without the QM/MM environment. Inclusion of the QM/MM environment leads to changes in the absorption spectrum of comparable size as in our explicit model M_4. In particular, we also observe a redshift of the first charge-transfer excitation of ~200 meV. However, the redshift of the coupled Q_y and Q_x excitations due to the protein environment is smaller in the QM/MM model, and some of the detailed changes in the partial and full charge-transfer excitations are also not captured by the MM environment.

C. Effect of environment on A and B branch excited states

Due to the large size of the hexameric model of the RC discussed in Sec. III A (494 atoms), an LR-TDDFT calculation including the relevant charge-transfer states for a structural model that also includes significant parts of the protein environment as performed for the tetrameric model in Sec. III B is computationally not feasible. The largest hexameric RC model that we could run full LR-TDDFT calculations for includes the coordinating histidines close to P_A, P_B, B_A, and B_B (as in M_2) plus two leucines close to H_A and H_B. Table S2 shows that including these amino-acid residues has similar effects as those observed in Sec. III B, but the calculation of more than the first 13 excitations was not feasible for this system.

However, given the large spatial separation between the A- and B-branch accessory BCLs and bacteriopheophytins, we can assume that parts of the spectrum of the full RC arise as combinations of the A-branch and B-branch excitations, respectively. To test this assumption, we constructed two further structural models, A_1 and B_1, shown in Fig. 4(a), comprising P, B_A, and H_A for the A branch and P, B_B, and H_B for the B branch, respectively. We compare the excitation spectrum of the hexameric model with that of A_1 and B_1, respectively, in Fig. 4(b). As expected, excitations associated with P appear in all three spectra, albeit at different energies (e.g., the first excitation and the charge-transfer states $P_A^- P_B^+$ and $P_A^+ P_B^-$). On the other hand, excitations that are localized on the A- or B-branch can clearly be assigned to either A_1 or B_1. In particular, in our calculation of the spectrum of A_1, we find the charge-transfer state $B_A^- H_A^+$ at the same energy (~2.3 eV) as in our hexameric model. We can therefore study the effect of adding amino acids to the energy of this and other relevant charge transfer states using our structural models A_1 and B_1 as a starting point.

A comparison of the excitation energies of the relevant charge-transfer states in the A- and B-branch is shown in Fig. 4(c) and listed in Tables S9 and S10. The $B_A^- H_A^+$ state is significantly lower in energy than $B_B^- H_B^+$, in agreement with the experimentally observed directionality of charge-separation along the A-branch. By adding the coordinating histidines and leucines in model systems A_2 and B_2, both states are redshifted by more than 100 meV. Charge-transfer states from P to B_B and P to B_A are significantly higher in energy, in particular after the addition of the coordinating histidines and leucines. Adding further amino-acid residues (listed in Table S11), in analogy with M_3 in Sec. III B, leads to a further redshift of $B_A^- H_A^+$, bringing this charge-transfer state within 25 meV of the coupled Q_x excitations (see Table S9). It is, therefore, likely that the addition of further parts of the protein environment in concert with thermally-activated molecular vibrations could lead to a mixing of this and other charge-transfer states and the delocalized coupled Q_x excitations. This is supported by earlier studies using polarizable continuum models, which suggest that differences in the dielectric

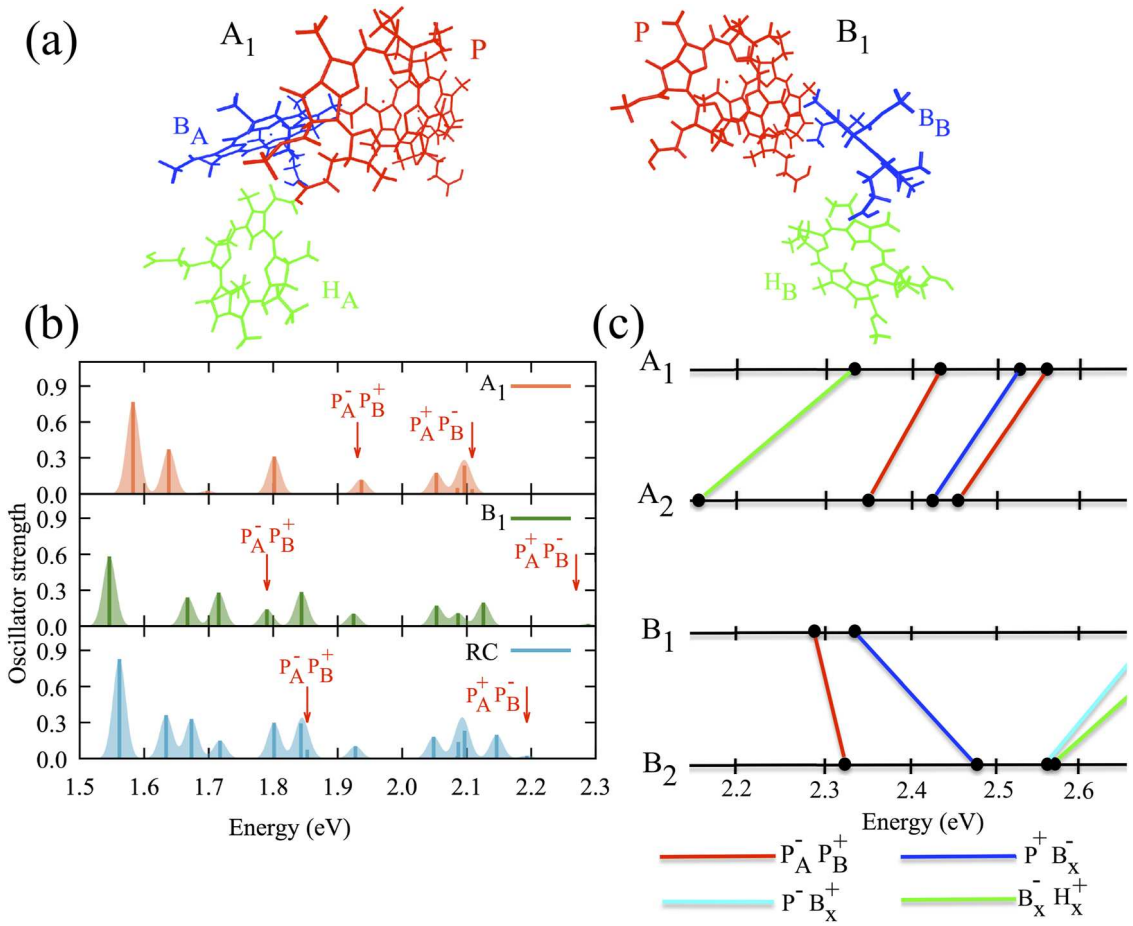

FIG. 4. (a) Structures of model systems A_1 ($P + B_A + H_A$) and B_1 ($P + B_B + H_B$). (b) Absorption spectra of A_1, B_1, and the full hexameric model system ($P + B_A + B_B + H_A + H_B$) in the energy region where coupled Q_y and Q_x excitations are expected. Red arrows mark excitations with charge-transfer character. (c) Energy of dark excitations (zero oscillator strength) in A_1, B_1 and A_2, B_2. The latter correspond to A_1 and B_1, respectively, but in addition include the coordinating histidines and leucines.

environment lead to a stabilization of charge-transfer excitations in the A branch in comparison with the B branch.[32]

IV. SUMMARY AND CONCLUSIONS

Our first principles calculations show a pronounced effect of the protein environment on the electronic structure and excited states of the six primary pigments comprising the RC of *Rhodobacter sphaeroides*. By systematically adding relevant amino acids in the vicinity of these chromophores, we find a significant redshift of the coupled Q_y and Q_x excitations. Charge-transfer excitations are observed in the form of dark excitations starting at ~200 meV above the coupled Q_x excitations. These charge-transfer states are strongly affected by direct inclusion of the protein environment with energy changes of up to ~0.2 eV. However, contrary to the coupled Q_y and Q_x excitations, the protein environment affects charge-transfer states of different characters differently. In particular, the lowest-energy charge transfer state in our calculations corresponds to $B_A^- H_A^+$ and is significantly lower in energy than other excitations that move charge into the A branch. It is also almost 500 meV lower than an equivalent excitation in the B-branch. The $B_A^- H_A^+$ excitation is redshifted by the inclusion of close-lying amino-acid residues and can mix with the coupled Q_x excitations.

Our calculations suggest that charge-transfer along the RC A branch of *Rhodobacter sphaeroides* is energetically favored and demonstrate the complex excited state landscape of the RC's chromophores. Analyzing the transition and differences densities of the excited states allows for several conclusions. While most of the *Q*-band excitations can be understood as a consequence of the coupling of Q_y and Q_x excitations of the special pair BCLs *P* and the accessory BCLs B_A and B_B, the close spatial proximity of these molecules leads to strong coupling, mixing in (partial) charge-transfer states of the type $P_A^- P_B^+$ at relatively low energies. Furthermore, only the first high-oscillator strength excitation of the spectrum can be interpreted as a coupled Q_y excitation of the special pair. All other excitations are strongly delocalized, some of them with significant transition density on all six primary pigments. The presence of strongly delocalized excited states corresponding to both energy- and charge-transfer excitations is relevant because delocalized excitations are expected to be more strongly affected by thermally activated molecular vibrations than localized excitations, as shown previously by Alvertis *et al.* for the oligo-acene series.[71] In our study, we have approximately shown this effect by calculating the exciton renormalization energies of tetrameric model structures distorted along vibrational normal modes. Based on our own calculations and previous literature,[30,31,34,35] we expect yet more pronounced effects for larger structural models that also include the vibronic coupling to the protein environment.

Finally, our calculations allow us to comment on the interpretation of experimental spectroscopy of pigment-protein complexes like the bacterial RC. Our results suggest that because of the delocalized nature of energy- and charge-transfer excitations in these systems, the assignment of spectroscopic features to linear combinations of localized excitations on individual pigments is not always justified. Care should be taken when modeling the strongly coupled pigments of the bacterial RC in terms of their constituting elements.

SUPPLEMENTARY MATERIAL

See the supplementary material for additional convergence data, excitation energies, difference densities, and transition densities not shown in the main text, a discussion of the spectral origin of the coupled Q_y and Q_x excitations, details on the QM/MM calculations, results for vibrationally excited structures, and structure files.

ACKNOWLEDGMENTS

This work was supported by the Bavarian State Ministry of Science and the Arts through the Elite Network Bavaria (ENB), the Collaborative Research Network Solar Technologies go Hybrid (SolTech), the Study Program "Biological Physics" of the ENB, and through computational resources provided by the Bavarian Polymer Institute (BPI).

AUTHOR DECLARATIONS

Conflict of Interest

The authors have no conflicts to disclose.

Author Contributions

Sabrina Volpert: Data curation (lead); Formal analysis (lead); Investigation (lead); Visualization (lead); Writing – review & editing (equal). **Zohreh Hashemi**: Data curation (equal); Formal analysis (equal); Investigation (equal); Visualization (equal); Writing – review & editing (equal). **Johannes M. Foerster**: Investigation (supporting); Validation (supporting); Writing – review & editing (equal). **Mario R. G. Marques**: Investigation (supporting); Writing – review & editing (equal). **Ingo Schelter**: Methodology (supporting); Software (supporting); Validation (supporting); Writing – review & editing (equal). **Stephan Kümmel**: Conceptualization (supporting); Formal analysis (supporting); Supervision (supporting); Writing – review & editing (equal). **Linn Leppert**: Conceptualization (lead); Funding acquisition (lead); Project administration (lead); Resources (lead); Supervision (lead); Writing – original draft (lead).

DATA AVAILABILITY

The data that support the findings of this study are available within the article and its supplementary material.

REFERENCES

[1] G. Renger, "Overview of primary processes of photosynthesis," in *Primary Processes of Photosynthesis*, edited by G. Renger (RSC Publishing, 2008), pp. 5–30.
[2] X. J. Jordanides, G. D. Scholes, and G. R. Fleming, "The mechanism of energy transfer in the bacterial photosynthetic reaction center," J. Phys. Chem. B **105**, 1652–1669 (2001).
[3] A. Camara-Artigas, D. Brune, and J. P. Allen, "Interactions between lipids and bacterial reaction centers determined by protein crystallography," Proc. Natl. Acad. Sci. U. S. A. **99**, 11055–11060 (2002).
[4] D. M. Jonas, M. J. Lang, Y. Nagasawa, T. Joo, and G. R. Fleming, "Pump-probe polarization anisotropy study of femtosecond energy transfer within the

photosynthetic reaction center of *Rhodobacter sphaeroides* R26," J. Phys. Chem. **100**, 12660–12673 (1996).
[5]G. S. Schlau-Cohen, E. De Re, R. J. Cogdell, and G. R. Fleming, "Determination of excited-state energies and dynamics in the B band of the bacterial reaction center with 2D electronic spectroscopy," J. Phys. Chem. Lett. **3**, 2487–2492 (2012).
[6]O. Rancova, R. Jankowiak, A. Kell, M. Jassas, and D. Abramavicius, "Band structure of the *Rhodobacter sphaeroides* photosynthetic reaction center from low-temperature absorption and hole-burned spectra," J. Phys. Chem. B **120**, 5601–5616 (2016).
[7]A. Niedringhaus, V. R. Policht, R. Sechrist, A. Konar, P. D. Laible, D. F. Bocian, D. Holten, C. Kirmaier, and J. P. Ogilvie, "Primary processes in the bacterial reaction center probed by two-dimensional electronic spectroscopy," Proc. Natl. Acad. Sci. U. S. A. **115**, 3563–3568 (2018).
[8]K. Kawashima and H. Ishikita, "Energetic insights into two electron transfer pathways in light-driven energy-converting enzymes," Chem. Sci. **9**, 4083–4092 (2018).
[9]M. A. Kavanagh, J. K. G. Karlsson, J. D. Colburn, L. M. C. Barter, and I. R. Gould, "A TDDFT investigation of the photosystem II reaction center: Insights into the precursors to charge separation," Proc. Natl. Acad. Sci. U. S. A. **117**, 19705–19712 (2020).
[10]R. J. Cogdell, A. Gall, and J. Köhler, "The architecture and function of the light-harvesting apparatus of purple bacteria: From single molecules to in vivo membranes," Quart. Rev. Biophys. **39**, 227–324 (2006).
[11]C. A. Wraight and R. K. Clayton, "The absolute quantum efficiency of bacteriochlorophyll photooxidation in reaction centres of Rhodopseudomonas spheroides," Biochim. Biophys. Acta, Bioenerg. **333**, 246–260 (1974).
[12]C. Kirmaier, D. Holten, and W. W. Parson, "Picosecond-photodichroism studies of the transient states in Rhodopseudomonas sphaeroides reaction centers at 5 K. Effects of electron transfer on the six bacteriochlorin pigments," Biochim. Biophys. Acta, Bioenerg. **810**, 49–61 (1985).
[13]W. Zinth and J. Wachtveitl, "The first picoseconds in bacterial photosynthesis—ultrafast electron transfer for the efficient conversion of light energy," ChemPhysChem **6**, 871–880 (2005).
[14]F. Ma, E. Romero, M. R. Jones, V. I. Novoderezhkin, and R. van Grondelle, "Vibronic coherence in the charge separation process of the *Rhodobacter sphaeroides* reaction center," J. Phys. Chem. Lett. **9**, 1827–1832 (2018).
[15]F. Ma, E. Romero, M. R. Jones, V. I. Novoderezhkin, and R. van Grondelle, "Both electronic and vibrational coherences are involved in primary electron transfer in bacterial reaction center," Nat. Commun. **10**, 933 (2019).
[16]V. R. Policht, A. Niedringhaus, R. Willow, P. D. Laible, D. F. Bocian, C. Kirmaier, D. Holten, T. Mančal, and J. P. Ogilvie, "Hidden vibronic and excitonic structure and vibronic coherence transfer in the bacterial reaction center," Sci. Adv. **8**, eabk0953 (2022).
[17]M. Tros, V. I. Novoderezhkin, R. Croce, R. van Grondelle, and E. Romero, "Complete mapping of energy transfer pathways in the plant light-harvesting complex Lhca4," Phys. Chem. Chem. Phys. **22**, 25720–25729 (2020).
[18]H. H. Nguyen, Y. Song, E. L. Maret, Y. Silori, R. Willow, C. F. Yocum, and J. P. Ogilvie, Charge separation in the photosystem II reaction center resolved by multispectral two-dimensional electronic spectroscopy (2022).
[19]M. E. van Brederode, J. P. Ridge, I. H. M. van Stokkum, F. van Mourik, M. R. Jones, and R. van Grondelle, "On the efficiency of energy transfer and the different pathways of electron transfer in mutant reaction centers of *Rhodobacter sphaeroides*," Photosynth. Res. **55**, 141–146 (1998).
[20]H. Zhou and S. G. Boxer, "Probing excited-state electron transfer by resonance Stark spectroscopy. 1. Experimental results for photosynthetic reaction centers," J. Phys. Chem. B **102**, 9139–9147 (1998).
[21]S. Lin, J. Jackson, A. K. W. Taguchi, and N. W. Woodbury, "Excitation wavelength dependent spectral evolution in *Rhodobacter sphaeroides* R26 reaction centers at low temperatures: The Qy transition region," J. Phys. Chem. B **102**, 4016–4022 (1998).
[22]L. Huang, N. Ponomarenko, G. P. Wiederrecht, and D. M. Tiede, "Cofactor-specific photochemical function resolved by ultrafast spectroscopy in photosynthetic reaction center crystals," Proc. Natl. Acad. Sci. U. S. A. **109**, 4851–4856 (2012).
[23]M. E.-A. Madjet, F. Müh, and T. Renger, "Deciphering the influence of short-range electronic couplings on optical properties of molecular dimers: Application to "special pairs" in photosynthesis," J. Phys. Chem. B **113**, 12603–12614 (2009).
[24]F. Zheng, M. Jin, T. Mančal, and Y. Zhao, "Study of electronic structures and pigment–protein interactions in the reaction center of thermochromatium tepidum with a dynamic environment," J. Phys. Chem. B **120**, 10046–10058 (2016).
[25]S. J. Jang and B. Mennucci, "Delocalized excitons in natural light-harvesting complexes," Rev. Mod. Phys. **90**, 35003 (2018).
[26]T. J. Frankcombe, "Explicit calculation of the excited electronic states of the photosystem II reaction centre," Phys. Chem. Chem. Phys. **17**, 3295–3302 (2015).
[27]A. Sirohiwal, F. Neese, and D. A. Pantazis, "Protein matrix control of reaction center excitation in photosystem II," J. Am. Chem. Soc. **142**, 18174–18190 (2020).
[28]A. Förster and L. Visscher, "Quasiparticle self-consistent GW-Bethe–Salpeter equation calculations for large chromophoric systems," J. Chem. Theory Comput. **18**, 6779–6793 (2022).
[29]P. K. Wawrzyniak, M. T. P. Beerepoot, H. J. M. De Groot, and F. Buda, "Acetyl group orientation modulates the electronic ground-state asymmetry of the special pair in purple bacterial reaction centers," Phys. Chem. Chem. Phys. **13**, 10270–10279 (2011).
[30]T. J. Eisenmayer, H. J. M. De Groot, E. Van De Wetering, J. Neugebauer, and F. Buda, "Mechanism and reaction coordinate of directional charge separation in bacterial reaction centers," J. Phys. Chem. Lett. **3**, 694–697 (2012).
[31]T. J. Eisenmayer, J. A. Lasave, A. Monti, H. J. M. De Groot, and F. Buda, "Proton displacements coupled to primary electron transfer in the *Rhodobacter sphaeroides* reaction center," J. Phys. Chem. B **117**, 11162–11168 (2013).
[32]H. Aksu, A. Schubert, E. Geva, and B. D. Dunietz, "Explaining Spectral asymmetries and excitonic characters of the core pigment pairs in the bacterial reaction center using a screened range-separated hybrid functional," J. Phys. Chem. B **123**, 8970–8975 (2019).
[33]H. Aksu, A. Schubert, S. Bhandari, A. Yamada, E. Geva, and B. D. Dunietz, "On the role of the special pair in photosystems as a charge transfer rectifier," J. Phys. Chem. B **124**, 1987–1994 (2020).
[34]K. Mitsuhashi, H. Tamura, K. Saito, and H. Ishikita, "Nature of asymmetric electron transfer in the symmetric pathways of photosystem I," J. Phys. Chem. B **125**, 2879–2885 (2021).
[35]H. Tamura, K. Saito, and H. Ishikita, "The origin of unidirectional charge separation in photosynthetic reaction centers: Nonadiabatic quantum dynamics of exciton and charge in pigment-protein complexes," Chem. Sci. **12**, 8131–8140 (2021).
[36]M. Brütting, J. M. Foerster, and S. Kümmel, "Investigating primary charge separation in the reaction center of heliobacterium modesticaldum," J. Phys. Chem. B **125**, 3468–3475 (2021).
[37]B. R. Brooks, R. E. Bruccoleri, B. D. Olafson, D. J. States, S. Swaminathan, and M. Karplus, "CHARMM: A program for macromolecular energy, minimization, and dynamics calculations," J. Comput. Chem. **4**, 187–217 (1983).
[38]A. D. MacKerell, D. Bashford, M. Bellott, R. L. Dunbrack, J. D. Evanseck, M. J. Field, S. Fischer, J. Gao, H. Guo, S. Ha, D. Joseph-McCarthy, L. Kuchnir, K. Kuczera, F. T. K. Lau, C. Mattos, S. Michnick, T. Ngo, D. T. Nguyen, B. Prodhom, W. E. Reiher, B. Roux, M. Schlenkrich, J. C. Smith, R. Stote, J. Straub, M. Watanabe, J. Wiórkiewicz-Kuczera, D. Yin, and M. Karplus, "All-atom empirical potential for molecular modeling and dynamics studies of proteins," J. Phys. Chem. B **102**, 3586–3616 (1998).
[39]I. Schelter, J. M. Foerster, A. T. Gardiner, A. W. Roszak, R. J. Cogdell, G. M. Ullmann, T. B. De Queiroz, S. Kümmel, A. T. Gardiner, R. J. Cogdell, M. Ullmann, B. D. Queiroz, and S. Kümmel, "Assessing density functional theory in real-time and real-space as a tool for studying bacteriochlorophylls and the light-harvesting complex 2," J. Chem. Phys. **151**, 134114 (2019).
[40]Y. Shao, Z. Gan, E. Epifanovsky, A. T. B. Gilbert, M. Wormit, J. Kussmann, A. W. Lange, A. Behn, J. Deng, X. Feng, D. Ghosh, M. Goldey, P. R. Horn, L. D. Jacobson, I. Kaliman, R. Z. Khaliullin, T. Kuś, A. Landau, J. Liu, E. I. Proynov, Y. M. Rhee, R. M. Richard, M. A. Rohrdanz, R. P. Steele, E. J. Sundstrom, H. L. Woodcock, P. M. Zimmerman, D. Zuev, B. Albrecht, E. Alguire, B. Austin, G. J. O. Beran, Y. A. Bernard, E. Berquist, K. Brandhorst, K. B. Bravaya, S. T. Brown, D. Casanova, C.-M. Chang, Y. Chen, S. H. Chien, K. D. Closser, D. L. Crittenden, M. Diedenhofen, R. A. Distasio, H. Do, A. D. Dutoi, R. G. Edgar, S. Fatehi,

L. Fusti-Molnar, A. Ghysels, A. Golubeva-Zadorozhnaya, J. Gomes, M. W. D. Hanson-Heine, P. H. P. Harbach, A. W. Hauser, E. G. Hohenstein, Z. C. Holden, T.-C. Jagau, H. Ji, B. Kaduk, K. Khistyaev, J. Kim, J. Kim, R. A. King, P. Klunzinger, D. Kosenkov, T. Kowalczyk, C. M. Krauter, K. U. Lao, A. D. Laurent, K. V. Lawler, S. V. Levchenko, C. Y. Lin, F. Liu, E. Livshits, R. C. Lochan, A. Luenser, P. Manohar, S. F. Manzer, S.-P. Mao, N. Mardirossian, A. V. Marenich, S. A. Maurer, N. J. Mayhall, E. Neuscamman, C. M. Oana, R. Olivares-Amaya, D. P. O'Neill, J. A. Parkhill, T. M. Perrine, R. Peverati, A. Prociuk, D. R. Rehn, E. Rosta, N. J. Russ, S. M. Sharada, S. Sharma, D. W. Small, A. Sodt, T. Stein, D. Stück, Y.-C. Su, A. J. W. Thom, T. Tsuchimochi, V. Vanovschi, L. Vogt, O. Vydrov, T. Wang, M. A. Watson, J. Wenzel, A. White, C. F. Williams, J. Yang, S. Yeganeh, S. R. Yost, Z.-Q. You, I. Y. Zhang, X. Zhang, Y. Zhao, B. R. Brooks, G. K. L. Chan, D. M. Chipman, C. J. Cramer, W. A. Goddard, M. S. Gordon, W. J. Hehre, A. Klamt, H. F. Schaefer, M. W. Schmidt, C. D. Sherrill, D. G. Truhlar, A. Warshel, X. Xu, A. Aspuru-Guzik, R. Baer, A. T. Bell, N. A. Besley, J.-D. Chai, A. Dreuw, B. D. Dunietz, T. R. Furlani, S. R. Gwaltney, C.-P. Hsu, Y. Jung, J. Kong, D. S. Lambrecht, W. Liang, C. Ochsenfeld, V. A. Rassolov, L. V. Slipchenko, J. E. Subotnik, T. Van Voorhis, J. M. Herbert, A. I. Krylov, P. M. W. Gill, and M. Head-Gordon, "Advances in molecular quantum chemistry contained in the Q-Chem 4 program package," Mol. Phys. **113**, 184–215 (2015).

[41] Turbomole V7.5 2020, a development of University of Karlsruhe and Forschungszentrum Karlsruhe GmbH, 1989-2007, TURBOMOLE GmbH since 2007; available from https://www.turbomole.org.

[42] S. G. Balasubramani, G. P. Chen, S. Coriani, M. Diedenhofen, M. S. Frank, Y. J. Franzke, F. Furche, R. Grotjahn, M. E. Harding, C. Hättig, A. Hellweg, B. Helmich-Paris, C. Holzer, U. Huniar, M. Kaupp, A. Marefat Khah, S. Karbalaei Khani, T. Müller, F. Mack, B. D. Nguyen, S. M. Parker, E. Perlt, D. Rappoport, K. Reiter, S. Roy, M. Rückert, G. Schmitz, M. Sierka, E. Tapavicza, D. P. Tew, C. van Wüllen, V. K. Voora, F. Weigend, A. Wodyński, and J. M. Yu, "TURBOMOLE: Modular program suite for *ab initio* quantum-chemical and condensed-matter simulations," J. Chem. Phys. **152**, 184107 (2020).

[43] F. Neese, "The ORCA program system," Wiley Interdiscip. Rev.: Comput. Mol. Sci. **2**, 73–78 (2012).

[44] O. a. Vydrov, J. Heyd, A. V. Krukau, and G. E. Scuseria, "Importance of short-range versus long-range Hartree-Fock exchange for the performance of hybrid density functionals," J. Chem. Phys. **125**, 074106 (2006).

[45] T. B. De Queiroz, E. R. De Figueroa, M. D. Coutinho-Neto, C. D. Maciel, E. Tapavicza, Z. Hashemi, and L. Leppert, "First principles theoretical spectroscopy of Methylene Blue: Between limitations of time-dependent density functional theory approximations and its realistic description in the solvent," J. Chem. Phys. **154**, 044106 (2021).

[46] Z. Hashemi and L. Leppert, "Assessment of the *ab initio* Bethe-Salpeter equation approach for the low-lying excitation energies of bacteriochlorophylls and chlorophylls," J. Phys. Chem. A **125**, 2163–2172 (2021).

[47] A. Sirohiwal, F. Neese, and D. A. Pantazis, "How can we predict accurate electrochromic shifts for biochromophores? A case study on the photosynthetic reaction center," J. Chem. Theory Comput. **17**, 1858–1873 (2021).

[48] S. Kümmel, "Charge-transfer excitations: A challenge for time-dependent density functional theory that has been met," Adv. Energy Mater. **7**, 1700440 (2017).

[49] S. Refaely-Abramson, R. Baer, and L. Kronik, "Fundamental and excitation gaps in molecules of relevance for organic photovoltaics from an optimally tuned range-separated hybrid functional," Phys. Rev. B **84**, 075144 (2011).

[50] S. Refaely-Abramson, S. Sharifzadeh, N. Govind, J. Autschbach, J. B. Neaton, R. Baer, and L. Kronik, "Quasiparticle spectra from a nonempirical optimally tuned range-separated hybrid density functional," Phys. Rev. Lett. **109**, 226405 (2012).

[51] T. Körzdörfer and N. Marom, "Strategy for finding a reliable starting point for G0W0 demonstrated for molecules," Phys. Rev. B **86**, 041110 (2012).

[52] S. Refaely-Abramson, S. Sharifzadeh, M. Jain, R. Baer, J. B. Neaton, and L. Kronik, "Gap renormalization of molecular crystals from density-functional theory," Phys. Rev. B **88**, 081204 (2013).

[53] T. B. De Queiroz and S. Kümmel, "Charge-transfer excitations in low-gap systems under the influence of solvation and conformational disorder: Exploring range-separation tuning," J. Chem. Phys. **141**, 084303 (2014).

[54] A. K. Manna, S. Refaely-Abramson, A. M. Reilly, A. Tkatchenko, J. B. Neaton, and L. Kronik, "Quantitative prediction of optical absorption in molecular solids from an optimally tuned screened range-separated hybrid functional," J. Chem. Theory Comput. **14**, 2919–2929 (2018).

[55] D. Wing, G. Ohad, J. B. Haber, M. R. Filip, S. E. Gant, J. B. Neaton, and L. Kronik, "Band gaps of crystalline solids from Wannier-localization based optimal tuning of a screened range-separated hybrid functional," Proc. Natl. Acad. Sci. U. S. A. **118**, e2104556118 (2020).

[56] L. Kronik, T. Stein, S. Refaely-Abramson, and R. Baer, "Excitation gaps of finite-sized systems from optimally tuned range-separated hybrid functionals," J. Chem. Theory Comput. **8**, 1515–1531 (2012).

[57] T. Körzdörfer, J. S. Sears, C. Sutton, and J.-L. Brédas, "Long-range corrected hybrid functionals for pi-conjugated systems: Dependence of the range-separation parameter on conjugation length," J. Chem. Phys. **135**, 204107 (2011).

[58] F. Plasser, M. Wormit, and A. Dreuw, "New tools for the systematic analysis and visualization of electronic excitations. I. Formalism," J. Chem. Phys. **141**, 024106 (2014).

[59] R. van Meer, O. V. Gritsenko, and E. J. Baerends, "Physical meaning of virtual Kohn–Sham orbitals and orbital energies: An ideal basis for the description of molecular excitations," J. Chem. Theory Comput. **10**, 4432–4441 (2014).

[60] A. Görling and M. Levy, "DFT ionization formulas and a DFT perturbation theory for exchange and correlation, through adiabatic connection," Int. J. Quantum Chem. **56**, 93–108 (1995).

[61] P. Puschnig, S. Berkebile, A. J. Fleming, G. Koller, K. Emtsev, T. Seyller, J. D. Riley, C. Ambrosch-Draxl, F. P. Netzer, and M. G. Ramsey, "Reconstruction of molecular orbital densities from photoemission data," Science **326**, 702–706 (2009).

[62] M. Dauth, T. Körzdörfer, S. Kümmel, J. Ziroff, M. Wiessner, A. Schöll, F. Reinert, M. Arita, and K. Shimada, "Orbital density reconstruction for molecules," Phys. Rev. Lett. **107**(1–5), 193002 (2011).

[63] R. L. Martin, "Natural transition orbitals," J. Chem. Phys. **118**, 4775–4777 (2003).

[64] R. J. Stanley, B. King, and S. G. Boxer, "Excited state energy transfer pathways in photosynthetic reaction centers. 1. Structural symmetry effects," J. Phys. Chem. **100**, 12052–12059 (1996).

[65] M. A. Steffen, K. Lao, and S. G. Boxer, "Dielectric asymmetry in the photosynthetic reaction center," Science **264**, 810–816 (1994).

[66] M. Hiyama and N. Koga, "Theoretical study of electron transfer in *Rhodobacter sphaeroides* reaction center," Photochem. Photobiol. **87**, 1297–1307 (2011).

[67] D. J. Lockhart, C. Kirmaier, D. Holten, and S. G. Boxer, "Electric field effects on the initial electron-transfer kinetics in bacterial photosynthetic reaction centers," J. Chem. Phys. **94**, 6987–6995 (1990).

[68] R. G. Alden, W. W. Parson, Z. T. Chu, and A. Warshel, "Calculations of electrostatic energies in photosynthetic reaction centers," J. Am. Chem. Soc. **117**, 12284–12298 (1995).

[69] M. R. Gunner, A. Nicholls, and B. Honig, "Electrostatic potentials in Rhodopseudomonas viridis reaction centers: Implications for the driving force and directionality of electron transfer," J. Phys. Chem. **100**, 4277–4291 (1996).

[70] M. Saggu, S. D. Fried, and S. G. Boxer, "Local and global electric field asymmetry in photosynthetic reaction centers," J. Phys. Chem. B **123**, 1527–1536 (2019).

[71] A. M. Alvertis, R. Pandya, L. A. Muscarella, N. Sawhney, M. Nguyen, B. Ehrler, A. Rao, R. H. Friend, A. W. Chin, and B. Monserrat, "Impact of exciton delocalization on exciton-vibration interactions in organic semiconductors," Phys. Rev. B **102**, 081122 (2020).

Supplementary Material - Delocalized Electronic Excitations and their Role in Directional Charge Transfer in the Reaction Center of Rhodobacter Sphaeroides

Sabrina Volpert,[1] Zohreh Hashemi,[1] Johannes M. Foerster,[1] Mario R. G. Marques,[1] Ingo Schelter,[1] Stephan Kümmel,[1] and Linn Leppert[2,1]

[1)]*Institute of Physics, University of Bayreuth, 95440 Bayreuth, Germany*

[2)]*MESA+ Institute for Nanotechnology, University of Twente, 7500 AE Enschede, The Netherlands*

(Dated: 7 March 2023)

I. FURTHER INFORMATION ON METHODS

A. Convergence Tests

We tested how well our results converged with respect to the basis set size by calculating the first 15 excitations of *P* with the basis set 6-31G(d,p) and the bigger basis set 6-311G(d,p). The excitation energies, shown in Table S1, differ by less than 30 meV and the smaller basis set leads qualitatively to the same spectrum.

	P 6-31G(d,p)	*P* 6-311G(d,p)
Exc.	En.[eV] (Osc.Str.)	En.[eV](Osc.Str.)
1	1.611 (0.574)	1.585 (0.580)
2	1.716 (0.055)	1.689 (0.056)
3	1.873 (0.093)	1.858 (0.084)
4	1.946 (0.101)	1.924 (0.103)
5	2.061 (0.167)	2.041 (0.169)
6	2.234 (0.017)	2.211 (0.018)
7	2.347 (0.001)	2.342 (0.001)
8	2.494 (0.000)	2.519 (0.000)
9	2.553 (0.001)	2.583 (0.001)
10	2.648 (0.002)	2.635 (0.003)
11	2.693 (0.007)	2.677 (0.006)
12	2.745 (0.001)	2.732 (0.001)
13	2.891 (0.019)	2.882 (0.025)
14	2.927 (0.009)	2.939 (0.003)
15	3.005 (0.018)	2.993 (0.028)

TABLE S1: The excitation energies of *P* with the Pople basis sets 6-31G(d,p) and 6-311G(d,p).

To check convergence of the eigenvalues of the Casida matrix equation of TDDFT, we used the smallest model system M_1 and calculated 20 and 30 excitations with a convergence criterion of 10^{-6} and 10^{-7}, respectively. The excitation energies differed by up to 8 meV in the comparison of 20 and 30 excitations with a convergence criterion of 10^{-6} for the eigenvalues. When we set the

value to 10^{-7}, the deviations were smaller with a maximum deviation of $\sim$1 meV. We therefore used a criterion of 10^{-7} for all calculations. For M_1 and M_2 we calculated 30 excitations, for M_3 20 excitations. For M_4 we could only calculate ten excitations due to technical limitations of Q-CHEM that prevented successful TDDFT calculations for a system this large.

To check if at least the first CT excitation that shifts an electron from B_B to P is stable under inclusion of larger parts of the environment, we calculated twelve excitations with TURBOMOLE, using the same basis set and equivalent convergence critera as in our Q-CHEM calculations. The excitation energies calculated with TURBOMOLE differ by less than 10 meV from the Q-CHEM results as shown in Table S4.

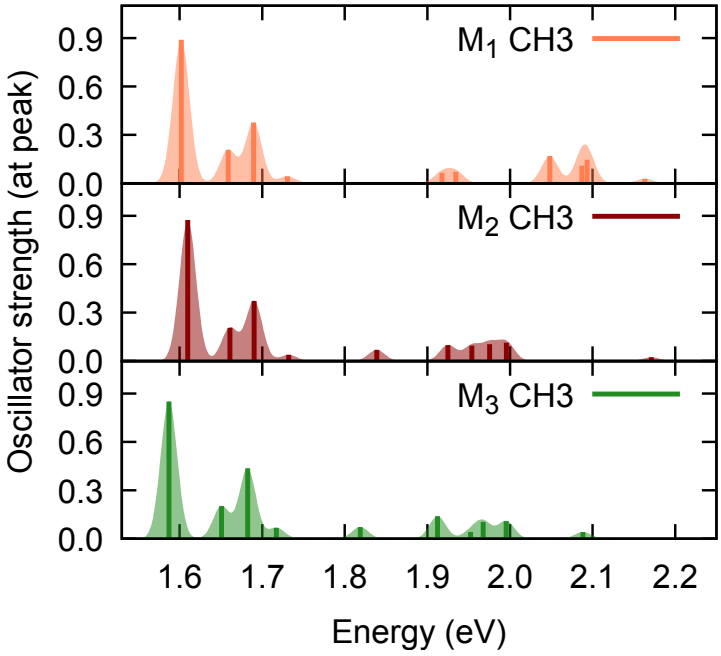

FIG. S1: The spectra of M_1 to M_3 with the phytyl tail cropped in the ester link and saturated with a methyl group.

We also checked the effect of the saturation of the BCLs phytyl tail on our findings. For this purpose, we calculated model systems M_1 to M_3 with a methyl group at the corresponding end. The spectra shown in figure S1 are slightly different from those saturated with hydrogen, but the environment still has a very similar impact on the character and energy of these excited states.

B. Choice of Range-Separation Parameter

We have used the same range-separation parameter ω in all calculations for general reasons: Using the same ω for each system allows us to compare the electronic structure of all model systems on the same footing. Furthermore, it was shown, for example in Ref.s 1 and 2 that using the optimal tuning procedure for conjugated molecular systems of increasing size leads to artificially low values of ω and thus a dominance of semilocal exchange at long range and a deterioration of the description of charge-transfer excitations. This can be seen in the Figure S2, in which we show the absorption spectra of a single BCL plus histidine (Figure S2(a)), the two BCLs of the special pair (Figure S2(b)) and the four BCLs of our model system M_1 (Figure S2(c)). In each panel, we compare the absorption spectrum of the system calculated with $\omega = 0.171\ a_0^-1$ (used throughout our manuscript) with that obtained using the optimal tuning procedure for each system[3]. These parameters are $\omega = 0.162\ a_0^-1$ (BCL + His), $\omega = 0.130\ a_0^-1$ (special pair P), $\omega = 0.114\ a_0 - 1$ (tetrameric model M_1). This comparison shows that the "optimal" ω decreases with increasing system size leading to increasing differences between the spectra obtained with the ”tuned” and the “untuned” functional. As expected, smaller values of ω lead to a dominance of semilocal exchange at the long range which leads to a spurious stabilization of charge-transfer excitations which are appearing at increasingly lower energies with increasing system size.

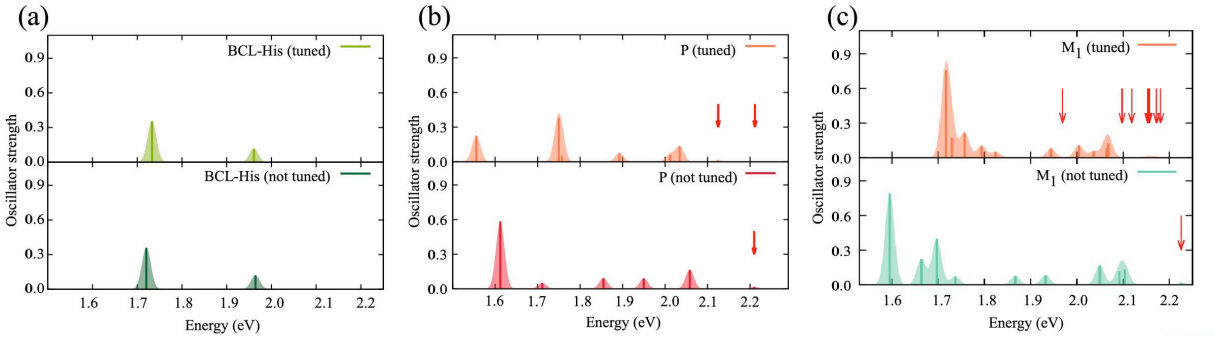

FIG. S2: Absorption spectra of (a) BCL-His, (b) P, and (c) M_1. The upper panel spectra are calculated with ωPBE using an "optimally" tuned ω value for each structure while the lower panel spectra were calculated using the same $\omega = 0.171 a_0^{-1}$ based on tuning for a gas-phase BCL a molecule[4].

II. ADDITIONAL RESULTS AND DISCUSSION

A. Additional Information on the Bare Hexameric RC Model

1. Excitation Energies

	RC	*RC* + *His*
Exc.	En.[eV] (Osc.Str.)	En.[eV](Osc.Str.)
1	1.5615 (0.83)	1.5703 (0.81)
2	1.6341 (0.36)	1.6358 (0.36)
3	1.6733 (0.33)	1.6748 (0.32)
4	1.7176 (0.15)	1.7186 (0.13)
5	1.8014 (0.30)	1.7962 (0.29)
6	1.8431 (0.29)	1.8324 (0.10)
7	1.8528 (0.07)	1.8391 (0.24)
8	1.9275 (0.10)	1.8676 (0.09)
9	2.0489 (0.18)	1.9435 (0.14)
10	2.0856 (0.02)	1.9781 (0.09)
11	2.0870 (0.13)	1.9882 (0.09)
12	2.0968 (0.23)	2.1235 (0.17)
13	2.1466 (0.20)	2.1493 (0.23)
14	2.1931 (0.02)	
15	2.3373 (0.00)	
16	2.3421 (0.00)	

TABLE S2: The excitation energies of the hexameric *RC* model without and with the coordinating histidines and leucines.

2. Transition Densities and Difference Densities

Both the transition and difference densities can be derived from the density matrix $\gamma^{ii}(\mathbf{r},\mathbf{r}') = N\int \Psi^i(\mathbf{r},\mathbf{r}_2,\ldots,\mathbf{r}_N)\Psi^i(\mathbf{r}',\mathbf{r}_2,\ldots,\mathbf{r}_N)d^3r_2...d^3r_N$, where N is the number of electrons and Ψ^i is the excited state wavefunction, here constructed from a sum of Slater determinants of generalized Kohn-Sham orbitals with coefficients from linear-response TDDFT. The ground state density is $n^0(\mathbf{r}) = \gamma^{00}(\mathbf{r},\mathbf{r})$ The density of excited state i is $n^i(\mathbf{r}) = \gamma^{ii}(\mathbf{r},\mathbf{r})$. The difference density is obtained by subtracting n^i from n^0, and allows to visualize the change of density upon excitation of the system into excited state i.

The transition density is obtained as the diagonal part of the density matrix for a transition from the ground state into an excited state i $\rho^{0i}(\mathbf{r}) = \gamma^{0i}(\mathbf{r},\mathbf{r})$ and is particularly useful for determining the interaction strength of electronic transitions with light and efficiencies of excitation energy transfer[5]. For charge-transfer excitations there is no overlap between ground and excited state, thus the transition density vanishes. Therefore, the difference density is a more useful tool for visualizing charge-transfer excitations and quantifying their charge-transfer character.

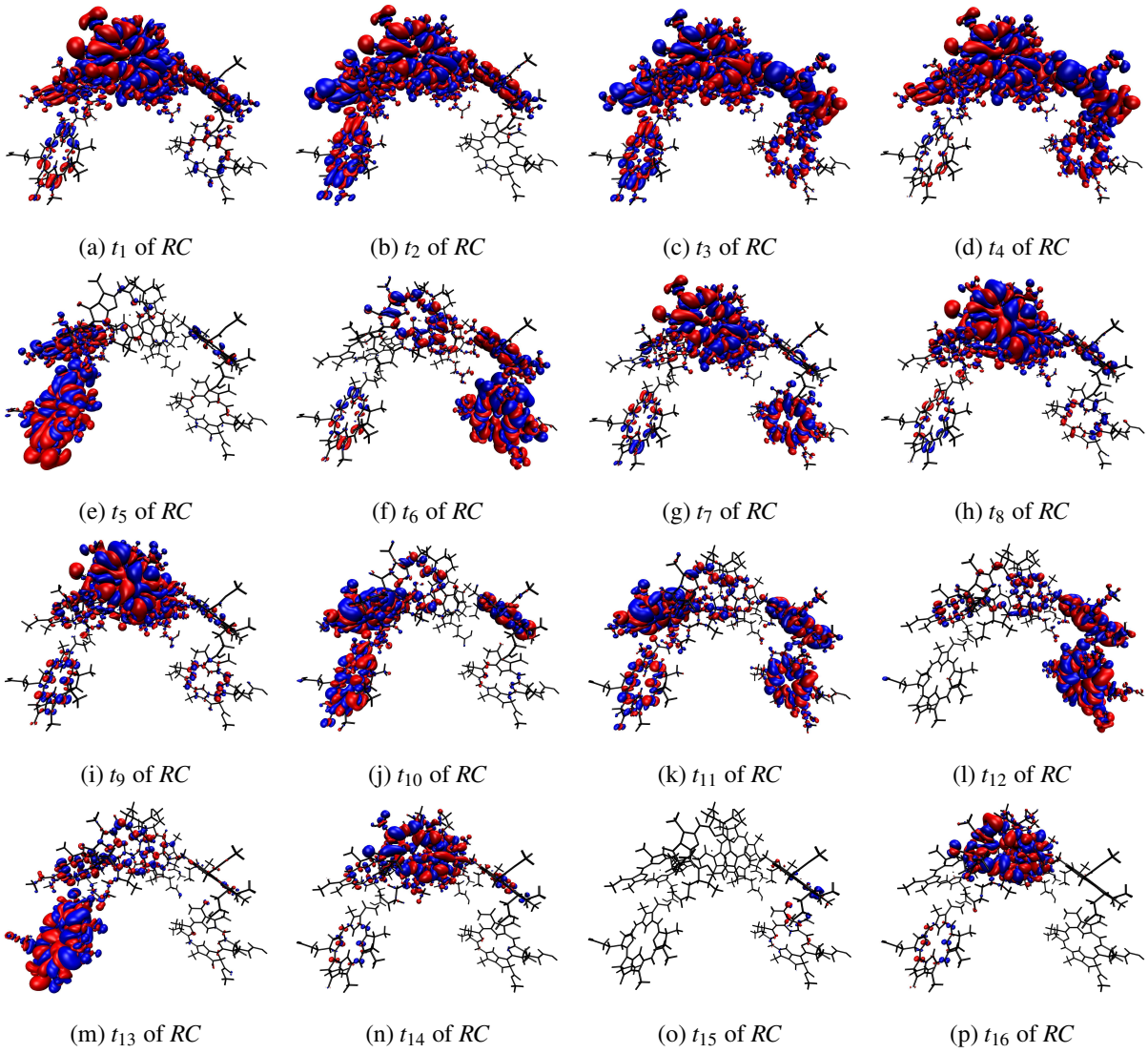

(a) t_1 of *RC* (b) t_2 of *RC* (c) t_3 of *RC* (d) t_4 of *RC*

(e) t_5 of *RC* (f) t_6 of *RC* (g) t_7 of *RC* (h) t_8 of *RC*

(i) t_9 of *RC* (j) t_{10} of *RC* (k) t_{11} of *RC* (l) t_{12} of *RC*

(m) t_{13} of *RC* (n) t_{14} of *RC* (o) t_{15} of *RC* (p) t_{16} of *RC*

FIG. S3: The transition densities t_1 to t_{16} of the hexameric *RC* model. The red surface of the transition density shows the isovalue -0.0001a_0^{-3} and the blue surface shows 0.0001a_0^{-3}. The A-branch is located on the right-hand side.

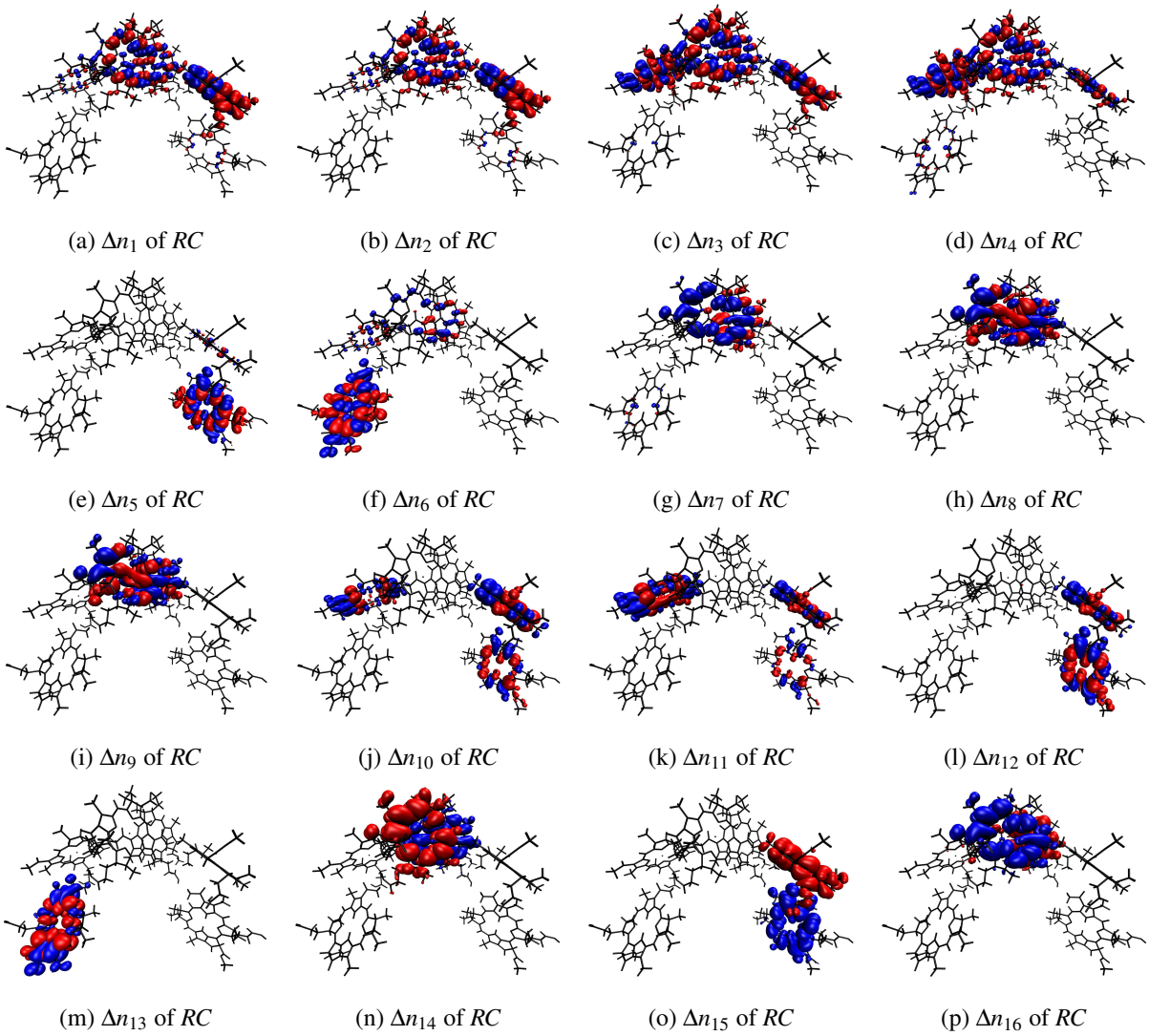

(a) Δn_1 of *RC* (b) Δn_2 of *RC* (c) Δn_3 of *RC* (d) Δn_4 of *RC*

(e) Δn_5 of *RC* (f) Δn_6 of *RC* (g) Δn_7 of *RC* (h) Δn_8 of *RC*

(i) Δn_9 of *RC* (j) Δn_{10} of *RC* (k) Δn_{11} of *RC* (l) Δn_{12} of *RC*

(m) Δn_{13} of *RC* (n) Δn_{14} of *RC* (o) Δn_{15} of *RC* (p) Δn_{16} of *RC*

FIG. S4: The difference densities 1 to 16 of *RC*. The red surface of the difference density shows the isovalue -0.0001a_0^{-3} and the blue surface shows 0.0001a_0^{-3}. The A-branch is located on the right-hand side.

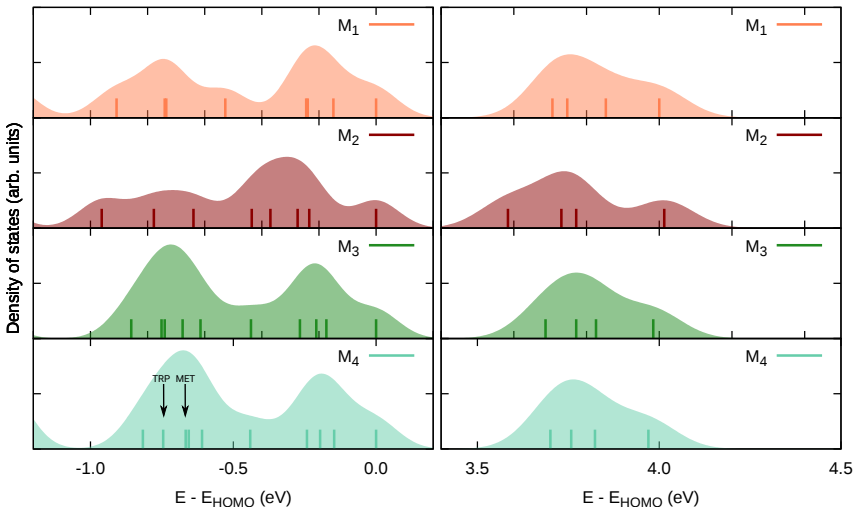

FIG. S5: Occupied (left panel) and unoccupied (right panel) DOS of model systems M_1 to M_4. Colored impulses mark eigenvalues. The shaded areas are calculated by folding the eigenvalues with Gaussian functions with a width of 0.08 eV as a guide to the eye.

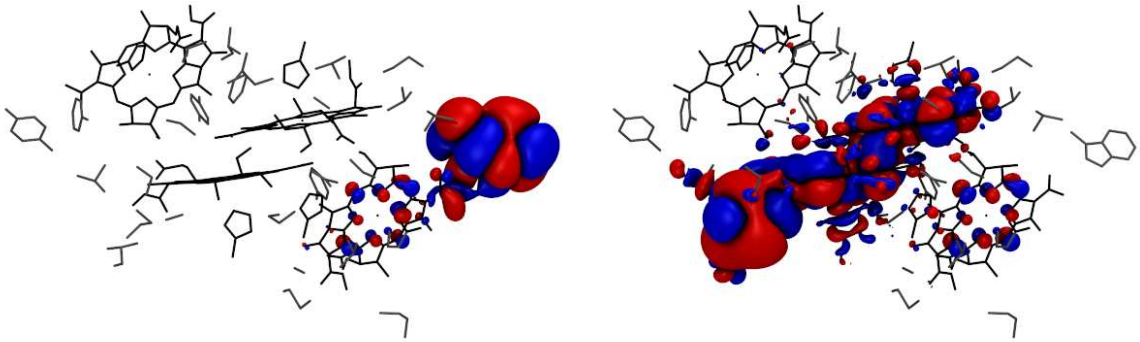

(a) HOMO-8 of M_4

(b) HOMO-7 of M_4

FIG. S6: The orbitals localized on TRP M157 (a) and MET L248 (b). The red surface shows the isovalue -0.001$a_0^{-3/2}$ and the blue surface shows 0.001$a_0^{-3/2}$.

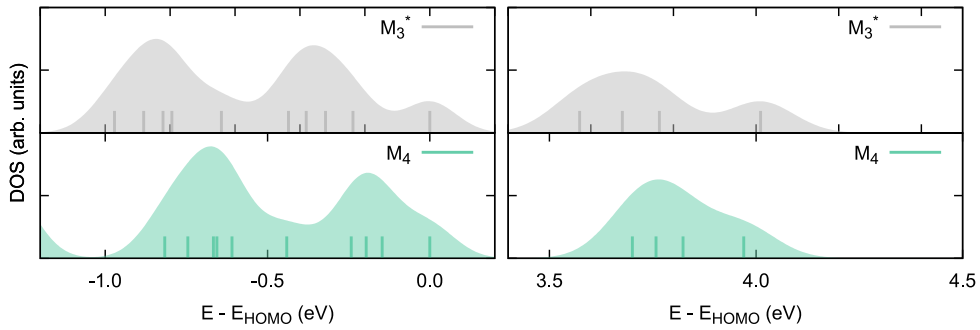

FIG. S7: Occupied (left panel) and unoccupied (right panel) DOS of model systems M_3^* and M_4. Colored impulses mark eigenvalues.

B. Additional Information on Tetrameric Models M_1 – M_4

1. *List of Amino Acids in M_4*

2. *Electronic Density of States*

3. *Assignment of Excitations of Tetrameric Model*

The lowest-energy excitations of single BCL *a* molecules are the Q_y excitation at ∼1.6 eV and the Q_x excitation at ∼2.1 eV with approximately perpendicular transition dipole moments[6]. Therefore, the first excitations of our tetrameric model systems are expected to arise from a coupling of the Q_y and Q_x excitations of the four RC BCL *a* molecules. Following Ref. 7, we start by dividing model systems M_1 and M_2 into subsystems and comparing their absorption spectra to those of P (P+HIS) and the B_A-B_B dimer (B_A+HIS-B_B+HIS) in Figure S8. To assign the character of these excitations, we calculated transition densities of all systems (Figures S8, S9, and S10). Figure S8 and Figure S9 show that the first two excitations of P are coupled Q_y excitations with characteristics of a J-aggregate featuring one bright excitation (parallel transition dipole moments) and one excitation with smaller oscillator strength (antiparallel transition dipole moments). The two BCL *a* of the special pair P are only 7.5 Å apart (measured as the distance between the central Mg ions). Short-range coupling, therefore, dominates the interaction of this "supermolecule". The distance of B_A and B_B is with 21.4 Å much larger. Consequently, we find one Q_y excitation on each BCL with similar oscillator strength and low coupling (Figure S10). Comparison with the full spectrum and the transition densities of M_1 shows that only the first excitation is localized on P while excitations 2 to 4 are coupled Q_y excitations spread across all four BCLs.

Δn_i	BCL	*RC*	Δn_i	BCL	*RC*	Δn_i	BCL	*RC*	Δn_i	BCL	*RC*
	P_A	0		P_A	0		P_A	0		P_A	0
	P_B	0		P_B	0		P_B	0		P_B	0
	B_A	0		B_A	0		B_A	0		B_A	0
Δn_1	B_B	0	Δn_5	B_B	0	Δn_9	B_B	0	Δn_{13}	B_B	0
	H_A	0		H_A	0		H_A	0		H_A	0
	H_B	0		H_B	0		H_B	0		H_B	0
	P_A	0		P_A	0		P_A	0		P_A	0.90
	P_B	0		P_B	0		P_B	0		P_B	-0.90
	B_A	0		B_A	0		B_A	0		B_A	0
Δn_2	B_B	0	Δn_6	B_B	0	Δn_{10}	B_B	0	Δn_{14}	B_B	0
	H_A	0		H_A	0		H_A	0		H_A	0
	H_B	0		H_B	0		H_B	0		H_B	0
	P_A	0		P_A	-0.69		P_A	0		P_A	0
	P_B	0		P_B	0.69		P_B	0		P_B	0
	B_A	0		B_A	0		B_A	0		B_A	-0.99
Δn_3	B_B	0	Δn_7	B_B	0	Δn_{11}	B_B	0	Δn_{15}	B_B	0
	H_A	0		H_A	0		H_A	0		H_A	0.99
	H_B	0		H_B	0		H_B	0		H_B	0
	P_A	0		P_A	0		P_A	0		P_A	-0.83
	P_B	0		P_B	0		P_B	0		P_B	0.83
	B_A	0		B_A	0		B_A	0		B_A	0
Δn_3	B_B	0	Δn_8	B_B	0	Δn_{12}	B_B	0	Δn_{16}	B_B	0
	H_A	0		H_A	0		H_A	0		H_A	0
	H_B	0		H_B	0		H_B	0		H_B	0

TABLE S3: The integral values over the spaces of the 4 BCLs and 2 Bacteriopheophytins of the difference densities calculated with method 1 defined in the main text. Values smaller than 0.01 are set to 0.

name	chain	sequence number
TYR	L	128
LEU	L	131, 154
PHE	L	146, 181
HIS	L	168, 153, 173
VAL	L	157
THR	L	160
MET	L	174, 248
SER	L	178, 244
ILE	L	177
ALA	L	245
TYR	M	210
LEU	M	156, 160, 183, 196
PHE	M	197
HIS	M	182, 202
THR	M	186
SER	M	190
ILE	M	179, 206, 284
ALA	M	207
ASN	M	187
TRP	M	157

TABLE S4: The 32 amino acids included in M_4.

To analyze the influence of the histidines on the first ten excitations, we perform a similar division into subsystems for M_2. We show the spectrum of M_2 and the corresponding subsystems P+HIS and B_A+HIS-B_B+HIS in Figure S8.

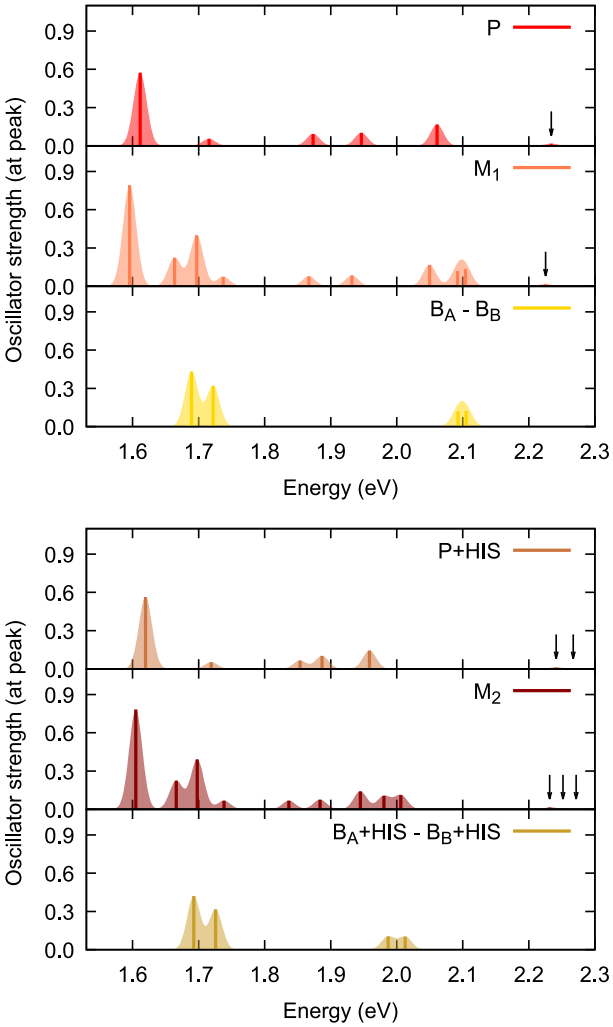

FIG. S8: (a) Absorption spectra of P, M_1 and B_A-B_B and (b) Absorption spectra of P+HIS, M_2 and B_A+HIS-B_B+HIS. Black arrows mark excitations with vanishing oscillator strength.

4. Excitation Energies, Transition Densities and Difference Densities

With Q-CHEM, the calculation of 10 excitations was possible for our largest model system M_4. We therefore performed an additional calculation with TURBOMOLE which allowed for the calculation of 12 excitations. Table S6 shows that Q-CHEM and TURBOMOLE result in very similar excitation energies for the first 10 excitations.

	M_1	M_2	M_3
Exc.	En.[eV] (Osc.Str.)	En.[eV](Osc.Str.)	En.[eV](Osc.Str.)
1	1.596 (0.792)	1.605 (0.783)	1.584 (0.790)
2	1.664 (0.223)	1.666 (0.224)	1.655 (0.203)
3	1.697 (0.400)	1.698 (0.391)	1.690 (0.442)
4	1.737 (0.074)	1.738 (0.067)	1.725 (0.105)
5	1.867 (0.077)	1.837 (0.067)	1.818 (0.071)
6	1.932 (0.084)	1.884 (0.075)	1.890 (0.079)
7	2.050 (0.167)	1.945 (0.141)	1.926 (0.125)
8	2.092 (0.118)	1.981 (0.105)	1.973 (0.104)
9	2.104 (0.133)	2.006 (0.111)	2.005 (0.109)
10	2.226 (0.018)	2.232 (0.014)	2.148 (0.027)
11	2.332 (0.002)	2.252 (0.005)	2.278 (0.002)
12	2.393 (0.000)	2.272 (0.000)	2.383 (0.000)
13	2.520 (0.001)	2.484 (0.000)	2.439 (0.006)
14	2.538 (0.000)	2.546 (0.001)	2.468 (0.000)
15	2.547 (0.000)	2.593 (0.000)	2.555 (0.000)
16	2.565 (0.000)	2.616 (0.000)	2.586 (0.001)
17	2.585 (0.001)	2.644 (0.000)	2.623 (0.001)
18	2.609 (0.000)	2.645 (0.002)	2.629 (0.005)
19	2.632 (0.001)	2.658 (0.000)	2.654 (0.000)
20	2.706 (0.006)	2.661 (0.007)	2.661 (0.000)
21	2.728 (0.000)	2.669 (0.002)	

TABLE S5: The excitation energies of M_1-M_3.

	M_4 (Q-Chem)	M_4 (Turbomole)
Exc.	En.[eV] (Osc.Str.)	En.[eV](Osc.Str.)
1	1.556 (0.860)	1.556 (0.861)
2	1.622 (0.185)	1.621 (0.184)
3	1.657 (0.475)	1.656 (0.467)
4	1.632 (0.103)	1.691 (0.101)
5	1.809 (0.085)	1.800 (0.080)
6	1.886 (0.076)	1.885 (0.088)
7	1.916 (0.105)	1.914 (0.090)
8	1.953 (0.105)	1.949 (0.104)
9	1.986 (0.105)	1.982 (0.104)
10	2.125 (0.029)	2.118 (0.030)
11		2.279 (0.002)
12		2.376 (0.004)

TABLE S6: The excitation energies of M_4. 10 excitations calculated with Q-Chem and 12 excitations calculated with Turbomole.

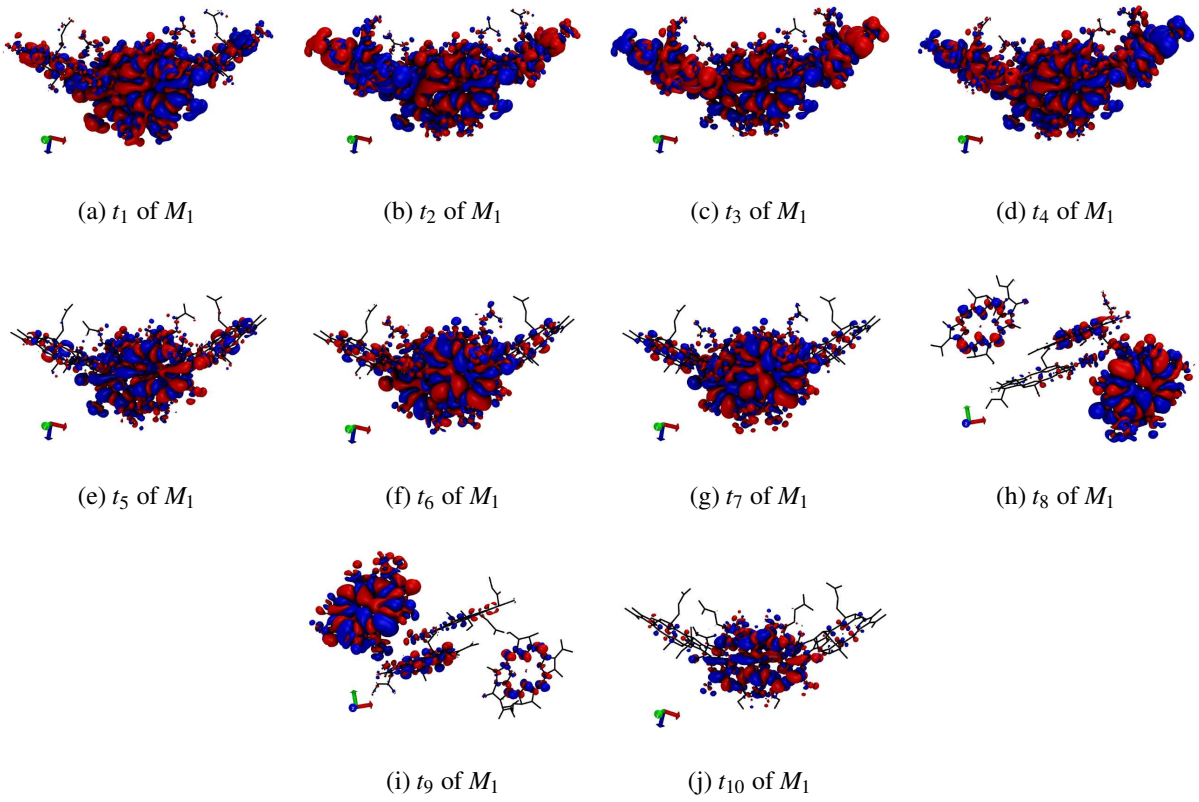

(a) t_1 of M_1 (b) t_2 of M_1 (c) t_3 of M_1 (d) t_4 of M_1

(e) t_5 of M_1 (f) t_6 of M_1 (g) t_7 of M_1 (h) t_8 of M_1

(i) t_9 of M_1 (j) t_{10} of M_1

FIG. S9: The transition densities t_1 to t_{10} of M_1. The red surface of the transition density shows the isovalue -0.0001a_0^{-3} and the blue surface shows 0.0001a_0^{-3}. The spatial orientation of t_8 to t_{10} was changed for reasons of clarity. However, in all plots, B_A is on the left hand side.

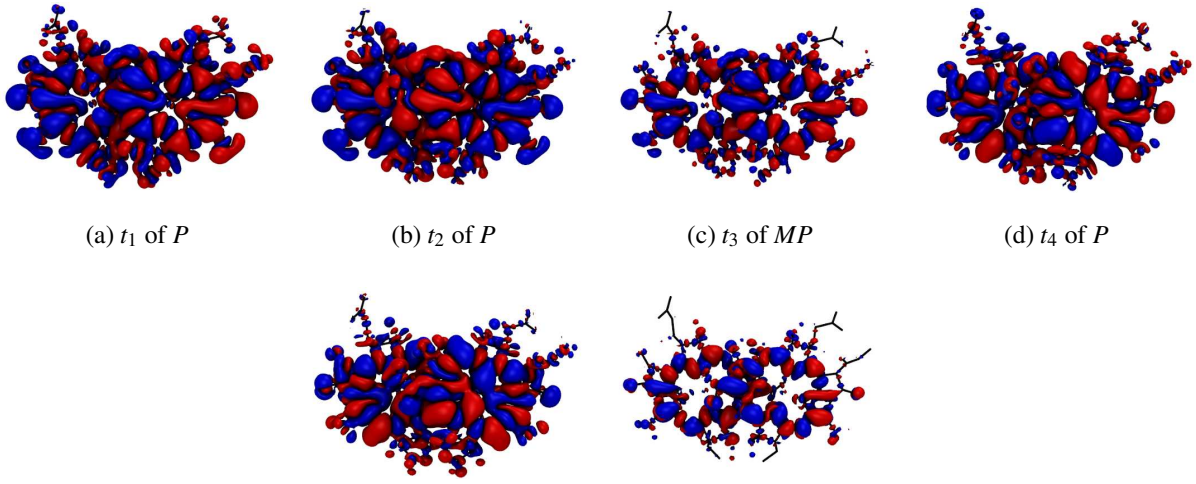

(a) t_1 of P (b) t_2 of P (c) t_3 of MP (d) t_4 of P

(e) t_5 of P (f) t_6 of P

FIG. S10: The transition densities t_1 to t_6 of P. The red surface of the transition density shows the isovalue -0.0001a_0^{-3} and the blue surface shows 0.0001a_0^{-3}.

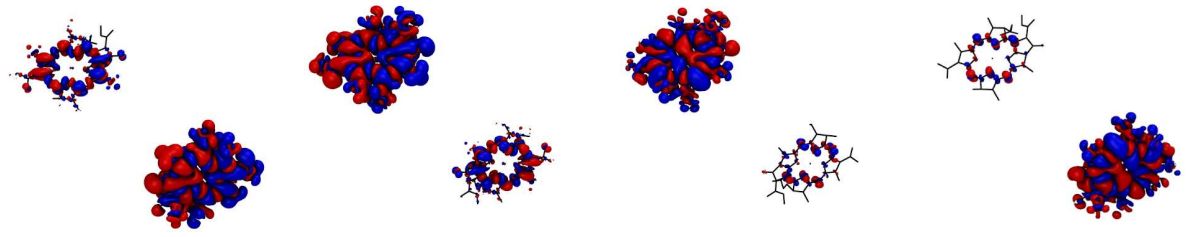

(a) t_1 of B_A-B_B (b) t_2 of B_A-B_B (c) t_3 of B_A-B_B (d) t_4 of B_A-B_B

FIG. S11: The transition densities t_1 to t_4 of B_A-B_B. The red surface of the difference density shows the isovalue -0.0001a_0^{-3} and the blue surface shows 0.0001a_0^{-3}. B_A is the upper left BCL.

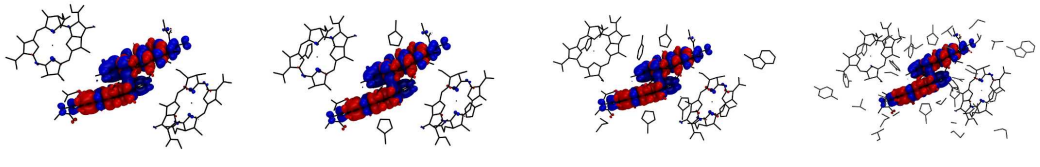

(a) Δn_1 of M_1 (b) Δn_1 of M_2 (c) Δn_1 of M_3 (d) Δn_1 of M_4

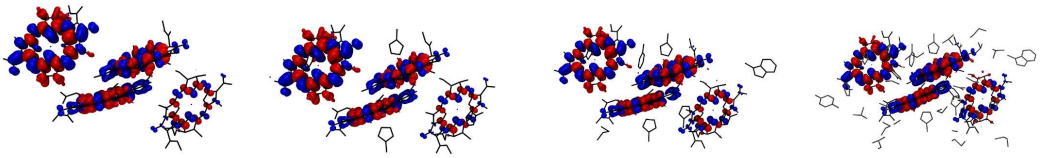

(e) Δn_2 of M_1 (f) Δn_2 of M_2 (g) Δn_2 of M_3 (h) Δn_2 of M_4

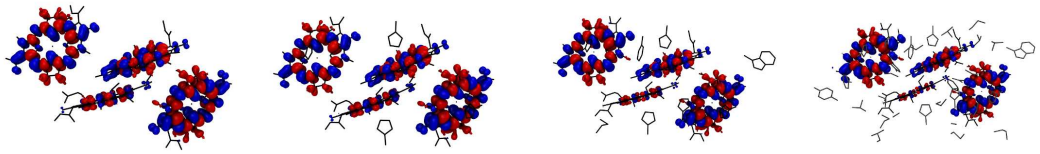

(i) Δn_3 of M_1 (j) Δn_3 of M_2 (k) Δn_3 of M_3 (l) Δn_3 of M_4

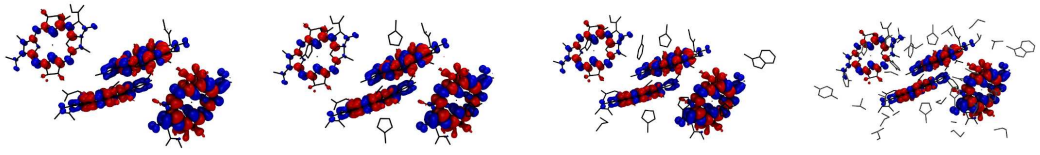

(m) Δn_4 of M_1 (n) Δn_4 of M_2 (o) Δn_4 of M_3 (p) Δn_4 of M_4

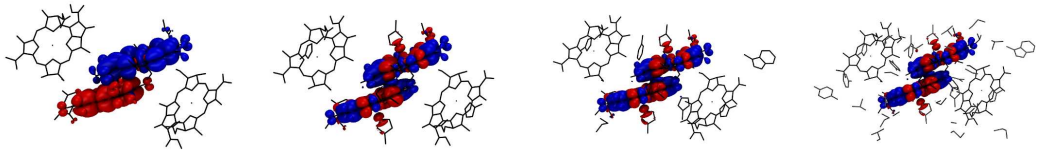

(q) Δn_5 of M_1 (r) Δn_5 of M_2 (s) Δn_5 of M_3 (t) Δn_5 of M_4

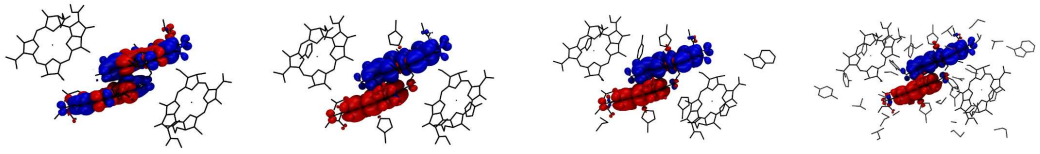

(u) Δn_6 of M_1 (v) Δn_6 of M_2 (w) Δn_6 of M_3 (x) Δn_6 of M_4

FIG. S12: The difference densities 1 to 6 of M_1-M_4. The red surface of the difference density shows the isovalue -0.0001a_0^{-3} and the blue surface shows 0.0001a_0^{-3}.

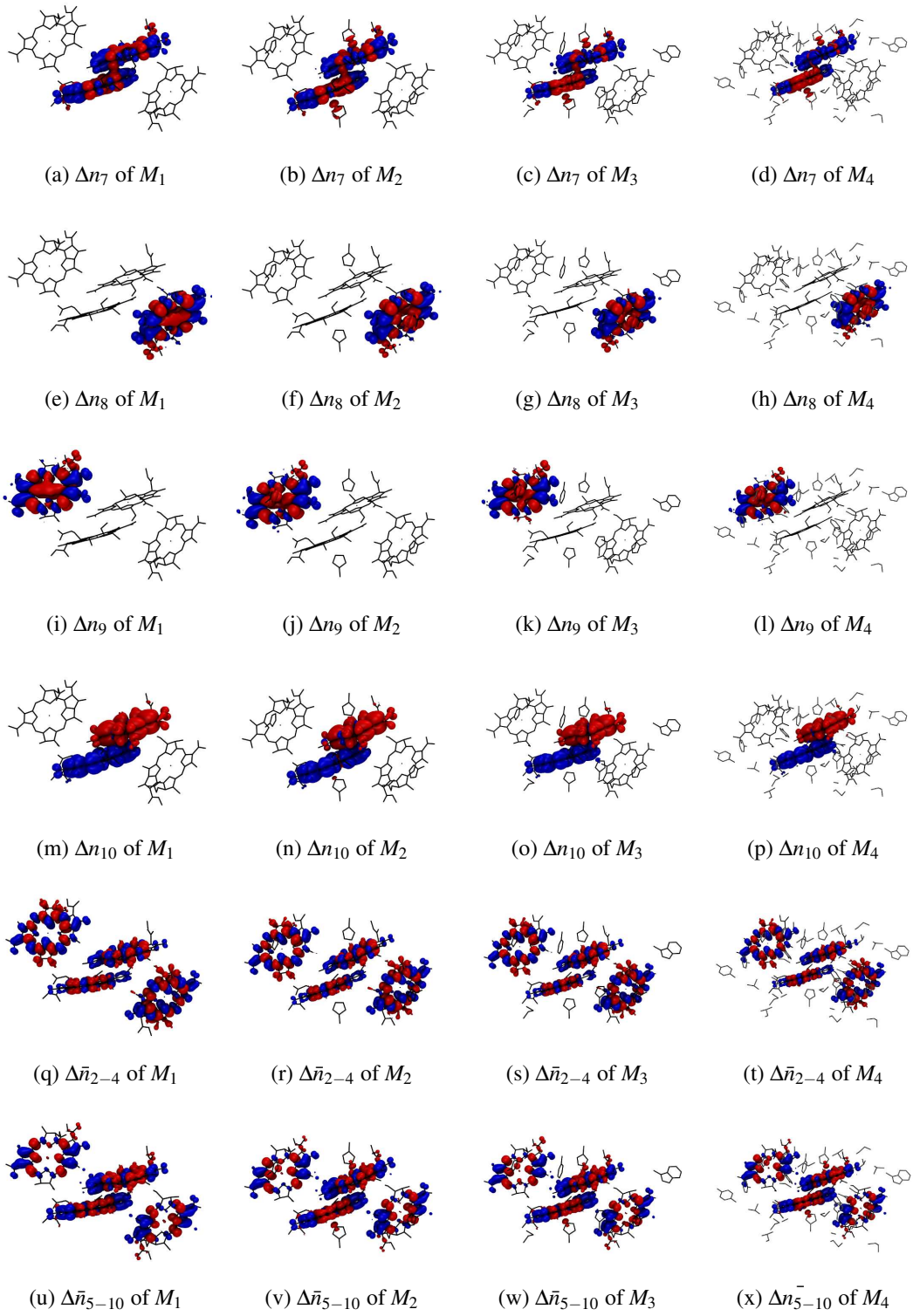

(a) Δn_7 of M_1 (b) Δn_7 of M_2 (c) Δn_7 of M_3 (d) Δn_7 of M_4

(e) Δn_8 of M_1 (f) Δn_8 of M_2 (g) Δn_8 of M_3 (h) Δn_8 of M_4

(i) Δn_9 of M_1 (j) Δn_9 of M_2 (k) Δn_9 of M_3 (l) Δn_9 of M_4

(m) Δn_{10} of M_1 (n) Δn_{10} of M_2 (o) Δn_{10} of M_3 (p) Δn_{10} of M_4

(q) $\Delta \bar{n}_{2-4}$ of M_1 (r) $\Delta \bar{n}_{2-4}$ of M_2 (s) $\Delta \bar{n}_{2-4}$ of M_3 (t) $\Delta \bar{n}_{2-4}$ of M_4

(u) $\Delta \bar{n}_{5-10}$ of M_1 (v) $\Delta \bar{n}_{5-10}$ of M_2 (w) $\Delta \bar{n}_{5-10}$ of M_3 (x) $\Delta \bar{n}_{5-10}$ of M_4

FIG. S13: The difference densities 7 to 10 and the average difference densities 2-4 and 5-10 of M_1-M_4. The red surface of the difference density shows the isovalue -0.0001a_0^{-3} and the blue surface shows 0.0001a_0^{-3}.

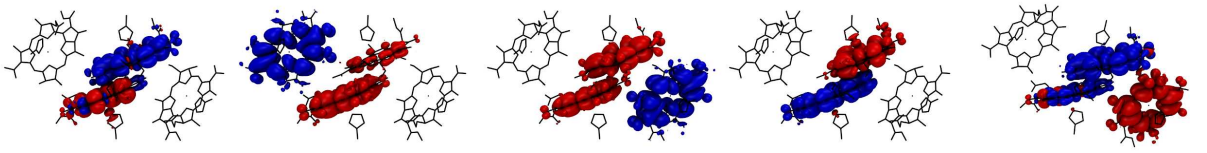

(a) Δn_{11} of M_2 (b) Δn_{12} of M_2 (c) Δn_{13} of M_2 (d) Δn_{14} of M_2 (e) Δn_{21} of M_2

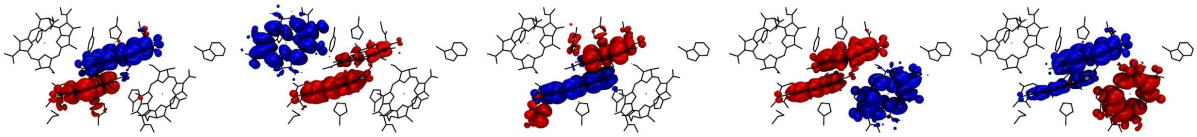

(f) Δn_{11} of M_3 (g) Δn_{12} of M_3 (h) Δn_{14} of M_3 (i) Δn_{15} of M_3 (j) Δn_{16} of M_3

FIG. S14: The difference densities of the CT excitations of M_2 and M_3, which are not shown in the main text. The red surface of the difference density shows the isovalue -0.0001a_0^{-3} and the blue surface shows 0.0001a_0^{-3}.

Δn_i	BCL	M_1	M_2	M_3	M_4
Δn_1	P_A	−0.15 (−0.12)	−0.13 (−0.11)	−0.10 (−0.09)	−0.08 (−0.07)
	P_B	0.15 (0.12)	0.13 (0.11)	0.10 (0.09)	0.07 (0.07)
	B_A	0 (0)	0 (0)	0 (0)	0 (0)
	B_B	0 (0)	0 (0)	0 (0)	0 (0)
Δn_2	P_A	0 (0)	0 (0)	0 (0.01)	0 (0.01)
	P_B	0 (0)	0 (0)	0 (−0.01)	0 (−0.01)
	B_A	0 (0)	0 (0)	0 (0)	0 (0)
	B_B	0 (0)	0 (0)	0 (0)	0 (0)
Δn_3	P_A	0 (0)	0 (0)	−0.01 (0)	0 (0)
	P_B	0 (0)	0 (0)	0 (0)	0 (0)
	B_A	0 (0)	0 (0)	0 (0)	0 (0)
	B_B	0 (0)	0 (0)	0 (0)	0 (0)
Δn_4	P_A	0 (0)	0 (0)	0 (0)	0 (0)
	P_B	0 (0)	0 (0)	0 (0)	0 (0)
	B_A	0 (0)	0 (0)	0 (0)	0 (0)
	B_B	0 (0)	0 (0)	0 (0)	0 (0)
Δn_5	P_A	−0.76 (−0.59)	−0.06 (−0.04)	−0.03 (−0.04)	−0.03 (−0.03)
	P_B	0.76 (0.59)	0.06 (0.04)	0.03 (0.04)	0.03 (0.03)
	B_A	0 (0)	0 (0)	0 (0)	0 (0)
	B_B	0 (0)	0 (0)	0 (0)	0 (0)
Δn_6	P_A	−0.07 (−0.05)	−0.74 (−0.57)	−0.67 (−0.51)	−0.57 (−0.44)
	P_B	0.07 (0.05)	0.74 (0.57)	0.67 (0.51)	0.57 (0.44)
	B_A	0 (0)	0 (0)	0 (0)	0 (0)
	B_B	0 (0)	0 (0)	0 (0)	0 (0)
Δn_7	P_A	0 (0)	−0.05 (0.04)	−0.14 (−0.10)	−0.25 (−0.19)
	P_B	0 (0)	0.05 (0.04)	0.14 (0.10)	0.25 (0.19)
	B_A	0 (0)	0 (0)	0 (0)	0 (0)
	B_B	0 (0)	0 (0)	0 (0)	0 (0)
Δn_8	P_A	0 (0)	0 (0)	0 (0)	0 (0)
	P_B	0 (0)	0 (0)	0 (0)	0 (0)
	B_A	0 (0)	0 (0)	0 (0)	0 (0)
	B_B	0 (0)	0 (0)	0 (0)	0 (0)
Δn_9	P_A	0 (0)	0 (0)	0 (0)	0 (0)
	P_B	0 (0)	0 (0)	0 (0)	0 (0)
	B_A	0 (0)	0 (0)	0 (0)	0 (0)
	B_B	0 (0)	0 (0)	0 (0)	0 (0)
Δn_{10}	P_A	0.92 (0.72)	0.73 (0.57)	0.90 (0.69)	0.89 (0.67)
	P_B	−0.92 (−0.72)	−0.74 (−0.57)	−0.90 (−0.69)	−0.90 (−0.67)
	B_A	0 (0)	0 (0)	0 (0)	0 (0)
	B_B	0 (0)	0 (0)	0 (0)	0 (0)

TABLE S7: The integral values over the spaces of the 4 BCLs of the difference densities which are not shown in the main text calculated with method 1 defined in the main text. Values in brackets are calculated with method 2. All values smaller than 0.01 are set to 0.

	BCL	M_1	M_2	M_3
$P_A^- P_B^+$	P_A	−0.84 (−0.67)	−0.68 (−0.54)	−0.86 (−0.69)
	P_B	0.84 (0.67)	0.67 (0.54)	0.86 (0.69)
	B_A	0 (0)	0 (0)	0 (0)
	B_B	0 (0)	0 (0)	0 (0)
$P^- B_A^+$	P_A	−0.94 (−0.90)	−0.94 (−0.90)	−0.92 (−0.87)
	P_B	−0.06 (−0.09)	−0.06 (−0.09)	−0.08 (−0.12)
	B_A	1.00 (0.99)	1.00 (0.99)	1.00 (0.99)
	B_B	0 (0)	0 (0)	0 (0)
$P^+ B_B^-$	P_A	0.07 (0.14)	0.07 (0.13)	0.11 (0.17)
	P_B	0.91 (0.84)	0.77 (0.71)	0.87 (0.80)
	B_A	0 (0)	0 (0)	0 (0)
	B_B	−0.99 (−0.98)	−0.84 (−0.84)	−0.98 (−0.97)
$P^- B_B^+$	P_A	−0.45 (−0.45)	−0.43 (−0.43)	−0.35 (−0.36)
	P_B	−0.55 (−0.54)	−0.56 (−0.56)	−0.65 (−0.63)
	B_A	0 (0)	0 (0)	0 (0)
	B_B	0.99 (0.99)	0.99 (0.99)	1.00 (0.99)
$P_A^+ P_B^-$	P_A	0.84 (0.67)	0.88 (0.71)	0.75 (0.57)
	P_B	−0.84 (−0.67)	−0.88 (−0.71)	−0.75 (−0.57)
	B_A	0 (0)	0 (0)	0 (0)
	B_B	0 (0)	0 (0)	0 (0)

TABLE S8: Integrated difference density of the charge-transfer excitations for subsystem charge densities P_A, P_B, B_A, and B_B as calculated with method 1 defined in the main text. The values in brackets are calculated with method 2.

5. *Effect of Molecular Vibrations*

We note that our calculation of the vibrational normal modes of M_1 produces a number of imaginary modes, as expected for an experimental crystal structure which does not correspond to a local minimum of the DFT potential energy surface. We therefore do not average over all modes to obtain a more complete picture of the vibrational renormalization[8]. Nonetheless, our calculations provide a mode-resolved picture of the effect of thermally-activated molecular vibrations on excitations of different character.

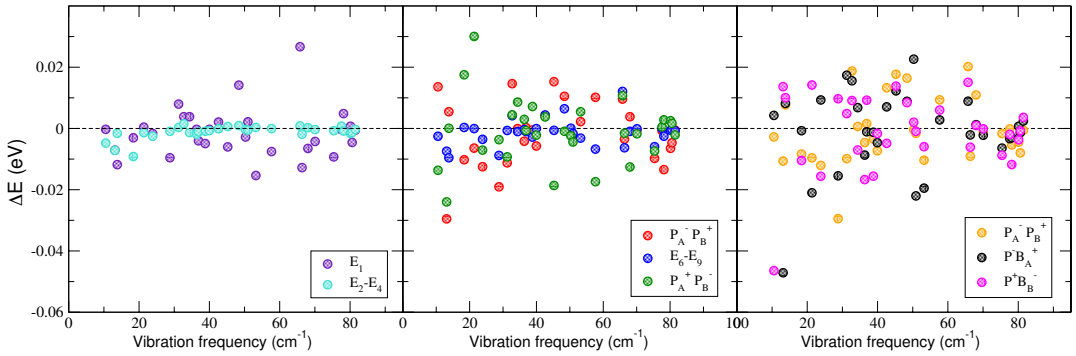

FIG. S15: Mode-resolved picture of excitation energy renormalization due to structural distortion along vibrational normal modes. Left: Coupled Q_y excitations, where excitation 1 can be assigned to P and we average over excitations 1 – 3, Middle: Coupled Q_x excitations and internal charge-transfer excitations of P, corresponding to excitations 5 – 10, Right: Charge-transfer excitations 11 – 13.

6. *QM/MM Calculations*

The QM/MM calculation was carried out using the pDynamo interface version 1.8.0 in combination with Orca version 5.0.2[9,10]. The protein environment was introduced in these calculations using point charges. For these calculations, we used the ωB97 exchange-correlation functional, since ωPBE is not implemented in Orca. ωB97 was shown to correctly predict reaction center site energy shifts with TDDFT[11]. However, we find that it underestimates the coupled Q_y excitations by $\sim$300 meV as compared to our calculations using optimally-tuned ωPBE (see Figure S16). Furthermore, the two internal partial charge transfer excitations that are part of the group of coupled Q_x excitations (excitations 5 and 10 of M_1 in the main text), appear at significantly higher energies

in these spectra. Employing the TDA (Figure S17) leads to a picture more in line with our ωPBE calculations, which we attribute to a fortuitous cancellation of errors. For both the full TDDFT and the TDA calculation, the effect of the MM environment on the excitations energies is qualitatively similar to our calculations with explicit inclusion of the environment. The main difference is that the redshift of the coupled Q_y and Q_x excitations induced by the MM environment is substantially smaller than that from the explicit model.

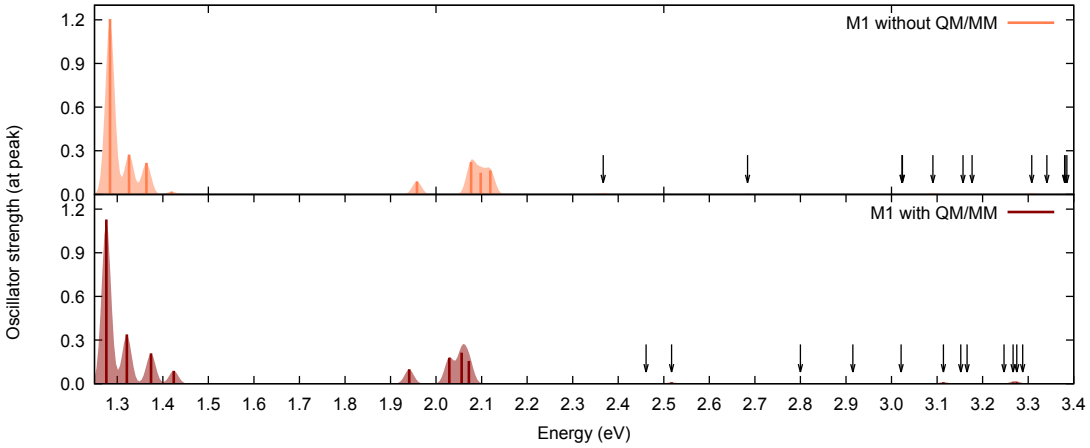

FIG. S16: TDDFT absorption spectrum of M_1 without and with QM/MM environment, calculated using the ωB97 functional as implemented in ORCA. Arrows mark dark states with vanishing oscillator strength.

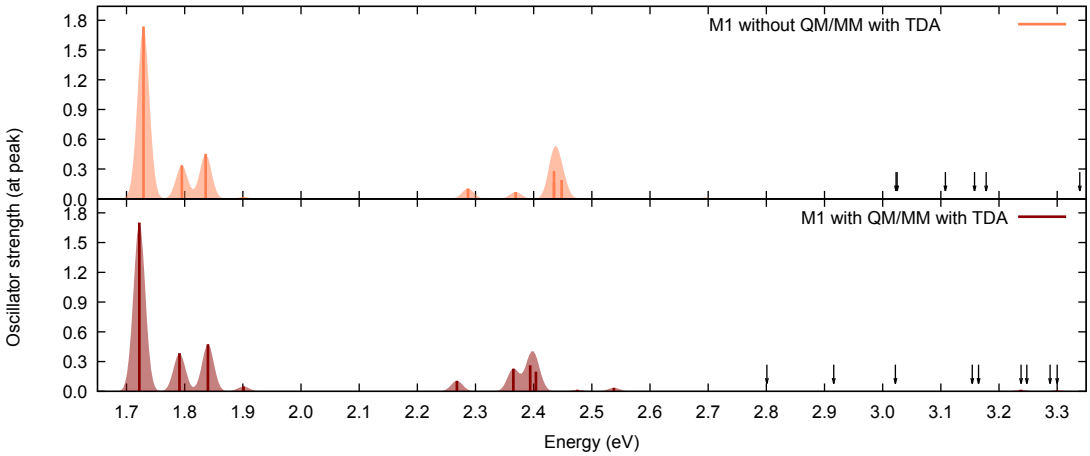

FIG. S17: TDA absorption spectrum of M_1 without and with QM/MM environment, calculated using the ωB97 functional as implemented in ORCA. Arrows mark dark states with vanishing oscillator strength.

C. Additional Information on A-branch and B-branch model systems A_n and B_n

1. Excitation Energies

	A_1	A_2	A_3
Exc.	En.[eV] (Osc.Str.)	En.[eV](Osc.Str.)	En.[eV](Osc.Str.)
1	1.5827 (0.76)	1.5908 (0.75)	1.5669 (0.70)
2	1.6384 (0.37)	1.6397 (0.36)	1.6319 (0.42)
3	1.6981 (0.02)	1.7013 (0.02)	1.6804 (0.03)
4	1.8017 (0.31)	1.7966 (0.30)	1.7756 (0.32)
5	1.9306 (0.01)	1.8409 (0.07)	1.8206 (0.08)
6	1.9369 (0.11)	1.9383 (0.11)	1.9239 (0.14)
7	2.0528 (0.17)	1.9645 (0.06)	1.9589 (0.00)
8	2.0855 (0.04)	1.9862 (0.08)	1.9927 (0.07)
9	2.0963 (0.23)	2.0853 (0.17)	2.0395 (0.09)
10	2.1085 (0.04)	2.1059 (0.03)	2.0749 (0.18)
11	2.3238 (0.00)	2.1527 (0.00)	2.0999 (0.00)
12	2.4277 (0.00)	2.3577 (0.00)	2.3369 (0.00)
13	2.5177 (0.00)	2.4122 (0.00)	2.4171 (0.00)
14	2.5429 (0.00)	2.4494 (0.00)	2.4571 (0.00)
15	2.5479 (0.00)	2.5630 (0.00)	2.4666 (0.00)
16	2.5671 (0.00)	2.5942 (0.00)	
17	2.5761 (0.00)	2.6289 (0.00)	
18	2.5823 (0.00)	2.6555 (0.00)	
19	2.6878 (0.00)	2.6648 (0.00)	
20	2.7034 (0.00)	2.6902 (0.00)	

TABLE S9: The excitation energies of $A_1 - A_3$ systems.

	B_1	B_2
Exc.	En.[eV] (Osc.Str.)	En.[eV](Osc.Str.)
1	1.5462 (0.58)	1.5515 (0.55)
2	1.6673 (0.24)	1.6699 (0.26)
3	1.7156 (0.28)	1.7165 (0.25)
4	1.7903 (0.13)	1.7919 (0.11)
5	1.8439 (0.28)	1.8289 (0.14)
6	1.9245 (0.10)	1.8396 (0.24)
7	2.0533 (0.17)	1.9471 (0.14)
8	2.0867 (0.10)	1.9748 (0.10)
9	2.1260 (0.19)	2.1214 (0.18)
10	2.2697 (0.00)	2.1723 (0.00)
11	2.2884 (0.01)	2.3127 (0.01)
12	2.3452 (0.00)	2.4741 (0.00)
13	2.4878 (0.00)	2.5407 (0.00)
14	2.6067 (0.00)	2.5619 (0.00)
15	2.6105 (0.00)	2.5743 (0.00)
16	2.6671 (0.00)	2.6139 (0.01)
17	2.6826 (0.00)	2.6636 (0.00)
18	2.7307 (0.00)	2.6768 (0.00)
19	2.7587 (0.00)	2.7038 (0.00)
20	2.7645 (0.00)	2.7140 (0.00)

TABLE S10: The excitation energies of B_1 and B_2 systems.

2. *List of Amino Acids in A_3 system*

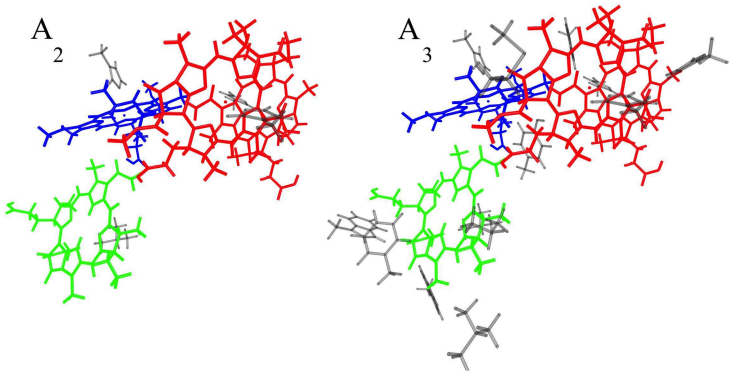

FIG. S18: A_2 and A_3 systems

name	chain	sequence number
HIS	L	152, 167, 172
PHE	L	120
VAL	L	240
LEU	L	237
MET	L	247
TRP	L	99
HIS	M	482
PHE	M	477
LEU	M	494
TRP	M	532
TYR	M	490

TABLE S11: The 13 amino acids included in A_3.

Δn_i	BCL	A_1	A_2	A_3	Δn_i	BCL	A_1	A_2	A_3
Δn_1	P_A	0	0	0	Δn_9	P_A	0	0	0
	P_B	0	0	0		P_B	0	0	0
	B_A	0	0	0		P_B	0	0	0
	H_A	0	0	0		P_B	0	0	0
Δn_2	P_A	0	0	0	Δn_{10}	P_A	-0.73	-0.78	0
	P_B	0	0	0		P_B	0.73	0.78	0
	B_A	0	0	0		B_A	0	0	0
	H_A	0	0	0		H_A	0	0	0
Δn_3	P_A	0	0	0	Δn_{11}	P_A	0	0	0
	P_B	0	0	0		P_B	0	0	0
	B_A	0	0	0		B_A	-0.99	-0.99	-0.99
	H_A	0	0	0		H_A	0.99	0.99	0.99
Δn_4	P_A	0	0	0	Δn_{12}	P_A	0.80	0.80	0.78
	P_B	0	0	0		P_B	-0.80	-0.80	-0.78
	B_A	0	0	0		B_A	0	0	0
	H_A	0	0	0		H_A	0	0	0
Δn_5	P_A	-0.71	0	0	Δn_{13}	P_A	-0.12	-0.14	-0.75
	P_B	0.71	0	0		P_B	-0.88	-0.86	0.75
	B_A	0	0	0		B_A	0.99	0.99	0
	H_A	0	0	0		H_A	0	0	0
Δn_6	P_A	0	0	0	Δn_{14}	P_A	-0.74	-0.81	0
	P_B	0	0	0		P_B	0.74	0.81	0
	B_A	0	0	0		B_A	0	0	0
	H_A	0	0	0		H_A	0	0	0
Δn_7	P_A	0	0.53	0	Δn_{15}	P_A	0	0	0
	P_B	0	-0.53	0		P_B	0	-0.15	0
	B_A	0	0	0		B_B	0	-0.84	0
	H_A	0	0	0		H_B	0	0.99	0
Δn_8	P_A	0	0	0	Δn_{16}	P_A			
	P_B	0	0	0		P_B			
	B_A	0	0	0		B_B			
	H_A	0	0	0		H_B			

TABLE S12: The integral values over the spaces of the 4 BCLs of the difference densities which are not shown in the main text calculated with method 1 defined in the main text. All values smaller than 0.01 are set to 0.

3. Integration over difference densities

Δn_i	BCL	B_1	B_2	Δn_i	BCL	B_1	B_2
Δn_1	P_A	0.32	0.33	Δn_9	P_A	0	0
	P_B	-0.32	-0.33		P_B	0	0
	B_B	0	0		B_B	0	0
	H_B	0	0		H_B	0	0
Δn_2	P_A	0	0	Δn_{10}	P_A	0.49	0.80
	P_B	0	0		P_B	-0.49	-0.80
	B_B	0	0		B_B	0	0
	H_B	0	0		H_B	0	0
Δn_3	P_A	0	0	Δn_{11}	P_A	-0.64	-0.93
	P_B	0	0		P_B	0.64	0.93
	B_B	0	0		B_B	0	0
	H_B	0	0		H_B	0	0
Δn_4	P_A	-0.59	-0.57	Δn_{12}	P_A	0.06	0.06
	P_B	0.59	0.57		P_B	0.93	0.93
	B_B	0	0		B_B	-0.99	-0.99
	H_B	0	0		H_B	0	0
Δn_5	P_A	0	0	Δn_{13}	P_A	0	0
	P_B	0	0		P_B	0	0
	B_B	0	0		B_B	0	0
	H_B	0	0		H_B	0	0
Δn_6	P_A	0.13	0.12	Δn_{14}	P_A	0	-0.27
	P_B	-0.13	-0.12		P_B	0	-0.72
	B_B	0	0		B_B	0	0.99
	H_B	0	0		H_B	0	0
Δn_7	P_A	0	0	Δn_{15}	P_A	0	0
	P_B	0	0		P_B	0	0
	B_B	0	0		B_B	0	-0.99
	H_B	0	0		H_B	0	0.99
Δn_8	P_A	0	0	Δn_{16}	P_A		
	P_B	0	0		P_B		
	B_B	0	0		B_B		
	H_B	0	0		H_B		

TABLE S13: The integral values over the spaces of the 4 BCLs of the difference densities which are not shown in the main text calculated with method 1 defined in the main text. All values smaller than 0.01 are set to 0.

REFERENCES

[1]T. Körzdörfer, J. S. Sears, C. Sutton, and J. L. Brédas, "Long-range corrected hybrid functionals for pi-conjugated systems: Dependence of the range-separation parameter on conjugation length," J. Chem. Phys. **135**, 204107 (2011).

[2]T. B. De Queiroz and S. Kümmel, "Charge-transfer excitations in low-gap systems under the influence of solvation and conformational disorder: Exploring range-separation tuning," J. Chem. Phys. **141**, 084303 (2014).

[3]L. Kronik, T. Stein, S. Refaely-Abramson, and R. Baer, "Excitation Gaps of Finite-Sized Systems from Optimally Tuned Range-Separated Hybrid Functionals," J. Chem. Theory Comp. **8**,

1515–1531 (2012).

[4]I. Schelter, J. M. Foerster, A. T. Gardiner, A. W. Roszak, R. J. Cogdell, G. M. Ullmann, T. B. De Queiroz, S. Kümmel, A. T. Gardiner, R. J. Cogdell, M. Ullmann, B. D. Queiroz, and S. Kümmel, "Assessing Density Functional Theory in real-time and real-space as a tool for studying bacteriochlorophylls and the light-harvesting complex 2," J. Chem. Phys. **151**, 134114 (2019), publisher: AIP Publishing, LLC.

[5]F. Plasser, M. Wormit, and A. Dreuw, "New tools for the systematic analysis and visualization of electronic excitations. I. Formalism," J. Chem. Phys. **141**, 024106 (2014).

[6]R. J. Cogdell, A. Gall, and J. Köhler, "The architecture and function of the light-harvesting apparatus of purple bacteria: from single molecules to in vivo membranes." Quarterly Reviews of Biophysics **39**, 227–324 (2006), iSBN: 0033-5835 (Print).

[7]M. Brütting, J. M. Foerster, and S. Kümmel, "Investigating Primary Charge Separation in the Reaction Center of Heliobacterium modesticaldum," J. Phys. Chem. B **125**, 3468–3475 (2021).

[8]B. Monserrat, "Vibrational averages along thermal lines," Physical Review B **93**, 014302 (2016).

[9]M. J. Field, "The pDynamo program for molecular simulations using hybrid quantum chemical and molecular mechanical potentials," J. Chem. Theor. Comput. **4**, 1151–1161 (2008).

[10]F. Neese, "The ORCA program system," WIREs Comput. Mol. Sci. **2**, 73–78 (2012).

[11]A. Sirohiwal, F. Neese, and D. A. Pantazis, "How Can We Predict Accurate Electrochromic Shifts for Biochromophores? A Case Study on the Photosynthetic Reaction Center," J. Chem. Theor. Comput. **17**, 1858–1873 (2021).

Acknowledgments

Throughout my academic journey, I have been fortunate to receive support and guidance from many individuals who have helped me in countless ways. Without their help, completing my thesis would not have been possible. Therefore, I would like to express my deepest gratitude and appreciation to the following people:

Dr. Linn Leppert, my supervisor, for her exceptional guidance and mentorship throughout my research journey. Her expertise in the field and unwavering dedication to my work have helped me develop both as a researcher and as an individual. I am particularly grateful for the freedom she gave me to pursue my own ideas and interests while also providing me with challenging yet fulfilling projects. I greatly appreciate her patience, encouragement, and valuable feedback that helped me shape my workflow and research direction. Working with her for the past five years has been an honor and I couldn't have asked for a better person to provide me with such outstanding support.

I would also like to express my sincere gratitude to the entire members of the Theoretical Physics IV research group, especially **Prof. Stephan Kümmel**, for providing me with the invaluable opportunity to work with their team. Prof. Kümmel's warm personality and willingness to help have been a source of comfort and strength for me, especially in the absence of my supervisor.

Prof. Benedetta Mennucci, for her great hospitality during my time in Italy, which played a huge role in making my stay truly memorable. The time I spent with them has given me a glimpse into what a highly competitive and rewarding academic life entails.

Monika Birkelbach, Susanne Süss, Markus Hilt, and Dr. Ingo Schelter for being extremely responsive in helping me with any technical and administrative matter I encountered.

In addition, I would like to thank my colleagues in **Leppert group**, specifically my office mate **Dr. Raisa Biega** for her joyful spirit that has created a warm and welcoming atmosphere in my daily working life. **Dr. Mario Rui Goncalves Marques** for her great engagement in our joint project, in the review of this thesis, and for sub-renting his apartment to me.

Among my best friends: **Fatemeh Sadat Tabatabaei**, who consistently motivated me to improve myself and carefully proofread large parts of this thesis. **Sanaz Hariri** who has been there for me in times of need and has been one of the most supportive people I know. **Mahla Mirzaee Kakhk, Maryam khourmehr, and Niloofar Ghafouri** for the good times we had on- and off-campus and will continue to have for many years to come.

Last, but by no means least, I would like to thank my wonderful family. My parents **Zahra** and **Aliakbar** and my sister and brother **Maryam** and **Jafar** who always have my back and were always understanding. I wouldn't be the person I am today without their love.

Eidesstattliche Versicherung

Hiermit versichere ich an Eides statt, dass ich die vorliegende Arbeit selbstständig verfasst und keine anderen als die von mir angegebenen Quellen und Hilfdmittel verwendet habe.

Weiterhin erkläre ich, dass ich die Hilfe von gewerblichen Promotionsberatern bzw. -vermittlern oder ähnlichen Dienstleistern weder bisher in Anspruch genommen habe, noch künftig in Anspruch nehmen werde.

Zusätzlich erkläre ich hiermit, dass ich keinerlei frühere Promotionsversuche unternommen habe.

Bayreuth, den .

Zohreh Hashemi